THE DEVICE APPLICATIONS AND CHARACTERIZATION OF NONSTOICHIOMETRIC GaAs GROWN BY MOLECULAR BEAM EPITAXY

by

FRANK WILLIAM SMITH, III

B.S., Yale University
(1980)

S.M., Massachusetts Institute of Technology
(1985)

Submitted in Partial Fulfillment of the
Requirements for the Degree of

Doctor of Philosophy

at the

MASSACHUSETTS INSTITUTE OF TECHNOLOGY

April 1990

© Massachusetts Institute of Technology 1990

Signature of Author________________________________
Department of Electrical Engineering and Computer Science
April 3, 1990

Certified by________________________________
Alan L. McWhorter
Thesis Supervisor

Accepted by________________________________
Arthur C. Smith
Chairman, Departmental Committee on Graduate Students

MASSACHUSETTS INSTITUTE
OF TECHNOLOGY

AUG 10 1990

ARCHIVES

LIBRARIES

THE DEVICE APPLICATIONS AND CHARACTERIZATION OF NONSTOICHIOMETRIC GaAs GROWN BY MOLECULAR BEAM EPITAXY

by

FRANK WILLIAM SMITH, III

Submitted to the Department of Electrical Engineering
and Computer Science on April 3, 1990 in partial
fulfillment of the requirements for the
Degree of Doctor of Philosophy

ABSTRACT

A GaAs layer grown by molecular beam epitaxy at low substrate temperature has been found to eliminate dc and ac sidegating effects in GaAs integrated circuits (IC's), both in the dark and under white-light illumination. As the temperature in MBE growth is reduced from the standard 500-600°C range (with post-growth annealing temperature maintained at 600°C), the resistivity of the annealed material increases, but the layer remains crystalline for growth temperatures as low as 200°C. In addition, the low-temperature (LT) GaAs displays a dilated lattice constant and approximately 1 at.% excess arsenic. Evidence has been found for arsenic antisite (As_{Ga}), arsenic interstitial (As_i), and gallium vacancy (V_{Ga}) defects. The LT GaAs layer appears to be stable at elevated temperatures, and high-quality, conducting GaAs can be grown on it at normal growth temperatures.

In electronic device applications, the LT GaAs buffer eliminates the duty-cycle effect, a serious problem for high-speed digital and microwave IC's that incorporate digital control circuitry, as well as the resistive component of RF coupling and sidegate-bias-induced changes in the scattering parameters of microwave field-effect transistors. Further, since the dielectric breakdown strength of LT GaAs is approximately an order of magnitude greater than that of semi-insulating GaAs, the use of the LT GaAs buffer permits higher voltages to be applied than are possible with conventional buffer layers or substrates. The LT GaAs buffer has also been shown to enhance submicrometer-gate-length MESFET performance by reducing short-channel effects.

Use of this buffer material as a photoconductive switch has enabled electrical pulses as short as 450 fs and picosecond pulses with peak voltages as large as 16 V to be produced, both record values. Possible applications of this device are in optical systems for high-speed electronic device and circuit testing and as a detector for optical interconnects.

Semi-quantative models of as-grown and annealed LT GaAs have been formulated using the results of numerous characterization techniques. As-grown LT GaAs contains $\sim 10^{20}$ cm^{-3} As_{Ga}–related defects of which $\sim 5 \times 10^{18}$ cm^{-3} are ionized. An

isolated V_{Ga} or V_{Ga} complex is hypothesized to be the compensating acceptor. Also As microclusters and As_i are present and contribute to the dilated lattice constant of LT GaAs. The deep-level band associated with the As_{Ga}–related defects can account for the observed quenching of photoluminescence, strong deep-level infrared (IR) absorption, and hopping conductivity at low temperature.

The deep-level density and the disorder in the LT GaAs epilayer are observed to decrease monotonically with post-growth annealing temperature. However, the ~1 at.% arsenic excess in the crystal is unchanged by an *in situ* anneal with an As overpressure. The V_{Ga}, As microclusters, and ionized As_{Ga}–related defects are reduced below detectable levels by the anneal, although As_i defects remain. After the anneal, the concentration of neutral As_{Ga}–related defects is $\sim 10^{19}$ cm^{-3} and the material has a high resistivity and a large breakdown voltage. As was the case for the as-grown material, the annealed LT GaAs shows quenched photoluminescence, strong deep-level IR absorption, and a hopping conductivity at low temperature.

Thesis Supervisor: Alan L. McWhorter
Title: Professor of Electrical Engineering

ACKNOWLEDGMENTS

This thesis represents a considerable body of work, and I owe much to the many persons who have contributed to the effort. I would like to take this opportunity to thank these individuals for their assistance and their encouragement.

It has been a privilege to be Professor Alan L. McWhorter's student during the past three and one-half years. His breadth of knowledge, his willingness to explain issues in detail, and his high standaras have not only guided my work to success but have helped me to grow as a scientist. My understanding of the mathematical and scientific basis of the field, as well as my written and verbal communication skills, have improved significantly under his tutelage. His interest in and direction of my research have been invaluable throughout this effort.

I have been most fortunate for the opportunity to work closely with A. Robert Calawa during my graduate program. Bob suggested this topic for research, and together we have jointly published ten papers and filed two patents on the processing and properties of low-temperature (LT) GaAs. His enthusiasm for research, his extensive background, and his guidance have helped to make our breakthrough for GaAs technology possible. He has helped me to become a proficient experimentalist and a contributing member of the scientific community.

I am very appreciative of the opportunity to have worked with Maria A. Kaminska of the University of California, Berkeley, on the characterization and modeling of LT GaAs. Maria performed a number of important characterization experiments and collaborated in constructing the model of LT GaAs presented in Sec. 5.6 of this thesis. It was a major disappointment to me that Maria had to leave the United States and return to Poland, and will no longer be actively involved with the characterization of LT GaAs. This will be a significant loss.

Two distinct advantages of doing thesis research at Lincoln Laboratory are the opportunity to work with state-of-the-art equipment and outstanding people. Numerous individuals at Lincoln Laboratory have contributed to this work, to whom I owe my sincere appreciation.

For their consistent support, advice, and encouragement I thank Yannick L. LeCoz (currently with RPI) and Elliott R. Brown.

For their assistance with the device fabrication and testing I thank Michael J. Manfra, Chang-Lee Chen, Vicki Diadiuk, Han Q. Le, Leonard J. Mahoney, Cheryl A. Graves, and Douglas Burrows. In particular, I thank Michael Manfra for numerous helpful discussions on MBE and for his support, advice, and encouragement throughout this research effort. I also thank Chang-Lee Chen for many useful discussions on GaAs MESFET testing and analysis.

For their assistance with the material characterization I thank George W. Turner, Bor-Yeu Tsaur, Brian F. Aull, Mary C. Finn, and Margolia N. Gilson. In particular, I thank George Turner and Bor-Yeu Tsaur for helpful discussions on the analysis of the material properties of LT GaAs.

I also thank Peter J. Daniels, Deborah J. Landers, K. Alexander McIntosh, Richard H. Mathews, Paul Cociani, Daniel R. Calawa, and Carl H. Anderson for their technical assistance.

I gratefully acknowledge Phoebe L. Wang, William A. Breen, Gregory E. Head, and the staff of the Lincoln Laboratory Publications Group for the artwork.

For numerous helpful technical as well as editorial discussions, I thank R. Allen Murphy, Alan J. Strauss, and the late William T. Lindley.

Collaboration with researchers at other laboratories has not only contributed to the success of this project, but has led to a number of joint publications, an enhanced understanding of LT GaAs, and the demonstration of new LT GaAs device applications. For all of their help, I thank Professor Eiche R. Weber and his group at the University of California, Berkeley, and the Lawrence Berkeley Laboratory, including Zuzanna Liliental-Weber, Kin-Man Yu, and, as previously mentioned, Maria Kaminska; Professor Gerard A. Mourou and his group at the University of Michigan (formerly at the University of Rochester), which includes Shantanu Gupta, Michael Y. Frankel, James M. Chwalek, and Douglas R. Dykaar (now with Bell Laboratories); Professor George N. Maracas and his students at Arizona State University; Professor Robert S. Berg and Nergis Mavalvala of Wellesley College; and John C. Huang (currently with Raytheon Co.) and Frank H. Spooner of Alpha Industries.

I am particularly appreciative of the numerous useful discussions with Robert Berg on the Raman scattering measurements of LT GaAs and with Shantanu Gupta on the testing and analysis of LT GaAs switch.

I also thank David C. Look and Philip W. Yu of the Avionics Laboratory at Wright-Patterson Air Force Base, and William J. Tanski and Gregory A. Peterson of the United Technology Research Center for measurements of LT GaAs.

I thank Gerald L. Witt of the Air Force Office of Scientific Research for making many of these collaborations possible. He has supported the Lincoln Laboratory research effort as well as that of Professors Weber and Mourou and Drs. Look and Yu. His financial support as well as his interest and enthusiasm have made possible the rapid progress of this research.

I thank Professors Clifton G. Fonstad and L. Raphael Reif of M.I.T., who served as readers of my thesis.

Lastly, for their loving support and encouragement throughout my years in graduate school I thank my family.

TABLE OF CONTENTS

ABSTRACT 2
ACKNOWLEDGMENTS 4

1 INTRODUCTION 8
1.1 Motivation and Summary of Work 8
1.2 Organization of Thesis 10

2 MBE GROWTH 13
2.1 MBE Background Discussion 13
2.2 MBE Growth of GaAs 16
2.3 LT GaAs Growth and Properties 21

3 ELECTRONIC DEVICE APPLICATIONS 34
3.1 Background 34
3.2 2-μm-Gate-Length MESFET's 35
3.2.1 Sidegating, dc, and Microwave Results 35
3.2.2 Implications of Sidegating Elimination for GaAs IC's 43
3.2.2.1 RF Coupling 45
3.2.2.2 Scattering Parameters 55
3.2.2.3 Digital Circuits 60
3.2.2.4 Interaction Between RF and Digital Circuits 64
3.2.2.5 Discussion 66
3.2.3 Elimination of Sidegating-Enhanced 1/f Noise 69
3.3 0.27-μm-Gate-Length MESFET's 71
3.4 Other Electronic Device Applications of LT GaAs 77
3.4.1 GaAs MESFET IC's Using the LT GaAs Buffer 77
3.4.2 AlGaAs/GaAs HEMT's 77
3.4.3 LT GaAs MISFET 78
3.4.4 Transient Radiation Upset 79
3.4.5 Low-Temperature $In_{0.52}Al_{0.48}As$ 79
3.4.6 Lattice-Mismatched Heteroepitaxy 80
3.4.6.1 LT GaAs-on-Silicon 80
3.4.6.2 LT $In_{0.53}Ga_{0.47}As$-on-GaAs 82

4 OPTOELECTRONIC DEVICE APPLICATIONS 84
4.1 Introduction to Photoconductive Switches 84
4.2 Autocorrelation Measurement of an LT GaAs Switch 88
4.3 Electro-optic Sampling Measurements of LT GaAs Switches 94
4.4 Influence of Growth Conditions 105
4.5 Electrode Dependence 106
4.6 Excitation Dependence 107

5 LT GaAs CHARACTERIZATION 110
5.1 Background 112
5.1.1 EL2 113
5.1.2 As_{Ga}-Related Defects 119
5.2 Compositional 121
5.2.1 AES and XPS 121
5.2.2 AEM and PIXE 125
5.2.2.1 AEM 125
5.2.2.2 PIXE 130
5.3 Structural 133
5.3.1 TEM 133
5.3.2 X-Ray 138
5.3.3 Ion Channeling 145
5.4 Optical 150
5.4.1 PL 151
5.4.2 IR Absorption 161
5.4.3 Raman Scattering 177
5.5 Electrical 199
5.5.1 EPR 200
5.5.2 Electrical Conductivity 215
5.5.2.1 Hall Effect 215
5.5.2.2 I-V-T` 228
5.6 Discussion 230
5.7 Reproducibility of MBE-Grown Epilayers 244
5.7.1 Substrate Temperature Variation 245
5.7.2 Nonuniform Flux Distribution 246
5.7.3 Improved MBE Reproducibility 248

6 CONCLUSIONS 250

REFERENCES 256

BIOGRAPHICAL SKETCH 266

CHAPTER 1. INTRODUCTION

1.1 Motivation and Summary of Work

The inability to fully isolate devices in GaAs integrated circuits (IC's) has stimulated research into techniques to prepare semi-insulating (SI) GaAs. Although in the past both bulk crystals and thin epitaxial layers of SI GaAs have been prepared by many techniques, none of these materials was able to eliminate the parasitic conduction problem in GaAs IC's known as sidegating [1]-[7]. Sidegating is the change of drain-source current in a field-effect transistor (FET) as a result of a voltage applied to the substrate or an adjacent, and nominally isolated, contact pad (sidegate).

In 1987, we reported the growth of a GaAs layer by molecular beam epitaxy (MBE) that is highly resistive and eliminated sidegating in GaAs metal-semiconductor field-effect transistor (MESFET) circuits fabricated in conducting GaAs layers grown upon this insulating layer [8]. Since that time we have continued to demonstrate the performance improvements possible in GaAs-based electronic and optoelectronic devices and circuits by using this material [9]-[15]. The physics of this material has also been studied to understand and model its unique and desirable properties [16], [17]. The demonstration of the device applications and the characterization of this material are the subject of this work. Not only will this thesis document results from our work on this material, but results from other research laboratories will also be summarized. As a result of our publications and the profound electronic and optoelectronic device improvements possible using this material, virtually every major organization involved with GaAs research and development is now actively investigating this material for their applications.

Although high-quality, conducting films of GaAs can be deposited by MBE at substrate temperatures T_s between 500 and 640°C, we demonstrated that GaAs depos-

ited by MBE at low T_s, between 150 and 300°C, is crystalline and highly resistive [8]. However, after the growth of this semi-insulating GaAs epitaxial layer, the T_s can be raised to the normal growth temperature and high quality GaAs, suitable for device and circuit fabrication, can be deposited. We call this semi-insulating epitaxial layer low-temperature (LT) GaAs. LT GaAs is nonstoichiometric, containing an ~1 at.% arsenic excess [10], exhibits no measurable photoluminescence (PL) [10], and yet is of high crystalline perfection, as determined by lattice-imaging transmission electron microscopy (TEM) [16].

In addition to eliminating dc sidegating in GaAs MESFET circuits as already mentioned, this LT GaAs buffer layer has also been shown to eliminate sidegating in GaAs/AlGaAs high electron mobility transistor (HEMT) circuits [18]. Sidegating effects relevant to GaAs MESFET analog, digital, and microwave IC's have been markedly reduced or eliminated by using the LT GaAs buffer layer [10],[11]. Short-channel effects in submicrometer-gate-length MESFET's have also been markedly reduced by incorporating the LT GaAs buffer immediately beneath the conducting channel [9]. Frequency divider circuits fabricated from 0.2-μm-gate-length GaAs MESFET's incorporating the LT GaAs buffer have demonstrated state-of-the-art performance [19].

Photoconductive detectors fabricated with 600°C-annealed LT GaAs layers have shown switching speeds of less than 500 fs with excellent sensitivity [13]-[15]. These results are the best for any photoconductive switch reported to date. The LT GaAs switch may find extensive use in high-speed device and circuit testing.

The unique properties of LT GaAs can be ascribed to the excess arsenic in the crystal. The ~1 at.% excess arsenic concentration in LT GaAs is over four orders of magnitude greater than the deviation from stoichiometry observed in GaAs crystals fabricated by any other growth technique. In as-grown and annealed LT GaAs epi-

layers, arsenic antisite (As_{Ga}) defects are observed at concentrations of approximately 10^{20} and $10^{19} cm^{-3}$ respectively. The excess arsenic is also incorporated in interstitial lattice positions, as evidenced by ion channeling and Raman scattering measurements. However, As precipitates have never been observed in LT GaAs, despite an arsenic concentration well in excess of the equilibrium solubility limits. Detailed material studies of LT GaAs have been reported [16],[17].

Also the success of LT GaAs has stimulated research into the low-temperature growth of other compound semiconductors by MBE. LT GaAs on GaAs-on-Si, LT $In_{0.53}Ga_{0.47}As$ on GaAs, and LT $In_{0.52}Al_{0.48}As$ on InP have all been published [20]-[22]. Improved material quality and device performance have been obtained for high quality conducting layers deposited on top of the low-temperature-grown material. Our research into the low-temperature growth of compound semiconductors by MBE has exposed a new class of materials that exhibit unique properties and enhance device and circuit performance.

1.2 Organization of Thesis

Chapter 2 is a discussion of MBE. Growth models and *in situ* analysis techniques are described. Previous investigations of the low-temperature growth of GaAs by MBE are summarized, and growth models consistent with these results are briefly discussed. The technique that we have used to prepare LT GaAs is detailed. The results of a few characteriztion experiments on LT GaAs are presented. This discussion is included only to provide enough information about the material to set the stage for the device results given in Chapters 3 and 4. The results of our extensive characterization study appear in Chapter 5.

The electronic device applications of LT GaAs are discussed in Chapter 3. Section 3.1 provides an introduction to the problems of sidegating in GaAs IC's and

short-channel effects in submicrometer-gate-length MESFET's. The dc and RF sidegating effects and the elimination of sidegating enhanced 1/f noise results are presented in Section 3.2. The improved performance of 0.27-μm-gate-length MESFET's using the LT GaAs buffer is summarized in Section 3.3. Other electronic device applications of LT GaAs, such as for HEMT's, MISFET's, and GaAs-on-Si, are briefly discussed in Section 3.4.

The optoelectronic device applications of LT GaAs are presented in Chapter 4. This discussion is devoted to the photoconductive switch application. After an introduction to the field, results on a LT-GaAs-based Auston switch, on photoconductive-gap switches, and on sliding-contact switches are presented [13]-[15]. The dependence of switch performance on growth conditions, switch geometry, metallization, and laser excitation power is discussed [15].

Chapter 5 begins with a brief discussion of the literature on arsenic-excess-related defects in GaAs. Arsenic antisite defects are observed in undoped, SI GaAs bulk crystals grown by the liquid encapsulated Czochralski (LEC) technique, and in GaAs damaged by plastic deformation and neutron and electron irradiation [16]. The principal deep level in LEC SI GaAs is EL2, which has been tentatively identified as As_{Ga}. However, EL2 in LEC SI GaAs and As_{Ga} generated by damaging the crystal exhibit different optical properties, as will be discussed in Chapter 5. This information is used in the identification of the arsenic-excess-related defects in LT GaAs.

The results of numerous characterization experiments on LT GaAs are also given in Chapter 5. Compositional, structural, optical, and electrical techniques have been used both to document the microscopic and macroscopic properties of LT GaAs, as well as to explain the physical origin of the defects in LT GaAs. From the results of these experiments, semi-quantitative models of as-grown and annealed LT GaAs are proposed.

The discovery of LT GaAs, the demonstration of its device and circuit applications, and its characterization have opened new avenues for device physics and materials science research. In the device and circuit applications area, LT GaAs and other LT-grown materials hold significant promise. In Chapter 6, a few of the additional applications of LT GaAs are presented, and additional characterization experiments are proposed that can be used to enhance our understanding of LT GaAs.

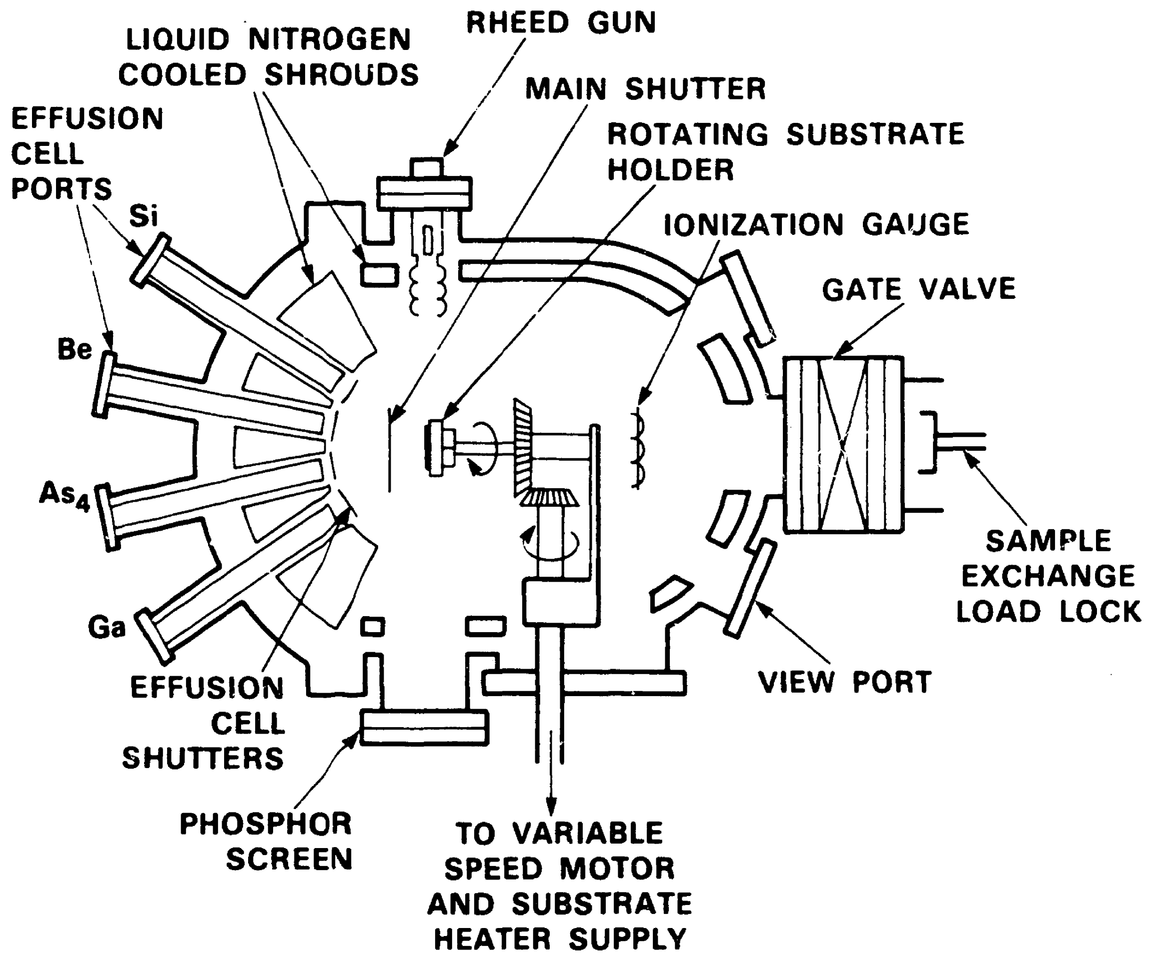

Fig. 2.1 Schematic cross section of an MBE growth chamber.

position. The As flux and the substrate temperature T_s determine the surface reconstruction (see below).

The gallium source is the liquid metal (effusion cell temperature $T_{Ga} \cong 1000°C$) and the vapor phase consists of elemental Ga atoms. In contrast, the typical arsenic source is a solid ($T_{As} \cong 300°C$) and the vapor phase is the tetramer, As_4. All the GaAs and AlGaAs layers discussed in this work were grown using an As_4 source. However, the dimer, As_2, and in some cases the monomer, As, can be achieved by cracking either As_4 or arsine gas (AsH_3) [26],[27]. The use of As_2 or As to grow LT GaAs will be discussed in Chapter 6.

The growth mechanism of GaAs is different depending on the arsenic species used. On the basis of modulated beam experiments, several models for the growth of GaAs have been proposed [28]. At the present time, the correct model is not entirely clear and is still the subject of research. The MBE deposition of GaAs is dominated by growth kinetics rather than by equilibrium considerations because MBE is a highly nonequilibrium process. Kinetic growth models will be discussed in more detail below.

To monitor the MBE growth of epitaxial films, two analytical instruments are generally included in the growth chamber. The first is a quadrupole mass spectrometer and the second is a reflected high energy electron diffraction (RHEED) system. The mass spectrometer is used to monitor the background impurities in the system and in modulated beam experiments to study reaction kinetics [28]. In RHEED, a high energy electron beam (~10 keV) is incident on the substrate at a glancing angle (1-2°). The diffraction of this beam is primarily from the surface of the growing crystal (1-2 monolayers) and not the bulk GaAs [29]. The projection of the diffracted beam onto a phosphor screen is a streaked pattern indicative of the reconstructed surface. The streaks are characteristic of diffraction from a two-dimensional

lattice net [29]. By observing the RHEED pattern during growth, information can be gained about the properties of the growing epitaxial layer on an atomic layer by atomic layer basis. If the RHEED pattern becomes spotted, this is indicative of "island growth" or three-dimensional growth [29]. The spots are characteristic of transmitted electron diffraction rather than reflected electron diffraction [29]. The Lincoln Laboratory MBE system has both a mass spectrometer and a RHEED system in the growth chamber. RHEED patterns will be discussed in more detail below (see Section 2.3).

2.2 MBE Growth of GaAs

A number of authors have studied the growth of GaAs by MBE as a function of T_s [30]-[36]. High quality GaAs (good electrical and optical properties) is generally grown by MBE at a growth rate of 1 μm/h over a range of T_s from ~500-640°C. The upper value of T_s is the congruent sublimation temperature T_{cs} for GaAs. Above 640°C, without an As overpressure, As preferentially evaporates from the GaAs surface leaving metallic Ga droplets. The lower limit is approximately 500°C, because below this temperature, for a growth rate of 1 μm/h, the film becomes compensated and the resistivity increases, as shown in Fig. 2.2 [30]-[36]. By decreasing the growth rate to 0.02 μm/h, high quality GaAs can be grown at T_s as low as 380°C [35]. Recently, high quality material has been grown at 200°C by using migration enhanced epitaxy, a modified form of MBE based on growth control using RHEED oscillations and separate applications of Ga and As_4 beams [37]. (RHEED oscillations are discussed in Sec. 2.3.)

For growth of high quality GaAs at a growth rate of 1 μm/h, and for $500<T_s<640$°C, the growing GaAs surface is either As stabilized or Ga stabilized. The As-stabilized surface has an excess of arsenic, whereas the Ga-stabilized surface

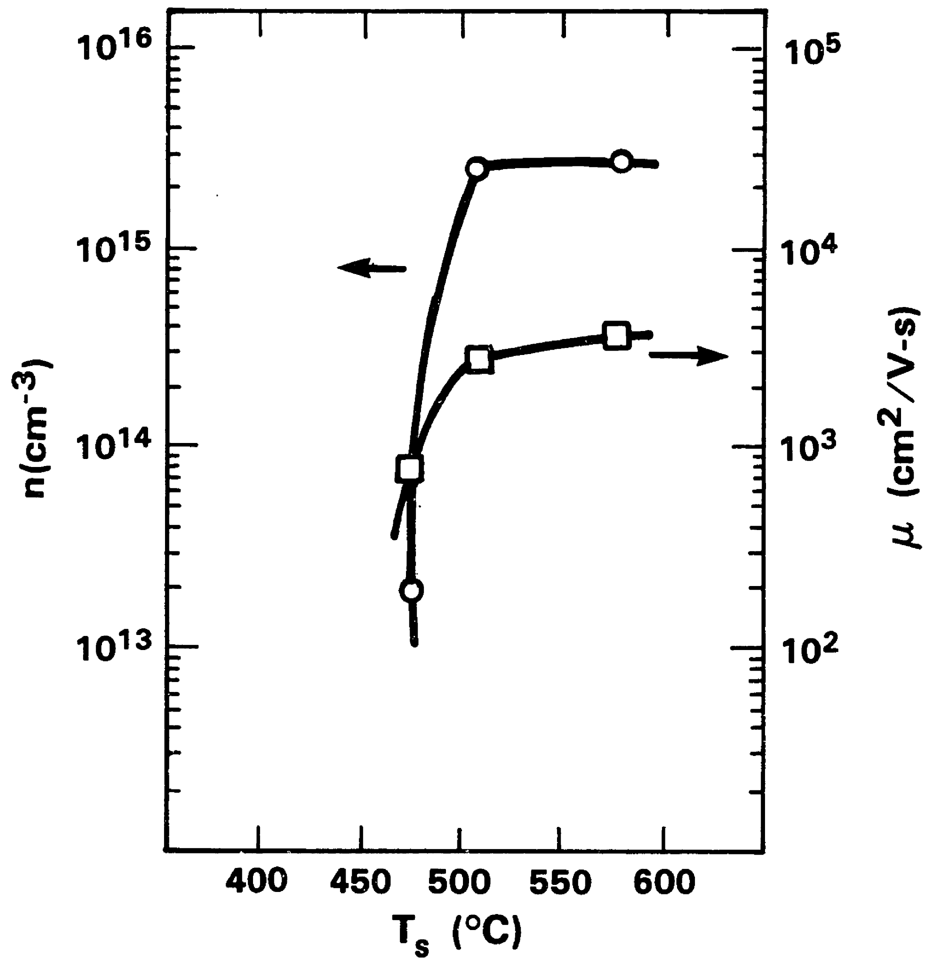

Fig. 2.2 Variation of electron density n and mobility μ as a function of substrate temperature for a growth rate of ~1 μm/h. After Metze and Calawa [35].

has an excess of gallium. (See below for models of an As-stabilized surface.) Whether the surface is As or Ga stabilized depends upon the flux ratios of the two species and T_s [29]. The higher T_s, the larger is the As to Ga flux ratio needed to maintain an As-stabilized surface. The As- and Ga-stabilized (001) GaAs surfaces can be differentiated by RHEED [29]. The surface reconstruction for an As-stabilized surface is (2x4) and for Ga-stabilized surface is (1x3). This notation is defined in Ref. [38]. The term (m x n) means that relative to the underlying bulk lattice the unit mesh of the surface is m times larger in the [110] direction and n times larger in the [$1\bar{1}0$] direction [38]. The unit mesh of a reconstructed surface is changed since additional rows and/or columns of atoms are incorporated between the bulk lattice sites in order to minimize the total energy of the surface [29],[38],[39]. All the growth results presented in this work are for As-stabilized growth conditions, where the BEP of the As_4 flux was ten times that of the Ga flux.

Using optical deep-level transient spectroscopy (o-DLTS) [40], Stall et al. found that as T_s was reduced from 580 to 300°C the concentration of electron traps EB3, EB6, and EL3 and hole trap HB6 increased significantly [34]. Stall et al. could use the o-DLTS technique for films grown at substrate temperatures only as low as 300°C, because below this temperature the film became semi-insulating and could not be made conducting, irrespective of the nominal doping level [34]. Muritoma et al. [31] and Neave et al. [30] have also observed highly resistive films for $T_s < 500$°C. The resistivity of GaAs films grown at $T_s < 500$°C is found to decrease as the growth rate is decreased [35] and is found to be larger for growth with As_4 flux than with As_2 flux [36].

All the aforementioned authors present qualitative theories as to the origin of the increased resistivity. To some extent, these authors draw upon the kinetic growth models of Foxon and Joyce [28]. Using the results of modulation spectroscopy

experiments, Foxon and Joyce proposed mechanisms for As_2 and As_4 growth of GaAs and calculated As_2, As_4, and Ga sticking coefficients, lifetimes, and surface energies. The kinetic models for Ga-stabilized growth of GaAs using As_2 and As_4 are shown in Figs. 2.3(a) and 2.3(b), respectively [28]. Foxon and Joyce found that the As_2 growth kinetics is a first-order process, whereas the As_4 kinetics is a second-order process. In both cases, the Ga sticking coefficient is essentially unity for $T_s <$ 640°C. Between ~500 and 640°C the sticking coefficients of As_2 and As_4 are unity and 0.5, respectively, when free Ga is present. The As_2 and As_4 residence times increase as T_s is lowered.

Drawing upon the qualitative aspects of Foxon and Joyce's model, Stall et al. hypothesized that the increased deep-level concentration in the epitaxial film observed as T_s is reduced is due to excess arsenic on the surface, resulting in arsenic interstitials (As_i), As_{Ga}, or Ga vacancies (V_{Ga}) [34]. Metze and Calawa explain their results by asserting that at reduced temperatures the Ga and As adatoms do not have time to move to their respective equilibrium lattice sites before they are incorporated into the growing film [35]. This leads to an increased number of defects in the film, possibly as As_{Ga}, V_{Ga}, and/or complexes or clusters.

Further qualitative support for the hypothesis that excess arsenic in GaAs films grown for $T_s <$ 540°C leads to the high resistivity is given by theoretical studies of surface reconstruction. Chadi, using energy-minimization calculations based on tight binding, showed that the standard (2x4) As-stabilized surface reconstruction observed by RHEED can arise from arsenic dimers bonded so as to form the upper surface of the growing GaAs film [39]. Chadi's model predicts that excess arsenic exists on the surface of the growing film. Foxon and Joyce have observed this same phenomenon [28]. Thus, if the growth rate is "fast enough " (the term "fast enough" is purely qualitative at this time) as compared with the arsenic lifetime on the surface, it is

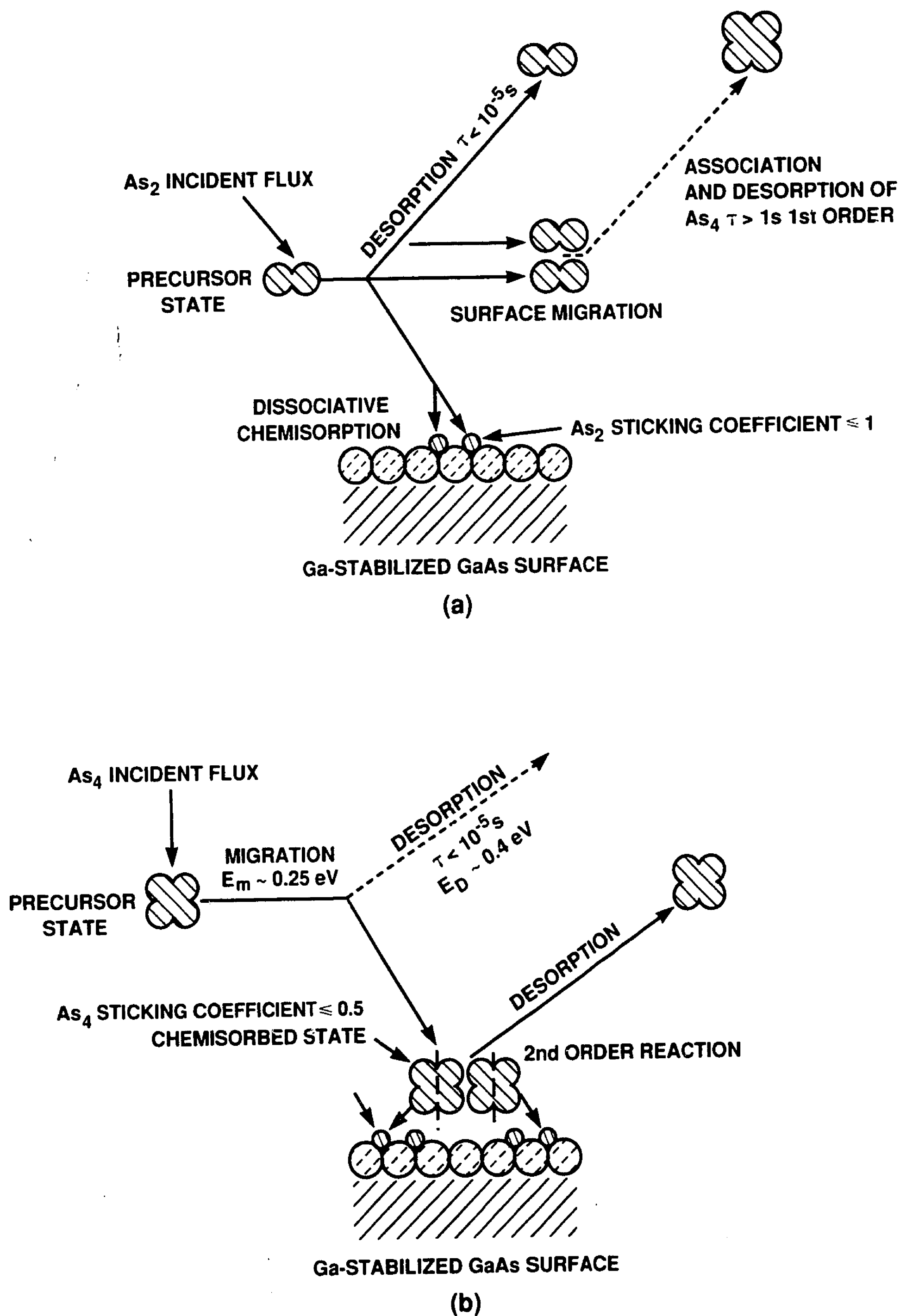

Fig. 2.3 Models for MBE growth kinetics of Ga-stabilized GaAs surfaces: (a) As_2 source, and (b) As_4 source. After Foxon and Joyce [28].

possible that the excess arsenic does not have time to desorb from the surface before it is captured in the growing film. In this way, the growing crystal would maintain the GaAs lattice but would have an excess of arsenic, both as insterstitials and antisite defects. Experimental evidence for excess arsenic in a GaAs epitaxial layer grown at low T_s (~200°C) is discussed in the next section.

These discussions of the origin of the defects in GaAs films grown at reduced T_s (T_s < 500°C) and the surface reconstructions observed by RHEED have been qualitative and lacking in detail both for brevity and because these topics are not well understood. The literature on surface reconstruction, RHEED patterns, and surface band structure is large and no attempt has been made to survey all the results. It has been the intent of this section simply to summarize some of the previous findings and set the stage for the experimental results presented in the next section. One of the goals of this thesis is to address the question of the physical origin of the defects in GaAs epitaxial films grown at reduced T_s.

2.3 LT GaAs Growth and Properties

The impetus for this thesis came from the work of Metze and Calawa [35]. Given the need for a high resistivity film as a buffer layer for GaAs MESFET's (as outlined in Chapter 1 and discussed in detail in Chapter 3), it was felt that GaAs grown by MBE at low T_s would be a likely candidate for this application. The results of using GaAs grown at low T_s as the buffer layer for MESFET's are presented in the next chapter. In this section, the LT GaAs growth parameters and some of the early characterization results that we obtained for GaAs films grown by MBE at low T_s are presented. The characterization results described in this section constitute only a fraction of the total work done to document the properties of LT GaAs. A more detailed discussion of the characterization experiments and results

will be given in Chapter 5. The results presented here are included only to provide a brief overview to the material and to serve as an introduction to the electronic and optoelectronic devices of Chapters 3 and 4.

We have found from current-voltage measurements and Hall effect measurements (see Chapter 5) that the resistivity of annealed LT GaAs epilayers increases as the substrate temperature used for growth is decreased. Thus, it was felt that the best isolation would be provided by growing the buffer at the lowest possible T_s. While epitaxial GaAs layers can be grown at low T_s, these layers will be crystalline only up to a critical thickness, after which the layer becomes polycrystalline. At 150°C, the growing film becomes polycrystalline for thicknesses greater than ~0.5 μm. At 200°C, the film becomes polycrystalline for thicknesses greater than ~3 μm. Since 2-μm-thick layers of this material were needed as the buffer layer for MESFET's (see Section 3.2), 200°C was chosen as the standard T_s for growth of LT GaAs. For this reason, virtually all of the device results that will be presented in Chapters 3 and 4 are for LT GaAs layers grown at T_s equal to 200°C. It is important to note that LT GaAs films can be grown at other T_s (up to ~500°C), and this has been used to help characterize the material (see Chapter 5). All LT GaAs epilayers reported in this thesis were grown under arsenic-stablized growth conditions (As_4:Ga BEP ratio of 10:1), at a growth rate of 1 μm/h, on (001)-oriented GaAs substrates.

It was found that epitaxial layers grown at low T_s exhibit different surface reconstruction from that observed at 580°C. Typical RHEED patterns observed during growth at 180°C are shown in Fig. 2.4. Figure 2.4(a) shows the RHEED pattern of the sample at 180°C, just after the sample has been cooled from 580°C, but before growth at 180°C has commenced. (A buffer layer is always grown initially on the substrate at 580°C to smooth the substrate surface. GaAs is not deposited as the sample is cooled to 180°C.) The (2x4) surface reconstruction, typical of arsenic-stabilized

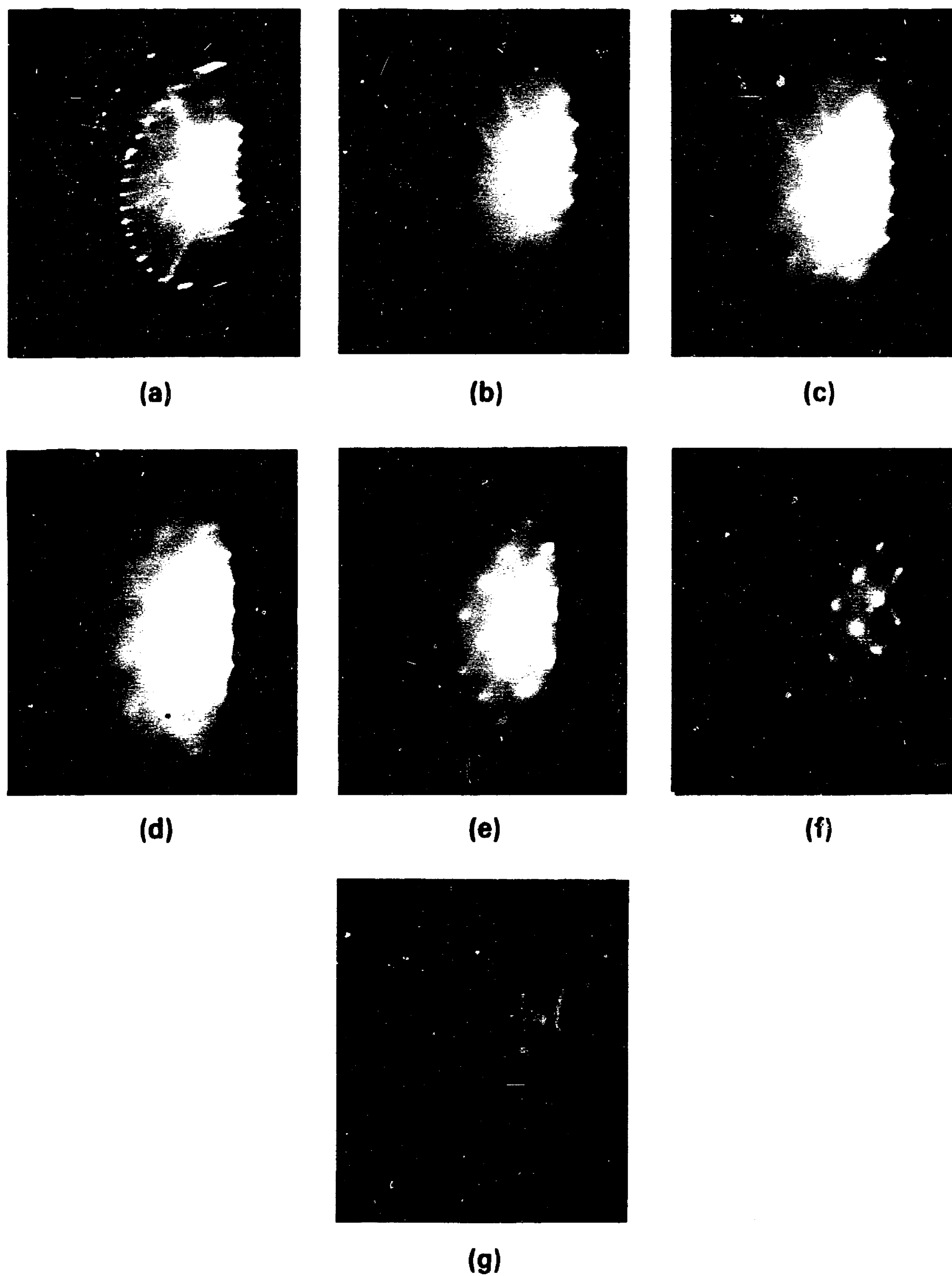

Fig. 2.4 RHEED patterns observed during growth of LT GaAs at ~180°C: (a) prior to LT GaAs growth at 180°C, (b) just after LT GaAs growth was initiated, (c) after ~0.5 μm of LT GaAs, (d) after ~1.0 μm of LT GaAs, (e) after ~1.5 μm of LT GaAs, (f) after ~2.0 μm of LT GaAs, and (g) after ~2.3 μm of LT GaAs.

growth at 580°C, is observed to be frozen-in as the temperature is reduced. Figure 2.4(b) is the RHEED pattern observed immediately after growth at 180°C is initiated. The surface is no longer reconstructed and the RHEED pattern (1x1) is indicative of the bulk GaAs lattice. This pattern indicates that the growing film is crystalline with roughly the same lattice constant as the GaAs substrate (see Section 5.3). Figures 2.4(c), (d), (e), (f), and (g) are RHEED patterns after approximately 0.5, 1.0, 1.5, 2.0, and 2.3 μm of growth at 180°C, respectively. Initially the film becomes spotted, indicative of "island growth" [29], and ultimately becomes polycrystalline, as indicated by the Debye-Scherrer rings [41].

For thicknesses less than or equal to ~3 μm, LT GaAs grown at 200°C is crystalline, and good quality GaAs can be grown upon this layer. RHEED patterns of LT GaAs grown at 200°C followed by GaAs growth at 580°C are shown in Fig. 2.5. Figure 2.5(a) is the RHEED pattern of a sample of GaAs at 580°C before growth of the 200°C layer. The (2x4) surface reconstruction is clearly evident. Figure 2.5(b) is the RHEED pattern after growth of a 2-μm-thick LT GaAs layer at 200°C. Although the RHEED pattern is spotted, the layer is still crystalline. Figure 2.5(c) is the RHEED pattern of the same sample after the temperature has been raised to 580°C and a 0.3-μm-thick layer of n-GaAs has been grown on top of the LT GaAs layer. Again the (2x4) surface is observed and RHEED oscillations [42] occur when growth is initiated. RHEED oscillation is the term used to describe the damped oscillations observed in the intensity of the RHEED patterns during growth [42]. The period of the RHEED oscillation corresponds to the deposition of one monolayer of GaAs. RHEED oscillations are thought to be related to changes in surface roughness on an atomic scale [42]. Since RHEED oscillations occur only for high quality, smooth films, the fact that RHEED oscillations can be seen for GaAs epitaxial layers grown at 580°C on top of the LT GaAs layer indicates that the epitaxial layers are of good

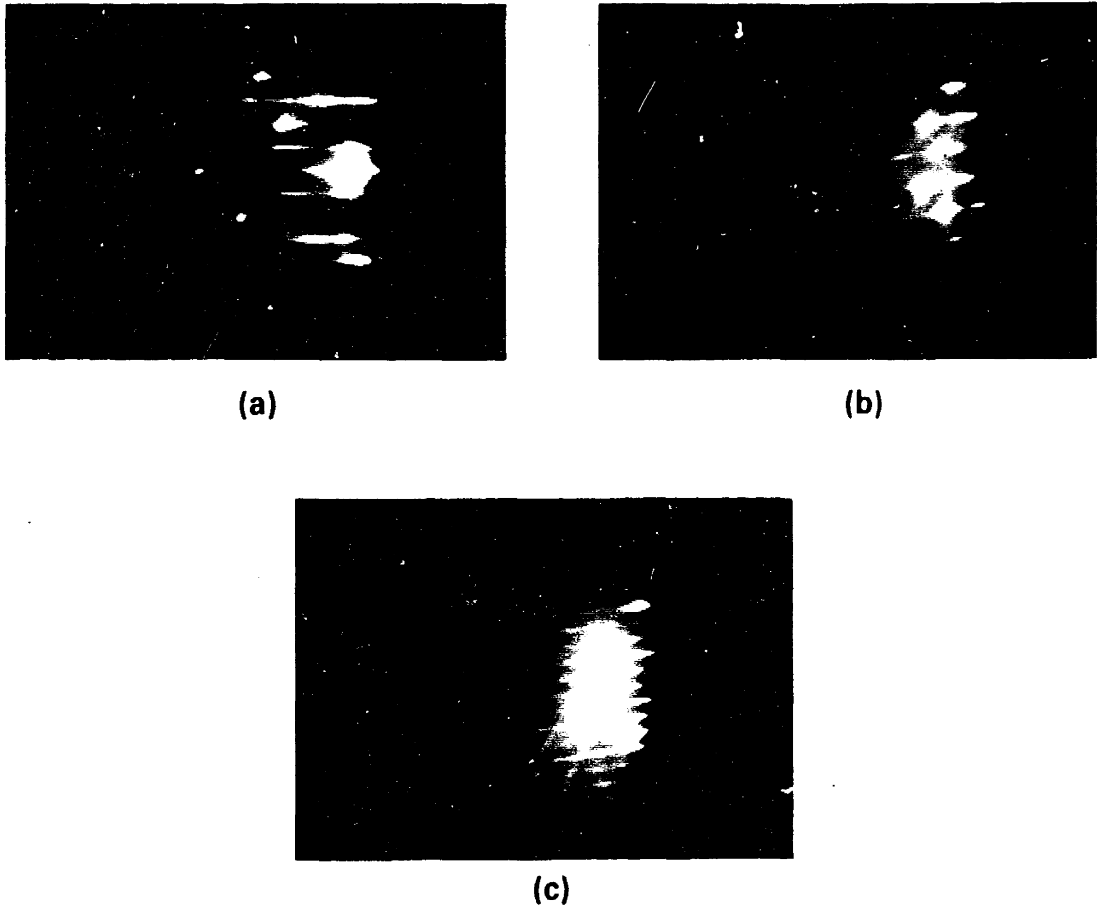

Fig. 2.5 RHEED patterns (a) of As-stabilized (2x4) GaAs surface at 580°C prior to LT GaAs growth, (b) after ~2 μm of LT GaAs at 200°C, and (c) after 0.3 μm of n-GaAs grown at 580°C on top of the 2-μm-thick LT GaAs layer.

crystalline quality and are smooth on an atomic scale.

As will be discussed in detail in Chapter 5, the as-grown 200°C LT GaAs epilayers exhibit distinctly different properties from a 200°C-grown LT GaAs layer that has been annealed at 600°C for approximately 10 min. All of the device results to be presented in Chapters 3 and 4 are for films of LT GaAs grown at approximately 200°C and annealed at 600°C. The remainder of this section is devoted to characterization results of annealed and unannealed films of LT GaAs grown at 200°C. This discussion is intended simply to demonstrate the unique properties of LT GaAs and to motivate the device applications discussed in Chapters 3 and 4. Detailed characterization results and a proposed model will be discussed in Chapter 5.

The crystal quality of the films grown at 200°C on (001)-oriented substrates has been examined by the techniques of single-crystal x-ray diffraction, double-crystal x–ray diffraction, transmission electron microscopy (TEM), and transmitted electron diffraction (TED). Single-crystal x-ray results for 2-μm-thick films grown at 200°C and unannealed show the characteristic (001) GaAs peaks. The peaks are only slightly broader for the LT GaAs epitaxial layer and substrate than for the SI GaAs substrate alone (almost imperceptibly). Single-crystal x-ray results for 3.5-μm-thick films grown at 200°C and unannealed show the appearance of (111) diffraction peaks in addition to the (001) peaks, which confirms the RHEED observation that the film is becoming polycrystalline. Figure 2.6 shows the double-crystal x-ray (400) peaks of a 2-μm-thick LT GaAs film grown at 200°C on an SI GaAs substrate and annealed at 600°C, as compared with another piece of the same SI GaAs substrate. The peak is slightly broader for the sample with the 2-μm-thick epitaxial layer grown at 200°C, but is still narrow. The broadening of the (400) peak for the sample with the 200°C layer may be simply due to stress induced in the film as a result of the growth at elevated temperature.

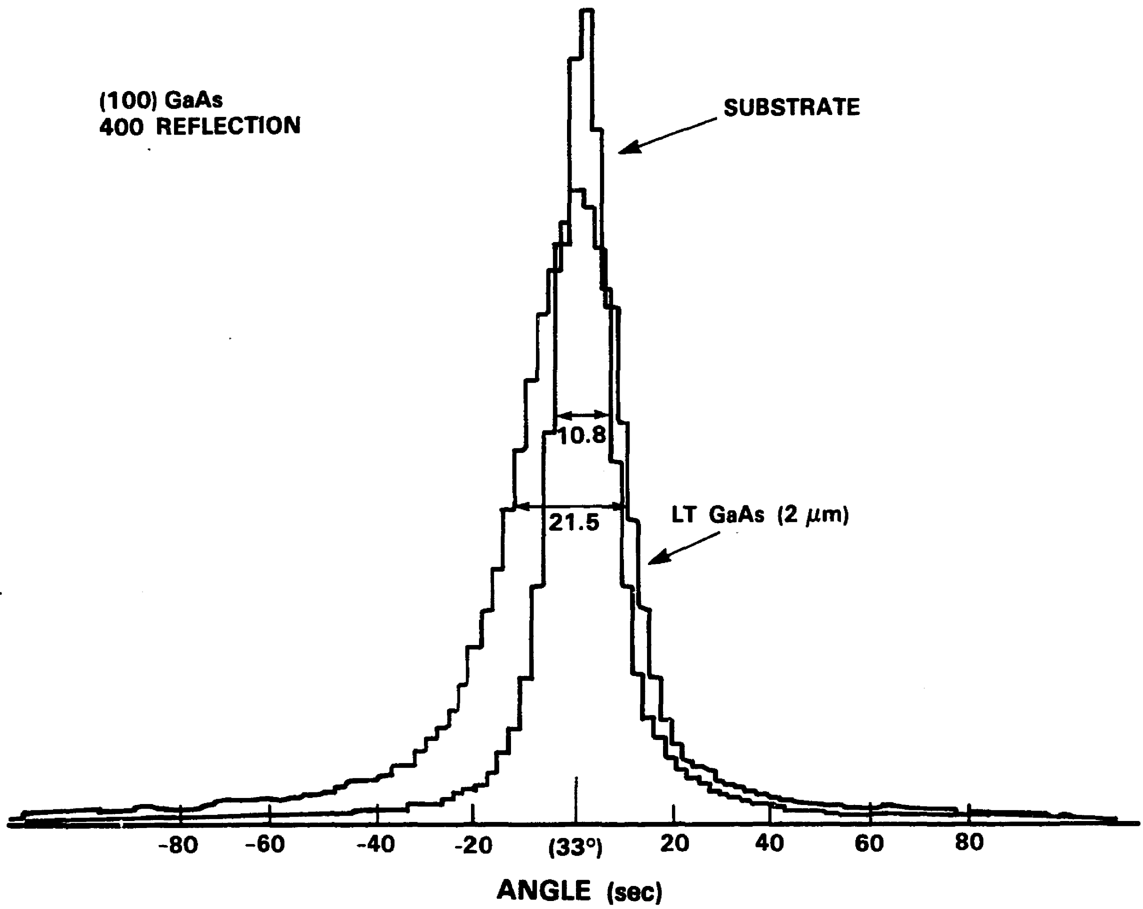

Fig. 2.6 Double-crystal x-ray (400) peaks of an annealed 2-μm-thick LT GaAs layer on an SI GaAs substrate and of the SI GaAs substrate.

One limitation of any x-ray technique is that the penetration depth of the x-rays is on the order of 4 to 5 μm. Since the epitaxial films grown at 200°C are always less than ~4 μm, the substrate is sampled by the x-rays along with the epitaxial layer (see Sec. 5.3.2). This sampling of the substrate tends to obscure the results for the epitaxial layer. To examine the epitaxial layer independent of the substrate, TEM and TED measurements were made. Planar TEM samples were prepared by jet etching the GaAs substrate and the LT GaAs layer so as to leave a thin (~1000 Å), transparent (to electrons), free-standing film of LT GaAs. The LT GaAs film was grown to an initial thickness of 2 μm. Hence, only the last 1000 Å of the as-grown LT GaAs material was observed by this technique.

The TED pattern of an unannealed LT GaAs planar TEM sample is shown in Fig. 2.7. The diffraction spots observed in Figure 2.7(a) are characteristic of GaAs; however, the spacing between the spots indicates that the lattice constant of the LT GaAs film is larger than that of GaAs (see Sec. 5.3.2). This result may explain why the growing LT GaAs film ultimately becomes polycrystalline. The same electron diffraction pattern is shown in Fig. 2.7(b), except that the intensity is higher in order to emphasize the Kikuchi lines. The pronounced Kikuchi lines are again an indication that the LT GaAs layer is of high crystalline perfection.

TEM studies of the same samples indicate a low dislocation density in the LT GaAs layer (comparable to the SI substrate). However, Nomarski constrast microscopy and scanning electron microscopy (SEM) indicate that the surface of the layer grown at 200°C is somewhat rougher than the surface of GaAs layers grown at 580°C. The results of a detailed TEM study of LT GaAs are presented in Sec. 5.3.1.

The photoluminescence (PL) spectrum of LT GaAs grown at 200°C does not display the peaks characteristic of GaAs. The near-band-gap PL spectrum of 1-μm-thick LT GaAs measured at 5 K is compared with that of a 1-μm-thick undoped

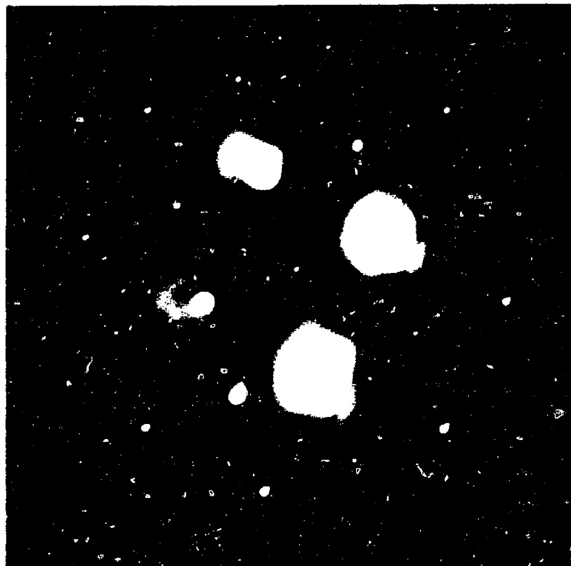

(a)

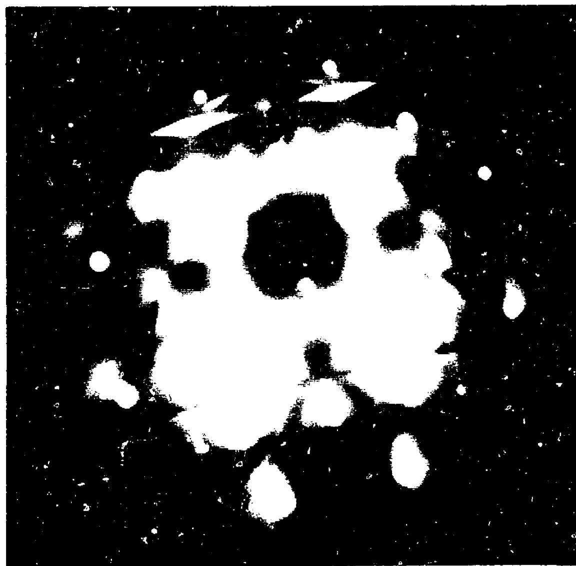

(b)

Fig. 2.7 (a) Transmitted electron diffraction pattern of as-grown LT GaAs. The spots are characteristic of GaAs but the spacing between spots is slightly different from that of GaAs. (b) Same diffraction pattern as in (a) except at higher intensity in order to highlight the pronounced Kikuchi lines.

GaAs film grown by MBE at 580°C in Fig. 2.8(a). The undoped GaAs film shows the characteristic exciton and carbon acceptor peaks. In contrast, the PL spectrum of LT GaAs, even magnified 100 times, is only noise. A buffer layer with reduced light sensitivity as compared with high-quality GaAs is desirable for both electronic and optoelectronic circuit applications. Extensive near-band-gap and deep-level PL data for annealed and unannealed LT GaAs epilayers are presented in Sec. 5.4.1.

Although 200°C-grown LT GaAs does not exhibit PL, doped layers of GaAs grown upon the LT GaAs buffer are of comparable optical quality to similar layers grown upon undoped GaAs buffers. This result is shown in Fig. 2.8(b), where the PL intensity at 5 K for 2-μm-thick epitaxial layers of n-GaAs grown on top of the two buffers of Fig. 2.8(a) are compared. The PL spectra for the doped films on the LT GaAs buffer are essentially identical to that for the doped films on the undoped GaAs buffer and are quantitatively reproducible. To further assess the quality of the n–GaAs grown on the LT GaAs buffer, 77-K Hall mobility measurements were also made on these samples. The bulk mobility of 21,000 cm^2/V-s found for the doped layers grown on the LT GaAs buffer is quantitatively reproducible and is essentially the same as the mobility of 24,000 cm^2/V-s measured for the layer grown on the undoped GaAs buffer.

Auger electron spectroscopy (AES) has been used to characterize LT GaAs [10]. The structure depicted in schematic cross section in Fig. 2.9 was grown by MBE. The starting material was an n^+-GaAs substrate. A thin, heavily doped n^+-GaAs layer was grown on the substrate at 580°C and was followed by 0.2 μm of the LT GaAs buffer grown at 200°C. The temperature was then raised to 580°C and, after a 10-min anneal to stabilize the surface, 0.2 μm of n^+-GaAs was grown. AES was performed as this sample was sputtered. The AES result is shown in Fig. 2.10. The upper and lower n^+-GaAs regions are seen to be stoichiometric GaAs, but the

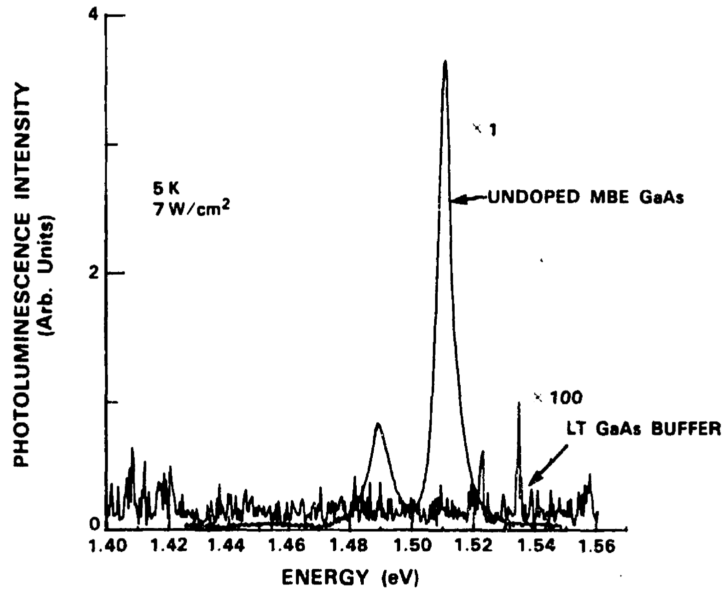

(a)

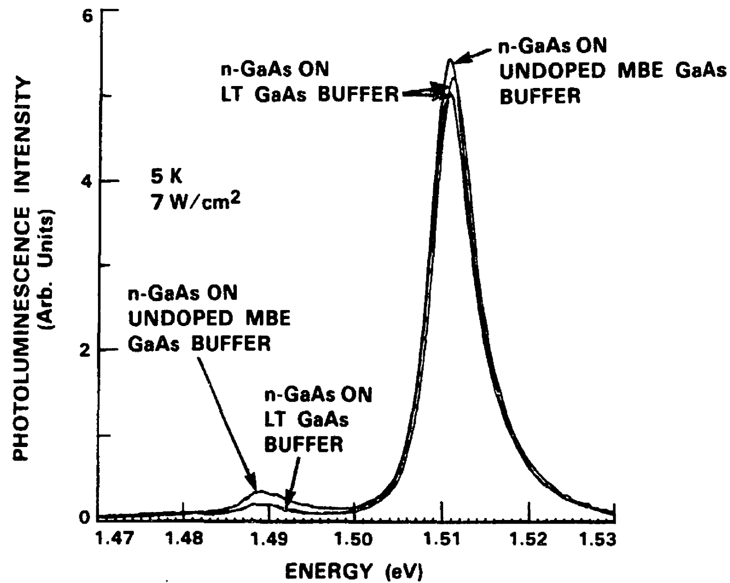

(b)

Fig. 2.8 (a) Photoluminescence of LT GaAs grown at 200°C and undoped GaAs grown by MBE at 580°C, both 1 μm thick. (b) Photoluminescence of 2-μm-thick n-GaAs layers (10^{16} cm^{-3}) grown at 580°C on top of two samples of the LT GaAs buffer and on top of the undoped MBE GaAs buffer.

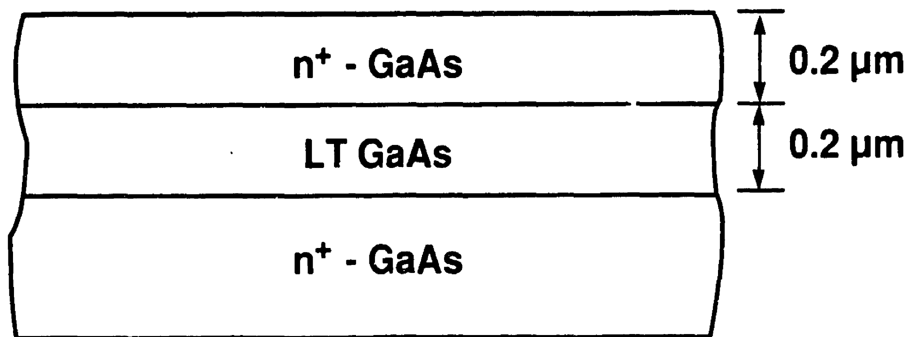

Fig. 2.9 Schematic cross section of the LT GaAs sample used in the AES study.

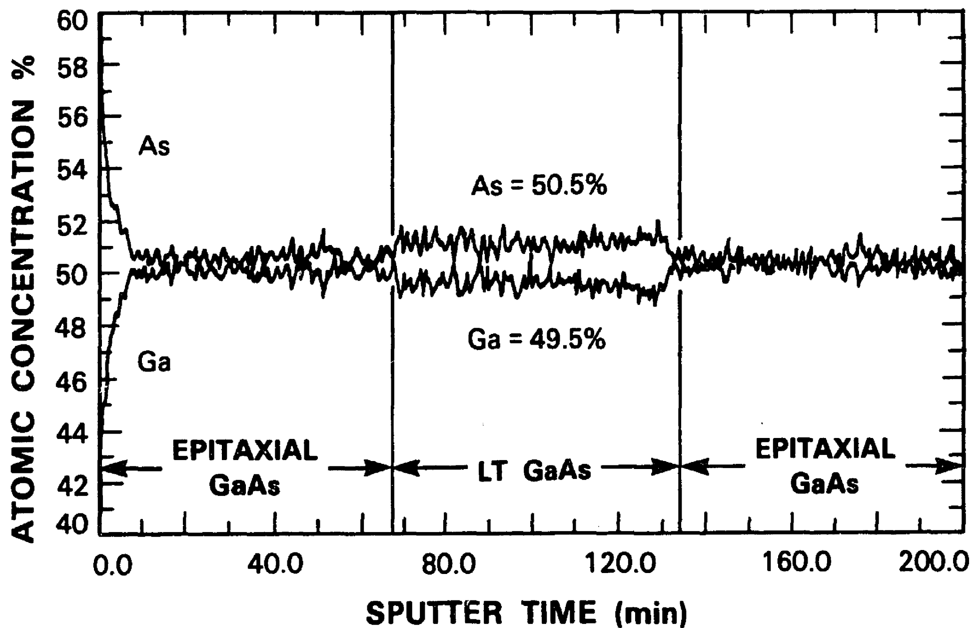

Fig. 2.10 AES result for the sample of Figure 2.9. The sputtering rate was approximately 3 nm/min.

layer grown at 200°C is seen to be $Ga_{0.495}As_{0.505}$. This is a tremendous amount of excess arsenic and is consistent with the predictions of Sections 2.1 and 2.2. For comparison, undoped LEC SI GaAs substrates are often grown arsenic rich to achieve the semi-insulating behavior. However, the excess arsenic in this material is of the order of 1 part per million, a full 4 orders of magnitude less than that observed for the LT GaAs layer grown at 200°C. Detailed studies of the composition of the LT GaAs are presented in Sec. 5.2.

CHAPTER 3. ELECTRONIC DEVICE APPLICATIONS

3.1 Background

GaAs IC's are typically fabricated on SI GaAs substrates, and the active layers are formed either by direct ion implantation into the SI GaAs substrate or by epitaxial deposition. A number of problems associated with GaAs MESFET devices and circuits are attributed to the SI GaAs substrate. Such problems include sidegating, hysteresis in the dependence of the drain-source current I_{ds} upon drain-source voltage V_{ds}, light sensitivity, low output resistance R_d, low source-drain breakdown voltage BV_{SD}, and low output power gain at RF frequencies [1],[43],[44]. Among these problems, sidegating is the most severe for both digital and analog circuit applications.

In addition, increased subthreshold leakage current, threshold voltage shifts, and the inability to fully pinch off the device for large V_{ds} can occur as the gate length of GaAs MESFET's is reduced to submicrometer dimensions [45],[46]. Also, R_d and BV_{SD} are further decreased as the gate length is reduced [46],[47]. These problems are called short-channel effects and the characteristics of the layer underlying the active region can have a profound influence on them [45],[46].

To alleviate the problems discussed in preceeding two paragraphs, researchers have often inserted a buffer layer between the active layer and the substrate. A number of possible buffer layers have been suggested, including undoped GaAs, AlGaAs, and superlattice (GaAs/AlGaAs) buffers [2]. Heretofore, such buffer layers have met with only limited success.

In this section, LT GaAs buffer layers grown at T_s of 200°C and annealed at 600°C are shown to eliminate sidegating in MESFET's and HEMT's, both for dc and RF bias conditions, and to dramatically reduce short-channel effects in

submicrometer-gate-length MESFET's. Results for 2-μm-gate-length MESFET's are summarized in Section 3.2. The dc sidegating results and microwave performance of discrete devices are presented in Section 3.2.1. The implications of the elimination of sidegating for analog, digital, and microwave MESFET IC's are discussed in Section 3.2.2. The sidegate-bias contribution to 1/f noise in MESFET's is discussed in Section 3.2.3. MESFET's with a gate length of 0.27 μm fabricated in active layers on the LT GaAs buffer are presented in Section 3.3. Lastly, a number of other electronic device applications are summarized in Section 3.4.

3.2 2-μm-Gate-Length MESFET's

3.2.1 Sidegating, dc, and Microwave Results

As the first device application of this technology, MESFET's with a gate length of 2 μm were fabricated in active layers grown upon the LT GaAs buffer [8]. A number of performance improvements to MESFET devices and circuits were found to result. Most significantly, sidegating was eliminated in our test structures and the dc and RF characteristics of the MESFET's have been improved by using the LT GaAs buffer.

A schematic cross section of a typical MESFET with a sidegate is shown in Fig. 3.1. Even though the sidegate and MESFET are isolated by mesa etching, sidegating arises because the substrate is of finite resistivity (shown as R_{BG} and R_{SG} in Fig. 3.1) and because there is a space-charge region at the interface between the active layer and the substrate. In response to changes in voltage on the substrate or adjacent devices, the substrate conducts enough current to modulate the interface space-charge region. When this interfacial depletion region widens into the active channel, the device current is reduced [6]. This effect is called sidegating when the bias is applied to an adjacent electrode and backgating when the bias is applied to the

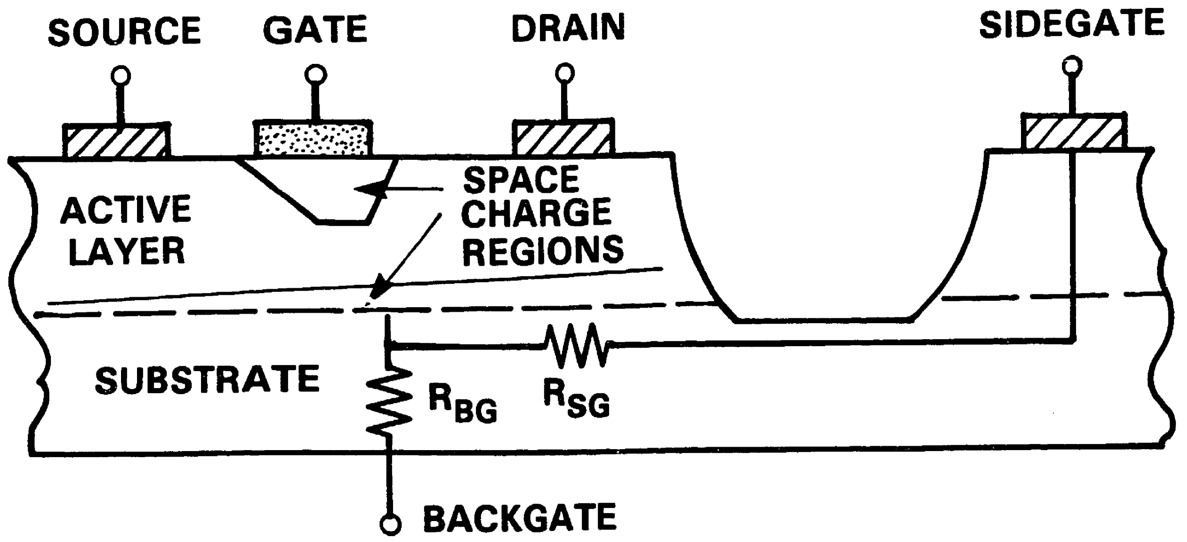

Fig. 3.1 Schematic MESFET cross section to illustrate sidegating.

substrate. Although the terms sidegating and backgating are sometimes used interchangeably in the literature, in this thesis the term sidegating will be used exclusively to describe our measurements of this phenomenon.

To demonstrate the sidegating performance improvement afforded by the LT GaAs buffer, MESFET's were fabricated using a number of different buffer layers and structures [8]. A schematic cross section of the MESFET structure used in this study is shown in Fig. 3.2. The measured gate length L_g, gate width W_g, and source-drain spacing of this device are 2, 98, and 5.5 μm, respectively. An ohmic contact, isolated from the MESFET by mesa etching, served as the sidegate. The MESFET's were fabricated in MBE n-GaAs layers grown upon the LT GaAs buffer and also in MBE n-GaAs layers grown upon buffer layers of undoped GaAs, AlGaAs, and GaAs/AlGaAs superlattices. All the buffer layers were grown by MBE and are 2 μm thick. The active layer is doped to approximately 2×10^{17} cm^{-3} with silicon and is 0.3 μm thick. MESFET's were also fabricated in commercial vapor phase epitaxy n-GaAs layers deposited on SI GaAs substrates and in layers made by direct ion implantation into the SI GaAs substrates. The gate recess depth is roughly half the active layer thickness, and mesa etching was used to isolate the devices. The ohmic contacts are alloyed Ni(or Pd)/Ge/Au and the Schottky contact is Ti/Au.

The most dramatic improvement in device performance provided by the new buffer is the elimination of sidegating [8], as illustrated by Fig. 3.3. The normalized I_{dss} [$I_{dss}(V_{sg})/I_{dss}(0)$] is plotted versus the applied sidegate voltage V_{sg}. A sidegate spaced 50 μm from the MESFET and V_{ds} = 2.5 V are used. Data obtained both in the dark and in white light are shown. The lines in the figure are included only as a convenience in visualizing the data.

Figure 3.3 compares sidegating in MESFET's fabricated in active layers on the LT GaAs buffer with sidegating in MESFET's fabricated in active layers on an

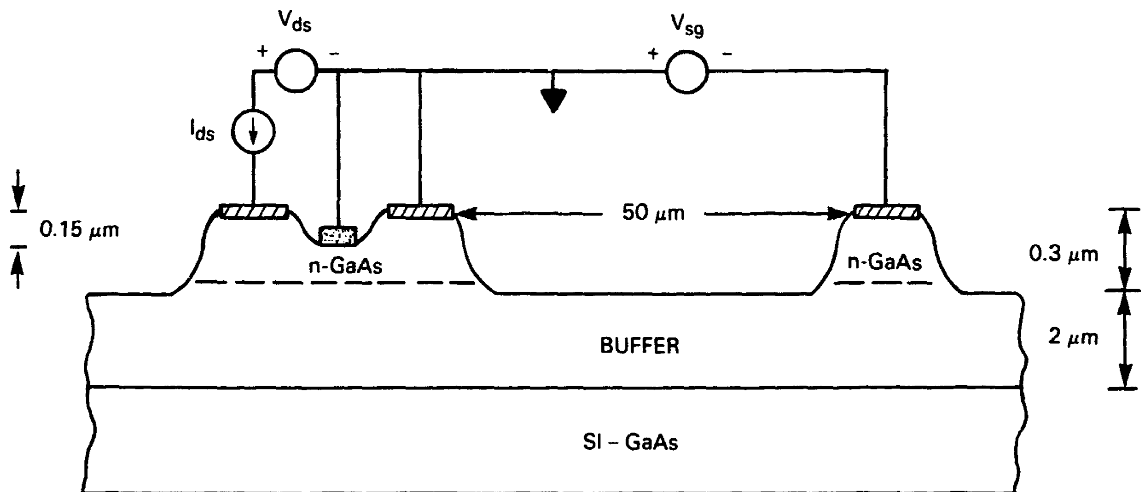

Fig. 3.2 Schematic cross section of the MESFET structure used to measure side-gating.

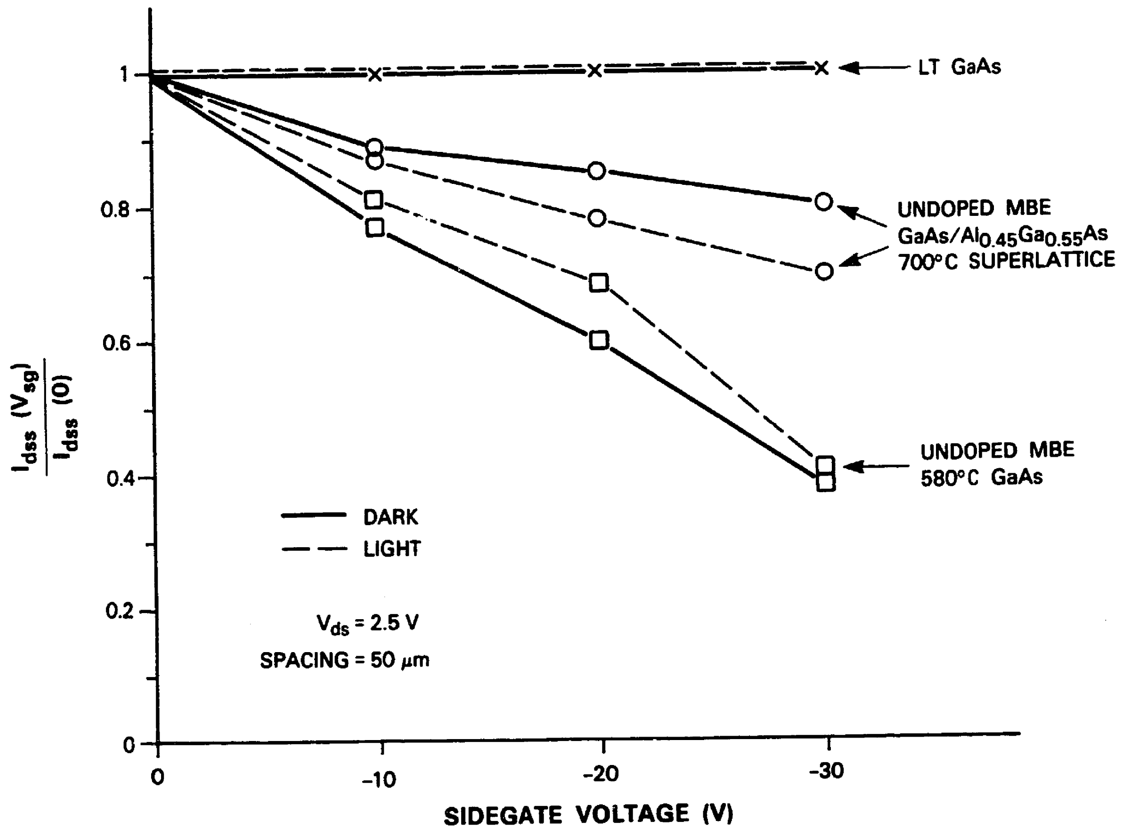

Fig. 3.3 Sidegating characteristics: LT GaAs buffer, undoped GaAs buffer, and undoped superlattice buffer. The points connected by the solid lines are the results obtained in the dark and the points connected by the dashed lines in the light. The lines themselves are included only as a convenience in visualizing the data.

undoped GaAs buffer and on an undoped GaAs/$Al_{0.45}Ga_{0.55}As$ superlattice buffer grown by MBE at 700°C. Both GaAs- and superlattice-buffered devices show sidegating and light sensitivity, while the device with the new buffer shows neither. Although not shown here, the other MESFET's listed in Table 3.1 also show light sensitivity and sidegating. Of the alternative buffers, the AlGaAs and superlattice buffers grown at 700°C were the best.

Although the data presented in Fig. 3.3 were measured using a sidegate spaced 50 μm from the MESFET, a sidegate spaced 15 μm from the MESFET was also used. For -50 V applied to the sidegate and V_{ds} = 2.5 V, the new buffered device still showed no sidegating. For the same voltages, I_{dss} of the superlattice-buffered MESFET was reduced by 50% and the GaAs-buffered devices destructively broke down.

Measurements of the dc characteristics of these MESFET's have also been made. (The dc and RF results reported here are for MESFET's fabricated on the same buffer layers as discussed above and have measured L_g, W_g, and source-drain spacing of 2, 780, and 5.5 μm, respectively.) The measured dc and RF results for the devices used in this sidegating study are summarized in Tables 3.1 and 3.2, respectively. The peak transconductance g_m of the MESFET incorporating the LT GaAs buffer was slightly lower than for some of the other structures. This lower g_m is attributed to a lower charge concentration in the active layer of the device with the LT GaAs buffer.

The R_d, BV_{SD}, and isolation breakdown voltage BV_{ISO} of the MESFET incorporating the new buffer were larger than for any of the other structures. The BV_{SD} was measured with the MESFET biased near pinch-off, and the BV_{ISO} was measured between the source/drain pads of the sidegating MESFET and the sidegate ohmic contact spaced 15 μm away. Relative to the undoped GaAs buffered device, R_d was

STRUCTURE	SIDEGATING % CHANGE LIGHT	DARK	LOOPING	R_d (Ω)	g_m (mS/mm)	BV_{SD} (V)	BV_{ISO} (V)
LT GaAs BUFFER	0	0	NO	4000	97	27	400
IMPLANT	100	10	YES	214	87	8	20
VPE EPILAYER	45	63	YES	—	106	18	25
NO BUFFER (MBE)	50	40	YES	400	97	15	25
UNDOPED MBE GaAs BUFFER	40	40	YES	272	107	17	30
UNDOPED MBE 610°C AlGaAs BUFFER	30	29	YES	222	105	13	60
UNDOPED MBE 700°C AlGaAs BUFFER	29	13	YES	600	103	16	40
UNDOPED MBE 610°C SUPERLATTICE BUFFER	33	16	NO	210	67	—	70
UNDOPED MBE 700°C SUPERLATTICE BUFFER	30	20	NO	—	—	—	80

Table 3.1 Summary of dc results: 2-μm MESFET.

STRUCTURE	f_T (GHz)	f_{max} (GHz)
LT GaAs BUFFER	7	10
IMPLANT	4.3	9
VPE EPILAYER	6	10.5
NO BUFFER (MBE)	7	10
UNDOPED MBE GaAs BUFFER	8	11
UNDOPED MBE 610°C AlGaAs BUFFER	6	9
UNDOPED MBE 700°C AlGaAs BUFFER	7.3	11

Table 3.2 Summary of RF results: 2-μm MESFET.

increased by over a factor of 10 (4000 vs 270 Ω), BV_{SD} was increased by almost a factor of 2 (27 vs 17 V), and BV_{ISO} was increased by over an order of magnitude (400 vs 30 V) by using the LT GaAs buffer. The measured BV_{ISO} for the LT GaAs and undoped GaAs buffered MESFET's are contrasted in Fig. 3.4. A large BV_{ISO} is essential for high-voltage electronic devices and circuits and for the production of high-voltage picosecond pulses (see Sec. 4.1).

A network analyzer was used to measure the scattering parameters for the MESFET structures investigated. The unity short-circuit current-gain frequency f_T and maximum frequency of oscillation, f_{max}, of all the MESFET's were approximately 7 and 10 GHz, respectively. These results are typical for the MESFET geometry used. The microwave gain of the MESFET was not degraded by using the LT GaAs buffer, which is further evidence that the active layer grown on the LT GaAs buffer is high quality n-GaAs.

3.2.2 Implications of Sidegating Elimination for GaAs IC's

Sidegating effects relevant to GaAs digital, analog, and monolithic microwave integrated circuits have been significantly reduced or eliminated by using the LT GaAs buffer. At radio frequencies the LT GaAs buffer reduced the signal coupling between devices, which is an important consideration in microwave integrated circuits. For digital circuit applications, the LT GaAs buffer eliminated the dependence of the voltage level of an inverter on the logic state of adjacent devices and on the duty cycle of a pulse train encountered in the circuit. The LT GaAs buffer enables us to experimentally identify the role that a buffer layer plays in sidegating.

In this section, four aspects of sidegating are addressed. First, the RF signal coupling from the sidegate through the buffer layer to the MESFET are characterized. Second, the effects of a sidegate bias on the S-parameters of a MESFET at

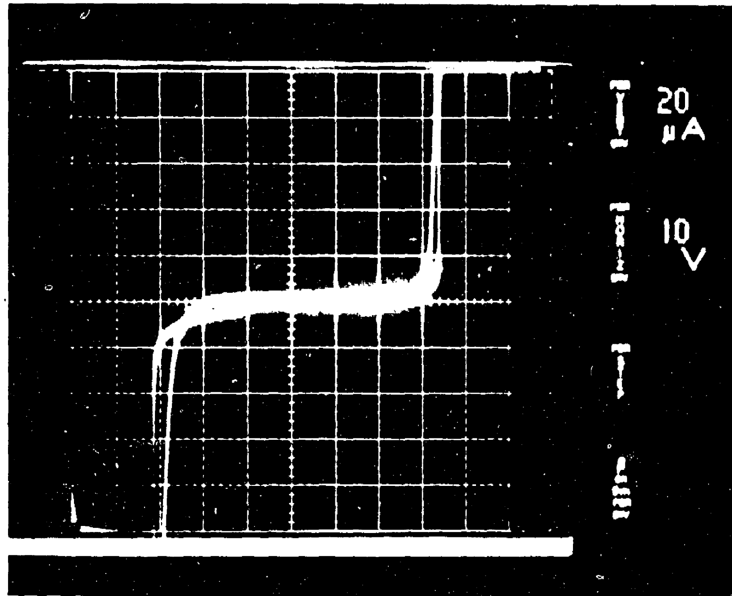

(a)

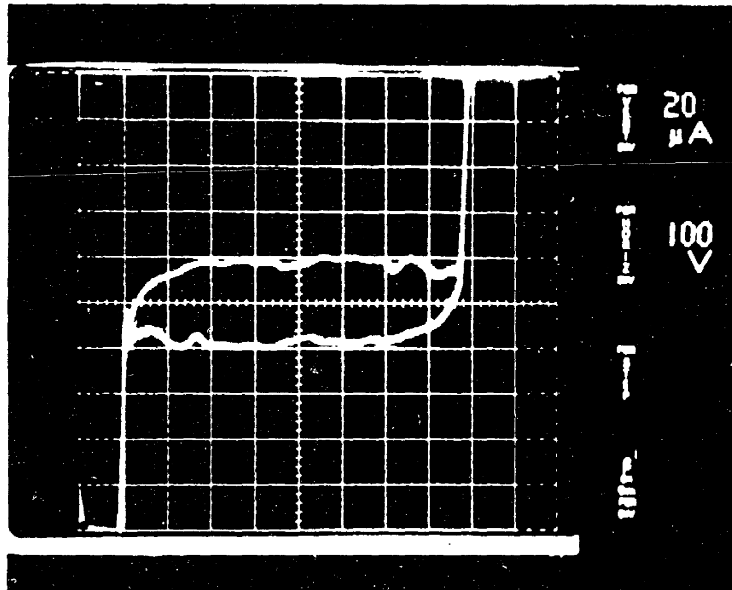

(b)

Fig. 3.4 Isolation breakdown voltage measured between the sidegate and drain contacts spaced 15 µm apart for (a) conventional buffer and (b) LT GaAs buffer.

microwave frequencies are discussed. Third, sidegating effects relevant to digital IC's are presented. In particular, the response of a MESFET to a pulse train applied to the adjacent sidegate, and the effect of duty cycle of the pulse train, are described. In the fourth part, the coupling of a pulse train to an adjacent MESFET acting as an amplifier is examined in order to simulate the interaction between a microwave circuit and a digital circuit.

The 2-μm-gate-length MESFET's discussed above were used in this study. As shown in Fig. 3.5, all the sidegating results reported here were measured using the sidegate contact spaced 15 μm from the MESFET. To demonstrate the performance improvements possible using the LT GaAs buffer, the sidegating results obtained for MESFET's fabricated using LT GaAs and undoped GaAs buffers are compared. The undoped GaAs buffer layer grown by MBE at 580°C is called the conventional buffer layer.

3.2.2.1 RF Coupling

The coupling of an RF signal from the sidegate to the MESFET was studied. MESFET's fabricated on LT GaAs and conventional buffer layers were packaged in separate microwave test fixtures. The source and the gate of the MESFET were grounded to the test fixture by bond wires, while the sidegate and the drain were each connected to separate 50-Ω microstrip lines used as the input and output. The input (sidegate) was connected to a signal generator, while the output (drain) was connected to a spectrum analyzer. Bias tees were used at both input and output so that dc bias could be applied to the drain and sidegate without interfering with the RF measurements. The experimental setup is illustrated in Fig. 3.6.

In the first experiment, RF signals of 40 MHz and 2 GHz were applied to the sidegate. Even with zero dc bias on the drain and on the sidegate, RF signals were

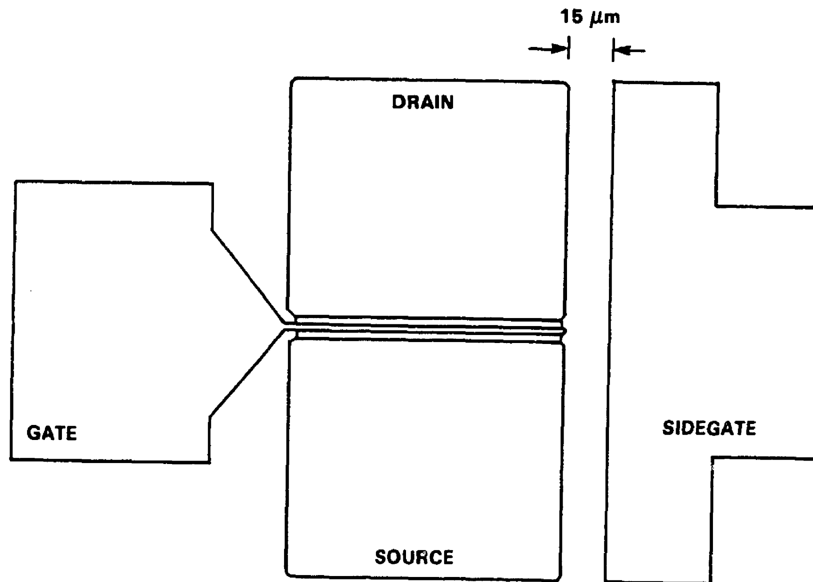

Fig. 3.5 MESFET layout for sidegating effect measurement.

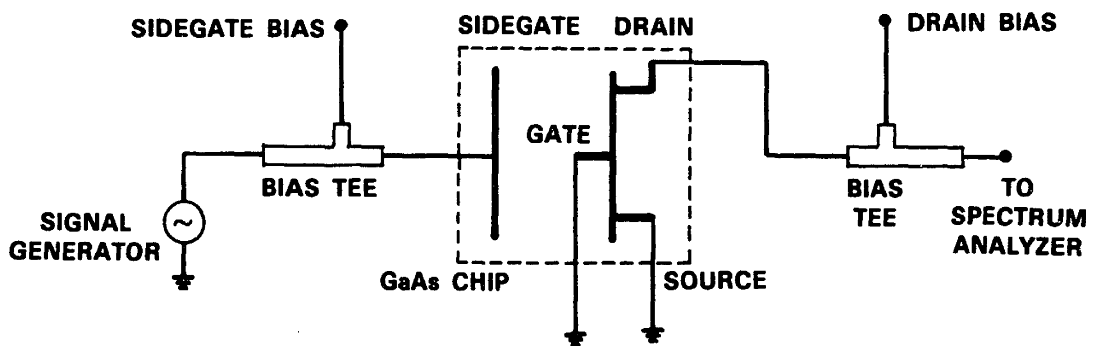

Fig. 3.6 Measurement setup for RF coupling experiment.

measured at the drain of the MESFET. For both MESFET's, the measured signals were below the input signal level by approximately 76 dB at 40 MHz and 42 dB at 2 GHz. This coupling is due to the interaction of fringing fields around the metal pads and is similar to that of coupled microstrip lines [48]. The Super-Compact® computer simulation program was used to calculate the coupling using the equivalent circuit shown in Fig. 3.7. The equivalent circuit of the source pad is a parallel LC network representing the bondwire inductance and the capacitance associated with the pad. The conducting channel of the MESFET is equivalent to a series resistance R_{ds} which varies with the Schottky-barrier gate bias. Because of the high resistivity at zero V_{sg}, the buffer-layer resistance R_{buffer} between the sidegate and the drain pad was assumed infinite in the simulations so that the calculated coupling is via the capacitors C_{buffer} associated with the buffer layer and the substrate. Calculated coupled signals were 77.8 and 43.7 dB below the input signal at 40 MHz and 2 GHz, respectively. The calculated and measured results are in very good agreement. The coupling is stronger at higher frequencies because capacitive coupling increases with frequency. From the equivalent circuit of Fig. 3.7, the degree of coupling is seen to depend on the dimensions and layout of the device, while the quality of the buffer layer has little effect when zero dc bias is applied to the sidegate.

When a negative bias is applied to the sidegate, the difference between the two buffer layers becomes apparent. Negative biases of 10 and 14 V were applied to the sidegates of the MESFET's on the two different buffer layers. The saturated drain current I_{dss} of the MESFET with the conventional buffer layer decreased by 25% for V_{sg} = -10 V and 35% for V_{sg} = -14 V, while no measurable change in I_{dss} of the MESFET with the LT GaAs buffer layer occurred. The measured and calculated (see discussions below) magnitudes of coupled RF signals with zero drain bias (V_{ds} = 0) are plotted as a function of V_{sg} in Fig. 3.8. Note the amount of coupling increased

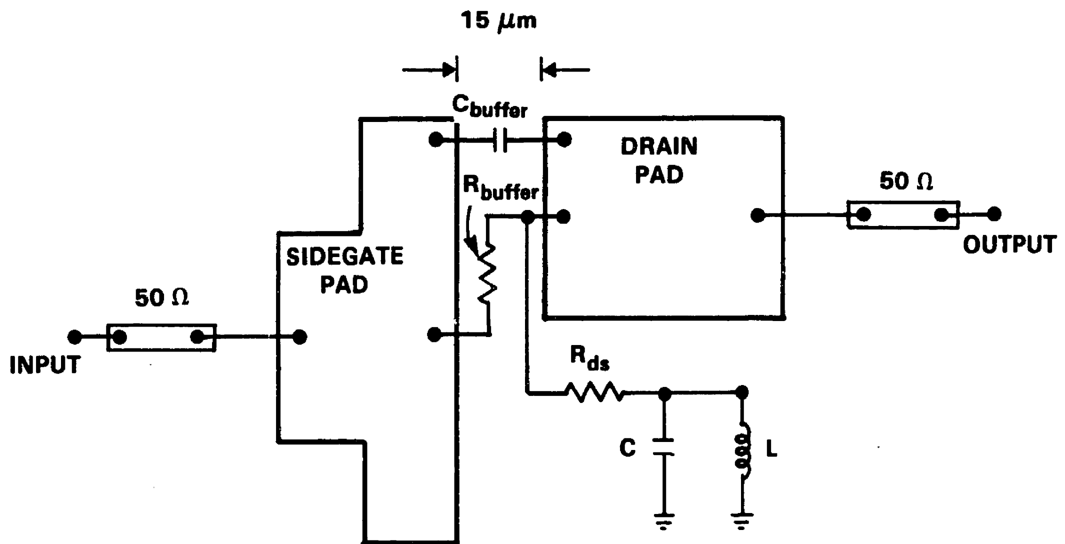

Fig. 3.7 Equivalent circuit used for simulating the coupling from the sidegate to the drain of the MESFET. The substrate is 175 μm thick and the metal pads are treated as transmission lines.

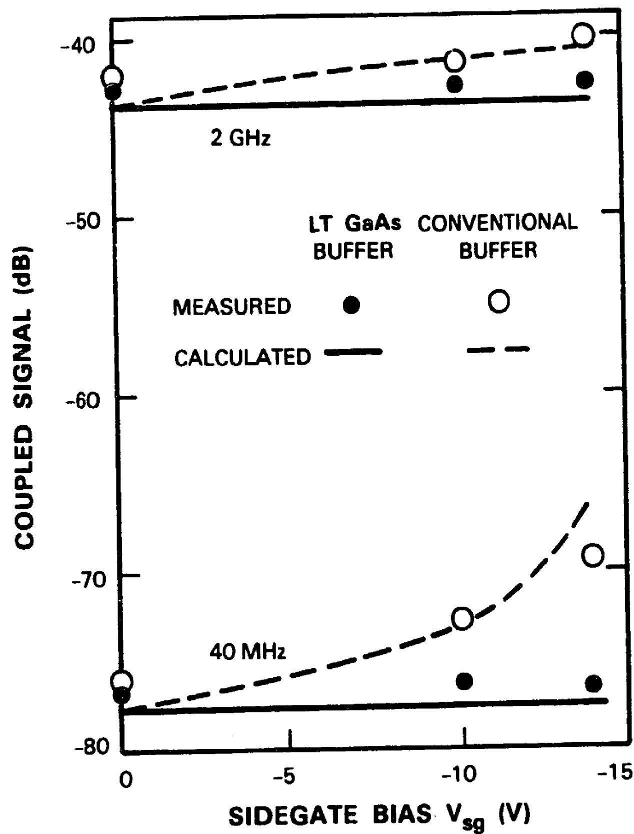

Fig. 3.8 Measured and calculated magnitudes of the coupled signal relative to the signal applied to the sidegate at 40 MHz and 2 GHz.

with sidegate bias for the MESFET with the conventional buffer layer, but the coupling did not change for the MESFET with the LT GaAs buffer layer.

Two factors contribute to the increase of signal coupling with V_{sg} for the device with the conventional buffer. First, for the MESFET with the conventional buffer layer, the resistance of that layer decreases rapidly with the voltage applied to the sidegate. This reduced value of R_{buffer} in Fig. 3.7 provides an additional conductive path for signal coupling. This coupling increases with decreasing resistance and is expected to be more important at lower frequencies where resistive coupling dominates. Resistive coupling through the LT GaAs buffer is insignificant because of the large R_{buffer}, which was found to be independent of sidegate bias for the voltages used in this experiment.

The second factor causing the stronger coupling for the conventional buffer is the increase of MESFET drain-source resistance R_{ds} with increased V_{sg}. The drain current of the MESFET with the conventional buffer decreases with increasingly negative V_{sg} because the conducting channel shrinks as the depletion region at the buffer/active-layer interface widens. Consequently, the proportion of the coupled signal bypassed from the drain pad to ground via the drain-source channel of the MESFET is reduced. As a result, a stronger coupled signal is measured at the drain pad. This R_{ds} effect is equally important at low and high frequencies. On the other hand, the drain-source resistance of a MESFET with the LT GaAs buffer does not change with the sidegate bias and, hence, this second factor does not affect the coupling of a MESFET with the LT GaAs buffer.

At zero drain and gate bias, the measured drain-source resistances for the MESFET with the conventional buffer are 50 Ω for 0 V sidegate bias, 105 Ω for -10 V, and 120 Ω for -14 V. The measured R_{buffer} is approximately 160 kΩ for V_{sg} = -14 V, 500 kΩ for V_{sg} = -10 V, and several megohms at zero sidegate bias. The

calculated results in Fig. 3.8 for different sidegate biases were obtained by substituting the measured R_{ds} and R_{buffer} in the equivalent circuit. The measured and calculated results are in good agreement.

Under normal MESFET operating conditions, a dc bias is applied to the drain of a MESFET and the situation becomes more complicated because the coupled signal from the sidegate is amplified by the MESFET. Figure 3.9 shows the schematic cross section and a simplified equivalent circuit of a MESFET with a sidegate which is mesa isolated from the MESFET. Although in reality the sidegate is equidistant from the source, drain, and gate as shown in Fig. 3.5, the configuration depicted schematically in Fig. 3.9(a) is used for clarity and does not affect the model derived in this section. The depletion regions under the Schottky-barrier gate and at the interface of the active and the buffer layers are indicated. If the width of the depletion region at the active-buffer interface can be modulated by the sidegate bias, the sidegate is equivalent to a second gate for the MESFET with an effective gate length extending from the source ohmic contact to the drain ohmic contact. Figure 3.10 shows the measured drain current I_{ds} versus drain-source voltage V_{ds} of the MESFET with the conventional buffer for sidegate biases from 0 to -14 V in increments of -2 V steps. The Schottky-barrier gate voltage is kept at 0 V. A sidegate-controlled transconductance $g_m' = \Delta I_{ds}/\Delta V_{sg}$ of 5.6 mS/mm is measured at $V_{sg} = 0$ V. The drain current of the MESFET with the LT GaAs buffer does not change with the sidegate bias and, thus, g_m' is 0.

To correspond to normal MESFET operating conditions, the RF coupling was measured with a dc bias applied to the drain. The Schottky-barrier gate of the MESFET remained dc and RF grounded. A dc bias of 1.2 V applied to the drain of either the MESFET with the conventional or LT GaAs buffer layer produced 15 mA of I_{dss} at zero sidegate bias. For the MESFET with the conventional buffer, I_{dss}

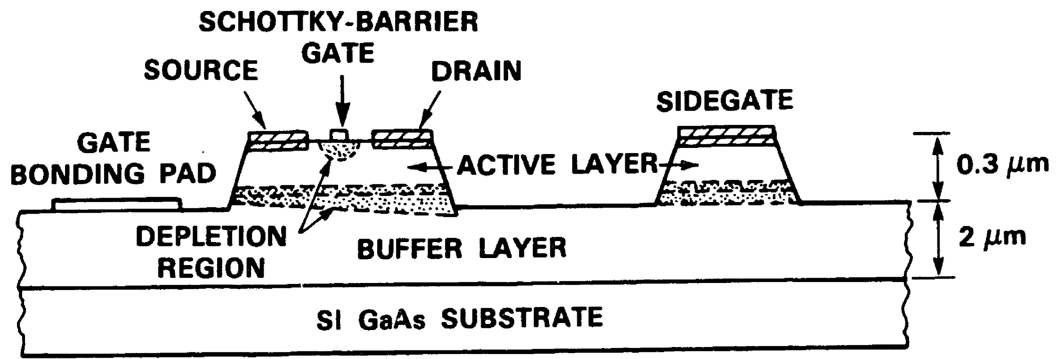

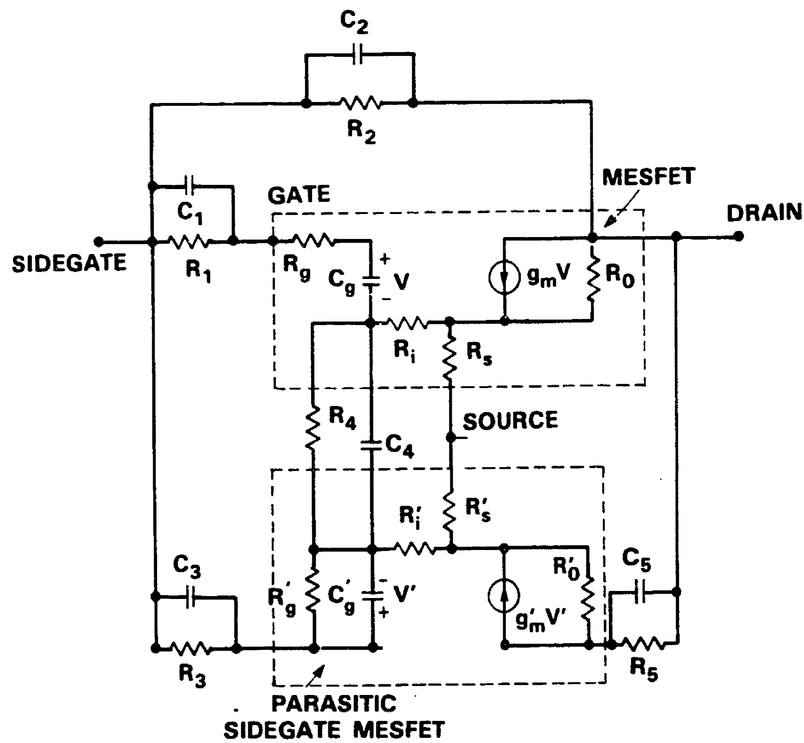

Fig. 3.9 (a) Schematic cross section of a MESFET with an isolated sidegate. (b) Simplified equivalent circuit for the MESFET and the parasitic sidegate FET.

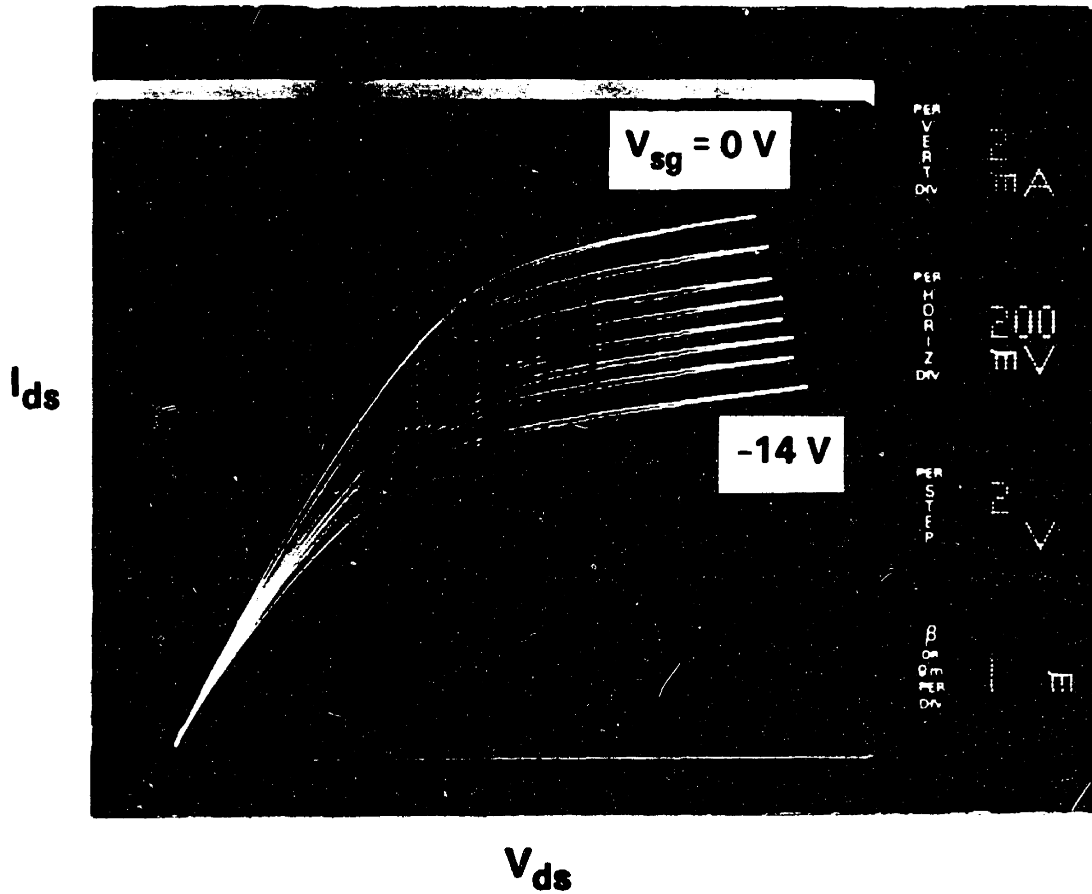

Fig. 3.10 I_{ds} versus V_{ds} of a MESFET with a conventional buffer layer and with V_{sg} as the parameter. The upper trace is for V_{sg} = 0 V and the V_{sg} increments are -2 V. The Schottky-barrier gate is kept at 0 V.

dropped to 12.3 mA for V_{sg} = -10 V and 10.4 mA for V_{sg} = -14 V. When both MESFET's were biased as described above, they amplified the signal coupled from the sidegate. Figure 3.11 shows this coupled signal normalized to the coupled signal with V_{ds} = 0 V as a function of V_{sg}. The normalized coupled signal is the increase in the magnitude of the signal coupled to the drain of the MESFET with V_{ds} = 1.2 V divided by that coupled at V_{ds} = 0 V, and is a measure of the gain provided by the biased MESFET. At 40 MHz the normalized coupled signal measured at the drain of the MESFET with the LT GaAs buffer is approximately 10 dB and decreases to 3.6 dB at 2 GHz. It does not appreciably change with the sidegate bias at either frequency. For the MESFET with the conventional buffer, the normalized coupled signal increases from 12.7 dB with 0-V sidegate bias to 15.4 dB with -10-V sidegate bias at 40 MHz. When the frequency is increased to 2 GHz it decreases to approximately 4.0 dB and does not change with the sidegate bias.

The coupling of the MESFET's biased in the saturation region can be explained qualitatively with the help of the simple equivalent circuit shown in Fig. 3.9(b). The actual MESFET is described by two circuits representing the modulation of the channel by the Schottky-barrier gate and the parasitic sidegate. These two MESFET circuits are coupled through the active layer and this coupled circuit is represented simply by circuit elements R_4 and C_4. Circuit elements R_1, C_1, R_2, C_2, R_3, and C_3 represent the coupling from the sidegate to the MESFET, while g_m and g_m' are the transconductances for the Schottky-barrier gate MESFET and the parasitic FET, respectively. R_g, C_g, R_g', and C_g' are the equivalent circuit elements for the depletion region at the Schottky-barrier gate and at the interface of the active and buffer layers.

An RF signal applied to the sidegate can couple through the buffer layer to the gate bonding pad directly and can couple to the gate via the buffer/active-layer inter-

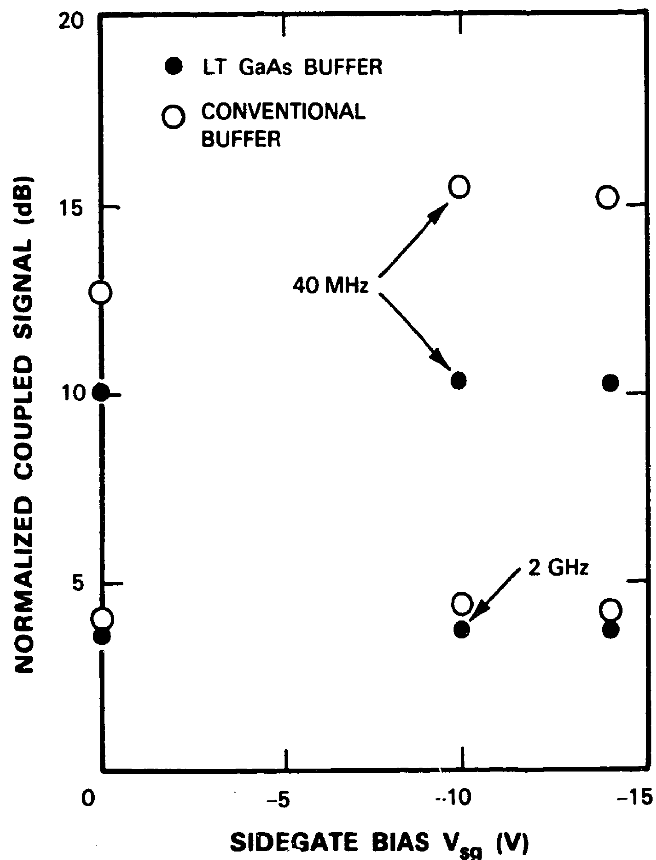

Fig. 3.11 Normalized coupled signal at the drain of MESFET's with the conventional and the LT GaAs buffer layers as a function of sidegate bias. The normalized coupled signal is defined as the increase in magnitude of coupled signal at V_{ds} = 1.2 V divided by the coupled signal at V_{ds} = 0 V.

face and the conducting channel (R_4C_4). The coupled signal present at the Schottky-barrier gate is then amplified by the MESFET. As previously discussed, the normalized coupled signal measured at the drain for $V_{sg} = 0$ V is approximately 10 dB at 40 MHz for the MESFET with the LT GaAs buffer and 12.7 dB at the same frequency for the MESFET with the conventional buffer. According to the S–parameters obtained in separate measurements (see next section), the RF gain for signals applied to the Schottky-barrier gates is approximately the same for both MESFET's. Therefore, the 2.7-dB difference in normalized coupled signals is attributed to the additional gain provided by the nonzero g_m' of the parasitic FET at the interface of the active layer and the conventional buffer layer. As also noted previously, at 2 GHz the total normalized gain for the coupled signal of the MESFET with the conventional buffer decreases to approximately 4 dB, which is comparable to the 3.6 dB gain measured for the MESFET with the LT GaAs buffer. The parasitic MESFET has a large input capacitance [C_g' in Fig. 3.9(b)] which is determined by the depletion layer at the interface of the active and the buffer layers under the entire channel region. As a result, the gain of the parasitic MESFET decreases rapidly with increasing frequencies.

3.2.2.2 Scattering Parameters

This section is included to show how the input reflection scattering parameter S_{11} and transistor gain vary with V_{sg}. Only data for MESFET's with the conventional buffer are given because no changes in S_{11} with V_{sg} were observed for MESFET's with the LT GaAs buffer. The MESFET's were connected in a common-source configuration and the small-signal S-parameters were measured using a network analyzer. As shown in the inset of Fig. 3.12(a), the gate of the MESFET is the input port, while the output is taken from the drain. The applied dc gate and drain biases

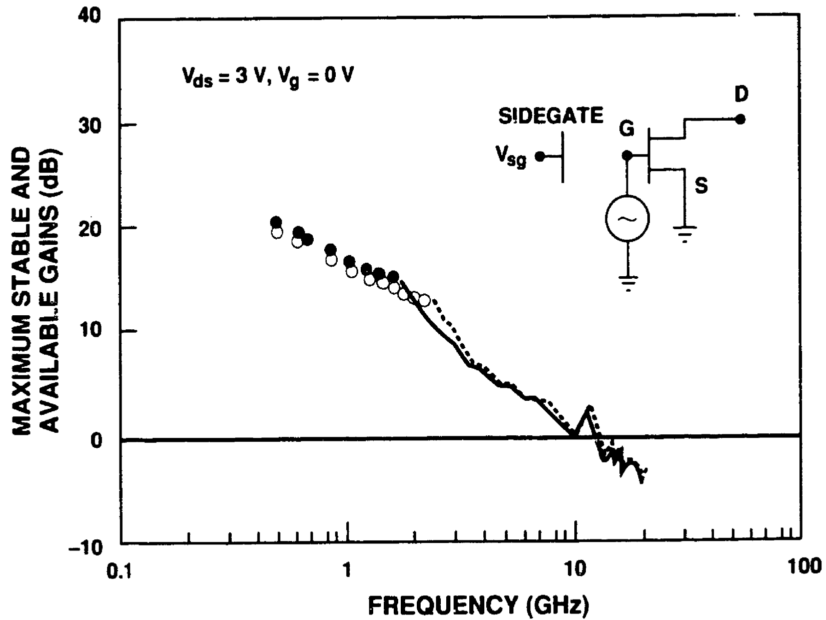

(a)

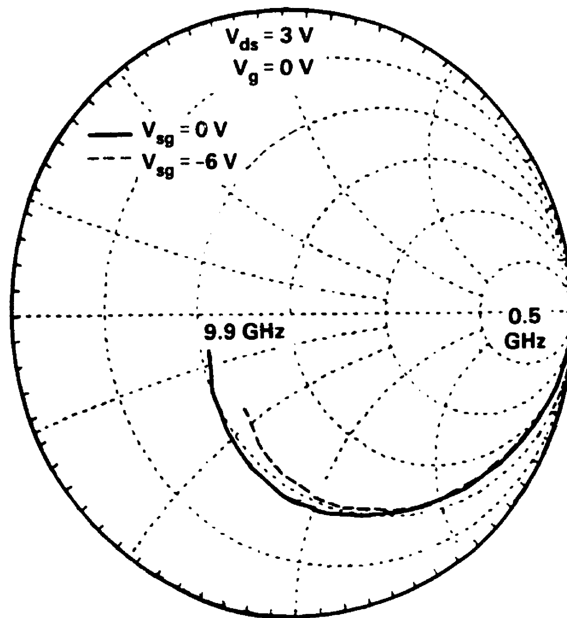

(b)

Fig. 3.12 Frequency dependence of the microwave performance of the MESFET with the conventional buffer layer for 0 and -6 V sidegate bias. (a) Measured maximum stable and available gains of the MESFET. The solid circles and the solid line are MSG and MAG, respectively, for V_{sg} = 0 V. The open circles and dashed line are MSG and MAG, respectively, for V_{sg} = -6 V. The inset shows the circuit configuration. (b) Smith chart representation of the measured S_{11}.

were 0 and 3 V, respectively. Figure 3.12(a) shows plots of the frequency dependence of measured maximum available gain (MAG) and maximum stable gain (MSG) of the MESFET with the conventional buffer layer for V_{sg} = 0 and -6 V. Plots of the S_{11} for the same MESFET for V_{sg} = 0 and -6 V are shown in Fig. 3.12(b).

A simple equivalent circuit for the MESFET and the values of the circuit elements for V_{sg} of 0 and -6 V are shown in Fig. 3.13. The S-parameters calculated from the Super-Compact® program using the equivalent circuit element values of Fig. 3.13 agree well with the measured S-parameters over the frequency range from 0.5 to 9.9 GHz. Figures 3.14(a) and (b) compare the measured and calculated values of S_{11} for V_{sg} of 0 and -6 V, respectively. Although the measured and calculated behavior of S_{11} as a function of frequency do not exactly coincide, the observed fit is quite good given that only a 9-element model of the packaged FET was used. The fit between data and calculation could be improved by using a more precise model of the MESFET with more equivalent circuit elements (e.g., a 13-element model). However, parasitic inductance and capacitance of the package and bond wire will still limit the accuracy of the model. Since we are primarily interested in the behavior of the source resistance R_s and the gate-source capacitance C_{gs} as a function of V_{sg}, we did not think that a more rigorous calculated fit was justified.

As indicated in Fig. 3.13, R_s increases when a negative sidegate bias is applied, because of the wider depletion region at the interface of the active and buffer layers. The larger source resistance increases the gate-source self-bias and, hence, the C_{gs} decreases. The g_m also decreases slightly with sidegate biases. At low frequencies, where the reactance of the gate capacitance is large compared with the input resistance, the increased source resistance and the lower transconductance decrease the gain of the MESFET when a negative sidegate bias is applied. On the other hand, the

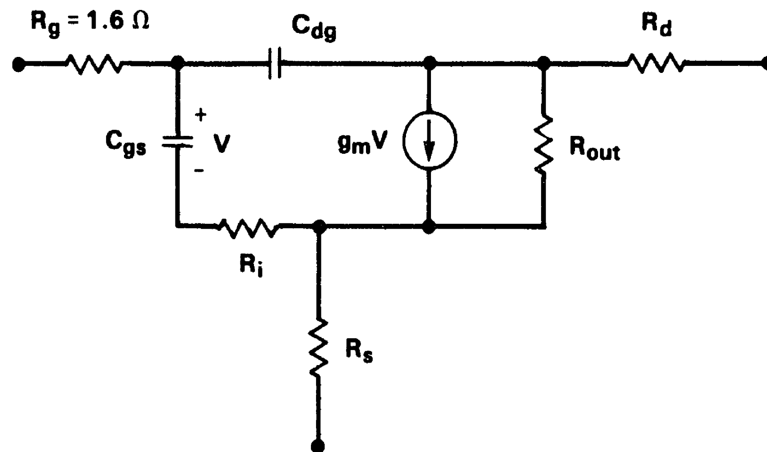

	$V_{sg} = 0$ V	$V_{sg} = -6$ V
g_m (mS)	14.7	14.2
C_{gs} (pF)	0.454	0.376
R_s (Ω)	21	29.8
R_i (Ω)	8.8	8.9
R_{out} (Ω)	375	337
R_d (Ω)	13.8	16.3
C_{dg} (pF)	0.0089	0.0084

Fig. 3.13 Equivalent circuit and the values of the circuit elements for the MESFET on the conventional buffer layer.

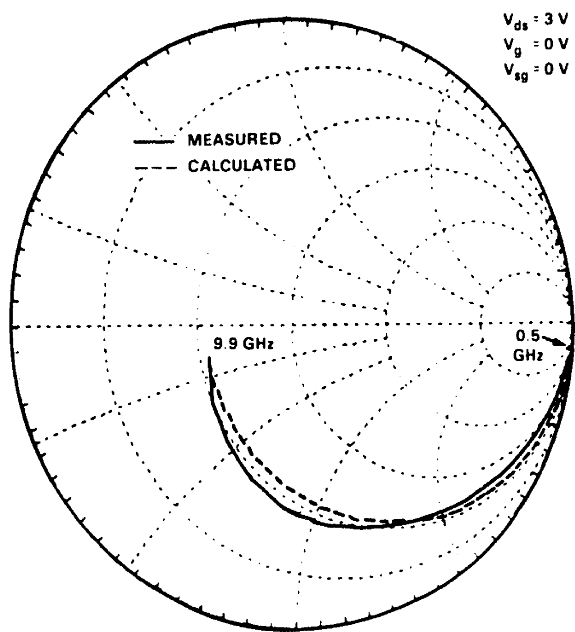

(a)

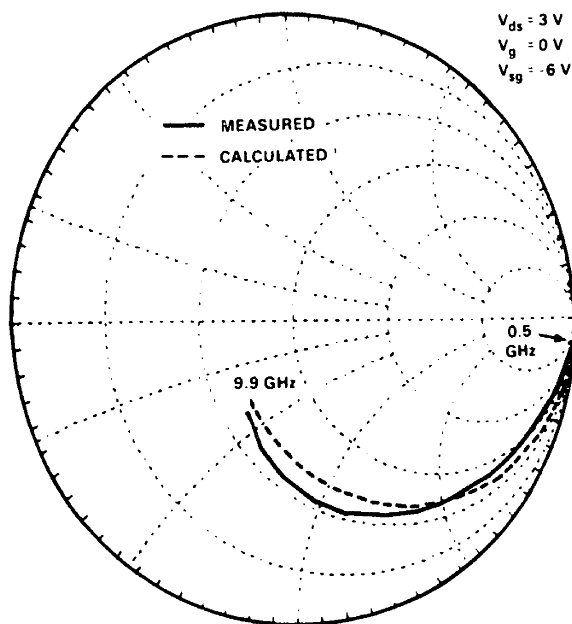

(b)

Fig. 3.14 Smith chart representation of the measured and calculated S_{11} between 0.5 and 9.9 GHz for (a) V_{sg} = 0 V and (b) V_{sg} = -6 V. The calculated S_{11} values were obtained using the Super-Compact® program for the equivalent circuit of Fig. 3.13.

smaller gate capacitance results in higher gain with increasing frequencies. This explains why the difference in MSG or MAG for different V_{sg} becomes negligible at higher frequencies.

However, variations of the input impedance of the MESFET with sidegate bias increase the complexity of the input circuit design, and, hence, optimal impedance matching conditions may not be satisfied for all the devices in a complicated circuit. The changes in the equivalent circuit elements shown in Fig. 3.13 translate into a degradation of more than 10 dB in the input return loss at 8 GHz for an amplifier using this MESFET. The output reflection scattering parameter S_{22} of the MESFET is found to be insensitive to the sidegate bias.

3.2.2.3 Digital Circuits

Two experiments have been carried out to examine sidegating effects in digital circuits. The first experiment addresses the influence on a MESFET of a pulse train on the adjacent sidegate. This simulates interactions between closely spaced devices in very large scale IC's. The second experiment is concerned with the duty-cycle effect of MESFET's, which is a commonly used method for characterizing the side-gating effect in digital circuits [3].

In the first experiment, a MESFET was configured as a simple inverter as shown in Fig. 3.15(a). The drain was connected to a 3-V power supply through a 100-Ω load resistor and the gate was grounded. The square-wave input to the sidegate is shown as the upper trace in Fig. 3.15(b). The period of the input square wave was 4 ms and the high and low voltages were 0 and -6 V, respectively. The lower trace in Fig. 3.15(b) is the observed waveform at the drain of the MESFET with the conventional buffer layer in response to the input square wave at the sidegate. A coupled signal with an amplitude of approximately 0.2 V and a rise time of 0.45 ms was

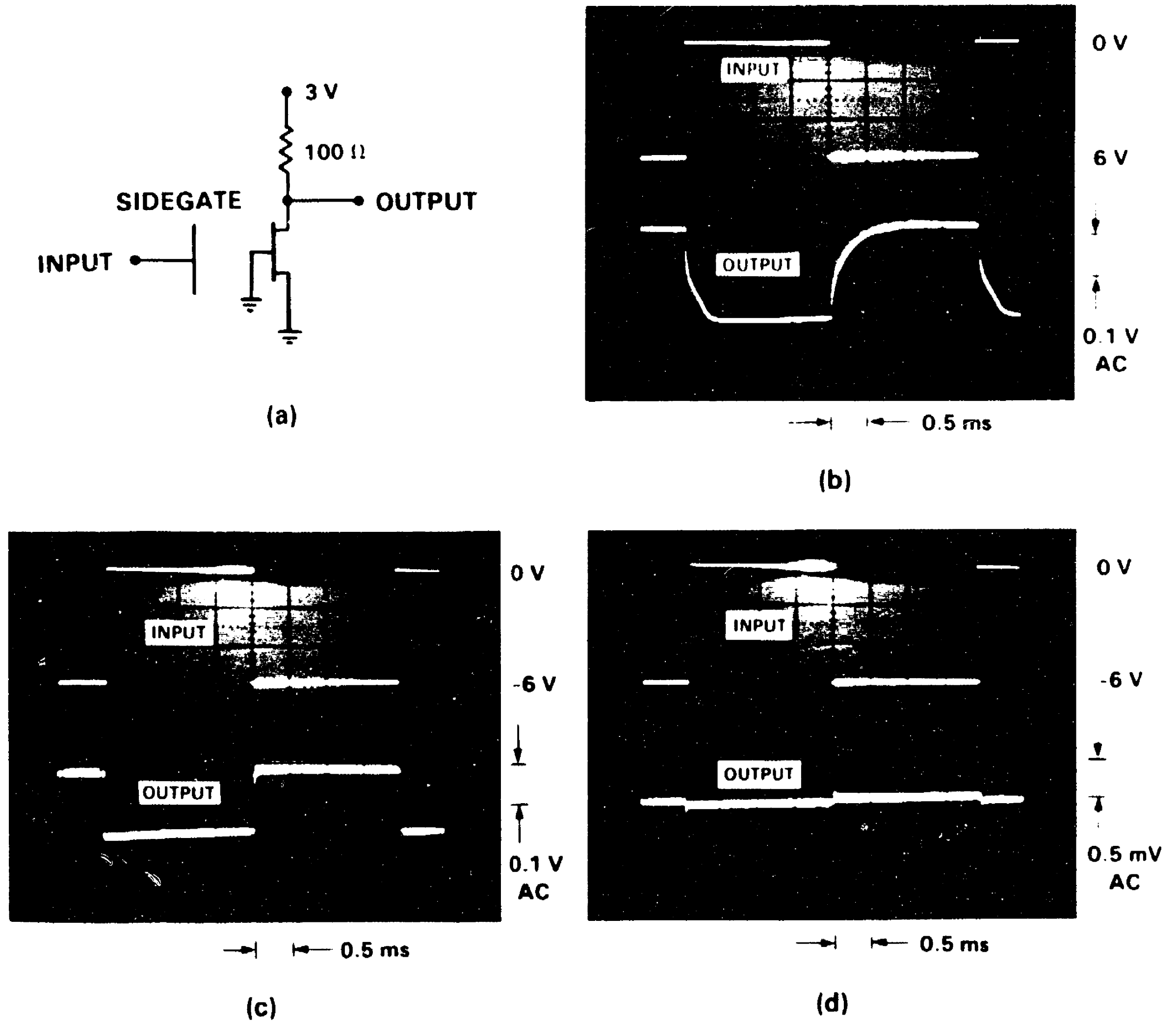

Fig. 3.15 Circuit diagram and results of the sidegating experiment using a digital pulse train. (a) Circuit diagram and bias configuration of the inverter used in the experiment. (b) Measured results for the MESFET with the conventional buffer layer in the dark. (c) Measured results for the same MESFET under illumination. (d) Measured results for the MESFET with the LT GaAs buffer layer in the dark. For all three photographs, the upper trace is the input waveform to the sidegate and the lower trace is the output waveform of the drain.

measured.

This signal is due to the modulation of drain current caused by the expansion and contraction of the depletion region at the active-buffer interface. The observed step in the voltage-decay waveform shown in Fig. 3.15(b) suggests that there may be more than one type of trap in the buffer layer. When the MESFET is illuminated by a microscope lamp, the conductance of the buffer layer increases, and both rise and fall time decrease substantially, as shown in Fig. 3.15(c). These results demonstrate that the signal coupling is strongly related to traps in the buffer layer. However, further studies are needed to identify the type and source of these traps.

The same signal-coupling effect in a MESFET with the LT GaAs buffer was also investigated. The result is shown in Fig. 3.15(d). There is virtually no signal coupling for the MESFET with the LT GaAs buffer layer and, furthermore, the coupling is not affected by light.

Since the time constants associated with changing the width of the depletion region near the active-buffer interface layer are slow compared with the normal switching time of a MESFET, the degree of sidegating depends upon the duty cycle of the pulse trains encountered in a digital circuit. The inset of Fig. 3.16 shows the circuit diagram and the pulse train used in an experiment to measure this dependence. Although in this experiment the pulse trains are applied to the sidegate instead of to the source of the MESFET [3], both circuit configurations measure the same sidegating effect. The duty cycle is defined as the amount of time the sidegate is at -6 V divided by the total period of the pulse waveform. A constant -6 V pulse with 100–ns width was used for all the measurements, and the period was varied to obtain different values of duty cycle. By this definition the sidegate bias was 0 V at zero duty cycle.

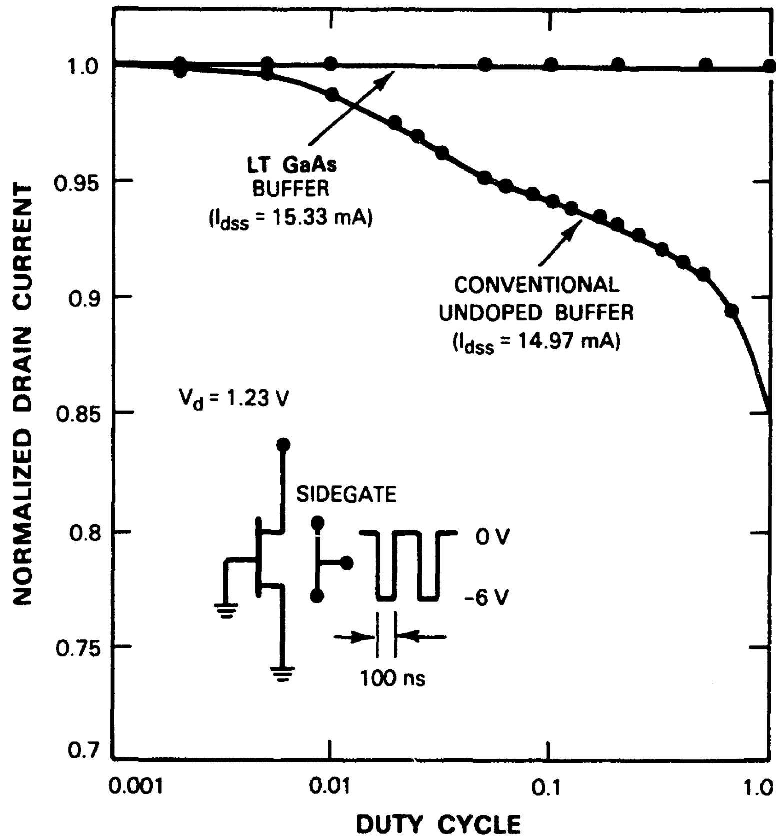

Fig. 3.16 Measured drain current, normalized to the drain current at zero duty cycle, of MESFET's fabricated on conventional and LT GaAs buffer layers as a function of the duty cycle of the pulse train applied to the sidegate. The inset shows the bias configuration and applied pulse train.

The measured drain current, normalized to the drain current at zero duty cycle, is plotted as a function of duty cycle in Fig. 3.16. Note that the drain current for the MESFET with the conventional buffer decreases with increasing duty cycle, as has been previously reported in the literature [3]. This current reduction is caused by a larger average negative voltage on the sidegate when duty cycle increases. As expected, the drain current for the MESFET with the LT GaAs buffer does not change with duty cycle, because, as was shown, the voltage on the sidegate does not affect the drain current. This experiment demonstrates once again that the use of a LT GaAs buffer layer can provide a very stable logic state in a digital IC.

3.2.2.4 Interaction Between RF and Digital Circuits

Digital signals are often needed for control purposes in many RF analog circuits. For instance, high and low voltages are required to control MESFET's or diodes that are used as RF switches, and even more complicated multiple logic states are needed to control phase shifters or attenuators at RF and microwave frequencies. There is a growing interest in integrating the microwave circuits with their digital control circuits on a single GaAs chip to improve performance and reliability. Therefore, it is important to understand how unintentional interaction between digital and microwave signals may occur. In this experiment, we investigated the interaction of digital signals applied to the sidegate of a MESFET with RF signals which were being amplified by the MESFET.

The circuit configuration used in this experiment is identical to that shown in Fig. 3.12(a) for the S-parameter measurement. The drain and gate were biased at 2 and 0 V, respectively, and source was grounded. A 200-MHz RF signal with -20 dBm power level was applied to the gate of the MESFET for amplification. A digital signal was applied to the sidegate simultaneously. The measured rectangular waveform at the sidegate is shown in Fig. 3.17(a). The period of the pulse train is

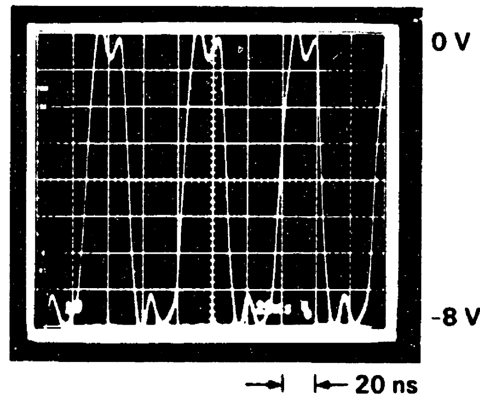

(a)

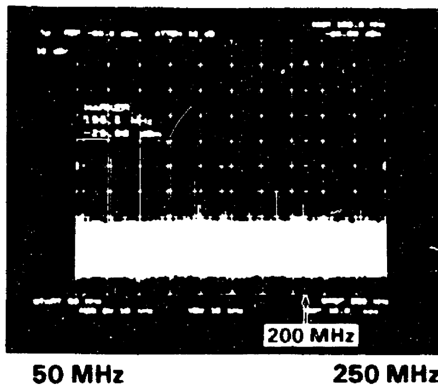

(b)

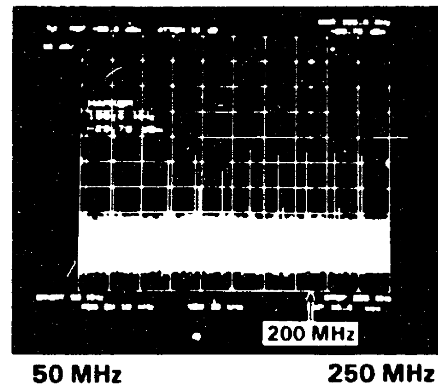

(c)

Fig. 3.17 Measured interaction of a digital control signal with a MESFET. (a) Measured rectangular waveform of the digital signal applied to the sidegate. The period of the pulse train is 56 ns (~ 18 MHz) and the two voltage levels are 0 and -8 V. (b) Measured output spectrum at the drain of the MESFET with a LT GaAs buffer layer. The -29.0 dBm spectrum at 200 MHz is the amplified signal and the remaining spectra are the various frequency components of the coupled digital signal. (c) Measured output spectrum at the drain of the MESFET on a conventional buffer layer. The power of the amplified signal at 200 MHz is -29.7 dBm.

56 ns and the voltage levels of the high and low state are 0 and -8 V, respectively. A spectrum analyzer was used to measure the output at the drain of the MESFET. The results for MESFET's with the LT GaAs buffer and with the conventional buffer are shown in Figs. 3.17(b) and 3.17(c), respectively. The pulse train is rich in high-frequency components which have been coupled to the MESFET through the buffer layer. The spectrum measured at 200 MHz is the amplified signal. Because the MESFET does not have input and output matching circuits, it actually introduced approximately 10 dB of insertion loss at 200 MHz. Coupled signals from the sidegate (peaks at frequencies other than 200 MHz) are observed at various frequencies, as the spectra show. A comparison of the magnitudes of the coupled spectra in Fig. 3.17(b) (LT GaAs buffer) and 3.17(c) (conventional buffer) shows that there is an approximately 15 to 20 dB reduction in coupling near 200 MHz by using the new buffer as compared with the conventional buffer. Although the absolute frequencies and magnitudes of coupled components vary with the period, duty cycle, magnitude, and shape of the pulse train applied to the sidegate, the coupling is always stronger for the MESFET with the conventional buffer. The LT GaAs buffer provides much better coupling immunity than the conventional buffer. Hence, the LT GaAs buffer layer should allow for much better isolation between digital control signals and the active devices in MMIC's.

3.2.2.5 Discussion

In this section, it has been shown that the drain current of a MESFET on the LT GaAs buffer does not vary with the voltage on the sidegate. As a result, for a digital circuit, the voltage levels of logic states are not affected by the duty cycle of pulse trains, or by the magnitude of the voltage transition of the logic state on an adjacent device. Therefore, the restrictions on the device layout imposed by the sidegating

effect can be eliminated and the gate widths of critical MESFET's in the circuit need not be increased to compensate for the sidegating effects [7].

In response to the growing importance of GaAs MMIC's, we have studied sidegating effects relevant to microwave circuits in detail. To the best of our knowledge, this is the first study of its kind. In these experiments, we have used the LT GaAs buffer layer as a reference to identify the sidegating effects that are caused by an imperfect buffer layer.

The R_s, C_{gs}, and g_m of a MESFET fabricated on a conventional buffer layer vary with the voltage on the sidegate or any adjacent ohmic contact. Consequently, the S-parameters of a MESFET at microwave frequencies change significantly with the sidegate bias. For high-power MMIC applications, large signals will change the effective dc bias of a MESFET. This signal-dependent bias condition can lead to unpredictable device parameters, resulting in inaccurate matching-circuit designs. Therefore, the design of the microstrip matching circuit for MMIC's becomes very complicated and optimal circuit performance may not be obtained at all times. We have shown that the use of the LT GaAs buffer layer has eliminated this bias dependence completely.

Another sidegating effect in an analog circuit is that RF signals are coupled between MESFET's in close proximity. By comparing the results for two different buffer layers, we have demonstrated that the coupling is mainly through the buffer layer. The dominant coupling mechanism changes gradually from resistive to capacitive when the frequency increases. For a conventional buffer layer, the width of the depletion region at the interface of the active and buffer layers changes with both the dc sidegate bias and the RF signal at the sidegate. When a MESFET is biased as a common-source amplifier, the buffer/active-layer interface acts as the gate of a parasitic transistor. Because the parasitic transistor provides additional amplification,

the coupled signal is stronger under bias than it is with zero dc bias. This parasitic transistor does not exist when the LT GaAs buffer is used because the depletion region does not vary with either the dc or the RF voltage on the sidegate. The distinction of the signal coupling between the two buffer layers is increasingly apparent with decreasing frequency.

As advanced MMIC's continue to move to ever denser circuitry, the possibility of undesirable and parasitic interactions between the microwave signals and the digital control signals becomes increasingly likely. The Fourier components of the digital signal can couple to a MESFET in the same manner described in the previous paragraph. This coupling can be very troublesome because there are many uncontrollable Fourier components in a digital pulse train, and, hence, the interference with the microwave signal can be severe. It has been demonstrated that the MESFET with the LT GaAs buffer is also less susceptible to the interference from a digital signal. Therefore, when a digital control circuit is integrated with MMIC's on a single GaAs chip, the limitations of voltage swings and the minimum separation distance required between a microwave MESFET and the digital circuit can be reduced if the LT GaAs buffer layer is used. As a result, the chip size can be reduced and the performance of the MMIC can be improved.

The LT GaAs buffer layer has been shown to provide excellent device isolation and immunity to many of the sidegating effects encountered in digital, analog, and monolithic microwave integrated circuits. Furthermore, the quality of the active layer grown on top of the LT GaAs layer is as good as that grown on the conventional buffer. Thus, high performance devices and circuits can be fabricated in active layers on the LT GaAs buffer layer, thereby taking advantage of the isolation and sidegating improvements possible with this buffer.

3.2.3 Elimination of Sidegating-Enhanced 1/f Noise

GaAs MESFET's are increasingly being used in low-noise MMIC's [49]. However, the low-frequency noise performance of GaAs MESFET's remains inferior to that of silicon bipolar transistors [12],[49]. Low-frequency noise is particularly important for MMIC's such as oscillators and mixers [49]. As is the case for most semiconductor devices, the low-frequency noise in GaAs MESFET's is typically inversely proportional to frequency. This type of noise is generally called 1/f noise. The use of the LT GaAs buffer in GaAs MESFET's has been shown to eliminate the dependence of 1/f noise on sidegate bias [12].

For this study, the sidegating MESFET discussed above was used. The sidegate was spaced 50 μm from the MESFET, and a device with the LT GaAs buffer was compared with a device with the conventional undoped GaAs buffer. The measurements were made using an experimental setup specifically designed for low-noise testing [12]. The device was biased into the forward active region and the noise at the drain was measured using a low-noise amplifier and a fast-Fourier-transform spectrum analyzer [12].

The noise spectra at the drain of the MESFET's with the conventional and LT GaAs buffers are shown in Figs. 3.18(a) and (b), respectively. The measured noise spectra are plotted against frequency, with sidegate bias as the parameter. In both cases the noise is seen to be inversely proportional to frequency. While the noise of the device with the conventional buffer increases by an order of magnitude as the sidegate bias is decreased from 0 to -9.5 V, the noise of the device fabricated on the LT GaAs buffer is insensitive to sidegate bias. We tentatively attribute the elimination of the sidegate-bias-induced increase in 1/f noise in the device with the LT GaAs buffer to the elimination of the sidegate-bias-induced variation in I_{ds}.

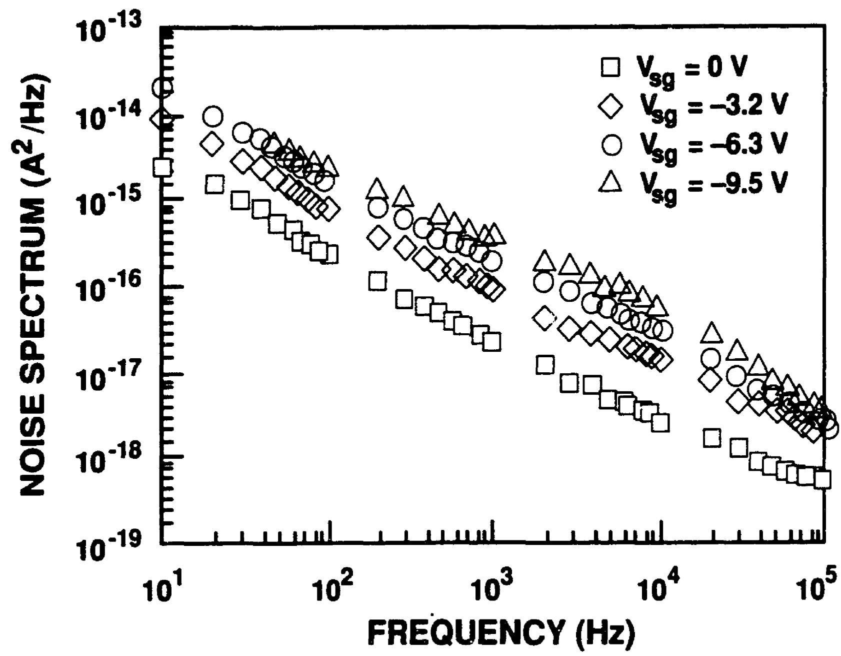

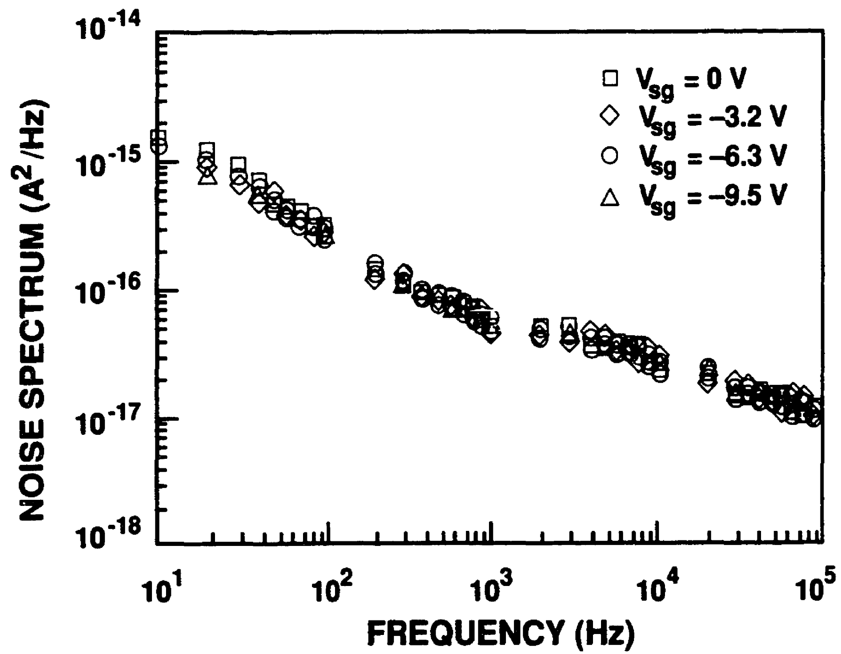

Fig. 3.18 Low-frequency noise measured at the drain of the MESFET as a function of sidegate bias: (a) conventional undoped GaAs buffer, and (b) LT GaAs buffer.

3.3 0.27-μm-Gate-Length MESFET's

Several of the short-channel effects noted in the introduction were substantially reduced by using the LT GaAs buffer in a 0.27-μm-gate-length MESFET [9]. Figure 3.19 shows a top view of the MESFET used in this study. Figure 3.19(a) is an SEM photograph of the entire device and Fig. 3.19(b) is a magnified view of the gate region. The MESFET has multiple gate connections to minimize gate resistance, and the segmented source is connected by air bridges. The gate was defined in a single layer of PMMA using electron beam lithography. The measured L_g, W_g, and source-drain spacing are 0.27, 200, and 2 μm, respectively. All the dc and RF measurements were made on this device.

Schematic cross sections of the 0.27-μm MESFET's are shown in Fig. 3.20. The starting material is SI GaAs and all epitaxial layers were deposited by MBE. Since the structure of the device with the LT GaAs buffer is slightly different from the structure of the device with the undoped GaAs buffer, both are shown in this figure. The device with the undoped GaAs buffer has a 330-nm-thick buffer layer, a 120-nm-thick active layer doped to $6x10^{17}$ cm^{-3} with silicon, and a thin heavily doped n^+-GaAs cap layer doped to $2x10^{18}$ cm^{-3} with silicon. The device with the LT GaAs buffer layer has a 1-μm-thick buffer, a 10-nm-thick undoped GaAs region that has a planar (impulse) doping of silicon halfway through it, a 120-nm-thick active layer doped to $6x10^{17}$ cm^{-3} with silicon, and a thin n^+ cap. The silicon planar doping of $4.8x10^{12}$ cm^{-2} is included in the device with the new buffer to increase g_m near pinch-off. The gates are recessed to a depth that yields the same I_{ds} for both devices, and mesa etching is used for device isolation. The ohmic contacts are alloyed Ni/Ge/Au and the Schottky contact is Ti/Au.

The I_{ds}-V_{ds} characteristics for the MESFET's are shown in Fig. 3.21. Both devices show a slight negative slope for the gate-source voltage V_{gs} near 0 V (the

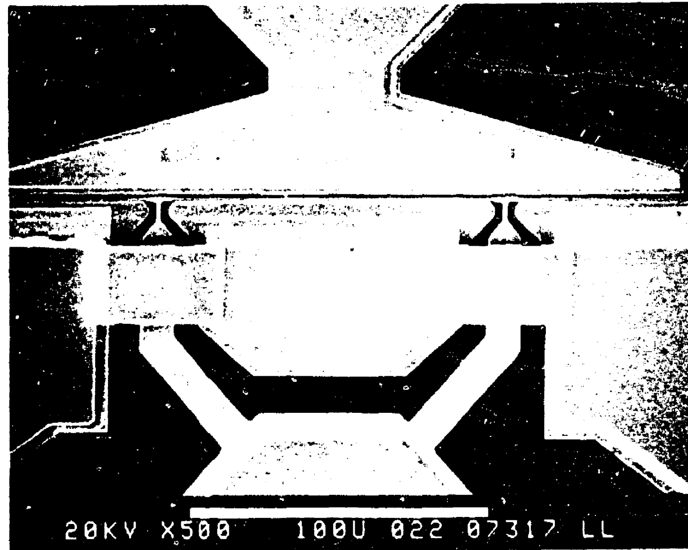

(a)

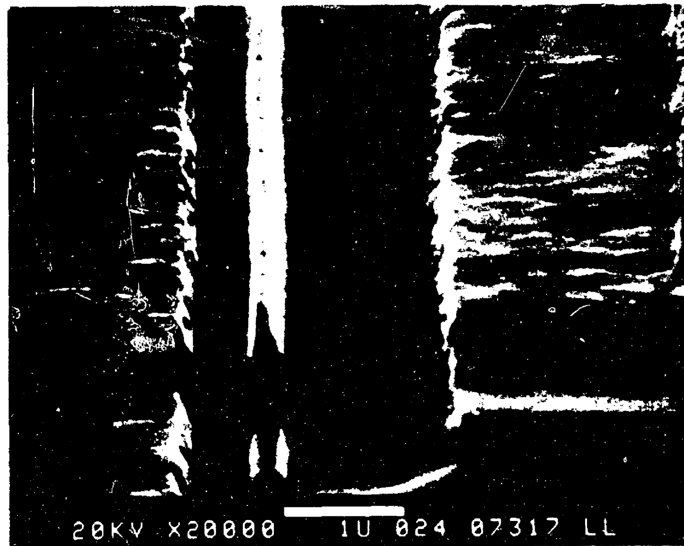

(b)

Fig. 3.19 SEM photographs of the 0.27-μm MESFET: (a) top view of the device, and (b) magnified view of the gate region.

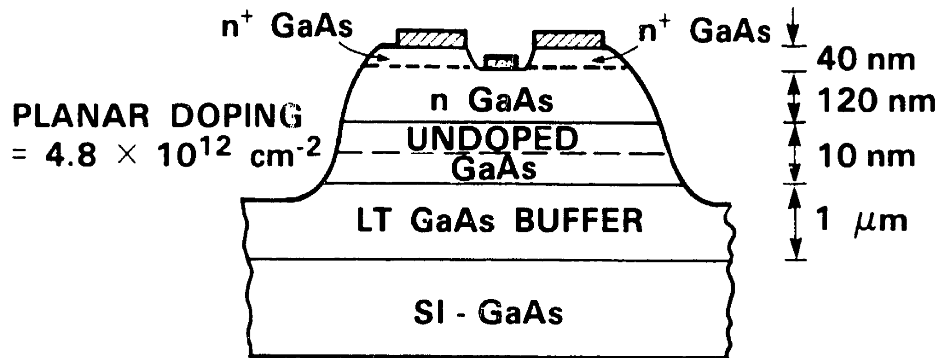

(a)

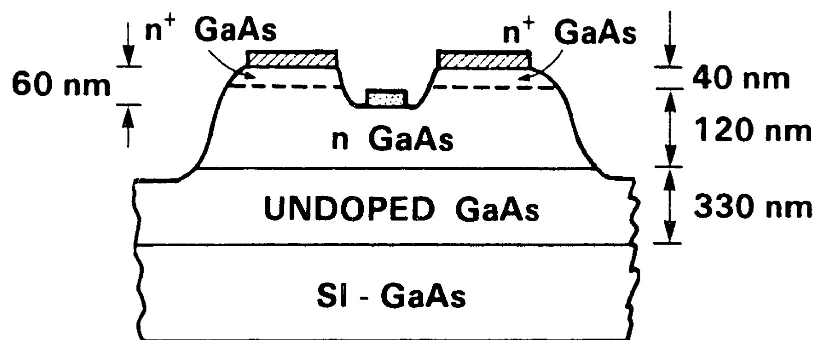

(b)

Fig. 3.20 Schematic cross sections of the 0.27-μm MESFET's: (a) LT GaAs buffer, and (b) undoped GaAs buffer.

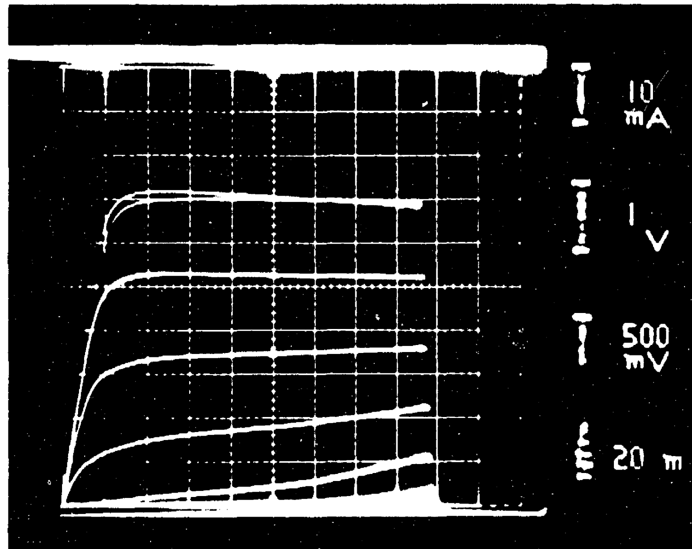

(a)

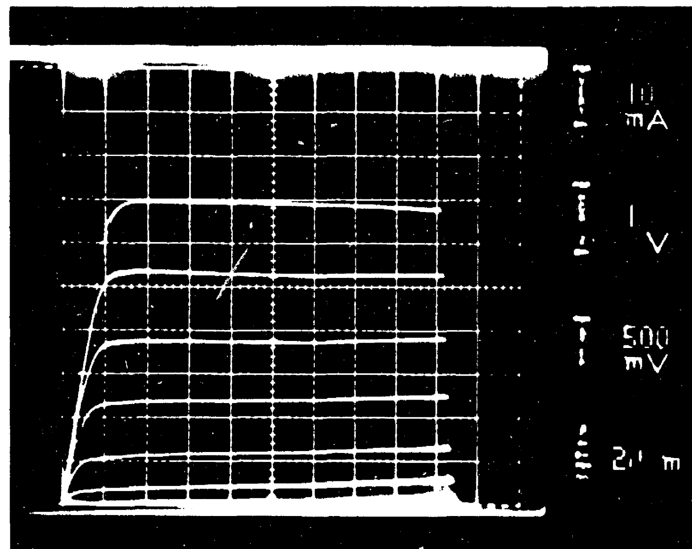

(b)

Fig. 3.21 0.27-μm MESFET I_{ds}-V_{ds} characteristics: (a) LT GaAs buffer, and (b) undoped GaAs buffer.

upper trace in each photograph). This effect can occur for a variety of reasons, such as thermal effects or high-frequency oscillations. These measurements were made on an unshielded probe station, and it is expected that packaging the devices will alleviate this problem.

Although the interpretation of the data for V_{gs} near 0 V is not clear, our experience indicates that the data near pinch-off provide a meaningful comparison of these devices. The 0.27-μm MESFET with the undoped buffer shows pronounced short-channel effects, namely, a low output resistance near pinch-off and incomplete pinch-off for large drain-source voltages. In contrast, the MESFET with the LT GaAs buffer has a large output resistance near pinch-off and fully pinches off even for drain-source voltages in excess of 10 V.

Selected dc results for these MESFET's are summarized in Table 3.3. Although the peak g_m is slightly lower for the MESFET with the LT GaAs buffer, R_d near pinch-off (V_{gs} = -1.5 V) is larger by a factor of 50 and BV_{SD}, as measured with the device biased to pinch-off, is larger by a factor of 2.

Improved RF performance of the 0.27-μm MESFET incorporating the LT GaAs buffer has also been observed. The values of f_{max} and f_T have been calculated from the measured scattering parameters and are shown in Table 3.4. The MSG at 26 GHz for the device with the LT GaAs buffer is 12 dB, and f_{max} and f_T are 91 and 28 GHz, respectively, for that device. These results were measured for V_{ds} = 2 V and did not change appreciably for V_{ds} up to 6 V. These values of MSG, f_{max}, and f_T for the MESFET's using the LT GaAs buffer are significantly better than those measured on comparable MESFET's using an undoped MBE GaAs buffer and are among the best we have measured for MESFET's fabricated by the same process with a gate length of 0.27 μm. Lastly, based on the larger BV_{SD} and the scattering parameter results for V_{ds} = 6 V, it is expected that significantly improved RF power

PROPERTIES	UNDOPED MBE GaAs BUFFER	LT GaAs BUFFER
g_m (mS/mm)	205	190
R_d (Ω)	1,000	50,000
BV_{SD} (V)	7	14
BV_{ISO} (V)	30	400

Table 3.3 Summary of dc results: 0.27-μm MESFET.

PROPERTIES	UNDOPED MBE GaAs BUFFER	LT GaAs BUFFER
MAXIMUM STABLE GAIN AT 26 GHz (dB)	10.4	12.0
f_T (GHz)	26	28
f_{max} (GHz)	80	91

Table 3.4 Summary of RF results: 0.27-μm MESFET.

performance will result for MESFET's incorporating the LT GaAs buffer.

3.4 Other Electronic Device Applications of LT GaAs

Several other electronic device applications of the LT GaAs buffer have been demonstrated or envisioned. Since this research is only preliminary, the discussion of each will be brief. However, many of these applications may be not only of considerable research interest but also of considerable commercial interest.

3.4.1 GaAs MESFET IC's Using the LT GaAs Buffer

Following our original publications, researchers at Hewlett-Packard and Hughes Corporations have fabricated high-performance GaAs-based MESFET and HEMT IC's using the LT GaAs buffer [18],[19],[50]. They too have found that sidegating effects and light sensitivity are eliminated in their digital and microwave IC's by incorporating the LT GaAs buffer. Hughes demonstrated that 0.2-μm-gate-length MESFET's with the LT GaAs buffer had a g_m of 600 mS/mm and an extrapolated f_T of 80 GHz [19]. Frequency dividers designed using source-coupled FET logic were fabricated from these transistors and exhibited a clock rate of 22 GHz [19]. This result is among the best ever reported for a GaAs-MESFET-based frequency divider.

3.4.2 AlGaAs/GaAs HEMT's

In our first publication describing MESFET's fabricated with the LT GaAs buffer, we noted the applicability of this buffer layer to HEMT's [8]. HEMT's (also known as MODFET's) are even more susceptible to backgating than MESFET's [51]. After learning from us how to grow this buffer layer, researchers from Hewlett-Packard fabricated HEMT's with the LT GaAs buffer layer. Using proton and oxygen implantation to achieve isolation between devices (as opposed to mesa etching)

and the LT GaAs buffer under the active layers, these researchers found that I_{dss} (see Section 3.2.1) changed only 0.2% for -70 V applied to an isolated sidegate contact spaced 3 μm away from the HEMT [18]. Since 70 V is considerably more voltage than will ever be used in most HEMT applications, it can be asserted that backgating has been eliminated in HEMT's by using the new LT GaAs buffer. LT GaAs has now become the buffer of choice at HP for both MESFET and HEMT IC's. Circuits using LT GaAs buffer layers are expected to enter manufacturing in the near future.

Researchers at Purdue University have also investigated the use of the LT GaAs buffer layer in HEMT's [52]. Using Shubnikov-de Haas oscillations and other electrical measurements, they found that the mobility of the two-dimensional electron gas formed at the AlGaAs/GaAs heterointerface with either an undoped GaAs buffer or a LT GaAs buffer is comparable. This result further confirms the results presented in Sec. 2.3 that GaAs grown on the LT GaAs buffer is of high quality and that high-performance electronic devices can be fabricated using this buffer.

3.4.3 LT GaAs MISFET

GaAs depletion-mode metal-insulator-semiconductor field-effect transistors (MISFET's) were fabricated using LT GaAs as the underlying buffer layer and the gate insulator. Although the devices worked (exhibited gain and could be pinched off), the gate was not well insulated from the device (i.e., nonnegligible gate current was measured). The large gate leakage arose because the 200°C LT GaAs layer used as the gate insulator was not annealed at 600°C. As will be shown in Chapter 5, as-grown 200°C LT GaAs, although resistive, is not semi-insulating. LT GaAs becomes SI only after being annealed at 600°C. Since the MISFET's were fabricated before this phenomenon was recognized, we expect that improved MISFET performance can be achieved by annealing the gate insulator.

3.4.4 Transient Radiation Upset

Transient radiation upset is a major problem plaguing manufacturers of radiation-hard GaAs VLSI circuits for military applications [53]. Measurements of transient radiation upset for 2-μm-gate-length MESFET's indicate that the LT GaAs buffer may be an effective solution to this problem. Although the devices were not appropriately designed to minimize sensitivity to ionizing radiation, the amplitude of the transient response of the device showed virtually no change in response to an order of magnitude increase in the dose rate. McDonnell Douglas, a leading manufacturer of state-of-the-art radiation-hard GaAs VLSI circuits, is interested in collaborating on studies of the LT GaAs buffer as applied to the problem of transient radiation upset.

3.4.5 Low-Temperature $In_{0.52}Al_{0.48}As$

Following our success with the low-temperature growth of GaAs by MBE, researchers at Hughes have investigated the use of low-temperature-grown $In_{0.52}Al_{0.48}As$ as a buffer layer for $In_{0.53}Ga_{0.47}As/In_{0.52}Al_{0.48}As$ HEMT's lattice matched to InP [22]. They found that $In_{0.52}Al_{0.48}As$ grown at 150°C enhances the performance of $In_{0.53}Ga_{0.47}As/In_{0.52}Al_{0.48}As$ HEMT's fabricated on this layer. Analogous to our 0.27-μm-gate-length MESFET results, they found that the output conductance of their 1-μm-gate-length HEMT was markedly improved using the LT $In_{0.52}Al_{0.48}As$ buffer layer. The growth mechanism and physical properties of LT $In_{0.52}Al_{0.48}As$ are currently being investigated [54].

3.4.6 Lattice-Mismatched Heteroepitaxy

3.4.6.1 LT GaAs-on-Silicon

GaAs grown on large-diameter silicon wafers may be an important step in the ultimate commercial success of GaAs technology. However, as a result of the large (~4%) lattice mismatch between these two materials, the GaAs epitaxial layer contains many dislocations (~10^7 cm^{-2}) and the interface between the GaAs and Si is of poor crystalline quality. As a result of this poor interface quality, sidegating can be a significant problem in GaAs-on-Si MESFET IC's. The LT GaAs buffer was grown on GaAs-on-Si wafers, and similar improvements to those cited in Section 3.1 were observed for MESFET's with a gate length of 2 μm fabricated in this material [20]. Although RF measurements have not been made on these devices, based on recent results for GaAs-on-Si MESFET's fabricated on an undoped GaAs buffer [55], it is expected that improved RF performance will be achieved by using the new buffer and semi-insulating silicon substrates.

Furthermore, we believe that it may be possible to reduce the dislocation density of GaAs-on-Si epilayers by using the LT GaAs buffer. Figure 3.22 is a cross-sectional TEM image of a MESFET sample grown on a Si substrate [20]. The large density of dislocations is evident. However, Dr. Z. Liliental-Weber of the Lawrence Berkeley Laboratory has observed that dislocations can turn over (be terminated) at the interface between the LT GaAs buffer layer and the GaAs active layer. Hence, by using alternating layers of LT GaAs and GaAs (a LT GaAs/GaAs superlattice), we may be able to reduce the dislocation density in GaAs-on-Si.

Fig. 3.22 Cross-sectional TEM image of LT GaAs on GaAs-on-Si. After Liliental-Weber [20].

3.4.6.2 LT $In_{0.53}Ga_{0.47}As$-on-GaAs

$In_{0.53}Ga_{0.47}As$ and $In_{0.52}Al_{0.48}As$ are lattice matched to InP and have recently been used to fabricate the highest perfomance HEMT's reported to date (see also Sec. 3.4.5) [56]. However, despite the demonstrated performance of these materials, the need to use the low quality, fragile, and expensive InP substrates makes this device unattractive for manufacturing. Recently, researchers at Honeywell have grown these layers with low dislocation density on a GaAs substrate [21]. By using a LT $In_{0.53}Ga_{0.47}As$ layer (300°C), they showed that the large density of dislocations generated by the lattice-mismatched growth were terminated. A cross-sectional TEM photograph of a Honeywell HEMT sample with a LT $In_{0.53}Ga_{0.47}As$ buffer layer is shown in Fig. 3.23.

By terminating the dislocations, the LT growth of $In_{0.53}Ga_{0.47}As$ made possible the growth of strain-free $In_{0.53}Ga_{0.47}As/In_{0.52}Al_{0.48}As$ HEMT's with the lattice constant of InP on the cheaper and more robust GaAs substrate. The performance of these HEMT's was comparable to that obtained for identical devices fabricated on InP substrates [21]. This LT $In_{0.53}Ga_{0.47}As$ result may also have implications for reducing the dislocation density of InP grown on Si and of $In_{0.53}Ga_{0.47}As$ grown on GaAs-on-Si.

The results presented in this section indicate that LT growth of binary and ternary alloys can be used to accommodate the lattice mismatch between materials of different lattice constant, allowing low-dislocation epilayers of one lattice constant to be grown on substrates of another lattice constant.

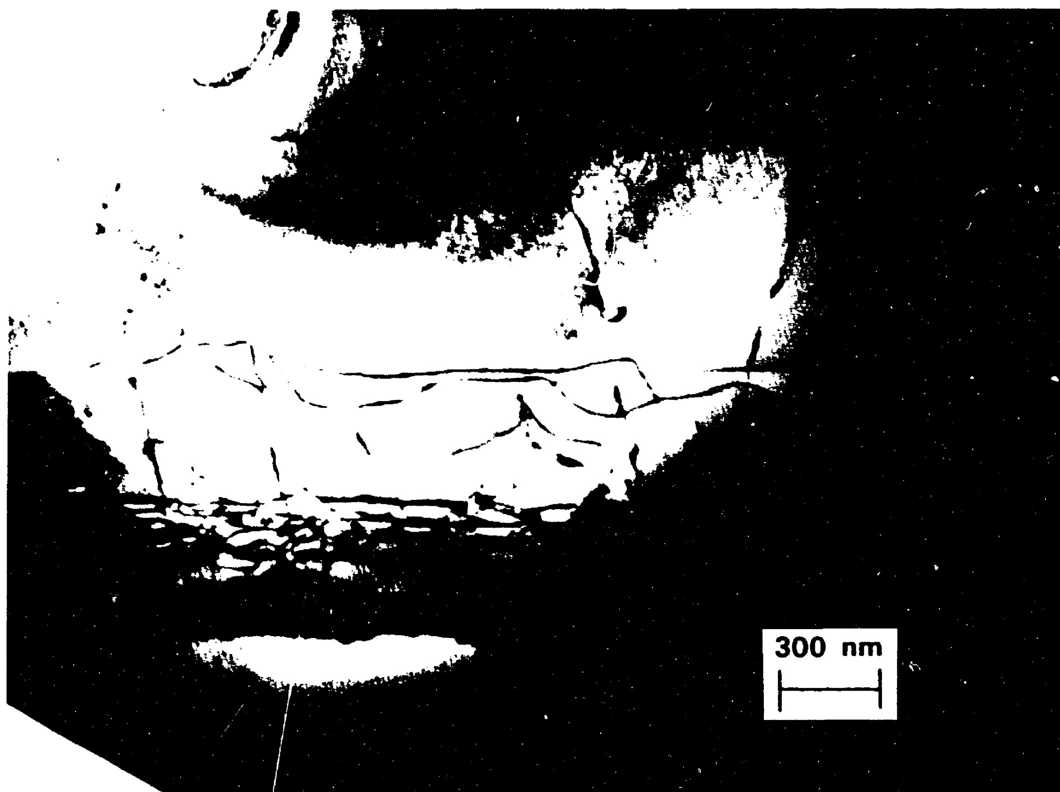

Fig. 3.23 Cross-sectional TEM image of an $In_{0.53}Ga_{0.47}As/In_{0.52}Al_{0.48}As$ HEMT structure using an LT $In_{0.53}Ga_{0.47}As$ buffer layer on a GaAs substrate. Note the reduction of dislocation density in the LT buffer. After Grider et al. [21].

CHAPTER 4. OPTOELECTRONIC DEVICE APPLICATIONS

This section is devoted to a discussion of photoconductive switches fabricated using LT GaAs. Results will be presented for a number of different switches fabricated using LT GaAs grown under a variety of conditions [13]-[15].

4.1 Introduction to Photoconductive Switches

Photoconductive switches are a means of converting ultrafast optical pulses into picosecond electrical pulses. This function is useful in a variety of applications such as picosecond optoelectronic switching and sampling [57],[58], high-speed detection for fiber-optic communication and optical-computing systems [59], signal processing [60], and far-infrared spectroscopy [61]. One of the most important of these is the characterization of high-speed semiconductor devices and circuits.

The ultimate speed of a photoconductive switch is determined by both the properties of the semiconductor material used as the active layer of the device and the configuration of its electrodes. For picosecond speed, short photoexcited carrier lifetimes are required. However, for good sensitivity, high carrier mobilities are needed. Since the damage that is often introduced into the semiconductor to shorten the carrier lifetime also generally reduces the carrier mobility, high speed and good sensitivity are often difficult to achieve in the same detector. The search for materials that can offer high speed with high sensitivity explains the voluminous literature on the subject of photoconductive switches.

Even if the material in question has a short recombination lifetime, the picosecond speed can be masked by slower transients associated with the parasitic capacitance and inductance of the device electrodes. Just as new materials have been investigated as possible active layers of picosecond switches, so too have new elec-

trode configurations been developed to realize these picosecond speeds.

The four most common test configurations of picosecond photoconductive switches are shown in Fig. 4.1. In the electronic correlation configuration developed by Auston and shown in Fig. 4.1(a), one photoconductive gap serves as the pulse generator and a second as the pulse sampler [57],[62]. The gaps are formed in microstrip transmission lines and the measured signal is the electronic correlation of the responses of the two gaps. Although widely used, this structure has large parasitic capacitance associated with the photoconductive gaps and suffers from pulse dispersion due to the microstrip transmission lines.

An improved version of the microstrip implementation of the electronic correlation configuration is the photoconductive-gap switch implemented on a coplanar stripline, as shown in Fig. 4.1(b). Here the picosecond electrical pulse is generated by a photoconductive gap and can be sampled either by using an electronic correlation technique or by electro-optic sampling [63],[64]. In this figure, the electrical pulse is shown being measured by electro-optic sampling. Although an improvement over the microstrip geometry, this structure is also plagued by the parasitic capacitance of the gap.

The fastest picosecond switching times have been measured using either of the configurations shown in Figs. 4.1(c) or 4.1(d). The Hertzian dipole configuration shown in Fig. 4.1(c) was also pioneered by Auston and operates similarly to the conventional electronic correlation configuration of Fig. 4.1(a), except that the first photoconductive gap launches the picosecond electrical pulse into free space (or dielectric) and this pulse is then sensed by the second gap [61]. The output is again the electronic correlation of the responses of the two switches. Far-infrared spectroscopy measurements are most easily implemented using variations of this configuration [61].

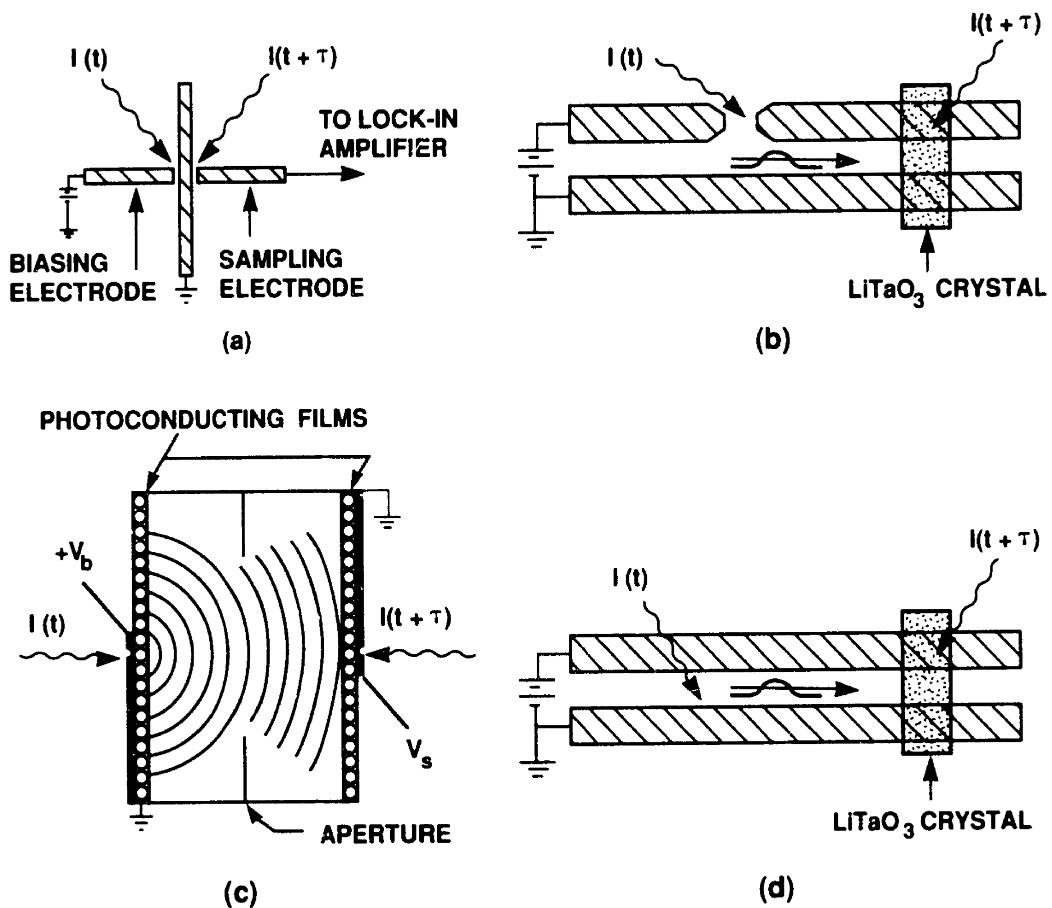

Fig. 4.1 Schematic diagram of commonly used photoconductive switch configurations: (a) Auston's electronic correlation switch (top view), (b) photoconductive-gap switch implemented on a coplanar stripline (top view), (c) Auston's Hertzian dipole electronic correlation switch (cross section), and (d) sliding-contact excitation switch (top view).

Perhaps the most useful configuration for both the generation and use of picosecond electrical pulses for high-speed device and circuit testing is the sliding-contact switch shown in Fig. 4.1(d) [65]. The only difference between this switch and the switch of Fig. 4.1(b) is the absence of the photoconductive gap, which reduces the parasitic capacitance. Electrical pulses of FWHM of 0.6 ps have recently been measured using this configuration [66]. In fact, when the photoconductive-gap switch and the sliding-contact switch were used to measure the same material, the photoconductive-gap switch yielded a FWHM of 1.7 ps, while the sliding-contact switch showed a pulse of 1.0 ps FWHM [67]. Clearly the effects of parasitic capacitance can be significant at ultrahigh speeds.

Using either the Hertzian-dipole or sliding-contact configurations, researchers have demonstrated that four different materials exhibit subpicosecond switch performance. The materials are oxygen-implanted silicon-on-sapphire (SOS) [65], implanted and radiation-damaged InP [68], amorphous silicon [58], and polycrystalline CdTe [66]. However, despite the high speeds, these materials have drawbacks which limit their use in high-speed testing applications. The silicon-based and InP-based switches tend to have low mobility, and, hence, exhibit poor sensitivity [66]. In addition, they cannot be easily integrated with the high-speed GaAs-based devices and circuits to be tested. The CdTe-based switch has been demonstrated to have both high speed and sensitivity, but these properties are a function not only of the growth parameters but also the substrate used for deposition [66]. Moreover, the CdTe switch has yet to be monolithically integrated with GaAs-based devices and circuits, although Nuss asserts that this can be done [66].

Photoconductive switches based on LT GaAs offer a number of distinct advantages over the switches dicsussed above. These include the fastest switching speed measured to date (FWHM = 470 fs, see Sec. 4.4), relatively high sensitivity, the abil-

ity to be integrated with high-speed GaAs devices and circuits, and, potentially, the ability to engineer the defects in the material to systematically trade speed for sensitivity. Also, since the measured dielectric-breakdown field of LT GaAs grown at 200°C is in excess of 3×10^5 V/cm (see Sec. 3.4.1), LT GaAs photoconductive switches should support high-voltage electrical impulses.

To demonstrate the picosecond performance of LT GaAs, photoconductive-gap and sliding-contact switches were fabricated. A modified form of the Auston correlation technique [62],[70] and the technique of electro-optic sampling [63],[64] were used to assess the speed of the LT GaAs switches. The correlation measurement is discussed first.

4.2 Autocorrelation Measurement of an LT GaAs Switch

Auston's original technique, depicted schematically in Fig. 4.1(a), used two photoconductive switches connected by microstrip transmission lines to perform cross-correlation measurements of the responses of the photoconductive switches [57],[58], [62]. In the measurement discussed here, the technique of Carruthers and Weller [70] involving a single-gap structure was used, eliminating the need for microstrip interconnect, and, hence, eliminating the pulse dispersion due to the transmission line. In their approach, one measures the nonlinear component of the response of a single photoconductive-gap switch to two correlated optical pulse trains. They have shown [70] that autocorrelation measurements of high-speed GaAs-based photodiodes and InP-based photoconductors made using their technique agree well with measurements of the same devices made using Auston's original technique [70]. The physics and mathematics of the Carruthers and Weller technique are summarized following a discussion of the device structure and test configuration of this measurement.

A schematic cross section and an optical micrograph of the top view of the LT GaAs photoconductive-gap switch used in this measurement are shown in Fig. 4.2 (a) and (b), respectively. Approximately 2 μm of LT GaAs were deposited at 200°C on a SI GaAs substrate. Following the LT GaAs growth, the substrate temperature was ramped to 580°C, at which time 20 nm of n^+ GaAs was deposited. The n^+ GaAs was included to facilitate ohmic contacts to the LT GaAs (see Sec. 4.6). The ohmic metal is Ni/Ge/Au and is 0.4 μm thick. The gap spacing between the ohmic contacts is 5 μm. Following the ohmic definition, chlorine ion beam assisted etching was used to remove the n^+ GaAs in the gap region [69].

The experimental setup is shown schematically in Fig. 4.3. Two synchronously pumped mode-locked dye lasers operating at 800 and 785 nm and emitting ~5 ps pulses were used to perform the autocorrelation measurement. By using two independent dye lasers, optical coherent effects were eliminated [70]. The pump and probe beams were chopped at 136 Hz and 27 kHz, respectively. The probe intensity was one order of magnitude lower than that of the pump beam. We used a less intense probe beam than pump beam to avoid excessive heating of the LT GaAs switch. Both beams were focused to a spot size of ~5 μm on the photoconductive gap. The bias arrangement of the switch is also shown in Fig. 4.3. A dc bias was applied across the two metal electrodes shown in Fig. 4.2. The back side of the sample was not biased.

This discussion of the nonlinear autocorrelation technique of Carruthers and Weller parallels that of Ref. [70]. They assume that the electrical output signal of the photoconductive switch depends only on the instantaneous number of photogenerated carriers N(t) that are present in the gap region of the device. They denote this output signal by I(N). The pump beam is assumed to generate carriers of number $N_1(t)$ and the probe beam is assumed to generate carriers of number $N_2(t+\tau)$, where τ

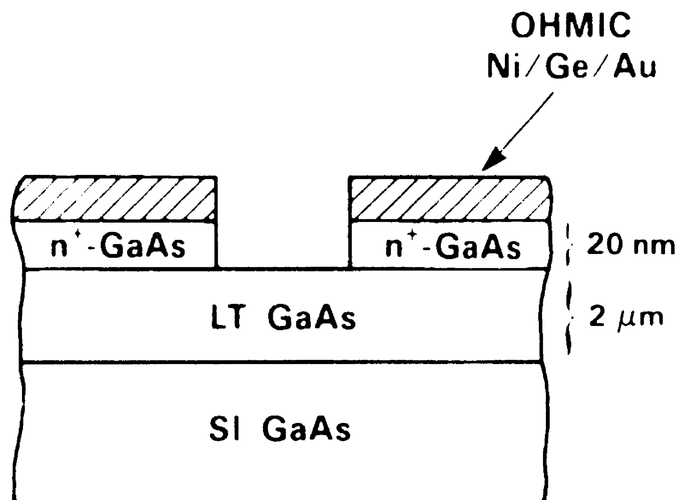

(a)

(b)

Fig. 4.2 LT GaAs photoconductive Auston switch used for the electronic autocorrelation measurement: (a) schematic cross section, and (b) optical micrograph of the device.

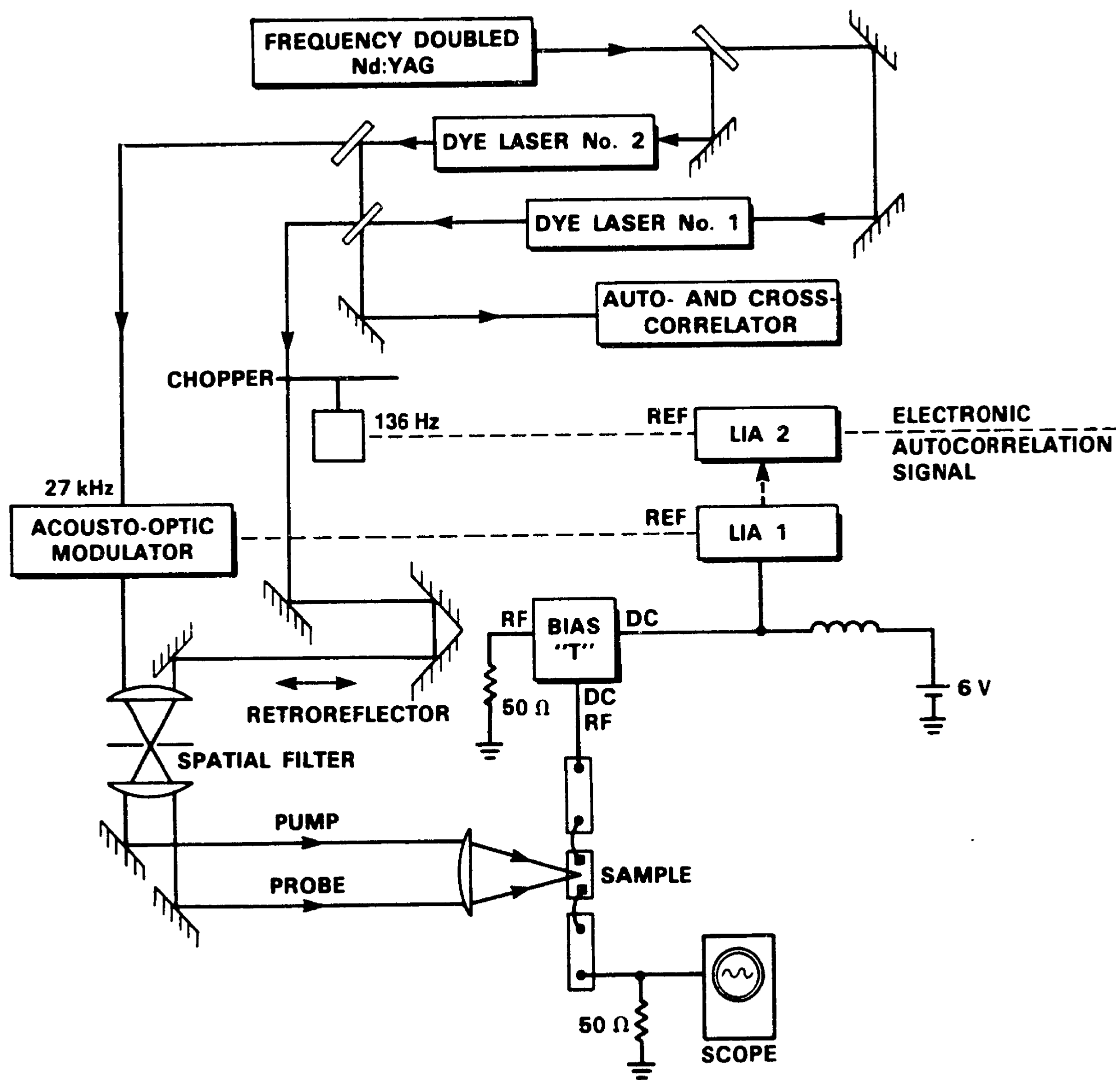

Fig. 4.3 Experimental configuration for the modified Auston correlation measurement.

is the time delay between the two optical pulses. The output of the switch in response to the two pulses can be expanded in a Taylor series about N=0 as follows:

$$I(N) = I(N_1+N_2) = I(N_1) + I(N_2) + N_1N_2\frac{d^2I}{dN^2} + \cdots \qquad (4.1)$$

where the derivatives are evaluated at N=0 and only terms to second order in N are shown.

The pump and probe beams are modulated at different frequencies, as depicted in Fig. 4.3, and a serial combination of two lock-in amplifiers (LIA's) is used to generate a dc output signal that is proportional to the time integral of the second-order term of Eq. (4.1) [70]. This output, $\delta Q(t)$, is given by

$$\delta Q(t) = \frac{d^2I}{dN^2}\int_{-\infty}^{\infty} N_1(t)N_2(t+\tau)dt \qquad (4.2)$$

where d^2I/dN^2 has been taken outside the integral since it is independent of time when evaluated at N=0. If $N_1(t)$ and $N_2(t+\tau)$ are identical except for the time delay, this integral is the autocorrelation function of the device response. Thus, the output of the second lock-in amplifier is proportional to the autocorrelation of the switch response.

The electronic autocorrelation result of the LT GaAs switch depicted in Fig. 4.2 is shown in Fig. 4.4. This result is for a dc bias of 6 V across the device. The dark current in response to the 6-V bias was less than the sensitivity of our ammeter (<1 μA).

Although the result depicted in Fig. 4.4 is not strictly an autocorrelation signal since N_1 does not identically equal N_2 (the laser pulses have the same temporal response but different intensities), other measurements with identical laser pulses

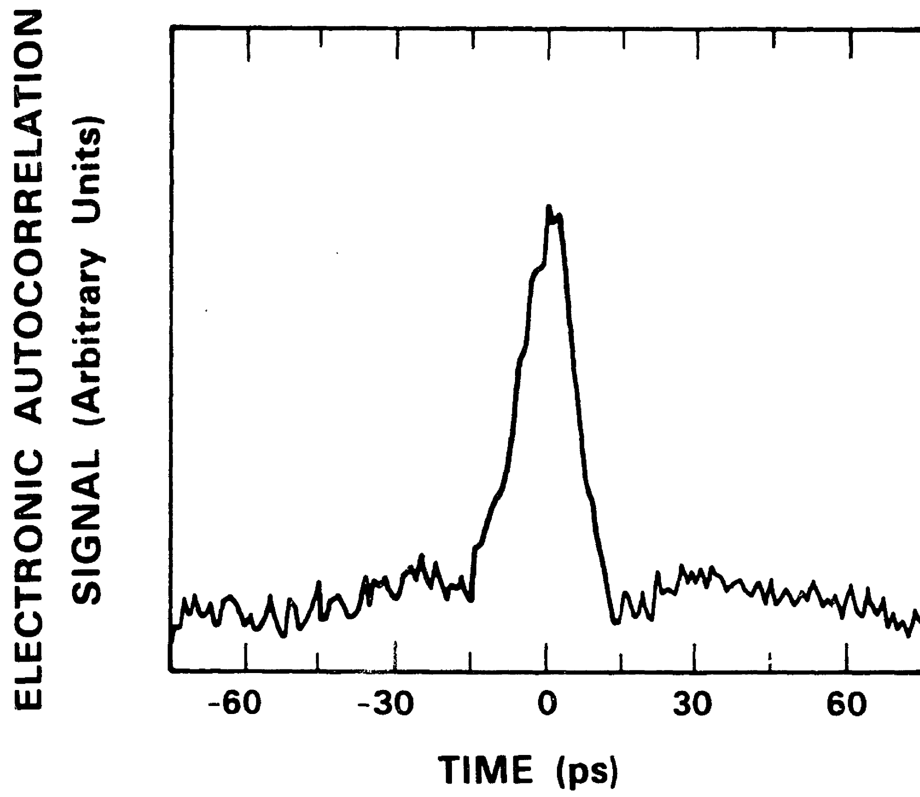

Fig. 4.4 Electronic autocorrelation signal of the LT GaAs Auston switch.

yielded essentially identical results to Fig. 4.4. For this reason, the y-axis of Fig. 4.4 is labeled as the electronic autocorrelation signal of the LT GaAs switch.

The LT GaAs photoconductive switch exhibits a system-limited time response of ~7.5 ps (one-half of FWHM). This time scale is roughly the temporal resolution of the measuring system, which is limited by the 5-ps duration of the laser pulses.

4.3 Electro-optic Sampling Measurements of LT GaAs Switches

To measure the actual performance of LT-GaAs-based photoconductive switches, photoconductive-gap and sliding-contact structures were used in conjunction with the technique of electro-optic sampling [15]. As shown in schematic cross section in Fig. 4.5, two different epitaxial layer structures were used to fabricate the photoconductive-gap and sliding-contact switches. The structure with the Ti/Au electrodes is discussed in this section and the structure with the Ni/Ge/Au electrodes is discussed in Sec. 4.5.

The four different switch geometries included on our mask set are shown in schematic top view in Fig. 4.6. The structures shown in Figs. 4.6(a) and (b) are coplanar striplines, while those depicted in Figs. 4.6(c) and (d) are coplanar waveguides. The coplanar striplines are 1.2 cm long and have a characteristic impedance Z_o of 50 Ω. The metal electrodes are 100 μm wide and are separated by a distance of 10 μm. One of the electrodes of the structure of Fig. 4.6(b) has a 10–μm gap located at the midpoint. The outer electrodes of the coplanar waveguides of Figs. 4.6(c) and (d) are the same as for the striplines. The center conductor is 15 μm wide and is separated from the outer electrodes by 10–μm spacings. Bonding pads are located at both ends of the center conductor. The coplanar waveguides also have a characteristic impedance of 50 Ω. The waveguide of Fig. 4.6(d) has a 10–μm gap located at the midpoint of the center conductor.

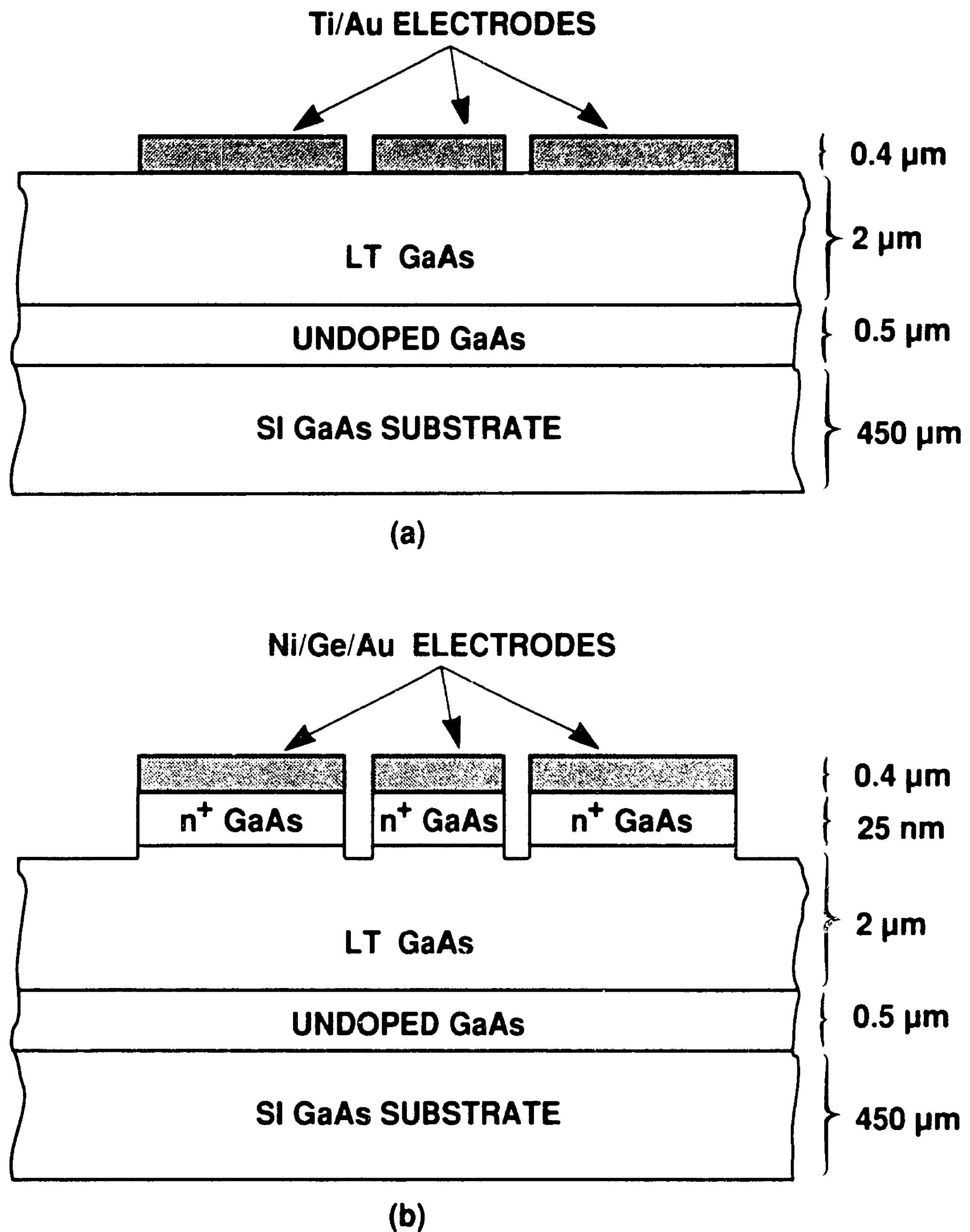

Fig. 4.5 Schematic cross section of the LT GaAs epilayers used for photoconductive-gap and sliding-contact switches: (a) metal electrode directly on the LT GaAs, and (b) n-type ohmic metal on n^+ GaAs on LT GaAs to facilitate ohmic contact formation.

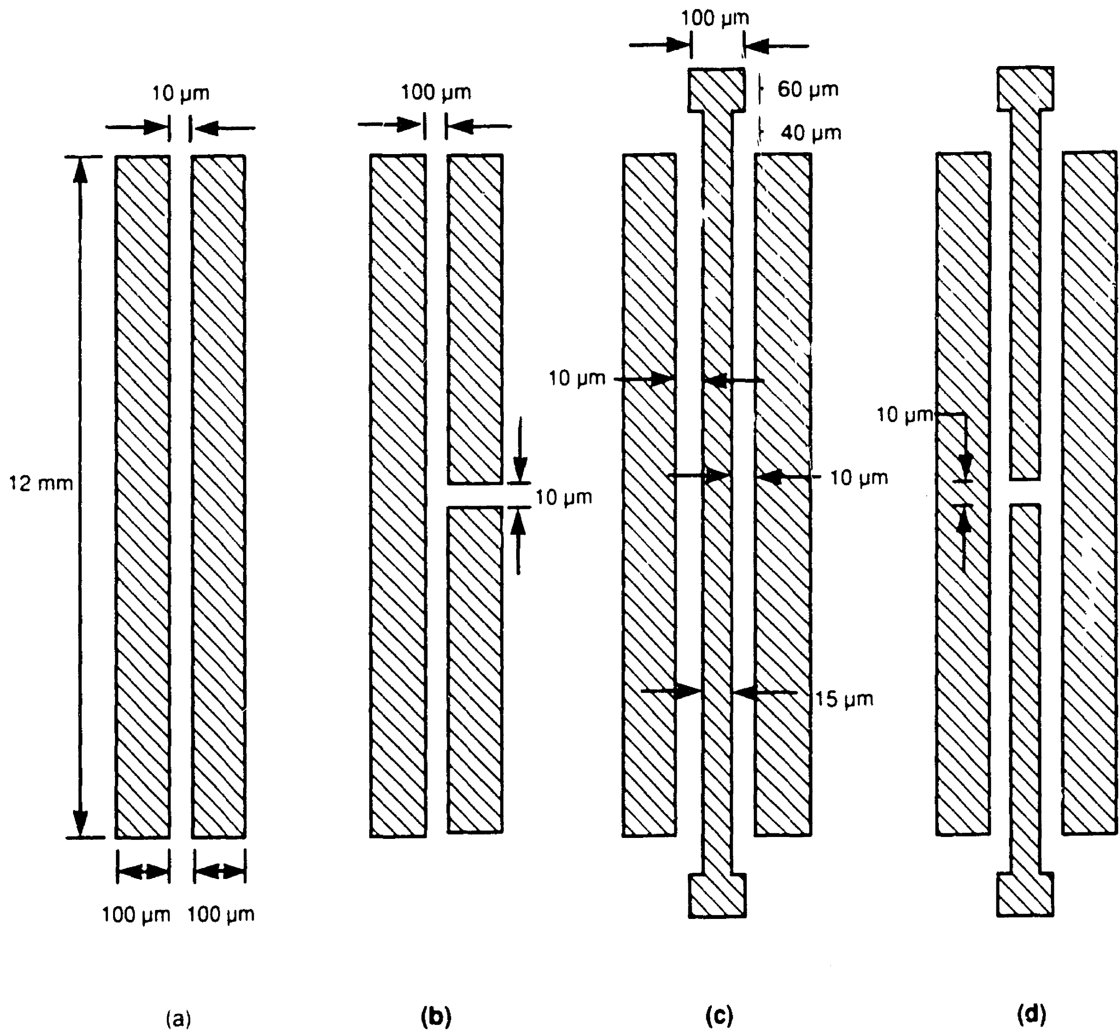

Fig. 4.6 Structures included on the photoconductive-switch mask set. The transmission line, gap, and bonding pad dimensions are indicated on each structure. All transmission lines have a characteristic impedance of 50 Ω. (a) Sliding-contact switch fabricated on a coplanar stripline. (b) Photoconductive-gap switch fabricated on a coplanar stripline. (c) Sliding-contact switch fabricated on a coplanar waveguide. (d) Photoconductive-gap switch fabricated on a coplanar waveguide.

The structures shown in Figs. 4.6(a) and (c) were used as sliding-contact switches, while the structures shown in Figs. 4.6(b) and (d) were used as photoconductive-gap switches. By fabricating both types of switches on the same mask, we were able to measure directly the effect of the gap capacitance on electrical pulse width. The transmission lines are long to facilitate pulse propagation studies. The dispersion of an electrical pulse on a coplanar waveguide can be directly compared with the dispersion of an identical pulse on a coplanar stripline. The gap capacitance C_g for the structures of Figs. 4.6(b) and (d) was ~3 pF. The temporal broadening associated with the gap can be estimated as Z_oC_g, which is ~0.15 ps for these structures. Since the resolution of the electro-optic measurement technique is of the order of 300 fs [64], the temporal broadening introduced by the gap capacitance of the structures shown in Figs. 4.6(b) and (d) is near the limit of what can be detected experimentally (see below and Table 4.1).

The technique of electro-optic sampling was used to measure the LT GaAs switches of Fig. 4.6. The experimental configuration of electro-optic sampling is shown schematically in Fig. 4.7 [64], and the position of the $LiTaO_3$ probe on the coplanar waveguide structure of Fig. 4.6(d) is shown in schematic top view and cross section in Figs. 4.8(a) and (b), respectively. A colliding-pulse mode-locked (CPM) laser was used to generate 120-fs laser pulses at a 100-MHz repetition rate with a wavelength of 620 nm and an average power of ~9 mW (90 pJ/pulse). For the measurements reported in this section, a square wave of frequency 3 MHz and amplitude of 10 V was used to bias the structure. The performance of the switch as a function of bias and as a function of laser pulse energy are presented in Secs. 4.6 and 4.7, respectively.

The laser pulse from the CPM laser is split into two beams as shown in Fig. 4.7. The first beam is focused onto the gap of the photoconductive switch

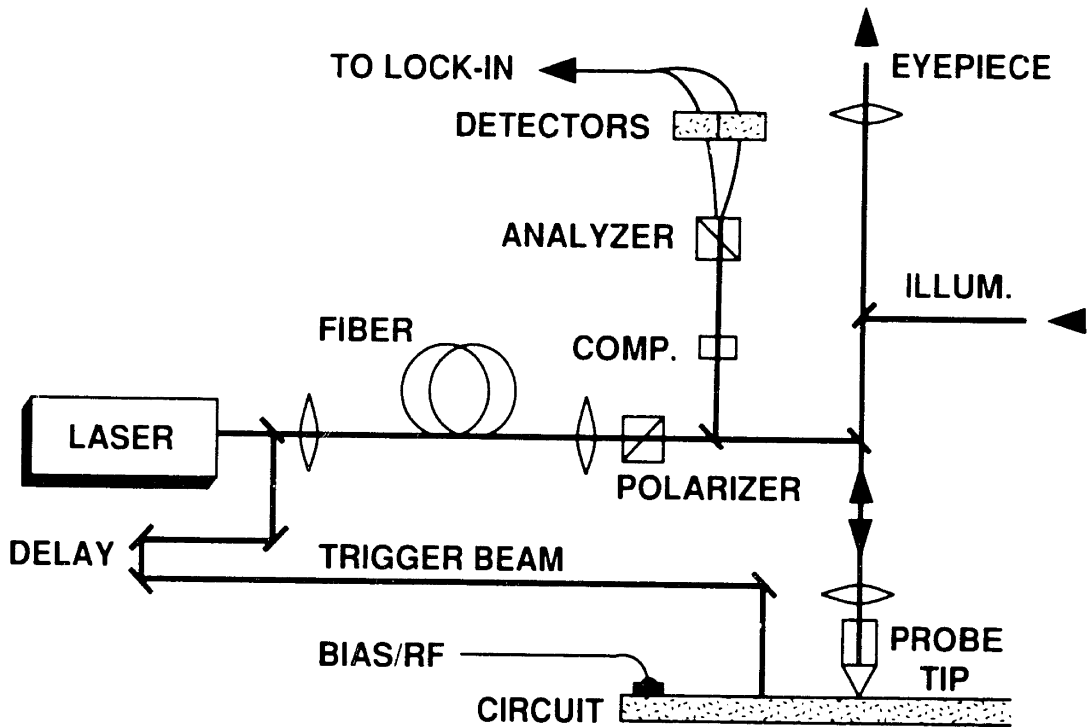

Fig. 4.7 Experimental configuration of the electro-optic sampling measurement using the finger probe technique. After Valdmanis [64].

shown in Fig 4.8(a) and excites a subpicosecond electrical impulse. This electrical impulse then propagates down the transmission line and is detected using a finger-probe of $LiTaO_3$ [63],[64]. The electric pulse induces a birefringence in the $LiTaO_3$ crystal, which in turn causes a change in the polarization of the second, time-delayed 120-fs laser pulse as it propagates through the finger probe. The path of the second laser pulse in the $LiTaO_3$ probe and the electric field lines of the pulse are shown schematically in Fig. 4.8(b). The change in polarization of the second laser pulse is measured using the analyzer depicted in Fig. 4.7.

Although in principle the absolute magnitude of the electric pulse can be calculated by knowing the induced change in polarization of the second laser beam, in practice we calibrated the tip by measuring the birefringence produced by various values of bias on the transmission line. The tip position relative to the transmission line and the surface of the LT GaAs epilayer was the same for both the calibration procedure and the picosecond pulse measurement. This calibration procedure was repeated for each tip position on the transmission line.

We chose to sample the electric pulse on the metal transmission line, as shown in Fig. 4.8, rather than on the semiconductor surface as was done in Refs. [63] and [64] in order to improve the temporal resolution of the electro-optic sampling system. When the $LiTaO_3$ probe is placed on the LT GaAs, the laser pulse is reflected by total internal reflection [64]. However, when the probe is placed on the metal electrode the laser beam is reflected by the metal, as shown in Fig. 4.8(b). The total optical path length traversed by the laser beam in the $LiTaO_3$ is less for reflection from the metal than for total internal reflection. We have found empirically that electrical pulses that are measured to be less than 500 fs with the probe positioned on the metal broaden to approximately 900 fs when measured with the probe on the LT GaAs. All the results reported in the remainder of this chapter were measured with

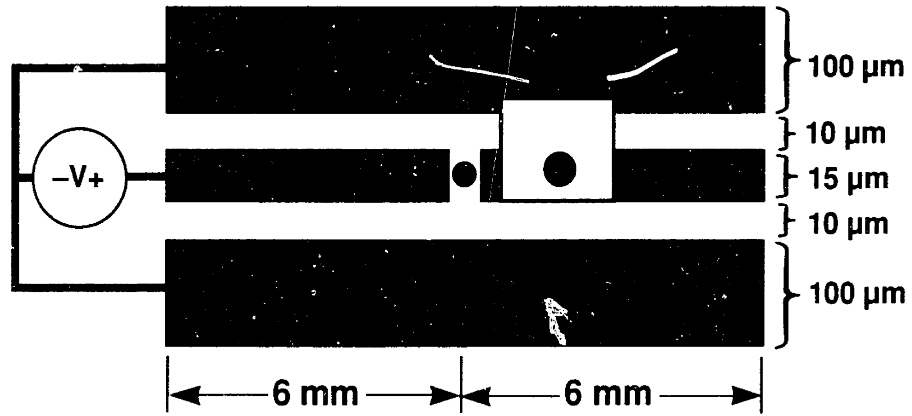

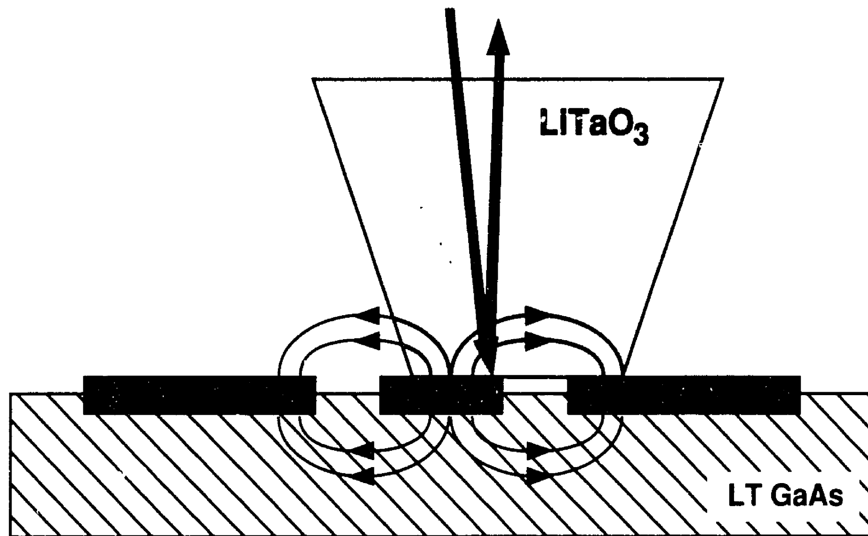

Fig. 4.8 (a) Schematic top view of the photoconductive-gap switch of Fig. 4.6(d) showing bias configuration, excitation point (smaller solid circle), and measurement point (larger solid circle). The light square represents the $LiTaO_3$ finger probe. (b) Configuration of the $LiTaO_3$ finger probe and laser beam path relative to the coplanar waveguide.

the $LiTaO_3$ probe on the metal electrode, as shown in Fig. 4.8(b).

The results of the electro-optic sampling measurement on a 200°C-grown LT GaAs switch of the form shown in Fig 4.6(d) are shown in Fig. 4.9. The trace shown in Fig. 4.9(a) was measured at a distance of 80 μm from the gap and the trace shown in Fig. 4.9(b) was measured 150 μm from the gap. The pulse width of 460 fs (FWHM) measured 80 μm from the gap broadened to 600 fs at a distance of 150 μm from the gap because of pulse dispersion. The pulse is virtually symmetric, with only a small tail on the falling edge. The measured pulse width of 460 fs is the fastest electronic switching speed ever reported for a photoconductive switch. Furthermore, the voltage of the pulse is again of the order of 0.5 V. Using the Auston formula [57], we calculated the mobility of the photoexcited carriers in these samples to be approximately 100 cm^2/V-s. We attribute the high speed of the LT GaAs switch to the large deep-level concentration in the crystal (see Chapter 5), and the relatively high mobility of LT GaAs to its high degree of crystalline perfection.

The 1/e fall time of the pulse gives an estimate of the lifetime of the photoexcited carriers. The measured 1/e fall time of 280 fs is the shortest ever obtained for a semiconductor-based photoconductive switch. The actual photoexcited carrier lifetime in LT GaAs is less than the 280 fs fall time because a number of factors associated with the electro-optic sampling measurement broaden the measured temporal response. Some of these factors, and estimates of the temporal broadening, are shown in Table 4.1. These sources of pulse broadening are discussed in detail in references [63] and [71]. As can be seen, the intrinsic $LiTaO_3$ response and the transit time of the laser pulse across the electric field of the propagating electrical pulse limit the temporal resolution of the measurement. The actual photoexcited carrier lifetime is the deconvolution of the measured response and the broadening due to the factors listed in Table 4.1. The LT GaAs switch is the first electronic device to

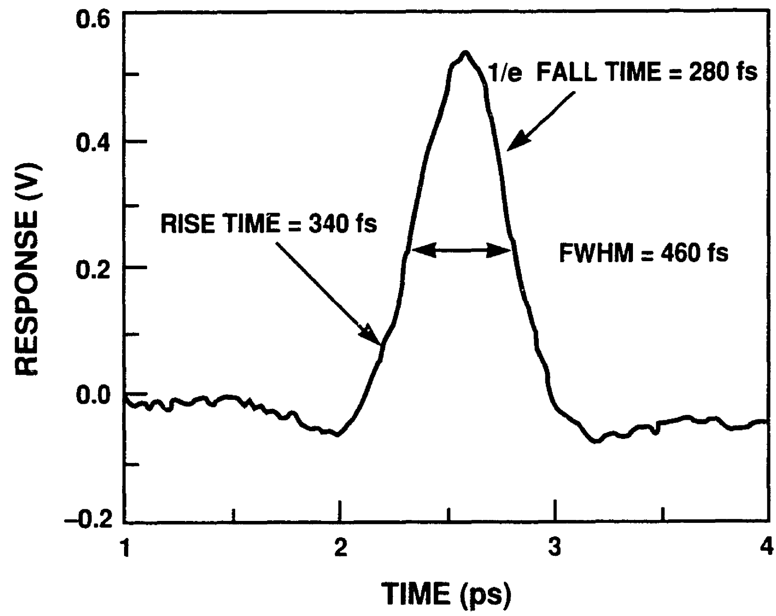

(a)

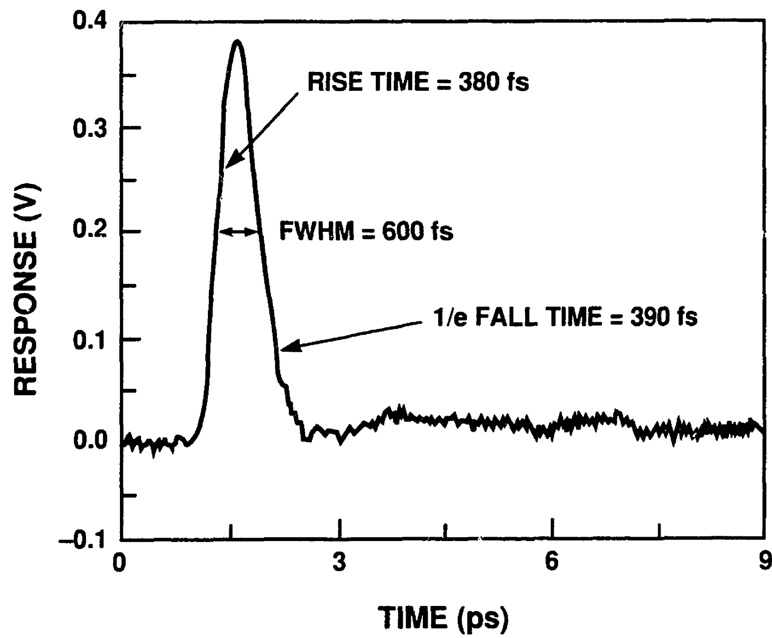

(b)

Fig. 4.9 Results of electro-optic sampling on the LT GaAs photoconductive-gap switch of Fig. 4.6(d): (a) 80 μm from the gap, and (b) 150 μm from the gap.

LASER PULSEWIDTH	120 fs
SWITCH GAP CAPACITANCE	150 fs
OPTICAL TRANSIT TIME ACROSS ELECTRIC FIELD OF PULSE	150 fs
INTRINSIC ELECTRO-OPTIC MATERIAL RESPONSE	250 fs
ELECTRICAL TRANSIT TIME ACROSS THE 4 μm PROBE BEAM	40 fs
DISPERSION OF PULSE IN $LiTaO_3$ TIP	$<$ 50 fs
CAPACITIVE LOADING OF LINE BY $LiTaO_3$ TIP	$<$ 50 fs
ELECTRICAL PULSE DISPERSION	$<$ 80 fs
CARRIER LIFETIME	$<$ 280 fs

Table 4.1 Factors affecting photoconductive switch fall-time measurements.

demonstrate speeds comparable to the theoretical limit of the electro-optic sampling system.

Recently, we have also demonstrated that LT GaAs can be used to generate high-voltage pulses [72]. For a bias of 400 V across the transmission line of Fig. 4.6(c), we observed an electrical pulse of ~16 V in response to the laser pulse [72]. The temporal response of the switch at this bias was still ~500 fs. To the best of our knowledge, this is the largest voltage ever switched at these speeds.

We have chosen to report the results for the coplanar-waveguide photoconductive-gap switch of Fig. 4.6(d) rather than report the results obtained using the sliding-contact switch configuration of Fig. 4.6(c) for two reasons. First, we have found that the temporal and voltage response of both switches are indistinguishable. As noted above, the temporal broadening associated with the gap is only of the order of 150 fs, which is less than the resolution of the test system. Second, we have found that a sliding-contact excitation can introduce spurious transients in the signal measured by electro-optic sampling. As can be seen in Fig. 4.9(a), just prior to and after the electrical impulse, the response dips to slightly negative values. The small negative excursion observed for the gap switch of Fig. 4.6(d) becomes larger for the case of a sliding-contact excitation. We attribute this negative excursion to radiation from the propagating electrical pulse [72].

Since the sliding-contact excitation [see Figs. 4.1(a) and 4.6(c)] shorts the transmission line, the axis of the induced dipole is 90° relative to that of the dipole induced for the case of the gap excitation [see Figs. 4.1(b) and 4.6(d)]. In the case of the sliding-contact excitation the axis of the induced dipole is perpendicular to the transmission line, whereas for a gap excitation the axis of the dipole is oriented along the transmission line. For a Hetzian dipole, the peak in the radiation power pattern is perpendicular to the axis of the dipole. Thus, the dipole created by the sliding-

contact excitation radiates primarily along the transmission line, while the dipole induced by the gap excitation radiates perpendicular to the transmission line. Since the $LiTaO_3$ probe is located down the transmission line from the point of excitation [see Fig. 4.8(a)], the radiative coupling from the excitation point to the finger probe is more pronounced for the sliding-contact excitation than for gap excitation. As this radiated signal passes through the $LiTaO_3$ probe, a birefringence is induced, which we detect as discussed above. This radiative coupling is undesirable because in this experiment we want to measure the pulse propagating along the transmission line and not the radiated signal. To minimize this radiative coupling, we have used gap excitation for the data presented here. However, as was discussed in conjunction with Fig. 4.1(c), the radiating Hertzian dipole can also be used to assess the speed of the photoconductive switch.

4.4 Influence of Growth Conditions

We have investigated the photoconductive switch response of LT GaAs grown at different temperatures and annealed at 600°C for different times. The results presented here represent only our initial experiments to study the influence of growth and annealing conditions on switch performance. The photoconductive-gap switch of Fig. 4.6(d) was fabricated using Ti/Au electrodes on the following LT GaAs epilayers: (1) an unannealed, 2-µm-thick layer grown at 200°C; (2) a 1.3-µm-thick layer grown at 160°C, and 2-µm-thick layers grown at 200°C and 240°C, all three annealed at 600°C for 10 min; (3) three 2-µm-thick layers grown at 200°C and annealed at 600°C for 1, 10, and 30 min; and (4) a 1-µm-thick layer grown at 200°C and annealed for 10 min at 600°C. For brevity, only the most significant results are presented here. The detailed data for these layers will be reported elsewhere [72].

The temperature used for LT GaAs growth, the annealing time at 600°C, and the thickness of the LT GaAs layer had little effect on the measured switch performance. The measured FWHM varied between approximately 400 and 600 fs and the voltage response was of the order of 0.5 V for a 10 V bias for all the annealed LT GaAs samples investigated. Furthermore, the results for switches fabricated on the same sample were virtually identical, indicating the annealed LT GaAs is uniform and quantitatively reproducible.

However, the sample of unannealed LT GaAs showed markedly different behavior. The as-grown LT GaAs was too conductive to measure any observable signal in response to the laser powers discussed above. Clearly, annealing is required to achieve high sensitivity. As will be shown in Chapter 5, annealing profoundly changes the properties of LT GaAs.

4.5 Electrode Dependence

We have also investigated the importance of electrode metallurgy on LT GaAs switch performance [72]. The results are summarized here.

Switches of the form shown in Fig. 4.6 with In, Ti/Au, alloyed Ni/Ge/Au (n–type ohmic metal), and alloyed Zn/Pd/Au (p-type ohmic metal) were fabricated on annealed 2-μm-thick layers of 200°C LT GaAs. All of the samples showed comparable voltage and temporal response, indicating electrode metallurgy does not influence the LT GaAs-based switch performance. Either the metal-to-LT GaAs contact does not contribute to the device operation, or all of the various metals form comparable contacts to LT GaAs. Since it has been shown that the electrode metallurgy can dramatically affect the performance of other semiconductor-based photoconductive switches [73], we speculate that the metal-to-LT GaAs contact is independent of electrode metallurgy. This result is consistent with our Hall-effect

measurements of LT GaAs (see Sec. 5.5.2.1) and with work done at the University of Rochester on photoconductive switches based on amorphous semiconductors and radiation-damaged semiconductors. Irrespective of the metal deposited on the amorphous or radiation-damaged semiconductor, an ohmic contact was observed to result. In our experience, it appears that semiconductors with a high density of deep levels form ohmic contacts, irrespective of the electrode metallurgy.

Before the above experiment was conducted, we were concerned about forming a rectifying metal/LT-GaAs contact that could impair switch performance. In an attempt to facilitate formation of an ohmic contact, the structure of Fig. 4.5(b) was also grown. Switches were fabricated on this sample using the mask shown in Fig. 4.6. The n^+-GaAs regions between the alloyed Ni/Ge/Au contacts were removed by wet chemical etching. The sample was overetched to fully remove the conducting n^+ GaAs. The temporal response of the photoconducitve-gap switch [Fig. 4.6(d)] was of the order of 500 fs and the signal strength was ~0.5 V. This result is encouraging for the fully planar, monolithic integration of an LT GaAs photoconductive switch with high-speed electronic devices or circuits.

4.6 Excitation Dependence

The response of a LT GaAs photoconductive-gap switch was investigated as a function of transmission line bias and laser pulse power [15],[72]. Figure 4.10 is a plot of the measured response for different values of bias across the transmission line. The FWHM is independent of bias, while the voltage response is linear with bias (see Sec. 4.2). This result is further evidence that Ti/Au on LT GaAs forms an ohmic contact. Results of increasing the laser pulse energy at constant bias are comparable to those shown in Fig. 4.10: the voltage response increases linearly with pulse energy (over the range of 2 - 8 pJ/pulse), while the temporal response is con-

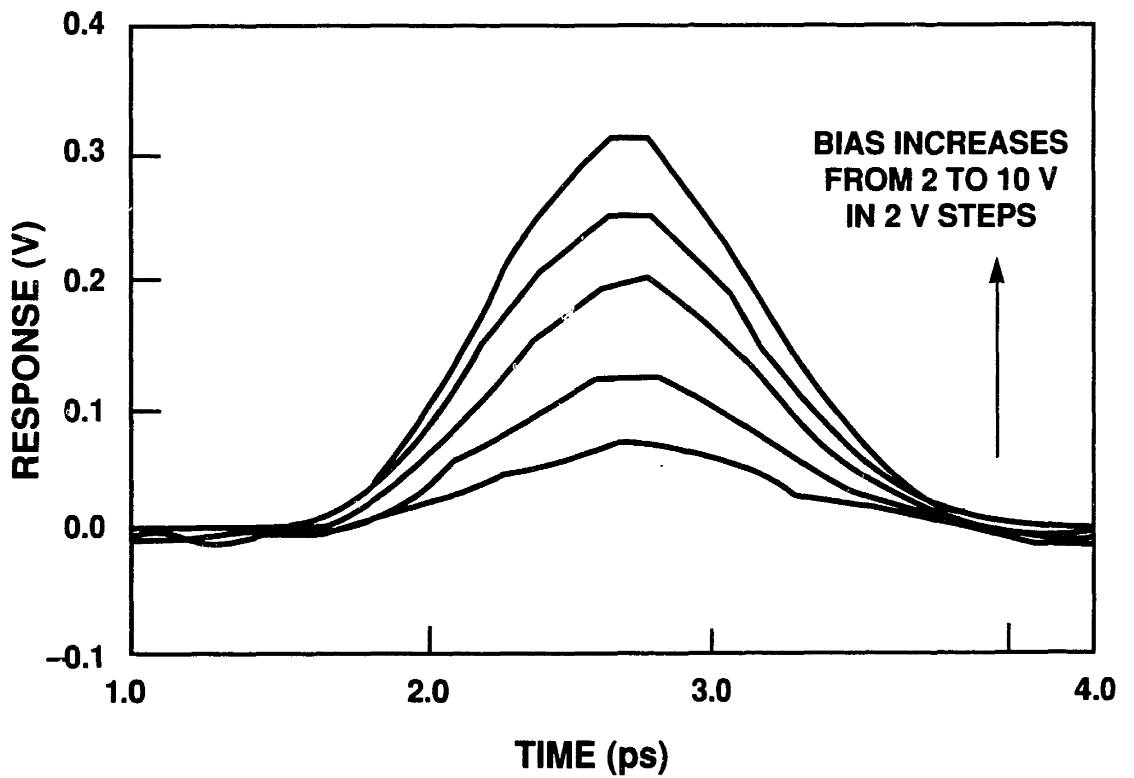

Fig. 4.10 Response of a LT GaAs photoconductive-gap switch for different values of bias across the transmission line.

stant. These results demonstrate that fast pulses (FWHM = 0.5 ps) can be generated with variable peak height. Pulses of variable peak height will be useful for characterizing both the large-signal and small-signal behavior of high-speed electronic devices.

CHAPTER 5. LT GaAs CHARACTERIZATION

The goal of the work presented in this chapter is twofold. The first is simply to document the properties of LT GaAs, particularly those properties that govern the device applications presented in Chapters 3 and 4. The second, and more ambitious goal, is to understand and describe in detail the microscopic origin of the defects in LT GaAs, and to correlate the microscopic defects with the measured properties. Using a panoply of characterization techniques, we have largely satisfied the first objective, although more experiments remain (see Chapter 6). However, identifying and modeling the specific microscopic defects in LT GaAs has proved more difficult. A qualitative model of LT GaAs has emerged and will be presented. Evidence for specific defects in LT GaAs will be discussed in this chapter and possible future experiments are presented in Chapter 6. Since the characterization of LT GaAs is an ongoing topic of research, not only at Lincoln Laboratory and the laboratories with which we are collaborating, but also at numerous research laboratories throughout the world, the discussion presented here represents our best understanding at this time.

Because 2-μm-thick LT GaAs epilayers grown at 200°C and annealed for approximately 10 min at 600°C resulted in what appeared to be optimum device performance (see Chapters 3 and 4), the majority of our characterization effort has been directed to both annealed (600°C) and unannealed layers of LT GaAs grown at 200°C. All of the device results presented in Chapters 3 and 4, with the exception of Sec. 4.4, were obtained using annealed layers of LT GaAs. We have included the characterization results for the unannealed as well as annealed material because, as will be seen repeatedly throughout this chapter, annealing profoundly changes the properties of 200°C-grown LT GaAs.

We have undertaken a number of coordinated experiments to study the properties of LT GaAs as a function of different growth and annealing conditions. In one

experiment, all the growth parameters were held constant except for the substrate temperature. Epitaxial layers of LT GaAs that were 2 μm thick were grown at T_s of 190, 220, 260, 300, 350, and 450°C. In future discussions, I will refer to this set of growths as the "growth-temperature experiment." In another experiment, several 2-μm-thick samples of LT GaAs were grown at 200°C and were then cleaved into smaller pieces. Some of the smaller pieces were then annealed *in situ* in the MBE system for 10 min, under an As overpressure, at temperatures of 300, 350, 400, 450, and 600°C. I will call this set of growths the "MBE-annealing experiment." Other LT GaAs samples grown at 200°C were annealed without a capping dielectric layer in a furnace containing an Ar/N_2 ambient at temperatures of 300, 350, 400, 450, 500, 550, and 600°C, for 30 min at each temperature. I will call this set of experiments the "furnace-annealing experiment." In other experiments, LT GaAs epilayers were grown to different thicknesses between 1 and 4 μm at 200°C. Lastly, 2-μm-thick LT GaAs films grown at 200°C were annealed *in situ* at 600°C under an As overpressure for times varying between 1 and 45 min.

The layers from these growth experiments, as well as a number of other layers grown at 200°C and unannealed or annealed at 600°C *in situ,* were used in the characterization experiments discussed in this chapter. While not all layers were measured by every characterization technique, a significant amount of data on these layers has been collected. The most informative experimental results will be discussed in some detail, while other data are only tabulated or briefly summarized. Since each 2-μm-thick LT GaAs growth represents approximately 5 h of sample preparation and growth, and many of the measurements such as the temperature-dependent Hall effect, AES, and proton-induced x-ray emission (PIXE) require hours per scan, the complete matrix of experiments will require additional time to complete.

The remainder of this chapter contains results for a number of LT GaAs sam-

ples subjected to different characterization techniques. The data for each characterization technique are described separately. A qualitative model based upon the results presented here will be proposed in Sec. 5.6.

Before discussing specific characterization results for LT GaAs, a brief summary of the properties of EL2 and As_{Ga} will be given. Since we have already shown that LT GaAs is arsenic rich (see Secs. 2.3 and 5.3.1), and because we have found evidence for As_{Ga} in unannealed LT GaAs epilayers (see Sec. 5.5.1), it is worth considering evidence for similar arsenic-excess-related defects in other GaAs crystals. The discussion below will concentrate primarily on summarizing the major experimental and theoretical results of EL2 in LEC SI GaAs and of As_{Ga} in plastically deformed and electron- and neutron-irradiated bulk SI GaAs. This discussion is intended to serve as background to the detailed characterization results of LT GaAs.

During the discussion of the LT GaAs characterization results presented in Secs. 5.2 - 5.5, evidence for similar observations in other types of GaAs crystals will be cited. In this way, the LT GaAs results can be compared and contrasted with what is known about similar defects in other GaAs samples. Results for these other GaAs samples can help to identify specific defects in LT GaAs and to qualitatively explain that material's unique properties.

5.1 Background

In this section we will briefly summarize some of the relevant information on the defects EL2 and As_{Ga} in various GaAs crystals. Since these defects are the subject of active, and often conflicting, research only those results are presented that have direct bearing on the analysis of the LT GaAs results. As will be seen, EL2 and As_{Ga}–related defects strongly influence the macroscopic properties of LT GaAs.

5.1.1 EL2

The defect EL2 is one of the most important deep levels in GaAs. EL2 governs the semi-insulating behavior of LEC SI GaAs substrates, the starting material for virtually all GaAs electronic IC's. Numerous review articles contain detailed descriptions of EL2 and summarize the current understanding of this defect [74]-[80].

In LEC SI GaAs, EL2 concentrations of the order of 10^{16} cm^{-3} are achieved by starting with an As-rich melt [74]-[80]. The concentration of EL2 in the crystal has been shown to be directly proportional to the arsenic excess in the melt [81]. From this result, it was speculated that EL2 is a point defect associated with an arsenic excess in the crystal. A number of models have been advanced for the microscopic origin of EL2 including the isolated As_{Ga} defect as well as complexes of As_{Ga} with an arsenic vacancy (V_{As}), V_{Ga}, and/or As_i, such as As_{Ga}–V_{As} [82], As_{Ga}–V_{As}–V_{Ga} [83], and As_{Ga}–As_i [84], among others [76]. On the basis of numerous experimental and theoretical investigations, EL2 is now believed by the majority of researchers in the field to be the isolated As_{Ga} defect in the neutral charge state [77],[78],[80],[85].

EL2 has been investigated using a number of disparate characterization techniques such as deep-level transient spectroscopy, thermally stimulated current, photocapacitance, photoconductivity, photoluminescence, electron paramagnetic resonance (EPR), and infrared (IR) absorption [74]-[80]. On the basis of these experiments, the properties of EL2 have been enumerated. EL2 has been shown to be a double donor with deep levels at E_c - 0.75 eV and E_v + 0.52 eV, where E_c and E_v are the conduction and valence band edges at the Γ-point in the Brillouin zone [76]-[80],[86]. Further, EL2 evidences a strong IR absorption band from ~0.7 to 1.5 eV [76],[77], PL peaks at 0.63 and 0.69 eV [87], and an As_{Ga}^{+} EPR spectrum [76]-[80],[86]. Most significantly, EL2 also exhibits a metastable state for temperatures less than ~130 K

[76],[77]. The energy levels, IR absorption, and metastability of EL2 will be discussed in more detail below, since these results are essential to the analysis of LT GaAs.

As noted above, EL2 is now considered by most researchers to be the isolated As_{Ga} defect in the neutral charge state. An As atom on a Ga lattice site has five valence electrons, while only three are needed for covalent bonding. When the two extra electrons reside on the As_{Ga}, the defect state is neutral and can donate two electrons to the crystal. This state is denoted by As_{Ga}^{o}. When one electron has been removed, the charge state is designated as As_{Ga}^{+}, and this defect can donate one electron to the crystal. When both electrons have been removed, As_{Ga}^{2+} results. The fraction of As_{Ga} in each charge state in the GaAs crystal depends upon the position of the Fermi level E_f, which in turn is governed by the concentration of all donors and acceptors in the crystal. In LEC SI GaAs most of the EL2 defects are in the As_{Ga}^{o} state, and, hence, it is the ionization of As_{Ga}^{o} to As_{Ga}^{+} that governs most of the electronic and deep-level optical properties of the crystal. In p-GaAs most of the EL2 centers are ionized, and thus transitions involving the ionized states govern the deep-level optical properties of the crystal.

The energy levels of EL2 in GaAs have been studied using the technique of EPR. As will be discussed in detail in Sec. 5.5.1, EPR can detect defects with unpaired spins, and, hence, As_{Ga}^{+} can be sensed by EPR but As_{Ga}^{o} and As_{Ga}^{2+} cannot. The larger the concentration of As_{Ga}^{+}, the larger is the intensity of the EPR signal. By measuring the intensity of the EPR signal as a function of the photon energy of illumination (so called photo-EPR), one can infer the energy separation between the As_{Ga} energy levels and the band edges. This experiment was performed by Weber [86] and his results are shown in Fig. 5.1. The traces labeled as (a) and (b) are of SI GaAs and p-GaAs substrates, respectively. Two types of GaAs crystals were used in

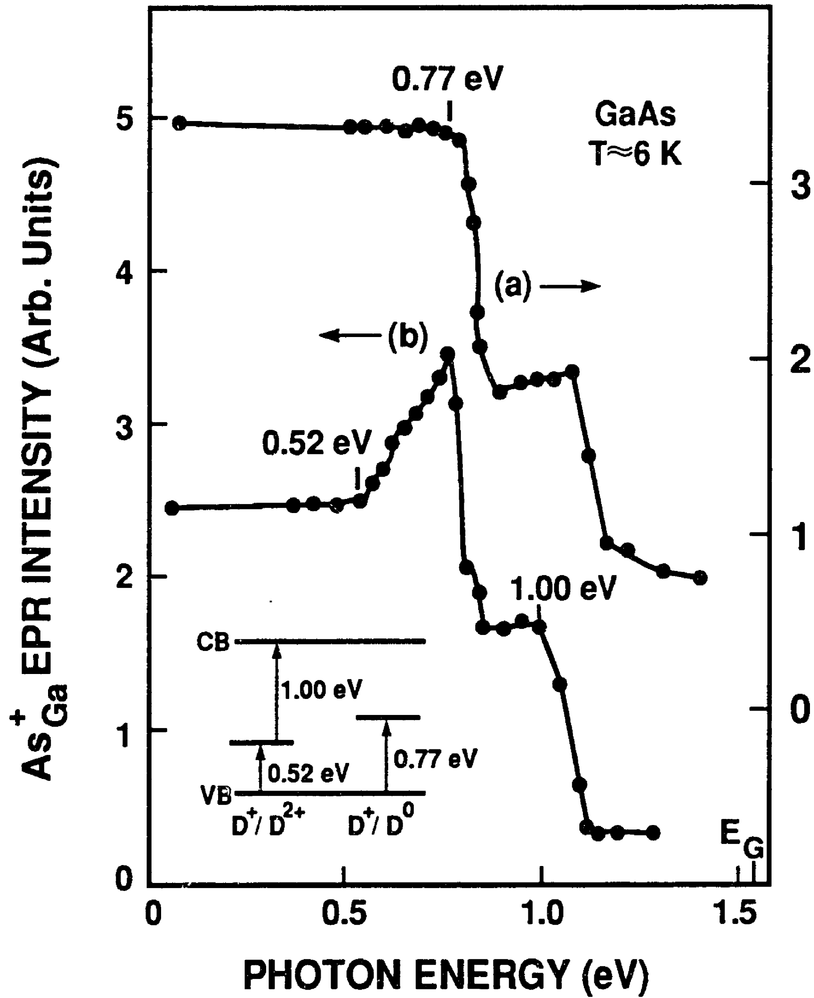

Fig. 5.1 Intensity of the As_{Ga}^{+} EPR signal in plastically deformed (a) LEC SI GaAs and (b) p-GaAs as a function of photon energy. The inset shows the energy level diagram for As_{Ga} as inferred from the photo-EPR measurement. In Weber's notation D^{o}, D^{+}, and D^{2+} correspond to As_{Ga}^{o}, As_{Ga}^{+}, and As_{Ga}^{2+}, respectively. After Weber [86].

this experiment to access the three charge states of As_{Ga}. As can be seen in Fig. 5.1, abrupt changes in the EPR intensity are observed at illumination energies of 0.52, 0.75, and 1.0 eV. Weber's analysis of these transitions in terms of the deep levels of As_{Ga} is shown in the inset to the figure. In Weber's notation, D^o, D^+, and D^{2+} represent As_{Ga}^o, As_{Ga}^+, and As_{Ga}^{2+}, respectively [86].

In p-type GaAs the EPR intensity increases for illumination at 0.52 eV because electrons are excited from the valence band into an As_{Ga}^{2+} site, thereby creating As_{Ga}^+. The EPR intensity decreases for illumination at 0.75 eV (SI GaAs) and 1.0 eV (p-GaAs) because at 0.75 eV electrons are excited from the valence band into an As_{Ga}^+ site, thereby creating As_{Ga}^o, and at 1.0 eV electrons are excited from an As_{Ga}^+ state into the conduction band, resulting in an As_{Ga}^{2+} charge state. Thus, as shown in the inset, the level at E_v + 0.52 eV can be associated with the transition between As_{Ga}^{2+} and As_{Ga}^+ and the level at E_c - 0.75 eV with the transition between As_{Ga}^+ and As_{Ga}^o.

The creation of As_{Ga}^+ states by exciting electrons from As_{Ga}^o states into the conduction band would also be expected to occur in SI GaAs at ~0.75 eV, which would lead to an increase in the EPR intensity. However, Weber's data [86] implies that there are more transitions from As_{Ga}^+ to As_{Ga}^o via the excitation of electrons from the valance band. We will return to this subject in Sec. 5.6.

To summarize, the results depicted in Fig. 5.1 demonstrate that As_{Ga} is a double donor with its first ionization energy located at E_c - 0.75 eV and its second at E_v + 0.52 eV. The ionization of As_{Ga}^o to As_{Ga}^+ gives rise to the activated conductivity of SI GaAs with an activation energy E_A of 0.75 eV, and the near-band-gap IR absorption from 0.75 to 1.5 eV.

The near-band-gap IR absorption of SI GaAs and the metastability of this absorption are fingerprints of the EL2 defect [76],[77]. Martin's measurements of the near-band-gap IR absorption coefficient of a SI GaAs substrate are shown in Fig. 5.2

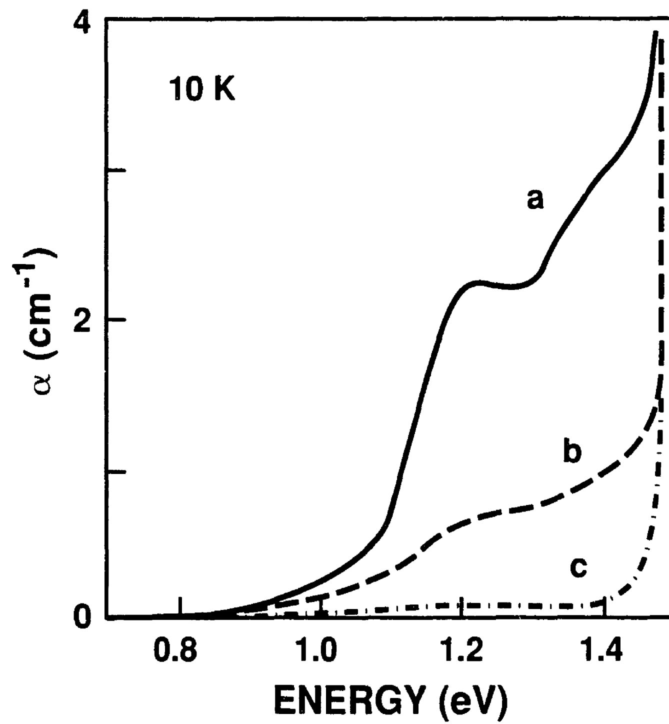

Fig. 5.2 Optical absorption spectra recorded at 10 K for an undoped LEC SI GaAs sample. Curve a was measured after cooling in the dark and curves b and c were recorded after white light illumination for 1 and 10 min, respectively. After Martin [88].

[88]. All measurements were made at 80 K. Trace a was recorded in the dark and traces b and c were recorded after intense white light illumination for 1 and 10 min, respectively.

The result recorded in the dark can be explained using Fig. 5.1 [76],[77]. The deep-level absorption arises largely from the As_{Ga}^{o} to As_{Ga}^{+} transtion. The onset of this absorption at 0.75 eV corresponds to the excitation of an electron from the As_{Ga}^{o} level at E_c - 0.75 eV to the conduction band at the Γ point. However, this transition is weak since the density of states in the conduction band at the Γ point is small. As the energy of the illumination is increased, the absorption coefficient α increases as more states in the conduction band near the Γ point become available. At an energy of ~1.0 eV the absorption coeffiecient increases rapidly as the electrons in the As_{Ga}^{o} center are excited to the conduction band at the L point. The density of states in the conduction band at the L-point is large, and, hence, the absorption from this process is large. Similarly, the absorption increases again at ~1.2 eV when the electrons in As_{Ga}^{o} ionize to the conduction band at the X point.

The distinct shoulder in the absorption at ~1.1 eV is attributed to an internal transition of the EL2 deep level [77]. This transition is represented as

$$EL2 + h\nu(1.1\ eV) \rightarrow EL2^{*} \tag{5.1}$$

where $EL2^{*}$ denotes the metastable state of EL2. The $EL2^{*}$ center is transparent to near-band-gap IR radiation. This transition of EL2 to the metastable state is clearly seen as a quenching in spectra b and c of Fig. 5.2.

This conversion phenomenon is a unique property of EL2. Conversion of EL2 can also be observed by other experimental techniques such as photocapacitance, photoconductivity, PL, and EPR [74]-[80]. The $EL2^{*}$ state is stable in SI GaAs for temperatures less than ~130 K; however, above this temperature the normal EL2 state

is recovered and the IR absorption shown as trace a in Fig. 5.2 is restored. From studies of relaxation kinetics at ~130 K, researchers have found that a barrier of ~0.3 eV exists between the metastable state and the normal EL2 state [76],[77]. The relaxation of $EL2^*$ to EL2 has been observed to occur only by thermal excitation, not by optical excitation.

The configuration of $EL2^*$ has been the subject of extensive experimental and theoretical research. Recently Dabrowski and Scheffler [89],[90] have proposed a model consistent with the known experimental properties of EL2 and $EL2^*$. According to their theory, the metastable transition from EL2 to $EL2^*$ arises when As_{Ga}^{o} absorbs a photon of energy equal to ~1.1 eV and the arsenic atom moves off the Ga lattice site into an interstitial location [89],[90]. They propose that $EL2^*$ is the V_{Ga}–As_i pair defect [89],[90]. Furthermore, they calculate that the barrier to recombination of V_{Ga} and As_i is ~0.3 eV [89],[90], in agreement with experiment. Dabrowski and Sheffler also speculate that a perturbation in the local environment of the As_{Ga} defect can preclude the metastable state [89],[90]. Experimental evidence for this is discussed next.

5.1.2 As_{Ga}–Related Defects

Electron and neutron irradiation and plastic deformation have been used to controllably introduce defects into GaAs crystals. Detailed studies of these systems have been made [91]-[95] and the results shed additional light on As_{Ga}–related defects in GaAs. The literature on damage-induced defects in GaAs is vast and no attempt is made to survey the field. Results that are relevant to the analysis of LT GaAs are briefly summarized.

As will be detailed in Sec. 5.5.1, electron [94] and neutron [95] irradiation and plastic deformation [86] of GaAs significantly increase the concentration of As_{Ga}^{+}, as

observed by EPR. The As_{Ga}^{o} concentration in these GaAs samples was also significantly increased, as indicated by the increased near-band-gap IR absorption [96],[97]. The increased As_{Ga}^{o} and As_{Ga}^{+} concentrations in these samples have been shown to increase the resistivity and quench the near-band-gap PL signal [91]-[93],[96],[97]. Although the increased near-band-gap IR absorption largely conforms to the behavior shown in Fig. 5.2, the increased absorption is not quenched by white light illumination [97]. This result suggests that although As_{Ga} is created by the damage process and evidences behavior similar to EL2, the As_{Ga} defects so introduced are not identical to EL2. It has been speculated that the local environment around the As_{Ga} defects introduced by irradiation or deformation is different from that in LEC-grown material, and as such the metastable state is forbidden [98]. Recent experimental results suggest that strain in the lattice or nearby point or extended defects may be responsible for the observed lack of metastability [99]. These experimental findings are consistent with the theoretical predictions of Dabrowski and Scheffler [89],[90]. To differentiate between the isolated As_{Ga} defect associated with EL2 and the As_{Ga} defect or defect complex introduced by irradiation or deformation, I will call any As_{Ga} defect other than the EL2 defect an As_{Ga}–related defect.

One other observation of neutron-irradiated GaAs should be noted. Although the resistivity of an initially conducting GaAs sample increases with increasing neutron dose, for neutron fluxes above a critical level the resistivity is observed to decrease [100]. The conductivity in this reduced resistivity region has been found to be due to a hopping mechanism, consistent with the large disorder in the crystal inferred from IR absorption measurements [91]. A similar result will be discussed in Sec. 5.5.2 for as-grown LT GaAs.

5.2 Compositional

The technique of AES [101]-[103], x-ray photoelectron spectroscopy (XPS) [101],[102],[104],[105], analytical electron microscopy (AEM) [101],[106],[107], and PIXE [102],[108]-[110] have all been used to assess the chemical composition of LT GaAs. In our experience, AEM and PIXE have demonstrated the best spatial and compositional resolution, respectively. AES and XPS results will be discussed first.

5.2.1 AES and XPS

Our initial AES results were presented in Sec. 2.3. The AES result of Fig. 2.10 demonstrated that LT GaAs grown at 200°C and capped with a 0.3-μm-thick epilayer of n^+ GaAs grown at 580°C contained an arsenic excess concentration of ~1 at.%. The n^+ GaAs layer was deposited on top of the LT GaAs to simulate the growth conditions used for MESFET layer deposition and to avoid charging effects during the AES measurement. Charging effects can arise because Auger electrons are emitted from the sample in response to the incident electron beam [103].

To assess the arsenic excess in as-grown LT GaAs, the structure of Fig. 5.3 was prepared. A 0.2-μm-thick layer of LT GaAs was deposited at 200°C on a 0.5-μm-thick n^+-GaAs epilayer that had been grown on an n^+-GaAs substrate. The n^+-GaAs substrate and thin epilayer were used to minimize charging effects. Following growth, the sample of Fig. 5.3 was cleaved in half, and one piece was put back into the MBE system for a 10-min, *in situ*, anneal at 600°C under an arsenic overpressure. AES spectra of the two halves of the sample are shown in Fig. 5.4. An excess arsenic concentration of ~1 at.% is observed in both the as-grown and annealed LT GaAs epilayers. As can be seen, excess arsenic incorporated into the LT GaAs epilayer at 200°C was not eliminated by the *in situ* anneal. However, the excess arsenic

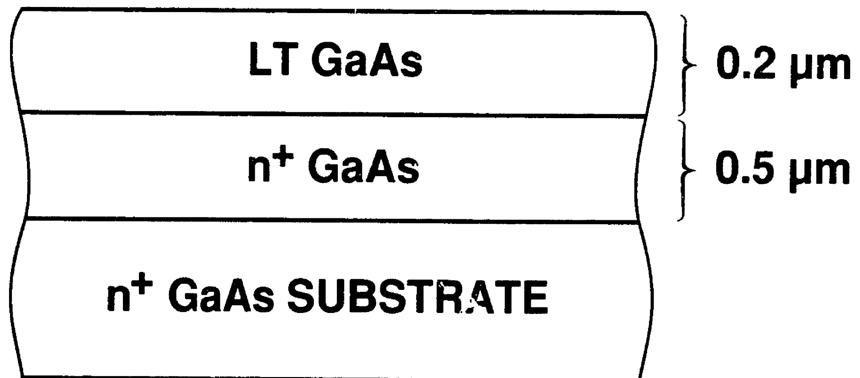

Fig. 5.3 Schematic cross section of the LT GaAs sample used in the AES study.

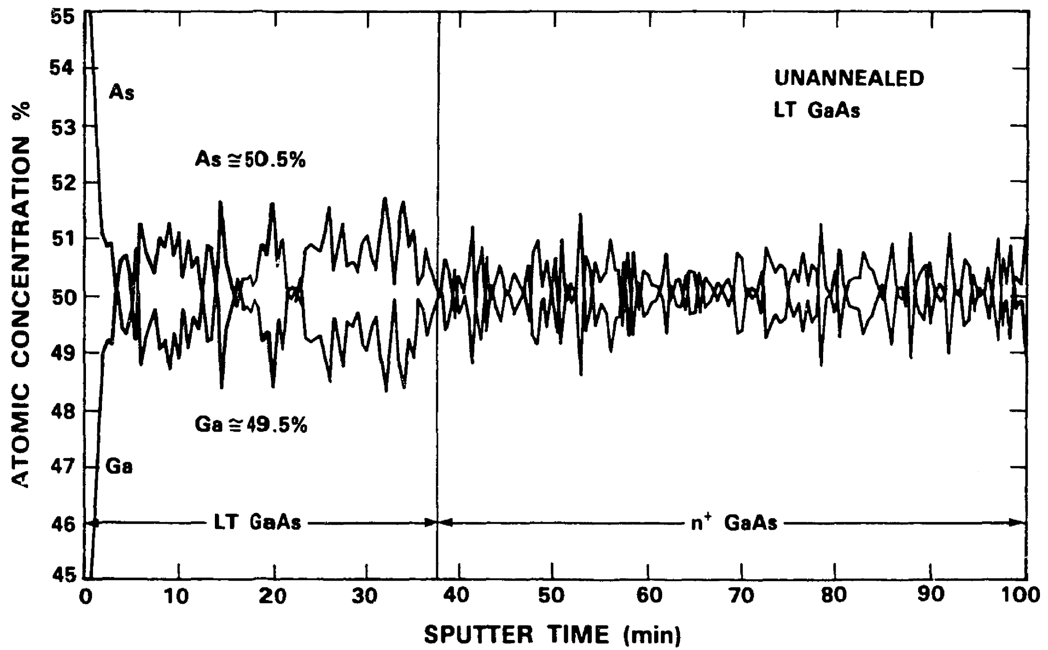

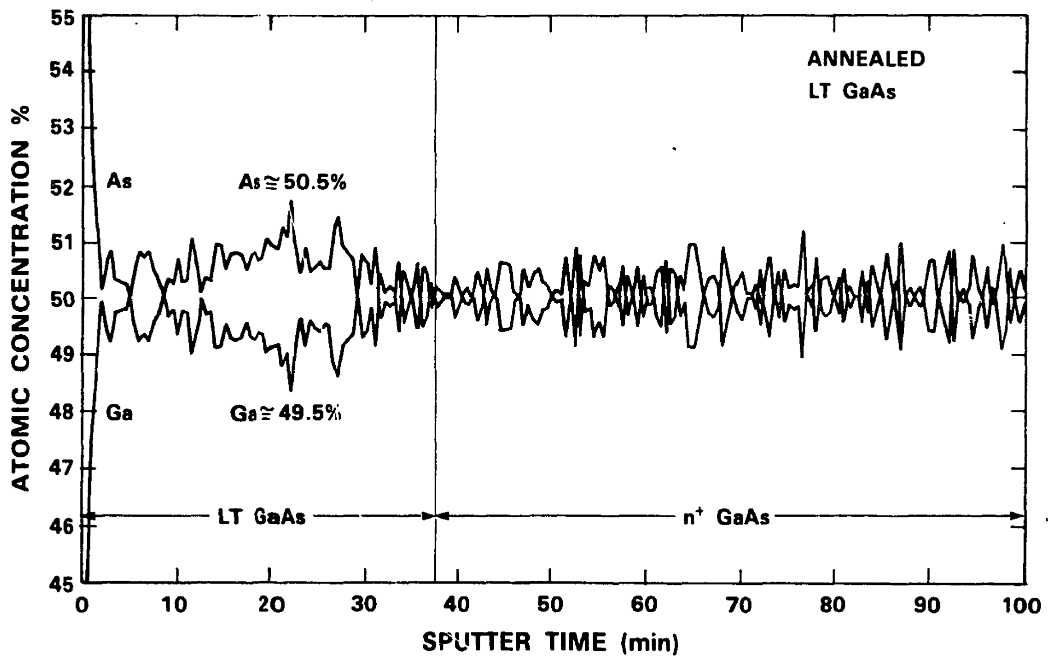

Fig. 5.4 AES results for the sample of Fig. 5.3: (a) unannealed, and (b) annealed at 600°C for 10 min. The sputtering rate was ~6 nm/min.

in LT GaAs does redistribute during the anneal (see Sec. 5.3) and some excess arsenic may leave the crystal.

The slightl[illegible]r As excess observed in the annealed sample near the surface (sputter time $<$ 10 min) and near the interface (30 min $<$ sputter time $<$ 38 min) as compared with the unannealed sample may be connected with this redistribution and may indicate a diffusion of As out of the epilayer during the anneal. However, since charging effects are more pronounced for the more highly resistive annealed material than for the more conductive unannealed material (the electrical conductivity of the annealed and unannealed material is discussed in detail in Sec. 5.5.2), we cannot definitively determine the As distribution in the LT GaAs epilayers on the basis of the AES data. The technique of AEM (see Sec. 5.2.2.1) is better suited to this study, as will be discussed below.

In addition to providing the elemental composition of the material under test, the energy and lineshape of the Auger electron peaks can often be used to provide information on the bonding environment of the constitutive elements [101]-[103]. However, no difference in peak position or lineshape was observed between LT GaAs, either as grown or *in situ* annealed, and stoichiometric GaAs.

In an attempt to learn more about the bonding environment of the excess arsenic in LT GaAs the technique of XPS was investigated. Since AES lines are broad and because Auger electrons arise from a two-electron process, shifts in AES peaks due to chemical bonding effects are both difficult to observe and to interpret [102]. In contrast, the energies of the core photoelectrons detected in XPS are sensitive to chemical bonding effects [102]. The chemical bonding environment influences the valence electron distribution around the atom, which in turn leads to core electron energy shifts [102]. It is the change in core electron binding energy with chemical bonding that makes XPS a useful technique for studying the chemistry, as well as the

composition, of a material [111]. The XPS spectra of the samples shown in Figs. 2.9 and 5.3 were measured. The observed XPS peak position and lineshape of As and Ga in LT GaAs was indistinguishable from that of stoichiometric GaAs [112]. Furthermore, the resolution of the XPS system was insufficient to measure the ~1 at.% excess As content in the material [112].

5.2.2 AEM and PIXE

The AES technique discussed above suffers from two serious limitations. First, the AES technique samples a relatively large area (the electron beam spot size is 0.2 μm in diameter for the Lincoln Laboratory system) [113] and thus cannot provide compositional information on a microscopic scale. Second, as can be seen from Figs. 2.10 and 5.4, the measured 1 at.% As excess is essentially the limit of resolution of AES [113]. For these reasons, AES cannot be used to quantitatively and reproducibly measure small changes in the excess As concentration of LT GaAs as a function of growth or annealing temperature. By using AEM, we can obtain quantitative compositional information of LT GaAs on a dimensional scale as fine as ~20 nm [114]. However, these techniques can only measure deviations from stoichiometry greater than ~0.5 at.% [114]. In contrast, the PIXE technique can be used to sample relatively large areas (~1 mm beam diameter) but with a resolution of ~0.01 at.% [115]. AEM and PIXE techniques have recently been used to characterize LT GaAs, and some of our early results are presented here. Detailed results of ongoing experiments will be reported elsewhere [116].

5.2.2.1 AEM

AEM is a term used to describe a number of characterization techniques possible using an incident high-energy electron beam and appropriate detection optics to

sense either emitted photons or electrons [101],[106],[107]. Two of the most commonly used AEM techniques for microchemical analysis are energy-dispersive x-ray spectroscopy (EDXS) and electron energy loss spectroscopy (EELS) [106],[107],[117].

In EDXS, a high-energy electron beam (~100 keV) removes core-level electrons of the constituent elements. When outer shell electrons fill the empty core levels, x–rays of characteristic energy are emitted. These x-rays are collected and analyzed in the EDXS system. From the energy of the peak, the elements in the irradiated sample can be identified, and from the relative peak intensity, the composion of the material can be calculated. EDXS has recently been applied to the study of LT GaAs [17]. The details of the EDXS technique are presented in Ref. [117]. Since this study has recently been initiated, only a limited number of the planned experiments have as yet been completed. These preliminary results are presented here.

Figure 5.5 shows the EDXS spectrum of an as-grown, 200°C LT GaAs epilayer (MBE run number 3-1593). The spectrum of the LT GaAs epilayer is superimposed on the spectrum of the SI GaAs substrate on which the epilayer was grown. The x–ray emission of the SI GaAs substrate is shown as the shaded region in the figure, while the emission for the LT GaAs epilayer is shown by the solid curve. The excess arsenic in the LT GaAs epilayer is represented by the unshaded area between the shaded substrate As peak and the LT GaAs As peak (solid line). The characteristic Ga peaks, $k_\alpha \cong 9.24$ keV and $k_\beta \cong 10.26$ keV, and the characteristic As peaks, $k_\alpha \cong$ 10.53 keV and $k_\beta \cong 11.73$ keV, are clearly visible on both spectra [102]. The absolute intensity of peaks is arbitrary, but the relative intensity of the LT GaAs and SI GaAs peaks are meaningful. The excess arsenic in the LT GaAs epilayer is calculated by comparing the total integrated intensity under the As k_α peak for LT GaAs

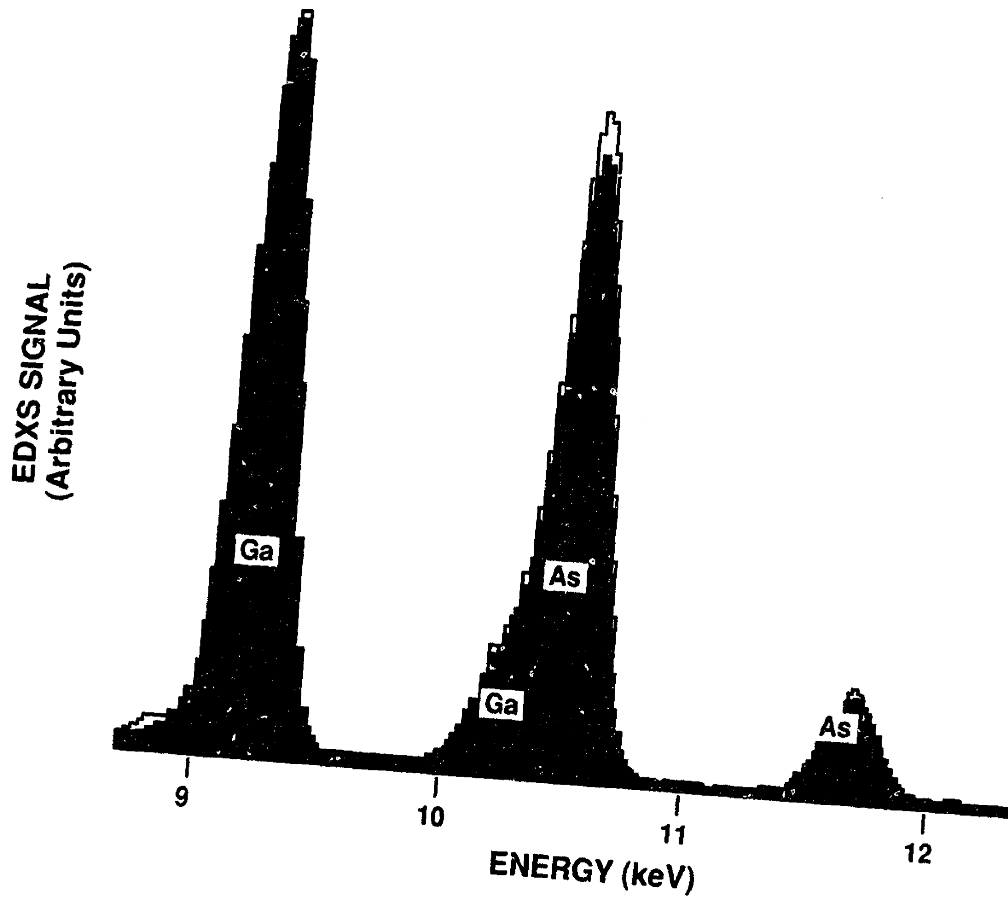

Fig. 5.5 Superimposed x-ray emissions of the GaAs substrate (shaded) and the LT GaAs epilayer (solid curve) measured using AEM. Note the increase in the As content of the LT GaAs epilayer.

with the integrated intensity of the same peak for SI GaAs. Assuming the SI GaAs substrate to be stoichiometric, we find the LT GaAs layer to contain ~1 at.% As excess. The EDXS measurements also show that the excess arsenic concentration in unannealed LT GaAs epilayers is nonuniform on a microscopic scale (tens of nanometers) and varies between ~1 and 1.5 at.% [116].

Several other observations can be noted. First, we have also investigated an LT GaAs layer grown at 200°C and annealed at 600°C (MBE run number 3-1591). The AEM analysis of this annealed LT GaAs layer is more difficult than for the as-grown material, because, unlike the latter, the annealed film does not exhibit a contrast with the SI GaAs substrate (see Sec. 5.3.1). This lack of contrast, coupled with the uncertainty introduced by the AEM sample preparation, makes it difficult to be certain exactly which part of the signal is due to LT GaAs and which is due to substrate. Nonetheless, we have observed an ~1 at.% excess arsenic concentration in annealed LT GaAs. As was the case for unannealed LT GaAs, the As distribution appears to be nonuniform, varying between ~0.5 and 1.5 at.%.

Although we have observed an excess As concentration of ~1 at.% in both as-grown and annealed crystalline LT GaAs, we have never observed As precipitates (diameters greater than approximately 1 nm) in either material. We have looked for such precipitates using both conventional TEM and high-resolution TEM (see Sec. 5.3.1).

In contrast to the single-crystal films of LT GaAs, we have observed numerous microscopic As precipitates in an annealed, polycrystalline 2-μm-thick LT GaAs epilayer grown at ~200°C on a GaAs-on-Si wafer. The LT GaAs growth was initially crystalline, but became polycrystalline for thicknesses greater than ~1.5 μm. A high-resolution TEM micrograph of one such As precipitate in this sample is shown in Fig. 5.6. This micrograph was taken in the two-beam condition for the (200)

Fig. 5.6 Lattice-image TEM of an LT GaAs epilayer on GaAs-on-Si. The LT GaAs epilayer became polycrystalline at a thickness of ~1.5 μm. The precipitate in the center of the micrograph is As, as determined by electron diffraction.

reflection. The cross-sectional sample was prepared in the [110] orientation. An As precipitate of ~16 nm in diameter is clearly visible. Recently we have also observed arsenic precipitates in annealed polycrystalline LT GaAs epilayers on SI GaAs substrates.

5.2.2.2 PIXE

The physics of the PIXE technique is virtually identical to the AEM/EDXS technique discussed in the previous section, except that the PIXE technique uses protons rather than electrons to produce the characteristic x-rays [102],[108]-[110]. PIXE spectra for LT GaAs closely resemble the data of Fig. 5.5, and, as such, will not be shown here. The excess As concentration in the crystal is calculated by comparing the integrated intensities of the Ga and As K_α peaks [102].

The use of protons rather than electrons to generate the x-rays results in advantages of PIXE. First, PIXE offers better compositional resolution because the background, or bremsstrahlung, radiation is lower for proton bombardment than for electron bombardment [102],[108]. Bremsstrahlung radiation decreases as the mass of the projectile increases [108]. Hence, as they decelerate in the sample, the ~1-MeV protons used in PIXE emit less bremsstrahlung radiation than the ~100-keV electrons used in the AEM/EDXS technique. Second, because 1-MeV protons have a penetration depth of ~3 μm in GaAs [115], PIXE samples the entire LT GaAs epitaxial layer, and, hence, provides information on the average composition of the film. The disadvantage of PIXE compared with AEM/EDXS is in spot size. The proton beam incident on the sample is ~1 mm in diameter, and consequently PIXE cannnot provide information on the microscopic variation of the As content in the film.

Given the ability of PIXE to resolve small deviations from stoichiometry (resolution ≅ 0.01 at.% [115]), we have extensively used this technique to measure the

excess arsenic content in LT GaAs as a function of growth temperature and annealing conditions [116]. Table 5.1 contains a list of the LT GaAs samples that we measured with PIXE. Sample number, growth temperature, annealing condition, epilayer thickness, and arsenic excess are all tabulated. These measurements were made using proton beams with energies between 1 and 1.5 MeV. The proton beam was directed onto the crystal at an angle of ~60° to the normal in order to reduce the depth of penetration of the protons to ~2 μm, the typical thickness of the LT GaAs epilayers. A random crystal orientation was chosen to avoid channeling effects (see Sec. 5.3.3) during the PIXE measurements. Also several sites on each sample were measured to check for reproducibility and to avoid radiation-induced changes in crystal structure. The PIXE measurements were observed to be quantitatively reproducible, both across a single sample and from sample to sample for epilayers grown at the same T_s.

The PIXE results for sample 3-1724 confirm and improve upon the AES results shown in Fig. 5.4. LT GaAs grown at ~200°C contains an excess arsenic concentration of ~1.3 at.%. The extra decimal places demonstrate the improved quantitative analysis possible with PIXE as compared with AES. *In situ* annealing does not change the excess arsenic content in the film. Also shown in Table 5.1 are results for unannealed LT GaAs epilayers grown at 190, 207, and 270°C. The excess arsenic content in the film is seen to increase monotonically as the substrate temperature is reduced.

The PIXE results for the furnance-annealing experiment are summarized in Table 5.1 [116]. The as-grown LT GaAs sample contains an excess arsenic concentration of 0.84 at.%. As the sample is annealed in the furnace at progressively higher temperatures, the excess arsenic content in the film is observed to decrease monotonically. The same sample was used for all anneals. PIXE data for annealing at temperatures greater than 450°C are not shown because the excess arsenic content in the

MBE SAMPLE	T_s (°C)	d (μm)	ANNEALING CONDITIONS	As/Ga RATIO	Δ As (at. %)
3-1724	195	3.0	UNANNEALED	1.026	1.28
3-1724	195	3.0	IS 600°C	1.025	1.24
3-1872	195	2.5	UNANNEALED	1.026	1.28
3-1685	190	2.5	UNANNEALED	1.028	1.38
3-1652	270	3.8	UNANNEALED	1.010	0.5
3-1650	205	2.5	UNANNEALED	1.017	0.84
3-1650	205	2.5	FA 250°C	1.016	0.79
3-1650	205	2.5	FA 350°C	1.008	0.41
3-1650	205	2.5	FA 400°C	1.003	0.15
3-1650	205	2.5	FA 450°C	1.002	0.11

Table 5.1 Summary of PIXE data: T_s is the growth temperature, d is the LT GaAs epilayer thickness, IS stands for an *in situ* anneal for 10 min at the indicated temperature, and FA stands for a furnace anneal for 30 min at the indicated temperature.

film was less than the resolution of the measurement. These results clearly demonstrate that the excess arsenic in LT GaAs moves in the sample during annealing, and can leave the crystal unless the sample is properly capped. Clearly, the As overpressure during the *in situ* anneal is essential to maintain the excess arsenic content in LT GaAs.

As will be seen repeatedly in the remainder of this chapter, the excess arsenic content in the film is correlated with the observed properties of LT GaAs.

5.3 Structural

TEM [106],[118], double-crystal x-ray diffraction [119], and ion channeling [120],[121] have been used to evaluate the crystal quality of LT GaAs grown at various temperatures and annealed under different conditions. TEM and high-resolution TEM have shown that both as-grown and annealed layers of LT GaAs are of high crystalline perfection [16]. However, x-ray and ion-channeling measurements show that LT GaAs layers grown at temperatures less than ~250°C and unannealed have a dilated, disordered lattice, which we attribute to the excess As in the crystal [115],[116]. Furthermore, LT GaAs layers grown at higher temperatures (>250°C), or grown at low temperatures (<250°C) and annealed at higher temperatures (>300°C), are, from the perspective of crystal quality, indistinguishable from the SI GaAs substrate or from MBE epilayers grown at normal temperatures [116]. Detailed results for these characterization techniques are presented in this section.

5.3.1 TEM

Both as-grown and annealed films of LT GaAs were shown to be crystalline by RHEED, TEM, and TED, as discussed in Sec. 2.3. However, all of the TEM and TED results presented in that section were recorded in the [100] direction. In order

to examine the crystal quality of LT GaAs in more detail, cross-sectional TEM samples in the [110] orientation were prepared from the four samples listed in Table 5.2 [16]. The layers were grown on (100) LEC SI GaAs substrates. The LT GaAs layer thickness d, T_s, and post-growth annealing procedure are given in the table. Samples 3-1591 and 3-1593 were grown at 200°C and sample 3-1591 was then annealed *in situ* at 600°C for 10 min. Sample 3-1652 was grown at 270°C and not annealed. Sample 3-1595 was grown at 275°C and then was annealed *in situ* at 600°C for 2 min. A sample of SI LEC GaAs substrate was used as a reference.

Bright- and dark-field micrographs were taken in an electron microscope, and high-resolution micrographs were taken in an atomic resolution microscope (1 MeV) [16]. The micrographs were taken in the two-beam condition for the (200) reflection, which is the most sensitive to changes in the structure factor. All samples showed a very high crystal quality. As shown in Fig. 5.7, a distinct epilayer of thickness approximately 3 μm was observed for sample 3-1593 [16]. The contrast between the unannealed LT GaAs epilayer and the substrate may result from either a change in structure factor of the epilayer because of the large deviation from stoichiometry, or to stress built into the epilayer during the low-temperature growth. In some areas of this sample, dislocations formed at the layer/substrate interface or within the layer were found. As a result, the density of dislocations in the epilayer was slightly higher than in the substrate ($\sim 10^4$ cm^{-2}). For the annealed sample 3-1591 and the samples grown at approximately 275°C, there was almost no difference in contrast between the epilayer and the substrate (see Sec. 5.2.2.1), and the dislocation density in the layers was comparable to the dislocation density in the substrate. High-resolution images of all investigated samples did not show any additional defects. A high-resolution TEM micrograph of sample 3-1593 is shown in Fig. 5.8 [16]. As noted in Sec. 5.2.2.1, we have not observed As precipates in any of the LT GaAs

SAMPLE No.	d (μm)	T_s (°C)	ANNEALING PROCEDURE
3-1593	2.5	200	NOT ANNEALED
3-1591	2.5	200	600°C FOR 10 min
3-1652	3.8	270	NOT ANNEALED
3-1595	4.0	275	600°C FOR 2 min

Table 5.2 Thickness d, growth temperature, and annealing procedure of LT GaAs epilayers used in the cross-sectional TEM investigation.

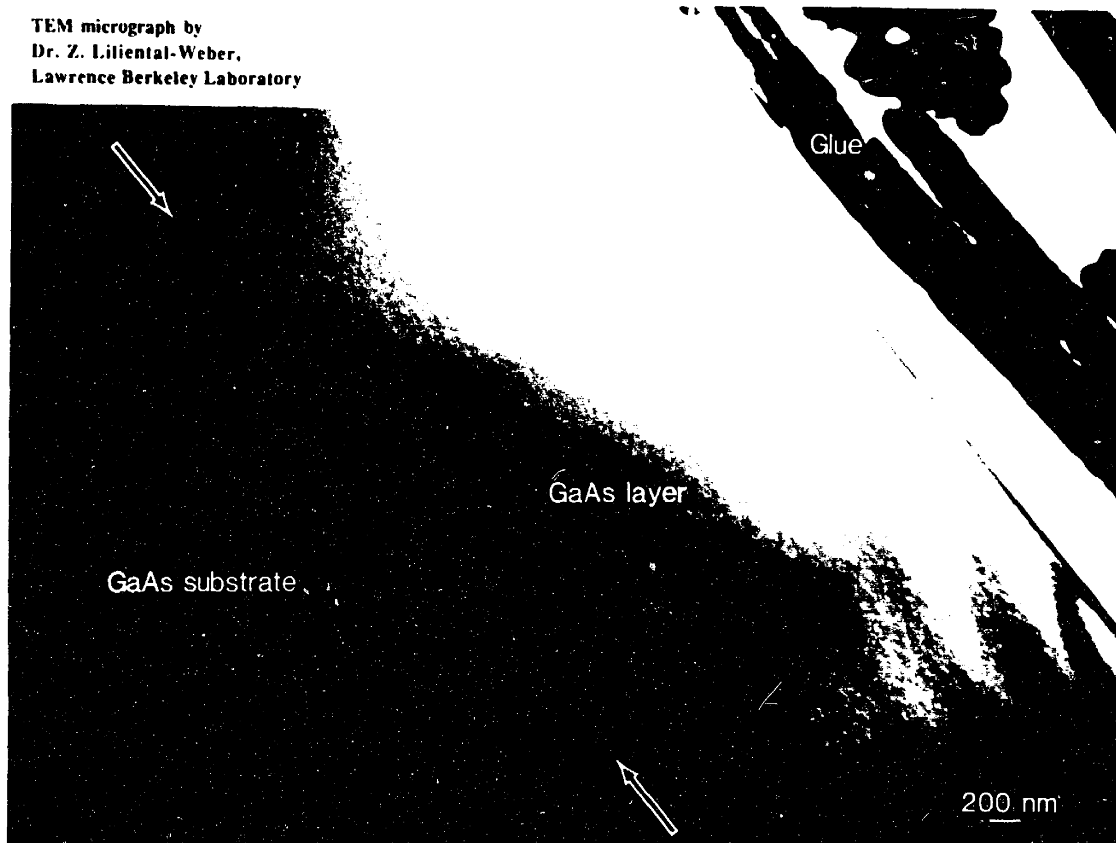

Fig. 5.7 Cross-sectional TEM micrograph of LT GaAs sample 3-1593, which was grown at 200°C and not annealed. A dislocation formed at the substrate/epilayer interface is seen.

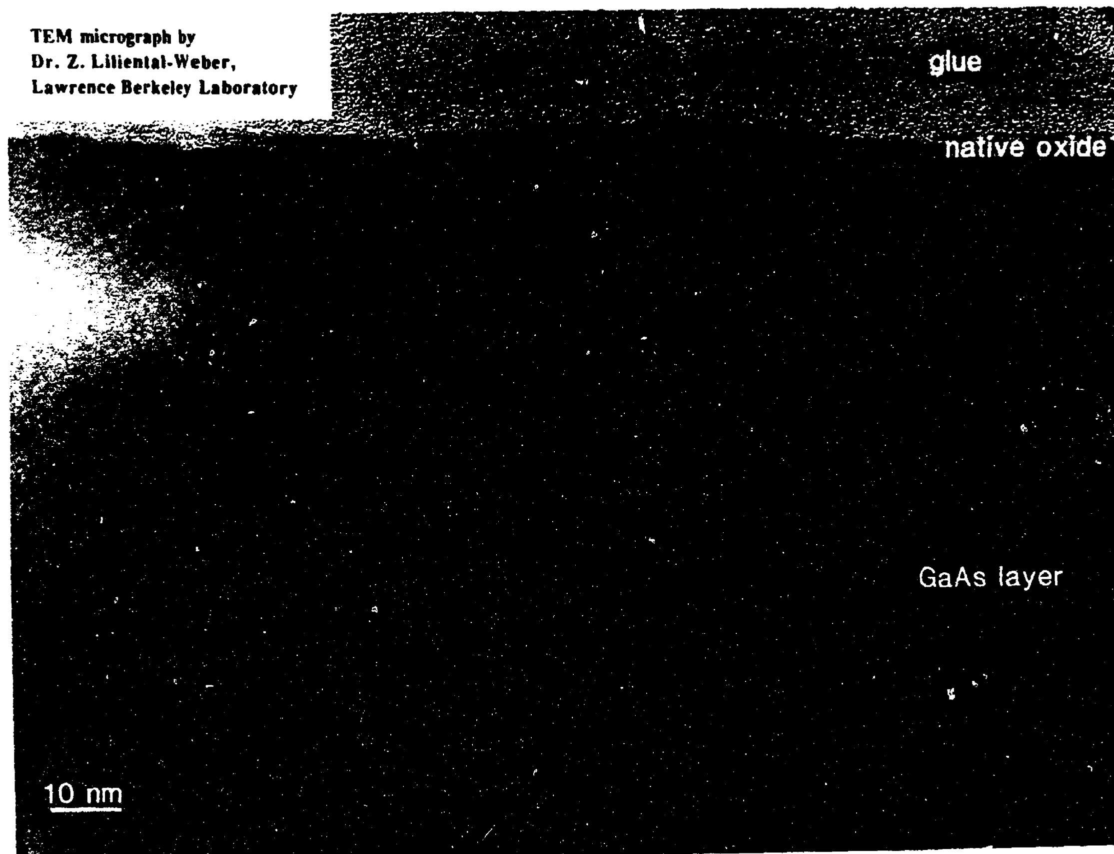

Fig. 5.8 High-resolution TEM micrograph of LT GaAs sample 3-1593 taken with an atomic resolution microscope (1 MeV) in the [110] projection showing the perfect crystalline structure of the epilayer.

layers listed in Table 5.2, or in any of the LT GaAs layers subjected to TEM in the [100] direction, or in any crystalline LT GaAs on GaAs-on-Si epilayers [16],[116].

5.3.2 X-Ray

In Sec. 2.3 double-crystal x-ray diffraction rocking curves were presented for an LT GaAs epilayer grown at 200°C and annealed *in situ* for 10 min at 600°C. Only one narrow peak was observed for this annealed epilayer. In this section, rocking curve measurements for a number of LT GaAs epilayers are presented [17],[116]. As will be seen, LT GaAs grown at the lowest temperatures (<250°C) exhibits a crystal structure markedly different from epilayers grown at higher termperatures (>250°C). Annealing of the samples grown at the lowest temperatures causes the crystal structure to revert to that of GaAs. The results of measurements of the lattice constant perpendicular to the (001) surface, $a_{\perp}$, are presented first [16],[17]. The samples of Table 5.2 are discussed initially, followed by the results of the furnance-annealing, MBE-annealing, and growth-temperature experiments. Lastly, the results of measurements of the lattice parameter parallel to the (001) surface, $a_{\parallel}$, are given for an unannealed LT GaAs epilayer grown at 200°C [17].

For rocking curve measurements, x-rays were generated by a Cu-K_{α} source and diffracted with a Ge (111) monochromator crystal [16]. The diffraction from GaAs (400) planes was recorded with the epilayer facing the beam. In this configuration, x-rays could penetrate both the epilayer and the substrate, since the epilayer thickness was about 3 μm. Two peaks due to Bragg reflection were found for sample 3-1593, whereas only one peak was found for the other samples, as shown in Fig. 5.9. The two peaks seen for sample 3-1593 are attributed to x-ray diffraction from planes of two lattices with different $a_{\perp}$ lattice parameter: the bulk GaAs substrate and the 200°C unannealed LT GaAs layer [16]. If the weaker peak is assumed to correspond

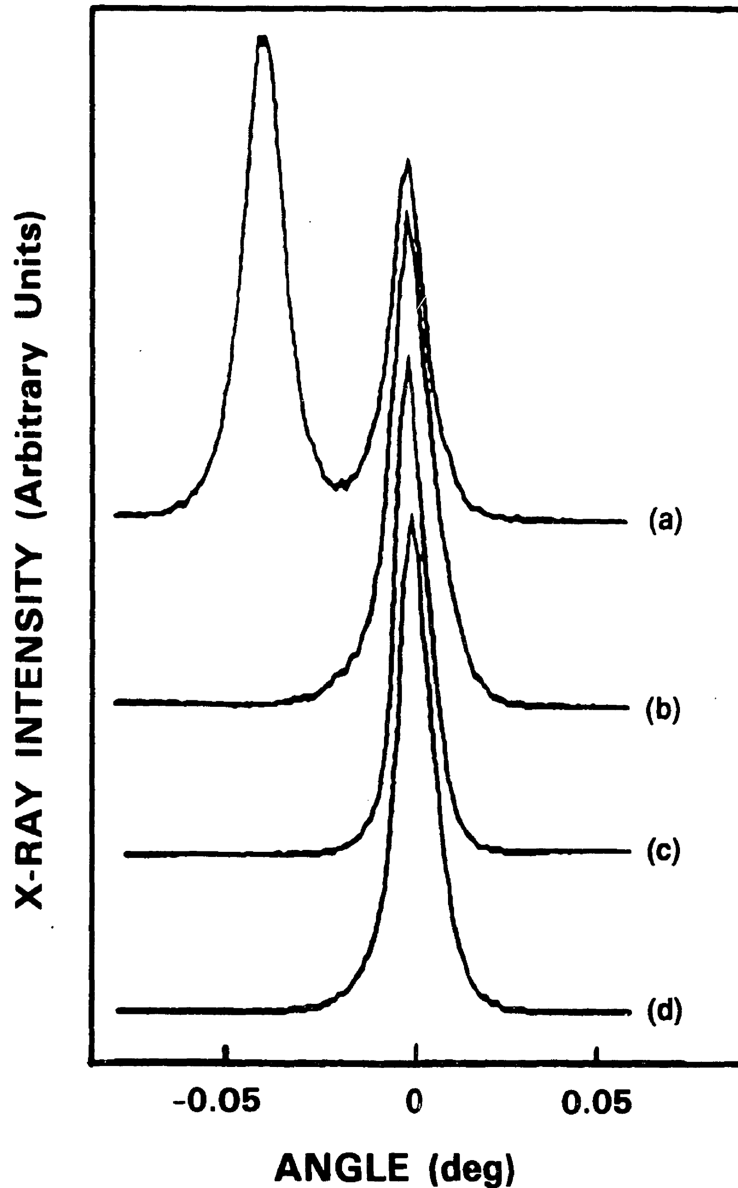

Fig. 5.9 X-ray diffraction from the (400) planes of LT GaAs on a SI GaAs substrate: (a) sample 3-1593, grown at 200°C and unannealed; (b) sample 3-1591, grown at 200°C and annealed for 10 min at 600°C; (c) sample 3-1652 grown at 270°C and unannealed; and (d) sample 3-1595, grown at 275°C and annealed for 2 min at 600°C. The absolute diffraction angles are influenced by the sample mounting and cannot be intercompared.

to the GaAs substrate, for which the lattice constant a_o = 5.653 Å [122], the perpendicular lattice constant of the LT GaAs layer is calculated to be 5.659 Å [17],[116]. This value corresponds to a relative increase in the lattice parameter of $\Delta a_\perp/a_o$ = 0.001 for the LT GaAs layer, which we ascribe to the excess arsenic in this layer (see below).

Lattice-parameter variations with crystal composition have been reported for undoped LEC GaAs crystals, and values of $\Delta a/a_o$ up to 10^{-5} for an As/Ga molar ratio of 1.0001 have been found [123]. The observed value of $\Delta a_\perp/a_o$ for LT GaAs is two orders of magnitude greater than has ever been found for LEC GaAs. If a linear extrapolation is made of the $\Delta a/a_o$ vs As/Ga molar ratio dependence presented in Fig. 2 of Ref. [123], the observed value of 0.001 gives an As/Ga molar ratio of 1.01 for the LT GaAs layer, in approximate agreement with the results of Sec. 5.1 [17].

Since only one x-ray diffraction peak has been found for the sample annealed at 600°C, as well as for those grown at 270°C, it can be concluded that the lattice parameter for these layers is, within the experimental uncertainty of ±0.001 Å (due to the x-ray apparatus linewidth), the same as for bulk GaAs [16]. This observation indicates that annealing a 200°C LT GaAs layer at 600°C results in a redistribution of the excess arsenic in the LT GaAs such that the lattice parameter is again equal to that of bulk GaAs [16].

To study the variation of the LT GaAs lattice parameter as a function of growth temperature and annealing conditions, samples from the growth-temperature, MBE-annealing, and furnance-annealing experiments were measured [116]. From the growth-temperature experiment, we have found that the LT GaAs lattice parameter is only dilated for the lowest growth temperatures (T_s<250°C), and $a_\perp$ increases monotonically as T_s is reduced. This result is consistent with the PIXE results of Sec. 5.2.2.2 and indicates that excess arsenic is responsible for the increase in lattice con-

stant.

From the data of the two annealing experiments, we have found that the lattice constant of 200°C-grown LT GaAs relaxes to that of GaAs for annealing temperatures greater than or equal to ~400°C [116]. The x-ray diffraction results for the sample of the furnance-annealing experiment are shown in Fig. 5.10. This temperature, ~400°C, is also comparable to the annealing temperature observed for the disappearance of the EPR As_{Ga}^{+} signal (see Sec. 5.5.1) [116]. We speculate that at temperatures between approximately 300 and 400°C the excess As in the LT GaAs becomes mobile in the crystal and can redistribute itself to a lower energy configuration that allows the lattice constant to relax to that of GaAs. This redistribution can happen even when the As content in the film remains constant, as in the case of the MBE-annealing experiment.

In order to assess the reproducibility of the dilation of the LT GaAs lattice, $a_{\perp}$ for numerous other samples has been measured. The perpendicular lattice parameter for different samples of unannealed layers of LT GaAs grown at 200°C varies between 5.657 and 5.660 Å. Despite difficulties with the precise determination of T_s (see Sec. 5.7), these measurements indicate that the lattice constant of unannealed 200°C is quantitatively reproducible.

All the x-ray diffraction results discussed above were made using the (400) reflection, and, hence, measured only $a_{\perp}$. To calculate the in-plane lattice parameter parallel to the (001) surface, $a_{\parallel}$, reflections from the (400) and (422) lattice planes of an unannealed sample of LT GaAs grown at 200°C have been measured [17]. The rocking curves of the (400) and (422) reflections are shown in Fig. 5.11(a) and (b), respectively [17]. For both reflections, the distance between planes in the LT GaAs epilayer is larger than for the GaAs substrate (larger peak is from the epilayer). As discussed previously, $a_{\perp}$ can be calculated from the peak separation of the (400)

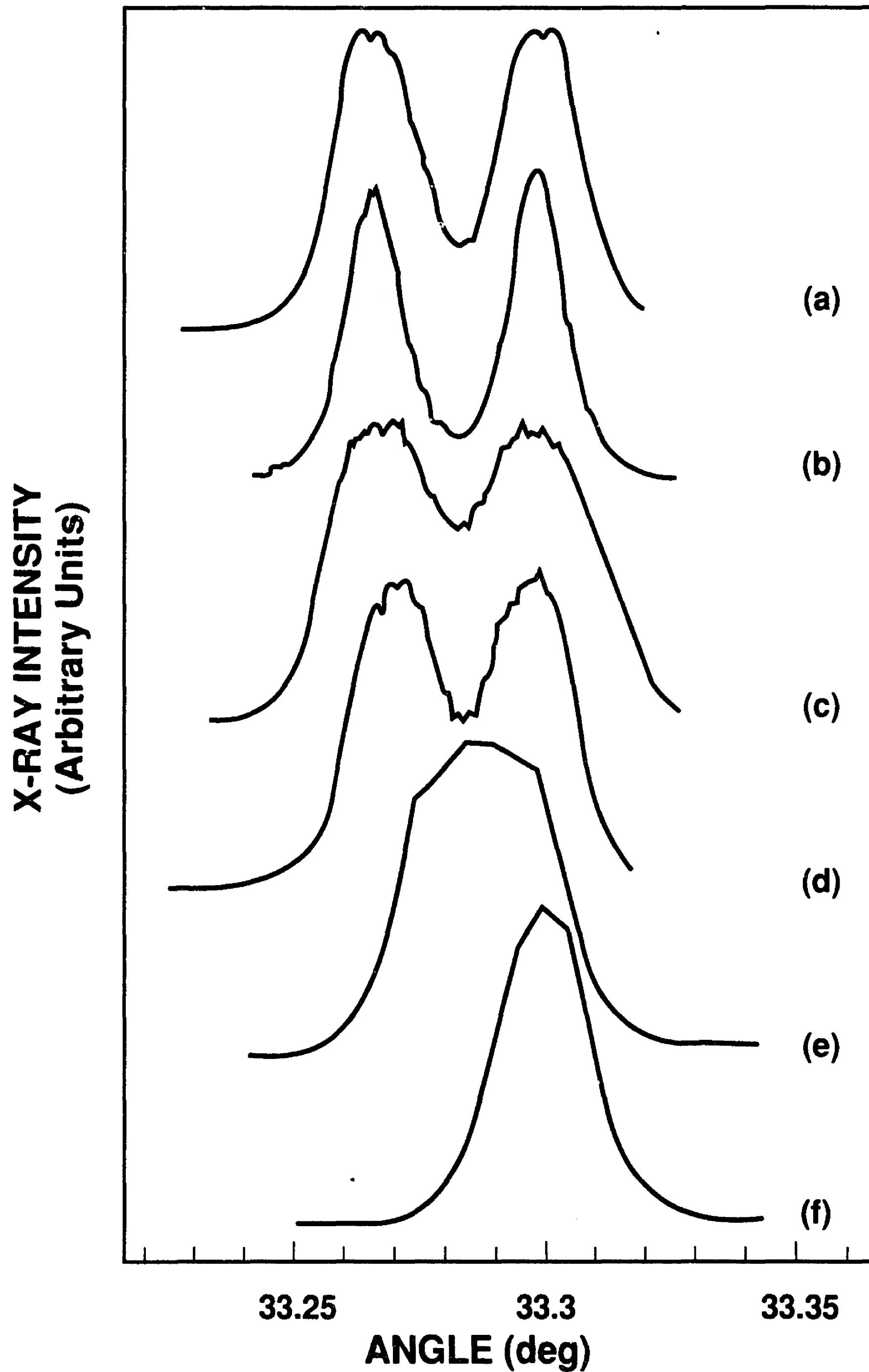

Fig. 5.10 X-ray diffraction from a 200°C LT GaAs sample as a function of furnance annealing temperature. All anneals were for 30 min at the following temperatures: (a) unannealed, (b) 250°C, (c) 300°C, (d) 350°C, (e) 400°C, and (f) 450°C.

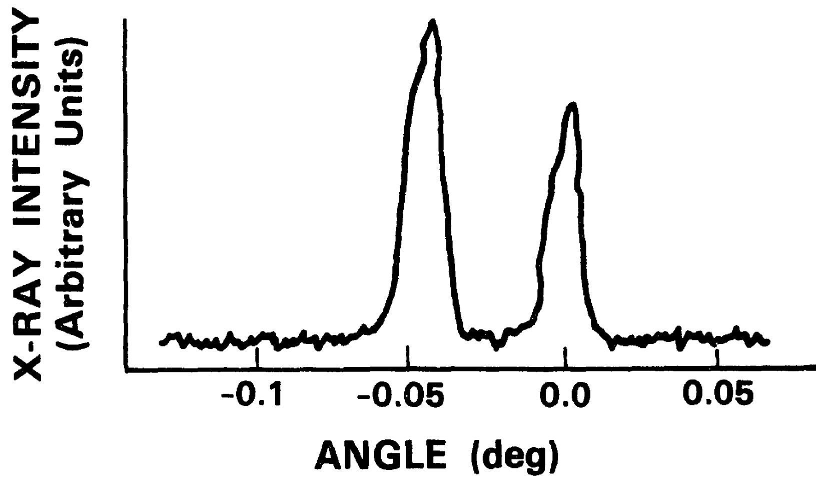

(a)

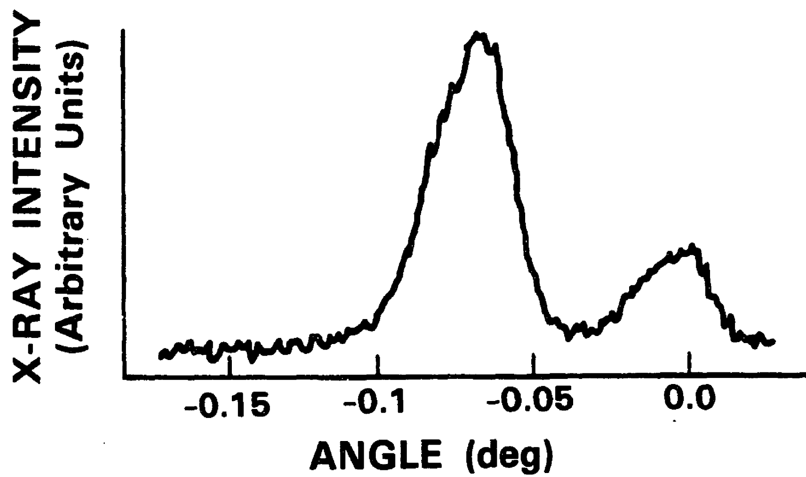

(b)

Fig. 5.11 X-ray diffraction from (a) (400) and (b) (422) planes of an LT GaAs epilayer grown on a SI GaAs substrate at 200°C. The absolute diffraction angles are influenced by the sample mounting and cannot be intercompared.

reflections [119]. For this sample $a_\perp$ = 5.660 Å. Since the (422) planes are inclined to the (001) surface, the separation between (422) planes is dependent on both $a_\perp$ and $a_\parallel$ [119]. The parallel lattice parameter of the epilayer can be calculated from the separation of the (422) peaks, given $a_\perp$ of the epilayer and a_o of GaAs [119],[124],[125]. For this sample, $a_\parallel$ = 5.660 Å, the same as $a_\perp$ of the epilayer, within experimental error [17].

Since the lattice parameter of the 200°C unannealed LT GaAs epilayer is larger than the lattice parameter of the LEC SI GaAs substrate ($\Delta a/a_o \cong 0.001$), LT GaAs on a SI GaAs substrate is a lattice mismatched system. For a lattice mismatched system, where the epilayer has not relaxed (so-called psuedomorphic growth), $a_\perp$ and $a_\parallel$ are not equivalent. The epilayer lattice parameter parallel to the interface will be forced to that of the substrate (psuedomorphic growth), but $a_\perp$ of the epilayer will be distorted. From simple Poisson's ratio considerations it can be argued that $a_\perp$ of the epilayer will be larger than its unstrained lattice parameter if $a_\parallel$ of the epilayer is smaller than its unstrained value, and vice versa. Quantitative calculations of $a_\perp$ require knowledge of the elastic tensor of the material [124],[125].

Once the critical thickness of psuedomorphic growth is exceeded, however, the epilayer relaxes to an unstrained condition by the formation of misfit dislocations [124],[126],[127]. For a cubic crystal in an unstrained condition, $a_\perp = a_\parallel$, as is the case for the LT GaAs epilayer. The equivalence of $a_\perp$ and $a_\parallel$ in the LT GaAs epilayer demonstrates that the thickness of the epilayer is greater than the critical thickness for the observed lattice mismatch [17],[126],[127]. It is possible that the dislocation seen in Fig. 5.7 and the slightly larger dislocation density observed for sample 3-1593 (see Sec. 5.3.1) are as a result of lattice relaxation. Additional support for this assertion is given by the cross-hatched surface of LT GaAs epilayers grown at 200°C as observed by Nomarski phase-contrast microscopy [128]. The cross-hatched

surface is indicative of the formation of misfit dislocations [129].

5.3.3 Ion Channeling

Ion-channeling [120],[121] measurements of unannealed and annealed LT GaAs epilayers are shown in Figs. 5.12 and 5.13 [116]. The spectra of Fig. 5.12 are for a high-quality LEC GaAs substrate, while the spectra of Figs. 5.13(a) and (b) are for an as-grown 200°C LT GaAs epilayer and another piece of the same epilayer after a 10 min, 450°C *in situ* anneal, respectively. The LT GaAs epilayers are 2.5 μm thick. All spectra were recorded using 1.8 MeV alpha particles. The ordinate of these plots is the backscattered yield and the abscissa is the energy of the backscattered ions. The depth into the sample, measured from the surface, can be calculated from the energy of the backscattered ions (see below) [120],[121]. The edge of the specta at an energy of approximately 1.45 MeV corresponds to the surface of the sample. Lower energies correspond to increased depth into the sample.

In Figs. 5.12 and 5.13, the upper trace corresponds to the backscattered yield measured with the ion beam incident on the sample in a direction that maximizes the backscattering, or equivalently, minimizes channeling effects [120],[121]. Such a trace is commonly called random since the ion beam "sees" a random arrangement of atoms [120]. The lower trace in both figures corresponds to the backscattered yield recorded with the ion beam incident parallel to the <110> axis of the crystal, in which direction ions can be channeled [120],[121]. The lower the backscattered yield for ion-channeling measurements parallel to the <110> axis, the higher is the crystal quality [120],[121].

As shown in Fig. 5.12, the backscattered yield from an LEC GaAs substrate recored with the incident beam parallel to the <110> axis is substantially less than that recorded in the random direction. This result is to be expected since the <110>

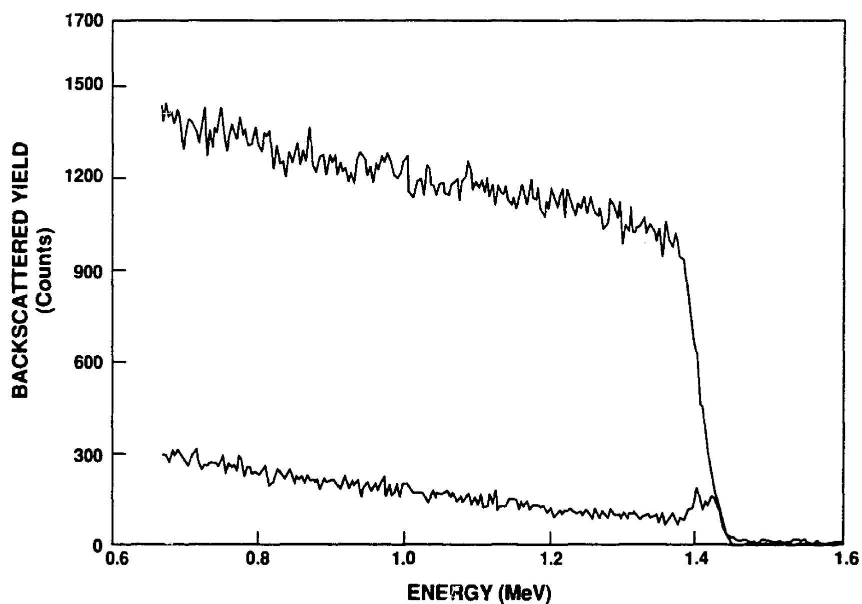

Fig. 5.12 Ion-channeling measurements of an LEC GaAs substrate using 1.8-MeV alpha particles. The upper trace in the figure is for the ion beam incident in a random crystallographic direction and the lower trace is for the ion beam incident parallel to the <110> axis of the crystal.

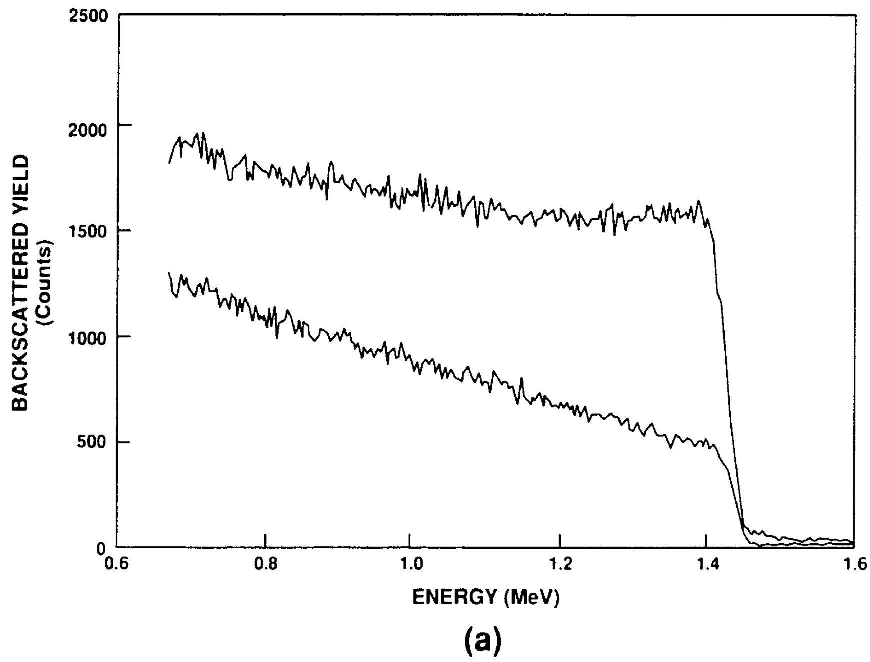

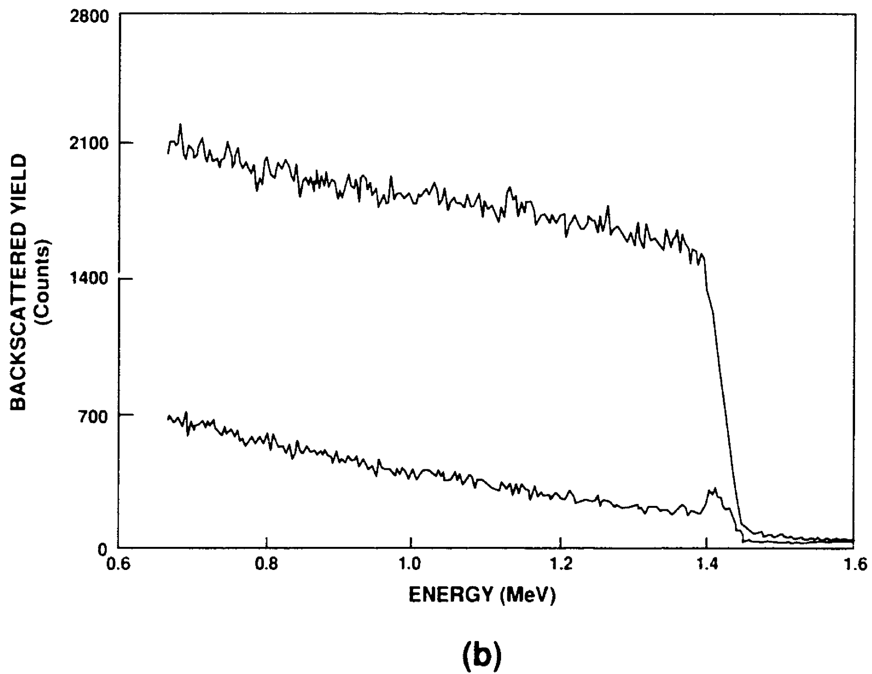

Fig. 5.13 Ion-channeling measurements using 1.8 MeV alpha particles of (a) an as-grown 200°C LT GaAs epilayer and (b) a 200°C LT GaAs epilayer annealed *in situ* at 450°C for 10 min. The LT GaAs epilayers are from the same growth and are 2.5 μm thick. The upper traces are for the ion beam incident in a random crystallographic direction and the lower traces are for the ion beam incident parallel to the <110> axis of the crystal.

axis of a high-quality GaAs crystal presents largely open channels to the ion beam. This spectrum serves as a reference for comparison with the LT GaAs results of Fig. 5.13.

Ion-channeling measurements of the unannealed 200°C LT GaAs epilayer are shown in Fig. 5.13(a). The random trace in this figure is comparable to the random trace for the reference sample shown in Fig. 5.12. However, the backscattered yield for ions incident parallel to the <110> axis of the unannealed LT GaAs sample is considerably larger than that for the reference sample. Increased backscattered yield for a channeling direction arises from disorder in the crystal [120],[121]. This disorder can include interstitial atoms in the channel, atoms displaced slightly from the lattice position, and crystalline defects such as stacking faults, dislocations, and microtwins [121]. Since as-grown LT GaAs is of high crystalline quality as determined by TEM (see Sec. 5.3.1), we attribute the observed increase in backscattered yield to point defects such as interstitials or atoms displaced slightly from the lattice sites. Additional experiments are needed to determine the position, density, and identity of the atoms in the channel. Although not shown here, preliminary flux peaking measurements [121] suggest that As_i with tetrahedral symmetry are present in the sample and contribute to the increased yield shown in Fig. 5.13(a) [115],[116].

The results of ion-channeling measurements of the annealed LT GaAs epilayer are shown in Fig. 5.13(b). The backscattered yield for ions incident parallel to the <110> axis for this sample is comparable to that for the GaAs reference crystal. This result indicates that the anneal has reduced the disorder in the LT GaAs epilayer. An annealing temperature of less than 450°C is consistent with the results of the x-ray diffraction experiments discussed in the previous section.

In order to quantitatively compare the results of ion-channeling measurements of the three samples of Figs. 5.12 and 5.13, Table 5.3 contains a summary of the rela-

Sample	Relative Yield at 50 nm Below Surface	Relative Yield at 350 nm Below Surface
LEC GaAs	0.08	0.14
As-grown LT GaAs	0.32	0.51
Annealed LT GaAs	0.11	0.21

Table 5.3 Relative yield, from ion-channeling measurements using 1.8 MeV alpha particles, at depths of 50 and 350 nm below the surface of high-quality LEC GaAs, as-grown 200°C LT GaAs, and 200°C LT GaAs annealed *in situ* at 450°C for 10 min. The LT GaAs epilayers are 2.5 μm thick. Relative yield is defined as the ratio of the backscattered yield measured for the ion beam incident parallel to the <110> axis to that measured in a random direction.

tive yield from these samples at depths below the surface of 50 and 350 nm. The relative yield is defined as the backscattered yield measured for ions incident parallel to the <110> axis divided by that in the random direction. Depths of 50 and 350 nm correspond to energies of the backscattered ions of approximately 1.4 and 1.1 MeV, respectively. As was previously noted, the relative yield from the as-grown LT GaAs epilayer is considerably larger than that of LEC GaAs. For the annealed LT GaAs sample, the relative yield is closer to that of LEC GaAs at a depth of 50 nm than at a depth of 350 nm. This result suggests that annealing of the disorder in the LT GaAs epilayer proceeds from the surface of the film into the bulk.

The ion-channeling results presented here confirm the x-ray diffraction findings presented in the previous section. The as-grown LT GaAs sample contains considerable disorder as evidenced by the large backscattered yield in the channeling direction. Annealing at 450°C is seen to markedly reduce the disorder, which is consistent with the annealing temperature of ~300-400°C found from the x-ray diffraction measurements (see Sec. 5.3.2). More work is needed to identify the point defects responsible for the enhanced backscattered yield from the unannealed epilayer, to measure more precisely the temperature for the annealing of the disorder, and to determine quantitatively the disorder reduction with annealing as a function of depth below the surface of the LT GaAs epilayer.

5.4 Optical

The related techniques of photoluminescence (PL), IR absorption, and Raman scattering (RS) have been used to assess the optical properties of LT GaAs. All these optical techniques have been employed because each provides different insight into the material and taken together allow a qualitative picture of the material to be deduced. Where PL provides information on radiative recombination processes, both

near band gap and deep level, IR absorption provides information on optical excitations. Absorption in the near IR (0.8 - 2.0 μm) can arise from both deep-level and band-to-band transitions. Far-IR absorption ($\lambda > 2\mu m$) and RS probe the vibrational properties of the material. Phonon modes of the host crystal as well as localized vibrational modes arising from point defects or clusters of defects have been observed by the two techniques [130]-[134].

The results for each technique are presented separately in the following discussion. In keeping with the approach taken throughout this chapter, results of similar measurements by other groups on samples containing EL2 or As_{Ga} will be summarized and compared with the results for LT GaAs. Since it is common in the literature of PL, IR, and RS measurements to present the measured intensity of the detected radiation in units of energy (eV), wavelength (nm), and wavenumber (cm^{-1}), respectively, I have followed these conventions. For the convenience of the reader, a number of commonly cited energies, frequencies, wavelengths, and wavenumbers are listed in Table 5.4. All wavelengths referred to in this thesis are for free space.

5.4.1 PL

Our preliminary results of PL measurements on LT GaAs and on conducting layers of GaAs grown on top of LT GaAs buffer layers were discussed in Sec. 2.3. The data presented in this section expand on those results in several directions. By using a different detector (see below), we have measured deep-level (0.7 to 1.4 eV) as well as near-band-gap (~1.4 to 1.5 eV) PL. We have used the MBE-growth-temperature experiment samples to investigate the PL of LT GaAs over this energy range as a function of T_s. We have also examined thin layers (~0.3 μm) of conducting n-GaAs layers on LT GaAs to investigate the presence of deep levels. These results have implications for electronic devices and circuits fabricated on LT GaAs

E (eV)	ν (THz)	λ (μm)	λ^{-1} (cm^{-1})
1.55	375	0.8	12,500
1.5	362	0.83	12,100
1.42	344	0.87	11,500
1.24	300	1.0	10,000
1.0	242	1.24	8,100
0.8	190	1.55	6,450
0.73	176	1.7	5,880
0.7	169	1.77	5,650
0.69	167	1.8	5,560
0.5	121	2.5	4,030
0.41	100	3.0	3,330
0.39	94	3.2	3,130
0.3	73	4.1	2,420
0.1	24	12.4	810
0.06	15	20	500
0.05	12	25	400
0.036	8.7	34.5	290
0.025	6	50	200
0.012	3	100	100
0.006	1.5	200	50

Table 5.4 Commonly cited energies, frequencies, wavelengths, and wavenumbers.

buffers.

Figure 5.14 is a schematic illustration of our PL experimental setup [135]. A Kr-ion laser emitting at a wavelength of 647 nm and a power of ~100 mW was focused to a spot size of ~3 mm on the cooled sample. All measurements were made at 4 K using a liquid He dewar. The collected luminescence was filtered to remove the laser background and dispersed using a spectrometer with a 1-m, 600-groove/mm grating blazed at 1 μm. We estimate the resolution of our system to be ~0.05 eV. Two detectors were used to measure the signal. The first, a cooled GaAs photomultiplier tube (PMT), was used to measure the near-band-gap PL reported in Sec. 2.3. The second, a cooled (77 K) Ge PIN photodiode and integrated Si preamplifier, was used to measure the near-band-gap and deep-level PL results reported in this section. Although of greater sensitivity near 1.5 eV, the GaAs PMT cuts off at energies less than ~1.4 eV. To access luminescence signals between 0.7 and 1.5 eV the Ge detector was used. Since the Ge detector cuts off for energies less than ~0.7 eV, we are presently unable to report results for PL below this energy. The laser beam was chopped at 100 Hz and lock-in detection was used to improve sensitivity. A computer was used to control the equipment and record the data.

The PL results for thin, conducting GaAs layers on a LT GaAs buffer and on an undoped GaAs buffer are shown in Figs. 5.15(a) and (b), respectively. For both samples the starting material is SI GaAs. For the sample of Fig. 5.15(a), MBE run number 3-1436, a 0.3-μm-thick n-GaAs layer doped with Si at $2x10^{17}$ cm^{-3} was deposited on top of a 1-μm-thick 200°C LT GaAs epilayer. For comparison, Fig. 5.15(b) is a sample (MBE run number 3-1463) of 0.3-μm-thick n-GaAs, also doped with Si at $2x10^{17}$ cm^{-3}, on top of a 0.2-μm-thick undoped GaAs buffer layer grown at 580°C. Although the PL signal is plotted in units of arbitrary intensity, the signal strengths relative to the near-band-gap signal of Fig. 5.15(b) are indicated on the

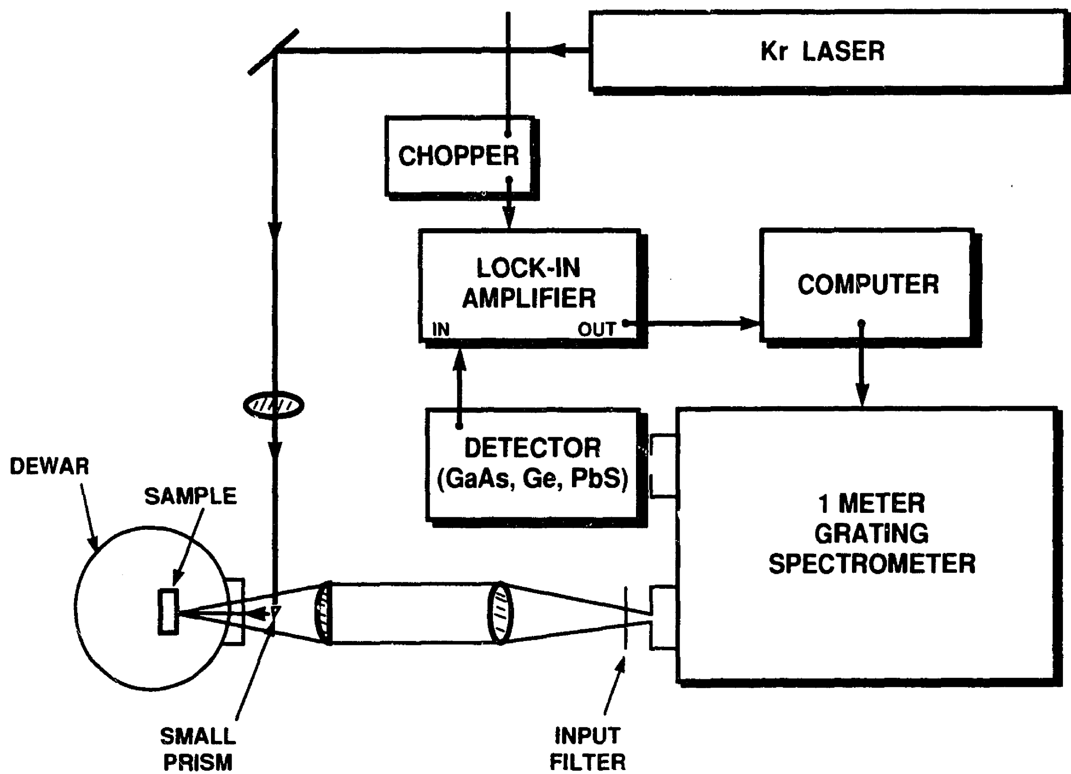

Fig. 5.14 Schematic illustration of the PL experimental configuration.

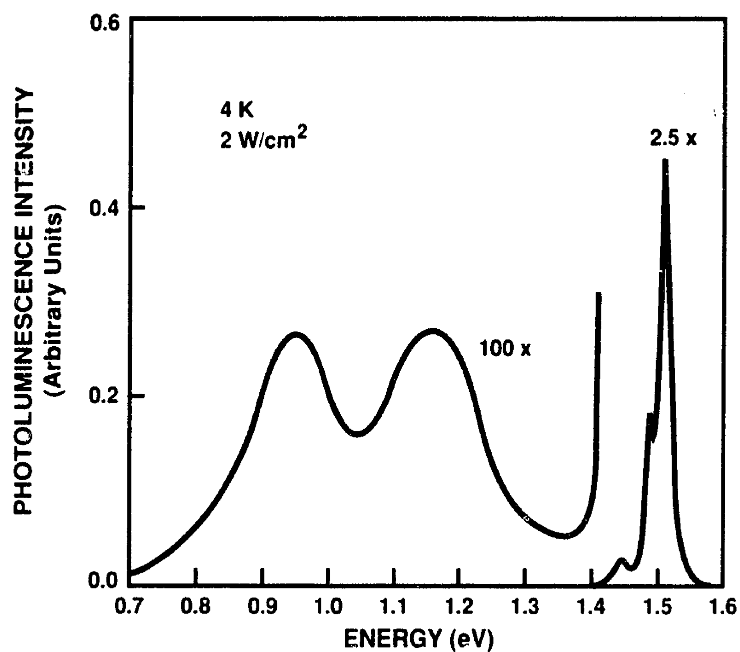

(a)

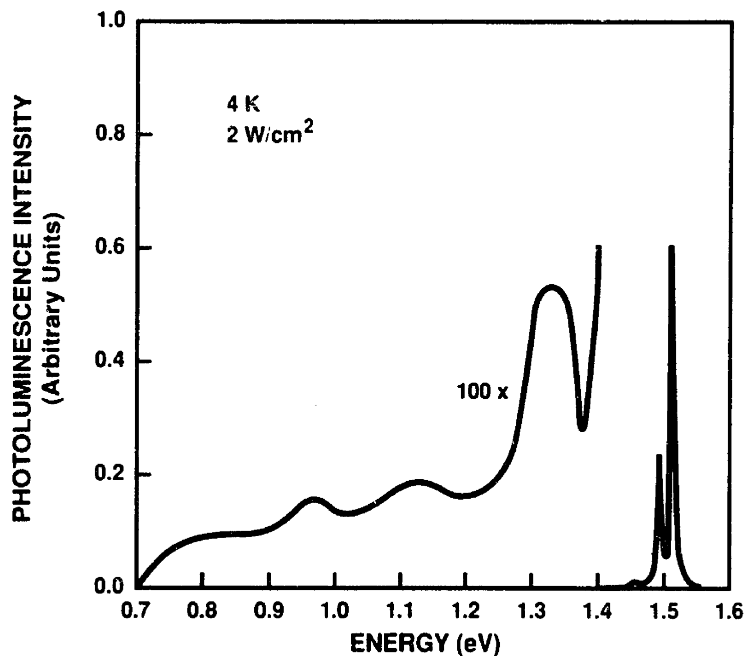

(b)

Fig. 5.15 PL spectra of 0.3-μm-thick n-type GaAs epitaxial layers grown at 580°C by MBE on (a) a 1-μm-thick buffer layer of 200°C LT GaAs, and (b) a 0.2-μm-thick buffer layer of undoped GaAs grown by MBE at 580°C.

figures. For example, the symbol 2.5× next to the near-band-gap PL signal of Fig. 5.15(a) indicates that the strength of this signal is a factor of 2.5 less than that of the corresponding signal of Fig. 5.15(b).

The well-resolved exciton (1.51 eV) and carbon acceptor (1.49 eV) peaks of Fig. 5.15(b) are not resolved in the spectrum of Fig. 5.15(a). One possible explanation of this result is that the n-GaAs epilayer on the LT GaAs buffer contains a larger deep-level concentration than the n-GaAs epilayer on the undoped GaAs buffer. This increased deep-level concentration reduces the near-bandgap PL signal by providing an alternative path for excess carrier recombination.

Another possible explanation for the reduced near-band-gap signal for sample 3-1436 is that the volume of high-quality material from which near-band-gap PL is emitted is less for this sample than for the sample grown entirely at 580°C. From the results of Sec. 2.3 and the results to be discussed below, we know that the LT GaAs layer does not emit near-band-gap PL. Thus, for the sample of Fig. 5.15(a), only the n-GaAs layer is emitting near-band-gap PL. In contrast, the n-GaAs epilayer and undoped GaAs buffer of sample 3-1463 can both emit near-band-gap PL since the penetration depth of the Kr laser light is of the order of several hundred nanometers.

The deep-level PL behavior of the two samples is markedly different. While both samples show weak deep-level PL, sample 3-1463 shows a broad peak at ~1.3 eV, whereas sample 3-1436 shows pronounced peaks at ~0.96 and 1.18 eV. The intensity of the deep-level peaks of both samples is approximately a factor of 100 weaker than the near-band-gap signal of sample 3-1463. Both deep-level peaks in sample 3–1436 have also been recently observed in an n-GaAs layer on an LT GaAs buffer by researchers at Hewlett-Packard [136].

The peak that we see in sample 3-1436 at 1.18 eV may be the same as a defect observed in bulk GaAs at 1.2 eV [137],[138]. Williams [137] and Chiang et al. [138]

both independently investigated deep-level PL of bulk-grown n-GaAs substrates. Based on their studies, they attribute the 1.2 eV peak to a pair defect, namely, a gallium vacancy combined with a silicon donor atom on a next nearest neighbor Ga lattice site, V_{Ga}-Si_{Ga} [137] [138]. Although the identification of the microscopic origin of this peak is somewhat speculative, the V_{Ga}-Si_{Ga} defect is consistent with their data and is clearly plausible for our material. Since LT GaAs is As-rich, it is possible that excess arsenic and/or V_{Ga} from the LT GaAs epilayer diffuse into the n-GaAs epilayer during growth at 580°C. This excess arsenic can give rise to gallium vacancies. Coupled with the silicon deliberately introduced into the epilayer growth, V_{Ga}-Si_{Ga} is a possible defect in the epilayer of sample 3-1436.

Although a PL peak at energies between 0.9 and 1.0 eV has been reported [136], [139], [140], the identity of this defect is largely still unknown. Turner et al. attributed a peak at 0.93 eV in their bulk grown samples to oxygen [139]. In contrast, Batavin and Popova attribute the 1.0 eV deep-level peak in their bulk-grown material to a complex of an arsenic vacancy and a silicon acceptor atom on a next nearest neighbor As lattice site, V_{As}-Si_{As} [140]. Neither of these identifications seems appropriate for our 0.96 eV peak. If an oxygen deep level, arising from residual oxygen in the MBE growth chamber, were responsible for the peak of sample 3-1436, we would expect a similar peak for sample 3-1463, which we do not see. Since LT GaAs is arsenic rich and the n-GaAs epilayer is grown under arsenic-stabilized growth conditions (see Sec. 2.3), it is unlikely that the epilayer contains V_{As}. Further, under arsenic-stabilized growth conditions at T_s = 580°C, Si preferentially incorporates as a donor rather than as an acceptor. At this time we can not make an identification of the 0.96 eV peak of sample 3-1436.

The presence of the peak at 1.33 eV in the spectra of sample 3-1463 and the absence of this peak in the spectra of sample 3-1436 suggests that the defect(s)

responsible for this peak may arise from the substrate. Since both samples were grown at roughly the same time (within a few weeks) it is unlikely that the background impurity level in the MBE system changed markedly between the two growths. However, since sample 3-1463 has only a thin, 0.2-µm-thick undoped GaAs buffer layer grown by MBE at 580°C, it is possible that residual impurities in the substrate have diffused into the n-GaAs active layer, giving rise to this signal. The low-temperature growth of the 1-µm-thick LT GaAs buffer layer of sample 3–1436 may serve as a barrier to this out-diffusion of impurities from the substrate into the active layer.

Using the LT GaAs epilayers from the growth-temperature experiment, we have investigated the near-band-gap and deep-level PL from six LT GaAs epilayers grown at different temperatures between 190 and 400°C. The PL spectra for LT GaAs samples grown at 400 and 220°C are shown in Figs. 5.16(a) and (b), respectively. As can be seen from Fig. 5.16(a), GaAs grown at T_s = 400°C evidences strong near-band-gap PL and a weak deep-level PL signal. The signal strength of the deep level peaks in Figs. 5.16(a) and (b) are referenced to the near-band-gap intensity of Fig. 5.16(a). The near-band-gap intensity of Fig. 5.16(a) is comparable to that observed in the spectrum of Fig. 5.15(b). The deep-level signal of Fig. 5.16(a) is broad band although the spectra does appear to be slightly peaked in the vicinity of 0.96 eV and 1.1 eV. Although the deep-level signal is weak and the peaks are faint, it is interesting to note that these peak energies are close to those observed for sample 3-1436 of Fig. 5.15(b). Since the 400°C-grown layer is undoped, this deep-level signal arises from intrinsic defects and not from impurity-related defects.

We have investigated other GaAs layers grown at 400°C and have found broad peaks at 1.0 and 1.2 eV in these layers as well [10]. Although we have also reported seeing a broad deep-level peak at ~1.3 eV in GaAs grown at 400°C [10], this level

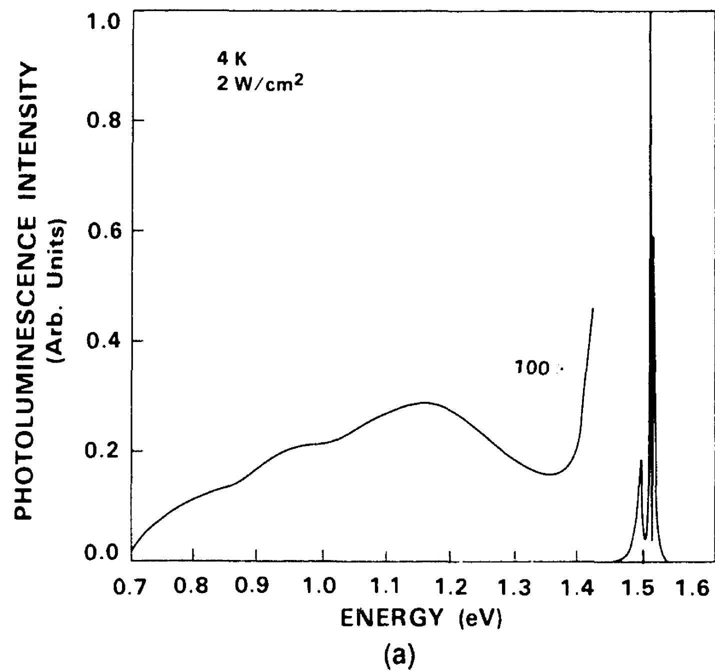

(a)

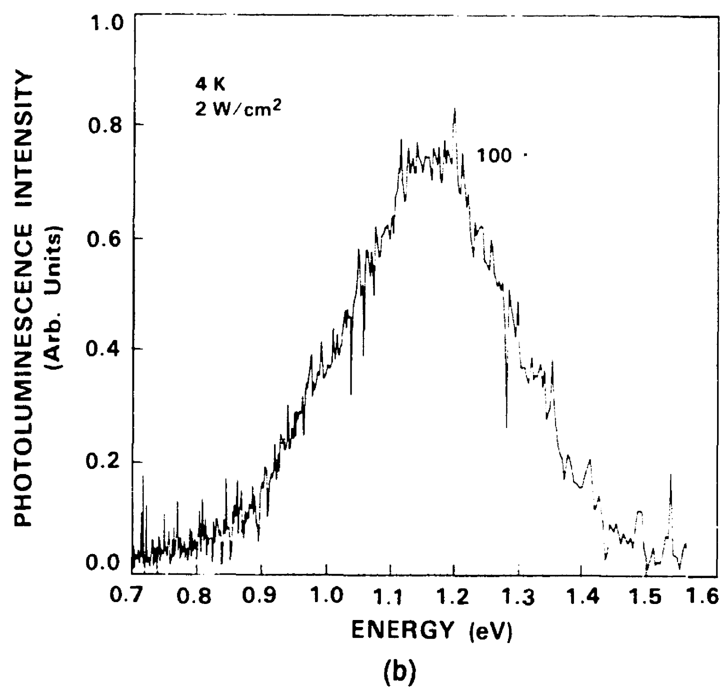

(b)

Fig. 5.16 PL spectra for 2-µm-thick LT GaAs epilayers grown at (a) 400°C and (b) 220°C.

has not been observed in our more recent growths, as exemplified by Fig. 5.16(a). As noted above, it is possible that the 1.3 eV peak arises from either impurities in the MBE system or the substrate and not from an intrinsic defect.

As T_s is reduced from 400 to 190°C, we find that the near-band-gap PL signal decreases monotonically until it is below detectable levels for T_s less than 300°C. In contrast, the deep-level PL signal appears to increase slightly in intensity as T_s is reduced from 400 to 220°C. The PL spectra of Fig. 5.16(b) shows a deep-level peak broadly centered about 1.16 eV and the absence of a near-band-gap signal. Below 220°C the deep-level PL signal decreases markedly, and is imperceptible for LT GaAs grown at 200°C. Both unannealed and annealed 200°C LT GaAs show no PL.

The primary inference to be drawn from this data is that as T_s is reduced, the deep-level concentration in the film increases monotonically. Some of the deep levels result in radiative recombination as evidenced by the deep-level PL signals of Fig. 5.16, but other deep levels result in nonradiative recombination. Ultimately, at the lowest temperatures used for growth, nonradiative recombination dominates and no PL is observed. For LT GaAs grown at 200°C, annealing at elevated temperatures does not produce a measurable PL signal.

At this time it is not clear whether LT GaAs has a band gap (see next section); however, assuming a band gap of 1.5 eV at 4 K and assuming that the observed PL peak at 1.16 eV arises from a transition between a deep level and a band, we find that the radiative deep level is either 0.34 eV above E_v or the same amount below E_c. As will be discussed in Sec. 5.4.3, a peak at 47 cm^{-1} has been observed in the RS spectrum of as-grown LT GaAs that we tentatively identify as a V_{Ga}–related defect. Defect complexes containing V_{Ga} are known to form acceptor levels in GaAs, as was noted above for the $V_{Ga} - Si_{Ga}$ defect [137]. Thus, we hypothesize that the deep-

level PL peak at 1.16 eV is associated with a transition between the conduction band and a V_{Ga}–related defect.

One of the principal reasons for investigating the PL properties of LT GaAs, in addition to simply documenting the behavior, was to determine if the well-known EL2 peaks were observed in our material [141]-[143]. Broad PL features centered at 0.65 eV and to a lesser extent at 0.8 eV have been reported for samples of LEC SI GaAs and have been correlated with EL2 [141]-[143]. Tajima reported a strong EL2 peak at 0.65 eV that is approximately a factor of 20 weaker than the band-edge signal [141]. Although we have not looked at deep-level PL for energies below 0.7 eV, we have never seen evidence for an increasing PL signal at energies < 0.9 eV. From Tajima's data, we would expect a strong peak to begin to manifest itself at approximately 1.0 eV and increase steadily as the energy is decreased to ~0.65 eV if an EL2 PL signal was present in our material [141]. We have never observed this type of behavior in LT GaAs grown at any temperature. Similarly, researchers at Hewlett-Packard and the Avionics Laboratory at Wright-Patterson Air Force Base have never observed an EL2-like deep-level-PL signal from LT GaAs [136],[144]. Lastly, it should be noted that although we have observed deep-level-PL signals from LT GaAs grown at temperatures above 220°C, these signals are several orders of magnitude less than the EL2 signals from LEC SI GaAs reported in the literature.

5.4.2 IR Absorption

The IR absorption of both unannealed and annealed 200°C LT GaAs has been measured from 0.3 to 25 μm. Three different spectrometers have been used to cover this spectral range. A commercial Fourier-transform infrared (FTIR) spectrometer was used to measure absorption from 2 to 25 μm and a commercial IR spectrometer was used between 0.3 and 3.2 μm. A home-built system was used to study the detailed IR

absorption behavior between 0.8 and 1.7 μm, the near-band-gap region of GaAs. By using these three instruments, we have been able to study the IR absorption of LT GaAs from the long-wavelength, lattice-vibrational region of the spectrum, through the region of deep-level absorption, to the band edge of GaAs.

The IR absorption results reported in this section are for three MBE-grown epitaxial layers. The samples are shown in schematic cross section in Fig. 5.17. Sample 3-1725, shown in Fig. 5.17(a), is a 3.5-μm-thick LT GaAs epilayer grown at 200°C on a SI GaAs substrate. An undoped GaAs epilayer grown at 580°C of thickness 0.5 μm was included between the LT GaAs layer and the substrate to provide a clean surface on which to initiate the LT growth. Following growth, this sample was removed from the MBE system and cleaved in half. One half was then reintroduced into the MBE growth chamber and annealed under an As overpressure for 10 min at 600°C. In the remainder of this section, the annealed and unannealed pieces of 3-1725 will be refered to as 3-1725A and 3-1725UA, respectively. Sample 3-1736 is shown in Fig. 5.17(b) and is a 3.5-μm-thick undoped GaAs epilayer grown at 580°C on a SI GaAs substrate. Different pieces of the same SI GaAs substrate were used for both 3-1725 and 3-1736 growth runs. Since sample 3-1736 was grown within one week of sample 3-1725, and was grown on the same substrate, this sample serves as the control or reference for our IR absorption measurements.

Following growth, the In metal and the In/GaAs alloy formed on the back side of all three samples was removed by etching and lapping. To reduce the amount of substrate, while maintaining mechanical stability for ease of handling, all three samples were polished to an average thicknes of ~250 μm. Also, the back side of all samples was polished at a ~1° angle to eliminate Fabry-Perot reflections from the substrate.

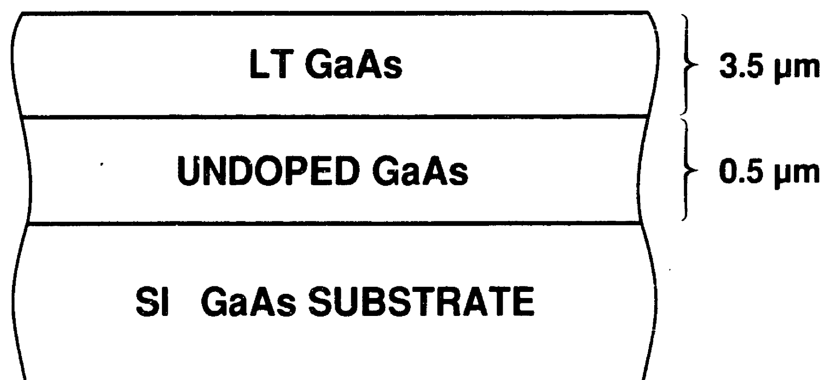

(a)

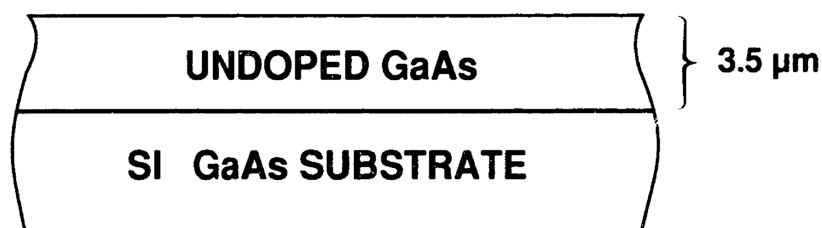

(b)

Fig. 5.17 Schematic cross section of MBE-grown samples used in the IR absorption experiments. (a) Sample 3-1725, a 3.5-μm-thick LT GaAs epilayer grown at 200°C on a 0.5-μm-thick undoped GaAs buffer layer, which was grown at 580°C on an LEC SI GaAs substrate. (b) Sample 3-1736, a 3.5-μm-thick undoped GaAs epilayer grown at 580°C on another piece of the same LEC SI GaAs substrate.

We have also made some near-band-gap IR absorption measurements of 2-μm-thick GaAs membranes supported by a glass slide. These membranes were fabricated using an epitaxial liftoff technique [145]. Although these samples have the advantage for IR transmission studies of no substrate absorption, the Fabry-Perot reflections for these samples in the range of 0.8 - 1.7 μm were pronounced, rendering these samples useless for our immediate purpose. The Fabry-Perot reflections arose from the dielectric discontinuity of the GaAs epilayer and the glass slide.

IR absorption in the region of wavelength λ greater than ~20 μm provides information both on lattice vibrations characteristic of the crystal and on impurity/defect-related localized vibrational modes (LVM) [132],[133]. Since our FTIR spectrometer extended only to $\lambda \cong 25$ μm, we were not able to access the long-wavelength LVM region of the spectrum ($\lambda > 25$ μm) [132],[133]. However, in the next section we will present RS data on localized modes of defects in LT GaAs. In assessing LVM in crystals, RS and far-IR absorption measurements are complementary techniques. The phonon absorption that we were able to observe by the absorption at 300 K between 20 and 25 μm was the same for LT GaAs as for GaAs.

At 300 K, in the range of 1.7 to 20 μm, the IR absorption spectra of the three samples were essentially identical. No pronounced absorption peaks were observed for either the unannealed or annealed films of 200°C LT GaAs. Although this region of the IR spectrum probes transitions between the valence band and shallow acceptors, between shallow donors and the conduction band, and between acceptors and donors within the bandgap, we did not measure any significant absorption. This result is similar to that of LEC SI GaAs, for which pronounced optical absorption is observed only for λ greater than ~1.5 μm [131].

Despite showing little IR absorption for $\lambda > 1.7$ μm, both unannealed and annealed LT GaAs show pronounced absorption for $\lambda < 1.7$ μm (energy $E > 0.7$ eV).

To explore the region of the IR spectrum between 0.8 and 1.7 μm (0.7 eV < E < 1.55 eV) in detail, we assembled an IR absorption spectrometer [146]. Our experimental configuration is shown in Fig. 5.18 [146]. An intense white light source and a 0.5-m-grating spectrometer were used to generate the incident monochromatic light.

An appropriate filter was used in front of the sample to remove harmonics that could pass through the spectrometer. (When the spectrometer is tuned to pass light of λ = 1.7 μm, for example, the spectrometer can also pass light of λ = 0.85 μm.) For measurements between 0.8 and 1.7 μm, a piece of SI GaAs was used to remove all light of λ < 0.87 μm, which corresponds to the room-temperature band gap of GaAs of 1.42 eV [147]. However, since the GaAs filter strongly attenuates the optical beam incident on the sample for wavelengths near the GaAs band gap, a red filter was used instead of the GaAs filter for IR absorption measurements of LT GaAs in the near-band-gap region. In the data that follows, all of the results shown for λ between 0.8 and 1.7 μm were made with the GaAs filter, and the results shown for λ between 0.8 and 1.2 μm were made with the red filter. A liquid-He dewar was used for measurements at 4 K and a room-temperature Ge photodiode was used as the detector. The monochromatic light was chopped at ~700 Hz to facilitate lock-in detection, and a computer was used to acquire and analyze the data.

For each sample investigated, the output of the lock-in amplifier was recorded and stored. The percent transmittance for each sample was then calculated by dividing the measured response for each sample by the responses of the filter and detector. By this means the spectral responses of the detector and filter were removed from the data. Lastly, the absorption coefficient for each sample, as a function of λ, was calculated using the following formula:

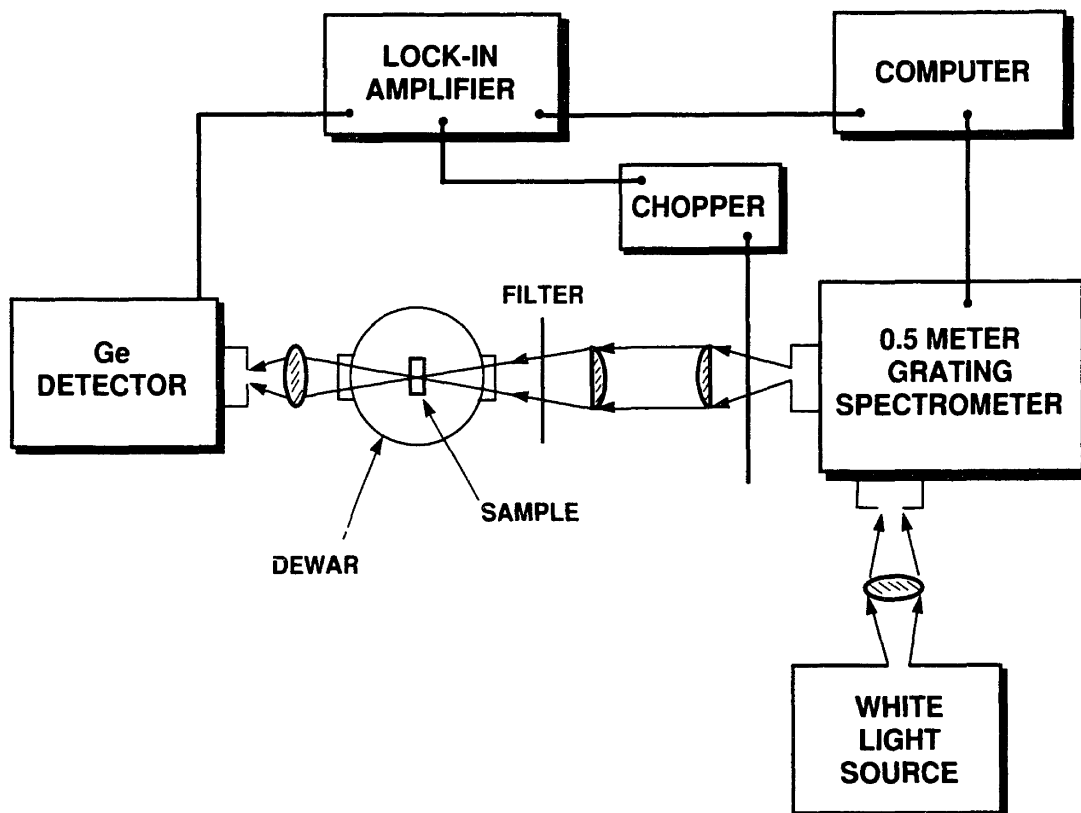

Fig. 5.18 Schematic illustration of the experimental configuration for the IR absorption measurements between 0.8 and 1.7 μm.

$$\alpha(\lambda) = \frac{1}{W} \ln \left[\frac{T(1.7\ \mu m)}{T(\lambda)} \right] \tag{5.2}$$

where T(1.7 μm) and T(λ) are the measured percent transmittance at 1.7 μm and the wavelength of interest, respectively, W is the thickness of the sample, and α(λ) is the absorption coefficient at the wavelength of interest. This formula clearly assumes that α(1.7 μm) is zero. Although not rigorously true, we know from our IR absorption measurements between 0.3 and 25 μm that the IR absorption for all of our samples only began to increase markedly for $\lambda < 1.7$ μm. Formula (5.2) permits us to avoid calculating or measuring precisely the reflectance of the sample. This approach is commonly used in measurements of IR absorption in semiconductors [88],[142], [148].

Because the absorption of the LT GaAs epilayers is significantly greater than that of the substrate, we have computed an effective absorption coefficient for samples 3-1725UA and 3-1725A as if their thickness were 3.5 μm, the thickness of the epitaxial layer. The absorption due to the substrate is given by the sample with the 3.5-μm-thick undoped GaAs epilayer. Sample 3-1736 has a total thickness, epilayer and substrate, of ~250 μm. The spectra of sample 3-1736 have been multiplied by a factor of 70 in Figs. 5.19 - 5.21 so that the absorption from the samples with the LT GaAs epilayers can be compared directly with that of the substrate. The absorption coefficient of the LT GaAs epilayers is therefore the difference between the measured effective absorption coefficient of samples 3-1725UA and 3-1725A and the trace shown for sample 3-1736. As will be seen below, the absorption due to the SI GaAs substrate is at least a factor of two less than the LT GaAs absorption in the region near the GaAs bandgap.

For the IR absorption study of LT GaAs, measurements were made at 300 and at 4 K. The 300 K results are shown in Fig. 5.19 and are discussed first. The 300 K

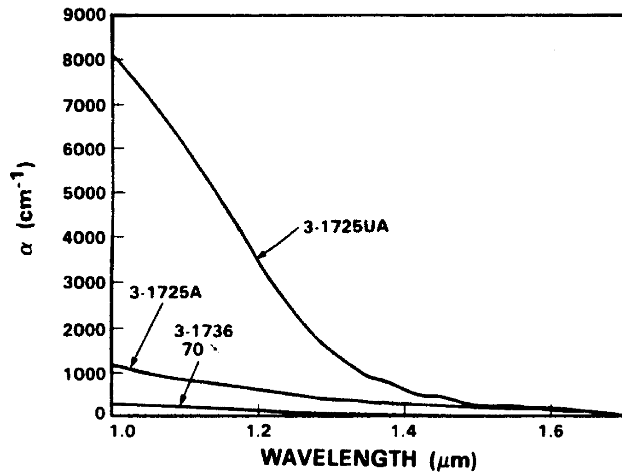

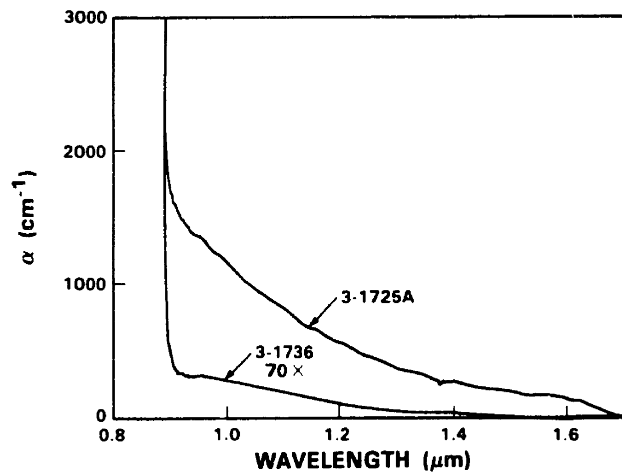

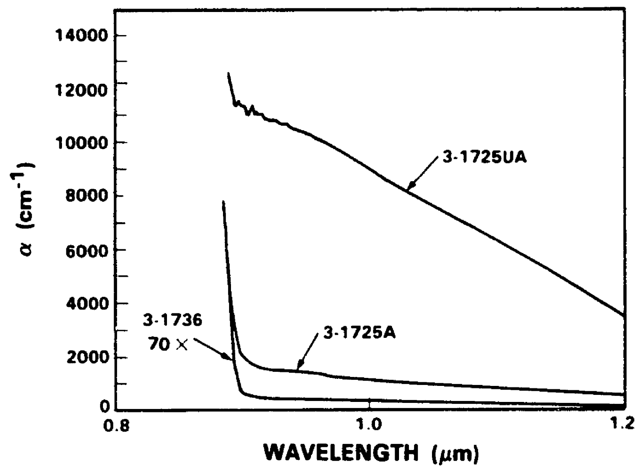

Fig. 5.19 Room-temperature IR absorption spectra of samples 3-1725A and 3-1725UA (annealed and unannealed portions of sample 3-1725 of Fig. 5.17, respectively) and sample 3-1736 of Fig. 5.17 for (a) 1 $\mu m < \lambda < 1.7 \mu m$, (b) 0.8 $\mu m < \lambda < 1.7 \mu m$, and (c) 0.8 $\mu m < \lambda < 1.2 \mu m$.

absorption coefficient of the three samples is shown between 1 and 1.7 μm in Fig. 5.19(a). As can be seen, α of sample 3-1725UA is substantially greater than α of either 3-1725A or 3-1736. The absorption due to the LT GaAs epilayer, both annealed and especially unannealed, are substantially larger than that of the substrate. The difference between as-grown LT GaAs and the substrate is obvious from Fig. 5.19(a). To better illustrate the absorption of the annealed LT GaAs epilayer, α of samples 3-1725A and 3-1736 are compared over the range of 0.8 - 1.7 μm in Fig. 5.19(b). As can be seen, α(1 μm) is ~1100 cm^{-1} for sample 3-1725A. Thus α(1 μm) of the annealed LT GaAs epilayer alone is approximately 800 cm^{-1}. The absorption coefficient of the substrate at 1 μm is only ~4 cm^{-1}, which is typical of LEC SI GaAs substrates [88],[148].

For future reference, it should be noted that the observed jitter at ~1.4 μm in the spectrum is due to absorption from the air. Also, we attribute the wavy appearance of the spectrum of sample 3-1725A between ~1 and 1.6 μm to Fabry-Perot reflections from the LT GaAs epilayer. The dielectric discontinuity between LT GaAs and SI GaAs is apparently sufficient to cause some reflection at the interface.

The near-band-edge absorption for these three samples at 300 K is shown in Fig. 5.19(c). Before discussing the data presented in this figure, another experimental detail should be noted. Since sample 3-1725UA is significantly more opaque than the other two samples, the use of a lower sensitivity on the lock-in amplifier was possible for this sample. This is why smaller signals, and thus a larger α, can be measured for sample 3-1725UA than for samples 3-1725A and 3-1736. Since we are exclusively interested in deep-level absorption, and not above-band-gap absorption, no attempt was made to accurately measure α above E_g. Hence, α is not shown for $E > E_g$ either in this plot or any subsequent plot.

The large absorption from the LT GaAs epilayers is readily apparent from Fig.5.19(c). The absorption from the unannealed LT GaAs epilayer is so large that the transmitted signal is at the limit of detection of our spectrometer for energies less than the GaAs band edge. The slight difference in α at 1 μm of sample 3-1725UA in Figs. 5.19(a) and (c) is attributed to measurement errors in the data of Fig. 5.19(a). The strong absorption of sample 3-1725UA for λ less than ~ 1.2 μm reduced the transmitted signal used in the calculation of Fig. 5.19(a) to levels near our detection limit. To improve the resolution of our experiment, we used the red filter to measure the IR absorption of LT GaAs between 0.8 and 1.2 μm. The data for sample 3-1725UA in Fig. 5.19(a) is included to illustrate the onset of strong absorption at ~1.4 μm. Quantitative values of α for λ less than 1.2 μm should be read from Fig. 5.19(c) and not from Fig. 5.19(a).

In contrast to sample 3-1725UA, the onset of band-edge absorption is clearly evident for samples 3-1725A and 3-1736. The inability to observe a band gap for sample 3-1725UA and the presence of a strong band edge for sample 3-1725A do not, unfortunately, imply that either annealed or unannealed LT GaAs has a band gap at ~1.4 eV. In the case of 3-1725UA, the deep level absorption is so large that it precludes seeing any band-edge absorption, either from the epilayer or the substrate. The presence of the band edge in the spectra for sample 3-1725A may arise from the substrate and not from the epilayer. In order to determine if a band gap exists in sample 3-1725UA, we need to use a more sensitive spectrometer, and to investigate the presence or absence of a band gap in 3-1725A we need to remove the substrate.

Several points can be noted from the data. LT GaAs, whether annealed or unannealed, contains a substantial concentration of deep levels. The absorption coefficient for unannealed and annealed LT GaAs epilayers at 1 μm are approximatley 3000 and 500 times larger, respectively, than α(1 μm) for LEC SI GaAs. It is this larger con-

centration of deep levels that is responsible for the absence of a PL signal as reported in Sec. 5.2. Further, the deep-level concentration of unannealed LT GaAs is larger than that of annealed LT GaAs, indicating that some defects are removed in the annealing procedure. The process of defect annealing is consistent with the structural rearrangements in the crystal lattice that occur in the annealing step, as noted in the previous section, and as will be discussed in the next section.

Since α of LEC SI GaAs changes significantly as a function of illumination at 4 K, which is evidence of EL2 (see Sec 5.1), we investigated the IR absorption of our three samples at 4 K. Figure 5.20 contains data obtained at 4 K before intense white light illumination, and Fig 5.21 shows data at 4 K after the illumination. Figures 5.20(a) and 5.21(a) are measurements of α between 0.8 and 1.7 μm and Figs. 5.20(b) and 5.21(b) are measurements of α between 0.8 and 1.2 μm. Before discussing these data, one point about the measurement must be addressed.

In order to align the sample in the optical beam, we removed the grating in the monochromator and removed the filter. Only in this way could we see the optical beam on the sample. Although at the time this method seemed appropriate, in retrospect the white light incident on the sample may perhaps have served to quench the LT GaAs IR absorption, as will be discussed below. In this regard then, the data of Fig. 5.20 should be viewed as measured at 4 K after ~1-2 min of white light illumination. Since full quenching of the EL2 level in LEC SI GaAs with intense white light illumination has been reported to take up to 10 min, with only partial quenching at times of 1-2 min (see Fig. 5.2) [88], we deliberately illuminated the samples with a focused, intense white light source for 30 min at 4 K after the measurements of Fig. 5.20 were completed. The data of Fig. 5.21 were then recorded. At worst, the data of Fig. 5.20 represents partial quenching of the IR absorption, and Fig. 5.21 is the IR absorption of the sample after complete quenching.

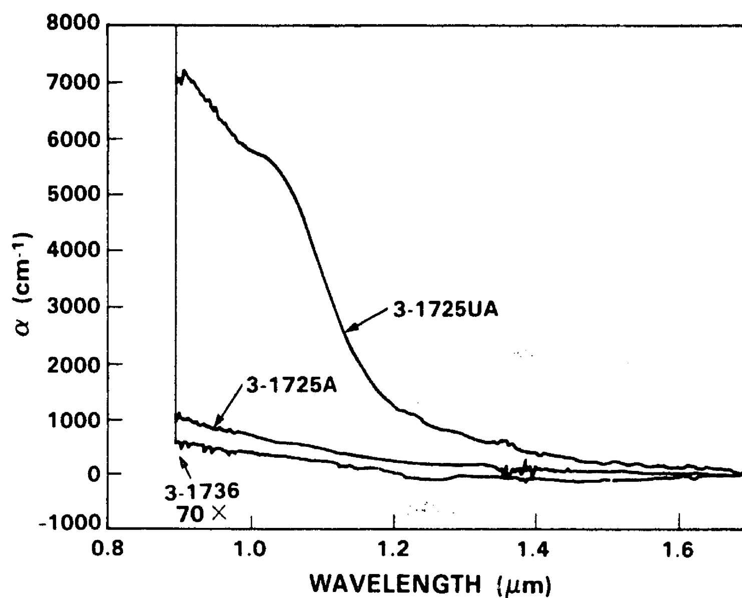

(a)

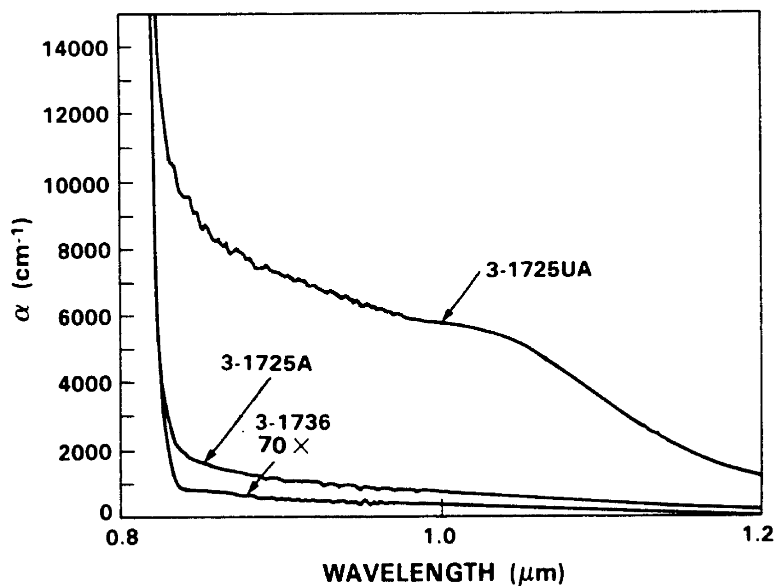

(b)

Fig. 5.20 IR absorption spectra at 4 K of the samples of Fig. 5.17 before intense white light illumination: (a) 0.8 μm < λ < 1.7 μm, and (b) 0.8 μm < λ < 1.2 μm.

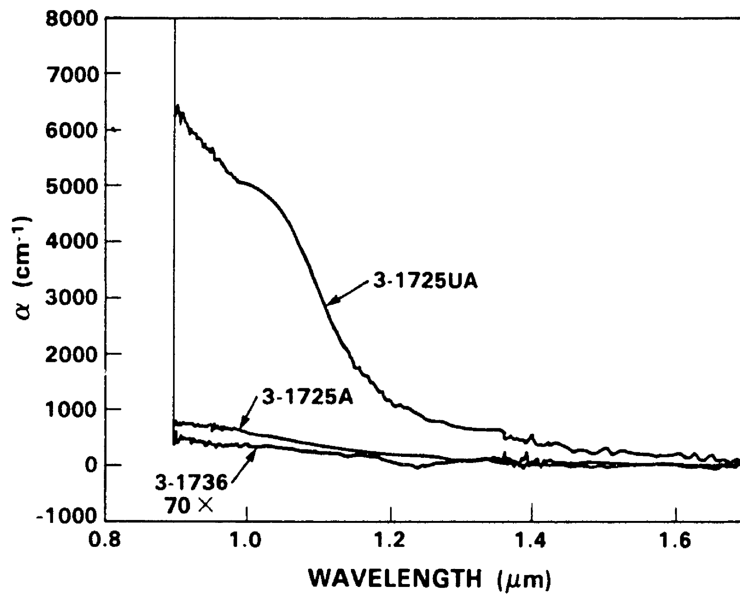

(a)

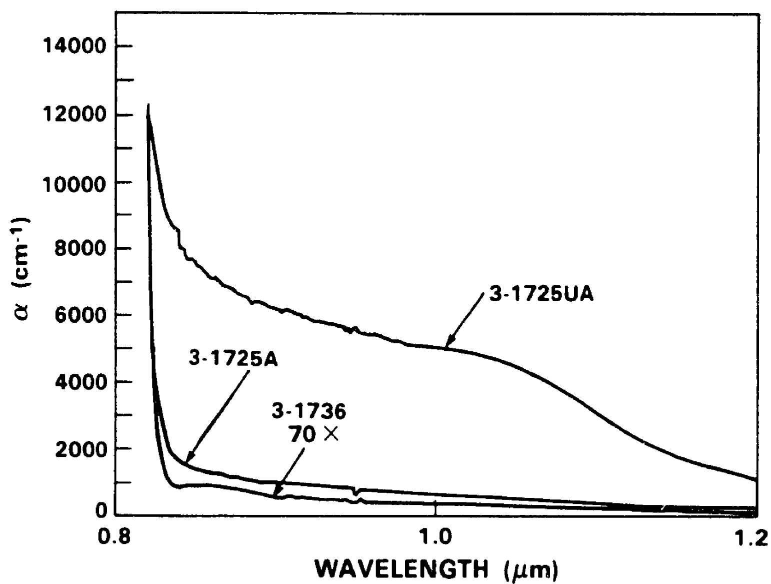

(b)

Fig. 5.21 IR absorption spectra at 4 K of the samples of Fig. 5.17 after intense white light illumination: (a) 0.8 μm $< \lambda <$ 1.7 μm, and (b) 0.8 μm $< \lambda <$ 1.2 μm.

An important observation can be made from the data of Figs. 5.20 and 5.21 in comparison with the data of Fig. 5.19. As expected, the band gap of GaAs has increased from ~890 to 822 nm or from approximately 1.4 to 1.5 eV. This increase in E_g complicates, to a degree, the comparison of the 4 K data with the 300 K results, because how the deep level energies vary relative to E_c and E_v as a function of temperature is not known. Thus, 1 μm absorption at 300 K may probe different deep levels than 1 μm absorption at 4 K.

Despite this shortcoming, several points can be noted. By comparing Figs. 5.20(b) and 5.19(c), it is clear that both annealed and unannealed LT GaAs are less absorbing at 4 K than at 300 K. Whether this is due to optical quenching or some other mechanism (e.g., carrier freeze-out) requires additional experiments. However, by comparing Figs. 5.20(b) and 5.21(b), we see that intense white light illumination quenches the IR absorption of both LT GaAs samples. In contrast, sample 3-1736 shows little evidence of quenching. Thus, the quenching of the LT GaAs samples can be attributed entirely to the epilayer and not to the substrate. For sample 3-1725UA, α(1 μm) ≅ 5600 cm^{-1} before the 30 min illumination and only 5000 cm^{-1} after illumination, an 11% decrease. For sample 3–1725A, α(1 μm) ≅ 700 cm^{-1} before illumination and 600 cm^{-1} after, a 14% decrease. Another conspicuous feature of the data of Figs. 5.20 and 5.21 is the distinct shoulder on the absorption curve for sample 3-1725UA at λ slightly greater than 1 μm.

The results of Figs. 5.20 and 5.21 indicate that the IR absorption of LT GaAs is very similar to the EL2 absorption shown in Fig. 5.2 and discussed in Sec. 5.1. The absorption of LT GaAs begins at ~1.7 μm (0.75 eV), rises sharply at ~1.1 μm (1.1 eV), and, for the case of the as-grown material at low temperature, exhibits a distinct shoulder at ~1.0 μm (1.2 eV). This behavior is identical to that discussed in Sec. 5.1 for the IR absorption characteristics of EL2. Further, approximately 10% of

the LT GaAs IR absorption is quenched by white light illumination at 4 K. As was shown in Sec. 5.1, quenching by white light illumination is characteristic of EL2. However, unlike the case of EL2, the defects responsible for the strong absorption in LT GaAs are not fully quenched, even after 30 min of intense white light illumination. This behavior is similar to that observed for plastically deformed and neutron- and electron-irradiated GaAs, as was briefly discussed in Sec. 5.1.

From these results, we hypothesize that the IR absorption observed for LT GaAs can be attributed to a high density of EL2-like defects near the center of the energy gap. As noted in Sec. 5.1, EL2 is believed to be the isolated As_{Ga} defect in the neutral charge state. Given the arsenic-rich deviation from stoichiometry in LT GaAs, and the observation of As_{Ga}^{+}–related defects in as-grown LT GaAs (see Sec. 5.5.1), a large concentration of As_{Ga}^{o}–related defects in LT GaAs seems reasonable. (Throughout the remainder of this thesis the term As_{Ga}^{o}–related will be used to describe these defects in LT GaAs. On occasion, the term EL2-like will also be used to describe these defects to emphasize their similarity to the EL2 center.) That ~10% of the LT GaAs IR absorption quenches, suggests that this fraction of the As_{Ga}^{o}–related defects are isolated and behave like EL2. The remaining As_{Ga}^{o}–related defects in LT GaAs do not quench, analogous to the irradiated and deformed material. As noted in Sec. 5.1, the stability of the As_{Ga}^{o}–related defects in these materials to illumination may result from either strain in the lattice or from adjacent defects or defect complexes [99].

If we assume that Martin's formula [88] for relating IR absorption at 1 μm to EL2 concentration pertains for LT GaAs, then we calculate that as-grown and annealed LT GaAs contain approximately 10^{20} and 10^{19} cm^{-3} As_{Ga}^{o}–related defects, respectively. These concentrations are well beyond those used by Martin in formulating his relation [88], and, hence, these numbers should be viewed as rough esti-

mates only. However, since 10^{20} cm^{-3} defects would be separated on average by ~2 nm, it is possible that the defects may behave as if they were independent of each other in their absorption properties. Further, an As^{o}_{Ga}–related defect concentration of the order of 10^{20} cm^{-3} is consistent with the 1 at.% deviation from stoichiometry in the as-grown material. The lower As^{o}_{Ga}–related density in annealed LT GaAs is less than the known deviation from stoichiometry. This point will be discussed in more detail in Sec. 5.6.

The anneal at 600°C is seen to reduce the IR absorption of LT GaAs by approximately an order of magnitude from the as-grown levels. This reduction in absorption can be associated with the annealing of the As^{o}_{Ga}–related defects, and is consistent with the annealing of the disorder in the crystal shown by the x-ray and ion-channeling measurements of the previous section. This result is also consistent with the conductivity results to be presented in Sec. 5.5.2.

Although not shown here, we have also recently made IR absorption measurements of the LT GaAs samples from the MBE-annealing and growth-temperature experiments [116]. We found that all these LT GaAs samples show the same type of absorption as in Figs. 5.19 to 5.21. The absorption coefficient of these LT GaAs samples was found to increase monotonically at T_s was reduced and to decrease monotonically as the annealing temperature was increased. On the basis of our hypothesis and using Martin's formula [88], we infer that the density of As^{o}_{Ga}–related defects increases monotonically as T_s is reduced and decreases monotonically as the annealing temperature is increased.

From these measurements we have also confirmed in all the LT GaAs samples that ~10% of the IR absorption at 1 μm is quenched by white light illumination. We have found that this quenched signal can be recovered only by heating the samples to temperatures of ~130 K, which is again consistent with the EL2 behavior discussed

in Sec. 5.1.

To summarize the results of this section, we have proposed the presence of As_{Ga}^{o}–related defects in both as-grown and annealed LT GaAs. Although defects other than As_{Ga}^{o} may contribute to the IR absorption shown in Figs. 5.19 to 5.21, attributing all of the absorption to As_{Ga}^{o}–related defects and using Martin's formula [88], we find an As_{Ga}^{o}–related defect concentration of the order of 10^{20} cm^{-3} in as-grown material, consistent with the known deviation from stoichiometry. Such a large concentration of As_{Ga}^{o}–related defects leads to a band of impurity states near the middle of the band gap, as will be discussed in Sec. 5.5.2. The As_{Ga}^{o}–related defects have been observed to decrease in concentration as a result of annealing, consistent with the annealing of the lattice disorder observed in the previous section. However, this decrease in As_{Ga}^{o}–related defect density is not reflected in a commensurate decrease in the As excess in the crystal (see Sec. 5.2). The results of this section will be used in conjunction with the results from the other characterization techniques to formulate a qualitative model of LT GaAs in Sec. 5.6.

5.4.3 Raman Scattering

RS has been used to characterize annealed and unannealed LT GaAs epilayers grown at 200°C [149]. These results provide information on both the crystal quality of the material and specific vibrational modes of defects. Our recent results on resonant RS will be summarized and inferences drawn. A detailed discussion of resonant RS of LT GaAs will appear in a future publication [149].

RS is a standard technique used to probe the vibrational properties of semiconductors [130]. When a laser beam is incident on a semiconductor surface, the reflected light contains not only photons of the original energy, but also photons of energy that are shifted from that of incident beam. The shift in energy of a photon in

the scattered beam relative to the photon energy of the incident beam reflects the energy lost or gained in the scattering event. In addtion to other sources of scattering, which will not be discussed here but are discussed in detail in the literature [130], both lattice vibrations and localized vibrational modes can participate in RS. For a crystalline semiconductor, the Raman tensor governs which of these phonon modes can participate in RS for a given crystallographic orientation of the sample and polarization of the incident light [130]. A laser beam of energy close to the fundamental band gap of the semiconductor enhances the RS from both the lattice and the localized vibrational modes in the crystal [134]. However, the enhancement for localized vibrational modes is greater than that for lattice vibrational modes [134]. The use of a laser with energy close to E_g of the semiconductor is known as resonant RS [134].

For the study of LT GaAs, the RS from the lattice modes can provide information on the quality of the crystal, while that from the localized vibrational modes can provide information on specific point defects or defect clusters in the material. By varying the crystal orientation and the polarization of the incoming laser beam, we obtain information on the symmetry properties of localized vibrational modes.

A schematic diagram of our Raman scattering experimental setup is shown in Fig. 5.22. All data reported here were obtained at 300 K. A laser was used to generate an intense optical beam of a known polarization. Three different lasers have been used to measure the Raman spectra of as-grown and annealed epilayers of LT GaAs. The 647-nm (15,448 cm^{-1}) line of a krypton-ion laser, the 514.5-nm (19,436 cm^{-1}) line of an argon-ion laser, and the 829-nm (12,000 cm^{-1}) line of an infrared dye laser were used in the measurements reported in this section. The energy of the dye laser (E = 1.49 eV) is slightly greater than that of the band gap of GaAs at room temperature ($E_g \cong 1.42$ eV), and, hence, this laser provides enhance-

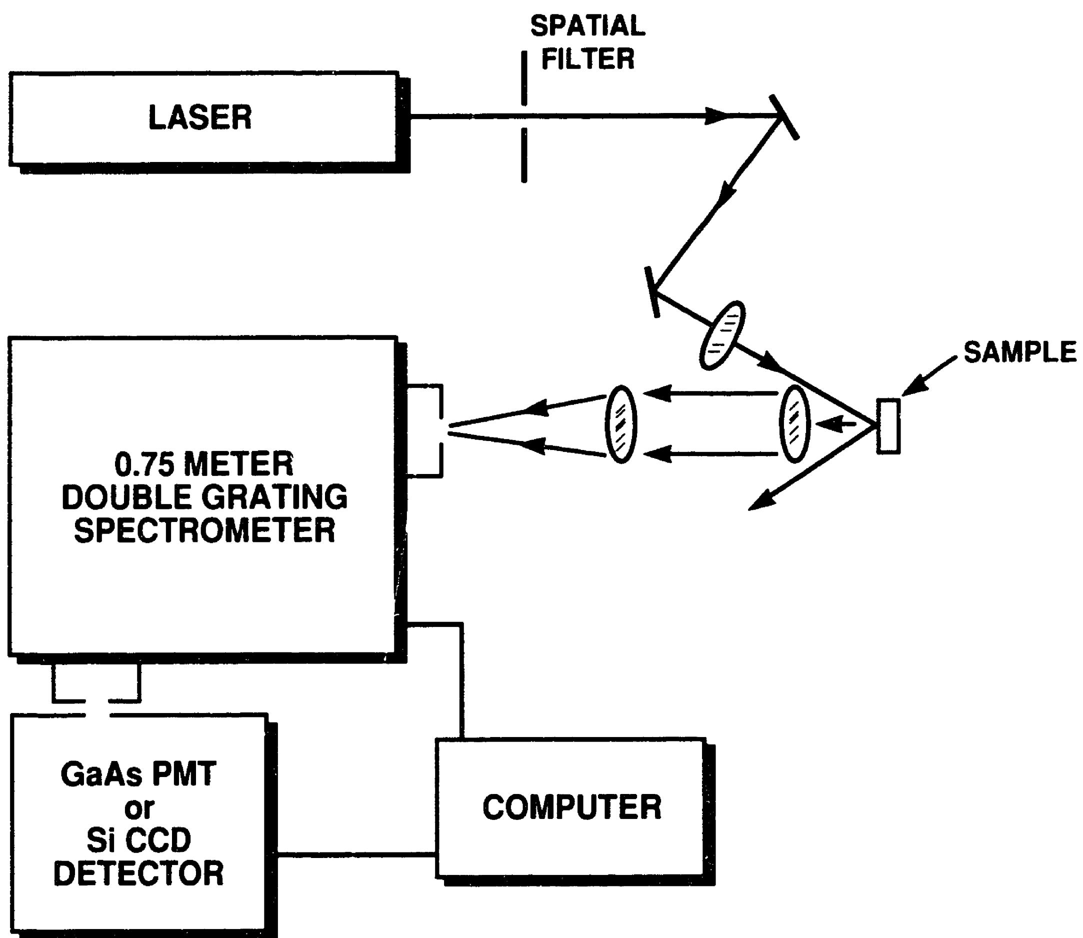

Fig. 5.22 Schematic diagram of the experimental configuration used for the Raman scattering measurements.

ment of scattering by localized modes through the resonant-RS effect [134]. As will be noted below, a number of localized modes in LT GaAs that were not observed for RS using the Kr and Ar lasers were observed using the dye laser. Since the energy of all three lasers is greater than the bandgap of GaAs, the penetration depth of the light was always less than ~0.5 μm [150]. Because all the LT GaAs epilayers used in this study were thicker than 1.5 μm, only the upper region of the LT GaAs epitaxial layers was probed by RS.

All RS measurements were conducted in a psuedo-backscattering geometry. The laser light was focused to a spot size of less than 1 mm on the sample, and was incident at an angle of ~30° from the normal to the sample. The continuous power incident on the sample was less than 100 mW. The polarization of the incident light was either along the cleavage planes of the (001) surface, the <110> directions, or was 45° to the cleavage planes, the <100> directions (see below) [4.17]. Backscattered light was collected by a lens, while the primary scattered beam was not collected. The backscattered light then passed through a variable polarizer (analyzer) to select the scattered polarization of interest, and was focused on the slits of a 0.75-m double spectrometer. A cooled GaAs PMT or a cooled Si CCD camera were used to detect the collected and analyzed light. Photon counting was employed to achieve a high signal-to-noise ratio, and a computer served to control the equipment and record the data.

For the identification of the symmetry of specific modes in the RS, it is necessary to know the scattering geometry used in the experiment. In this discussion I will adopt the following convention for describing our measurements of RS from (001)-oriented LT GaAs epilayers [149]. The incident laser light is along the z axis, where z is parallel to the [001] direction. The backscattered light is denoted by $\overline{z}$. For polarization selection rule analysis, x and y denote the [100] and [010] directions

respectively, and x′ and y′ denote the [110] and [1$\bar{1}$0] directions, respectively. To specify the scattering geometry for each experimental RS measurement, a shorthand notation of the form z(x′,y′)$\bar{z}$ is typically used [151]. In this notation, the first letter specifies the direction of the incident laser beam, and the last letter specifies the direction of the collected light. Since all of the measurements reported here were measured in a psuedo-backscattering geometry, all of the spectra have z as the first entry in this notation and $\bar{z}$ as the last entry. The two entries inside the parentheses specify the polarization of the incoming and scattered light, respectively. Thus, for the specification z(x′,y′)$\bar{z}$, the incident laser beam is polarized parallel to the x′ or [110] direction and only the backscattered light polarized parallel to the y′ or [1$\bar{1}$0] direction was collected.

RS spectra for an unannealed 2-μm-thick LT GaAs epilayer are shown in Fig. 5.23, and the RS spectrum of a 2-μm-thick LT GaAs epilayer that was annealed *in situ* for 10 min at 600°C is shown in Fig. 5.24. In both figures the RS signal (number of counts) in arbitrary units is plotted versus the Stokes energy shift of the backscattered light in wavenumbers. Since the photoluminescence is quenched in both annealed and unannealed LT GaAs epilayers (see Sec. 5.4.1), we were able to use the IR dye laser to measure resonant RS from the samples. The absence of a PL signal is essential for measurement of resonant RS because any near-band-gap PL signal would overwhelm the weak Stokes-shifted Raman signal. The spectra shown in Figs. 5.23(a)-(d) and in Fig. 5.24 were measured using the IR dye laser (12,000 cm^{-1}), while the spectrum of Fig. 5.23(e) was measured using the Ar-ion laser (19,436 cm^{-1}). The scattering geometries for Figs. 5.23(a)-(e) are z(x′,x′)$\bar{z}$, z(x,x)$\bar{z}$, z(x,y)$\bar{z}$, z(x′,y′)$\bar{z}$, and z(x,y)$\bar{z}$, respectively. Figure 5.24 was recorded in the z(x′,x′)$\bar{z}$ geometry.

For RS in a medium with a T_d point group symmetry (e.g., GaAs), the allowed

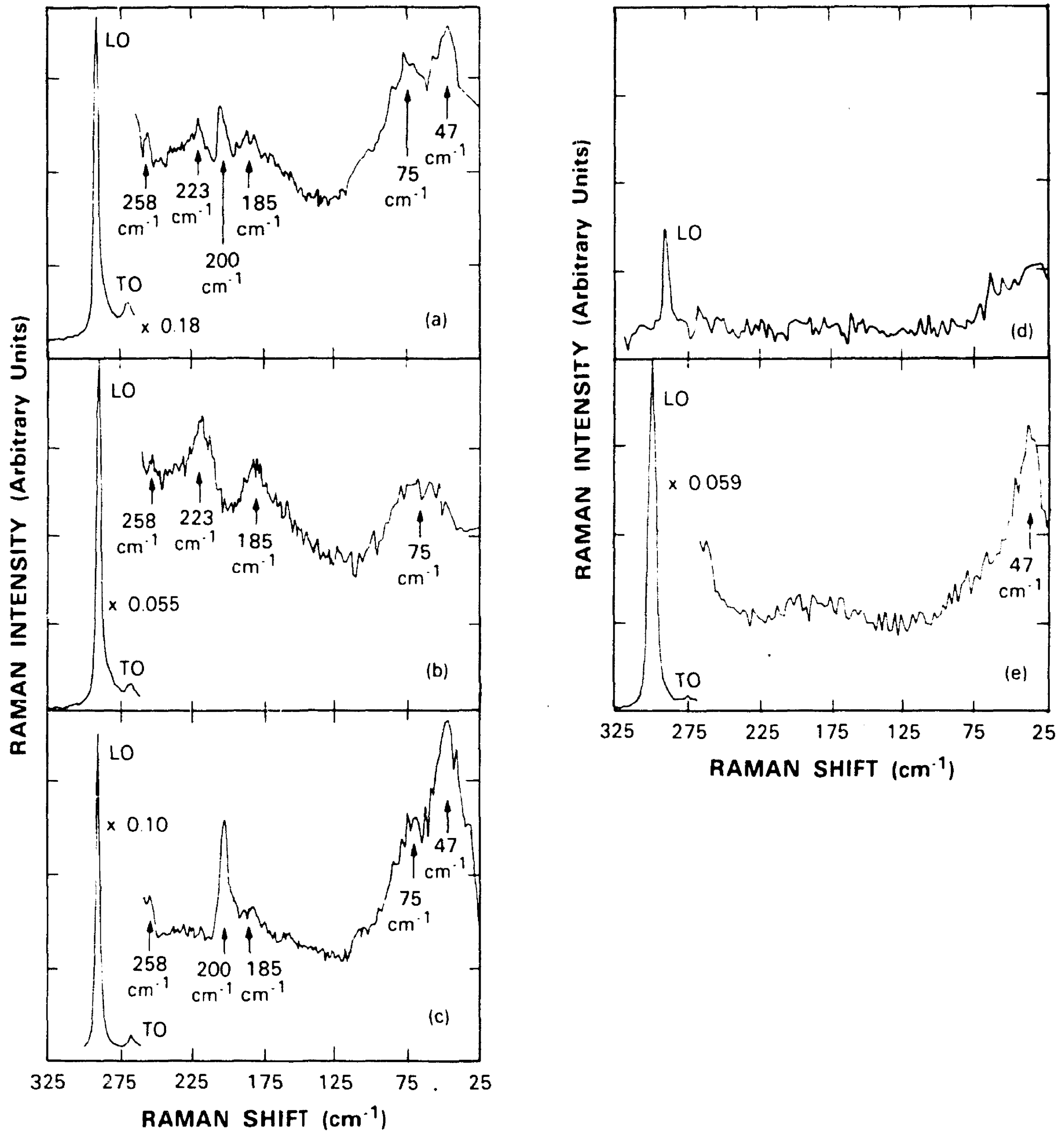

Fig. 5.23 RS spectra for a 2-μm-thick unannealed LT GaAs epilayer grown at 200°C. Spectra (a)-(d) were measured using 12,000 cm^{-1} excitation and spectrum (e) was measured using 19,436 cm^{-1} excitation. The scattering geometries for these spectra are as follows: (a) $z(x',x')\bar{z}$, (b) $z(x,x)\bar{z}$, (c) $z(x,y)\bar{z}$, (d) $z(x',y')\bar{z}$, and (e) $z(x,y)\bar{z}$. The vertical arrows mark the location of the various features discussed in the text.

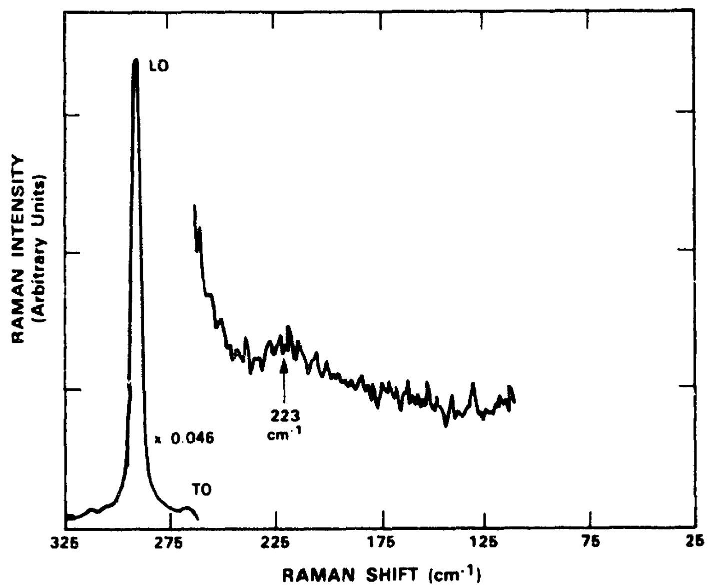

Fig. 5.24 RS spectrum for a 2-μm-thick LT GaAs epilayer grown at 200°C and annealed *in situ* for 10 min at 600°C. This spectrum was recorded in the $z(x',x')\bar{z}$ geometry using 12,000 cm^{-1} excitation. The vertical arrows mark the location of the various features discussed in the text.

phonon symmetries are $\Gamma_1 + \Gamma_{12} + \Gamma_{15}$, $\Gamma_1 + 4\Gamma_{12}$, Γ_{15}, and $3\Gamma_{12}$ [130],[149],[151], respectively, for the $z(x',x')\bar{z}$, $z(x,x)\bar{z}$, $z(x',y')\bar{z}$, and $z(x,y)\bar{z}$ scattering geometries. By investigating the presence or absence of a given mode in the Raman spectra as a function of the scattering geometry (see Fig. 5.23), we can determine the symmetry of the mode [130],[151]. For instance, a mode with Γ_1 symmetry is observed for the $z(x',x')\bar{z}$ and $z(x,x)\bar{z}$ configurations and not for the $z(x,y)\bar{z}$ and the $z(x',y')\bar{z}$ configurations [130],[151]. As will be discussed below, within the resolution of our setup, all of the localized modes that we observed in LT GaAs can be attributed to either the Γ_1 or Γ_{15} symmetries [149].

The Γ_1 mode in GaAs corresponds to a breathing mode and is isotropic, whereas the Γ_{15} symmetry corresponds to a vibration that transforms like a vector under the T_d symmetry operations [152]. To illustrate these symmetries for a specific point defect in GaAs, Fig. 5.25 shows examples of the Γ_1 and Γ_{15} symmetry vibrations of a GaAs vacancy that has tetrahedral symmetry [134]. We have tentatively identified specific point defects and clusters of defects in LT GaAs from the energy and symmetry of each of the localized modes.

The remainder of this section will address the data presented in Figs. 5.23 and 5.24. Specific vibrational modes, their energy and symmetry, will be noted. Each will be identified with a specific defect, cluster of defects, or bulk-crystalline modes. The defect-related modes observed in Figs. 5.23 and 5.24 are noted on the figures with vertical arrows and are labeled with the energy of the peak. The energy, symmetry, annealing temperature of the mode, and the proposed identification of the observed mode are summarized in Table 5.5. Also noted in this table are the excitation source or sources for which the mode is observed, and if the mode has also been observed for samples of electron-irradiated GaAs [134],[152]-[155]. That some modes are only observed using the dye laser indicates a resonant enhancement for

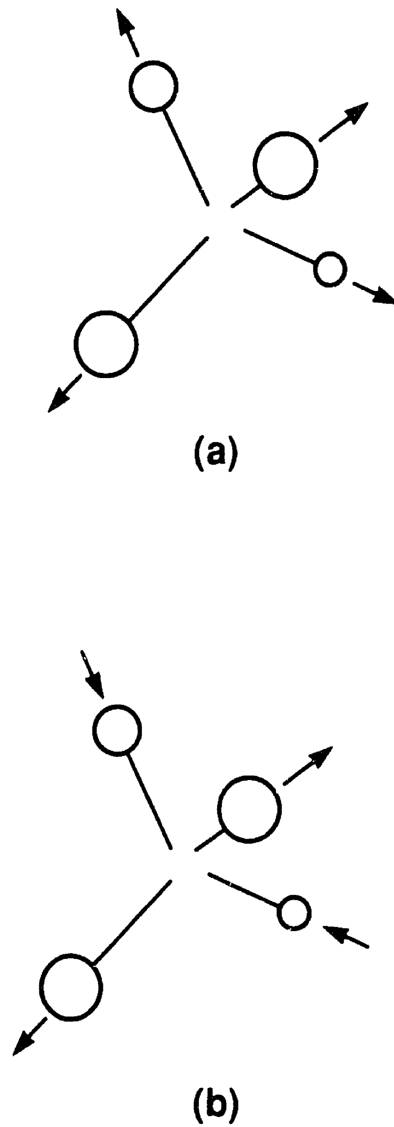

Fig. 5.25 Illustration of (a) Γ_1 and (b) Γ_{15} symmetry vibrations of a specific GaAs point defect, a vacancy that has tetrahedral symmetry. The arrows indicate the motion of atoms during the vibration. (a) The Γ_1 symmetry vibration corresponds to a breathing mode where all four nearest neighbor atoms move in and out together. (b) The Γ_{15} symmetry vibration corresponds to a stretching-like mode where two nearest neighbor atoms move in, when the other two nearest neighbor atoms move out, and vice versa. After Berg [134].

MODE FREQUENCY (cm^{-1})	SYMMETRY (based on T_d point group)	EXCITATION SOURCE(S) FOR WHICH MODE IS OBSERVED[1]	PRESENT IN ELECTRON-IRRADIATED SAMPLES	ANNEALING TEMPERA-TURE T_a (°C)	PROPOSED IDENTI-FICATION
47	Γ_{15}	IR, Kr, Ar	No	$300 < T_a < 600$	Γ_{15} mode of V_{Ga}
75	Nearly Γ_1	IR, Kr	Yes	$300 < T_a < 600$	DAFORS
185	Nearly Γ_1	IR, Kr	Yes	$300 < T_a < 600$	DAFORS
200	Nearly Γ_{15}	IR	No	$300 < T_a < 600$	Γ_3^+ mode of crystalline As
223	Γ_1	IR	Yes	$T_a > 600$	Γ_1 mode of As_i
258	Nearly Γ_1	IR	No	$300 < T_a < 600$	Γ_1^+ mode of crystalline As

[1]IR is 12 000 cm^{-1} infrared dye laser line; Kr is 15 448 cm^{-1} krypton laser line; Ar is 19 436 cm^{-1} argon laser line.

Table 5.5 Summary of disorder- and defect-related peaks observed by RS and resonant-RS measurements and their proposed identifications.

scattering from these defects [134]. Electron-irradiated GaAs results [134],[152]-[155] as well as results from RS of oxidized GaAs [156], damaged GaAs, and amorphous GaAs [157]-[163] will be used to identify the defect(s) responsible for the observed modes in RS from LT GaAs.

All the spectra in Figs. 5.23 and 5.24 show strong lines at approximately 290 and 260 cm^{-1}. These are the longitudinal-optical (LO) and transverse-optical (TO) phonon peaks of GaAs. For a (001) GaAs surface, in a backscattering geometry, the LO phonon peak is the only allowed transition [130],[151]. This accounts for its strength in the spectra. Since the TO scattering event is not allowed for backscattering from a (001) GaAs surface [130], its presence here indicates that our experiment is not conducted in a true backscattering configuration [158],[159].

The presence of the strong, sharp LO and TO phonon lines attests to the high crystalline quality of both as-grown and annealed LT GaAs, and confirms the results of Sec. 5.2. Close examination of the positions of the LO peak in both LT GaAs samples indicates that the LO line of the annealed LT GaAs sample is the same as that of GaAs (Stokes shift of 292 cm^{-1}), while the LO line of unannealed LT GaAs is shifted from that of GaAs by ~1 cm^{-1} (Stokes shift of 291 cm^{-1}). A number of recent articles have proposed associating the observed red shift and broadening of the LO phonon line with a correlation length of phonons in the crystal [157],[159],[160]. This theory was originally developed to interpret the RS results for polycrystalline silicon [164]; however, this approach has also been widely applied to ion-implanted GaAs [159],[160]. Although no TEM results were presented for these ion-implanted GaAs samples, the phonon correlation length was associated with the size of crystalline domains [159],[160]. The theories predict a coherence length, and hence crystallite size, of ~100 Å for an LO phonon shift of 1 cm^{-1} [160]. Since we know from our TEM measurements that as-grown 200°C LT GaAs is single crystal, this theory

is not appropriate for the interpretation of the LO shift in LT GaAs. Perhaps the LO phonon shift arises from stress in the unannealed LT GaAs epilayer [158].

In addition to the prominent LO and TO phonon lines of Figs. 5.23 and 5.24, a number of weaker and broader lines are also evident at frequencies between the optical phonons and the laser line (Stokes shift of 0 cm^{-1}). Distinct peaks at 47, 75, 185, 200, and 258 cm^{-1} are clearly visible in the spectra of Fig. 5.23 and are labeled. These peaks are not present in RS from perfect GaAs (001) crystals and are therefore associated with imperfections in the crystal, such as point defects, clusters of defects, or dislocations [134],[152]-[163].

In contrast to as-grown LT GaAs, LT GaAs annealed at 600°C exhibits only a single peak between the optical phonons and the laser line at an energy of 223 cm^{-1}, as shown in Fig. 5.24. Although we have examined numerous different scattering geometries for RS from annealed LT GaAs, the mode at 223 cm^{-1} is the only one detectable by our equipment after the 600°C anneal. To document the annealing properties of the defect-related modes of LT GaAs, we have also investigated an LT GaAs sample grown at 200°C and annealed *in situ* at 300°C. This sample is part of the MBE-annealing experiment. The results for this sample are essentially identical to the results for the as-grown LT GaAs sample shown in Fig. 5.23. Thus, we can conclude that, with the exception of the 223-cm^{-1} mode, the defect-related modes of as-grown LT GaAs anneal at temperatures between 300 and 600°C. This result is consistent with the structural rearrangement taking place in the LT GaAs lattice between ~300 and 400°C as observed by x-ray diffraction and ion-channeling studies (see Sec. 5.3).

In the remainder of this section, the localized modes observed in the spectra of as-grown LT GaAs are discussed. The modes observed at 75 and 185 cm^{-1} are described first, followed by the 200- and 258-cm^{-1} modes, the 223-cm^{-1} mode, and

the 47-cm^{-1} mode. The symmetry of the mode and the dependence of the mode observability on laser energy are noted. All of these modes have been seen previously for other types of GaAs crystals, which, with the exception of the 47-cm^{-1} mode, assists in our tentative identification of the defect(s) associated with the mode. The reasons for associating a particular mode with a specific defect are discussed in detail.

We have observed the modes at 75 and 185 cm^{-1} in unannealed LT GaAs epilayers using both the 647-nm and the 829-nm excitations [see Figs. 5.23(a), (b), and (c)], but we have not seen these modes with the 514.5-nm excitation [see Fig. 5.23(e)]. This result suggests a resonant enhancement associated with these peaks. Both peaks are observed to be broad and exhibit Γ_1 symmetry. Peaks at 75 and 185 cm^{-1} have been widely reported in the RS literature for both damaged (e.g., by neutron, electron, or ion bombardment) and amorphous GaAs [157]-[162].

For first-order Raman scattering from a perfect crystal, only scattering by LO and TO phonons essentially at the Brillouin zone center (Γ-point) is allowed by the requirement of energy and momentum conservation [130] since the photon wave vectors are negligibly small in comparison with the size of the Brillouin zone. As defects are introduced into the crystal, however, the momentum conservation requirement breaks down, and Raman scattering can arise not only from zone-center optical phonons, but from phonons distributed throughout the Brillouin zone [161],[162],[165]. First-order Raman scattering from these non-zone-center phonons is observed in the Raman spectra at frequencies less than the zone-center optical phonons, and mimics the one-phonon density of states. Figure 5.26(a) shows the phonon dispersion relation for GaAs as determined by measurements of inelastic neutron scattering, and Fig. 5.26(b) shows the phonon density of states for GaAs as a function of frequency [166]-[168]. Specific peaks in the phonon density of states

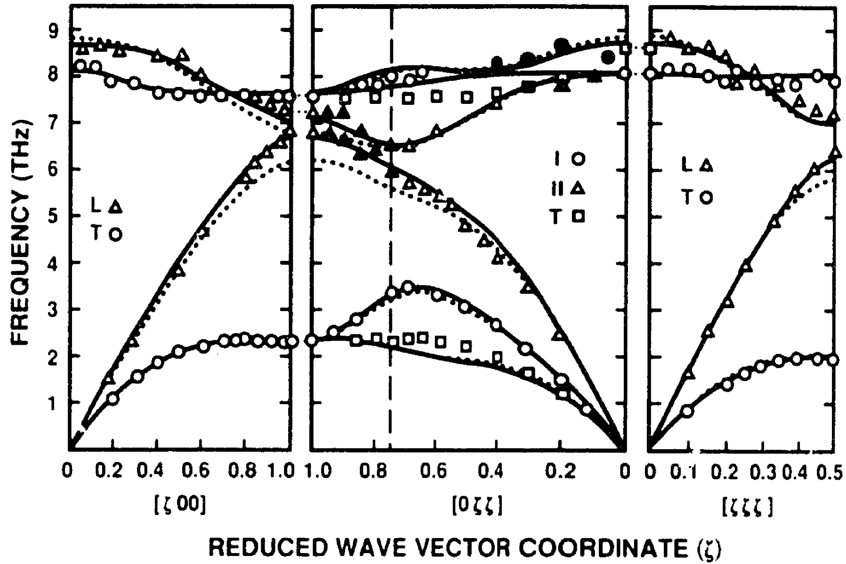

(a)

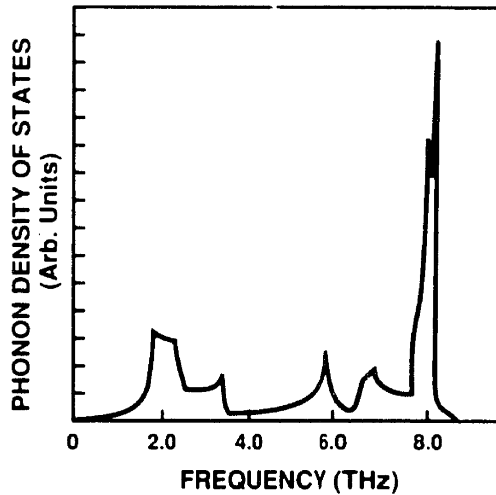

(b)

Fig. 5.26 (a) Dispersion curves for GaAs based on neutron scattering measurements at 296 K. The solid points denote undetermined polarization. The vertical dashed line in the [0ζζ] direction represents the zone boundary. In this direction, points labeled I, II refer to modes whose polarization vectors are parallel to the (011) mirror plane. Other modes are either strictly longitudinal (L) or transverse (T). The dotted and solid curves represent calculations based on two modifications, B and C, of the dipole approximation model. After Waugh and Dolling [166]. (b) Phonon density of states of GaAs calculated form the phonon dispersion curves. After Dolling and Cowley [167].

correspond to specific branches of the phonon dispersion curve [157],[158]. For instance, the peak at 2 THz arises from TA phonon modes at the L and X points in the Brillouin zone, and the peak at 5.6 THz arises from IIA phonons near the K point of the Brillouin zone [157],[158],[160],[161]. It is scattering by these phonons that give rise to the peaks at 75 and 185 cm^{-1} in Fig. 5.23. Peaks in the RS spectra associated with these normally forbidden scattering events are commonly called disorder-activated first-order Raman scattering (DAFORS). That the LT GaAs peaks at 75 and 185 cm^{-1} arise from DAFORS is further substantiated by the observed Γ_1 symmetry, since DAFORS peaks are known to evidence Γ_1 symmetry [154]. The absence of DAFORS peaks in 600°C-annealed LT GaAs is a further indication that 600°C-annealed LT GaAs epilayers are of high crystalline quality.

In contrast to the DAFORS peaks, we have only observed the modes at 200 and 258 cm^{-1} in unannealed LT GaAs using the IR dye laser excitation [see Figs. 5.23(a), (b), and (c)]. Although not clearly evident from Fig. 5.23, we have found from numerous other measurements that the scattering at 200 cm^{-1} is approximately six times stronger than the scattering at 258 cm^{-1}. Further, we have found that the 200–cm^{-1} mode largely exhibits Γ_{15} symmetry, while the 258–cm^{-1} mode exhibits nearly Γ_1 symmetry.

The frequencies of these two modes correspond almost exactly to the frequencies of the optical phonons in crystalline arsenic [168],[169]. The phonon dispersion curves and density of states of crystalline arsenic (rhombohedral, $\overline{3}$m point group) are shown in Fig. 5.27 [168],[169]. Also, the observed symmetry properties of the modes at 200 and 258 cm^{-1} in LT GaAs are what is expected for randomly oriented As microcrystals in a GaAs crystal [170]. Although we have never observed As precipitates in as-grown 200°C LT GaAs by TEM (see Sec. 5.3.1), the presence of As clusters is certainly consistent with the arsenic-rich deviation from stoichiometry

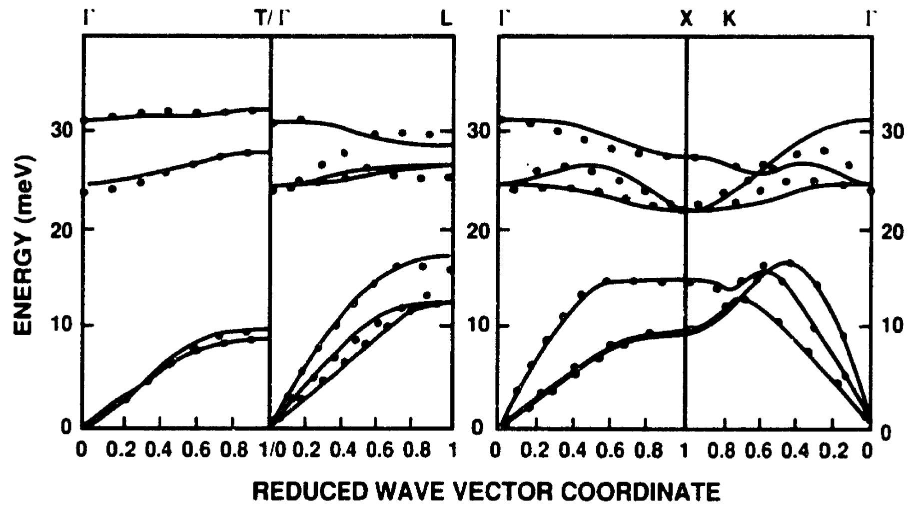

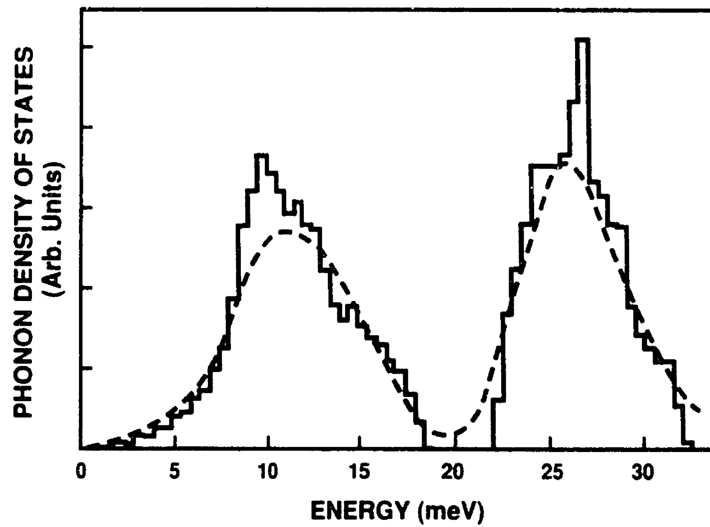

Fig. 5.27 (a) Phonon dispersion curves of crystalline arsenic (rhombohedral, $\bar{3}$m point group) at 297 K. The solid points are from neutron scattering measurements. The smooth curves are the results of a fit to the experimental data using a Born-von Karman model. (b) Phonon density of states of crystalline arsenic. The dotted curve was determined by neutron scattering from a polycrystalline As sample, and the solid curve was calculated from the dispersion curves shown in (a). After Reichardt and Rieder [169].

observed by AES. Further, since RS samples a relatively large volume of material (~1-mm spot size, ~500-nm penetration depth) as compared with TEM, it is possible that RS is more sensitive to small concentrations of As clusters than is TEM.

Our speculation that these modes, 200 and 258 cm^{-1}, arise from microcrystallites of As is further supported by two other observations. First, the factor of six difference in the intensity of the two peaks can be qualitatively explained by size considerations of the As precipitates. For bulk crystals of As, the two optical phonon peaks are expected to be of roughly equal intensity [149]. However, if the As crystals are no more than a few lattice constants in size, the momentum conservation rule breaks down (see DAFORS discussion), and phonons throughout the Brillouin zone can contribute to RS. In a simple one-dimensional model, assuming a crystallite size of L, the scattering probability for non-zone-center phonons is weighted by a factor of the form $[\sin(kL/2)/(kL/2)]^2$, where k is the phonon wave vector. As the crystallite size is reduced, scattering from phonons with larger wave vectors becomes possible [160],[164],[165], in accord with the above weighting factor. Since the optical phonon branches in crystalline As near $k = 0$ are dispersive [see Fig. 5.27(a)], scattering from non-zone-center phonons leads to a broadening of the linewidth and a reduction in the peak intensity of the optical phonon RS spectra [160],[164]. Thus, because the dispersion for the two optical phonon branches in crystalline As is different (see Fig. 5.27), it is not unreasonable that the scattering at 258 cm^{-1} is attenuated relative to that at 200 cm^{-1}.

The second support for our identification of As microcrystallites as responsible for the 200- and 258-cm^{-1} modes is given by the work of Farrow et al. [156]. Farrow et al. observed these same two peaks for Raman scattering from GaAs that was oxidized in pure oxygen at 450°C [156]. Since it is well known that during oxidation Ga is consumed from the GaAs surface to form the Ga-based oxide, they

hypothesized that As microcrystallites are formed at the interface between the Ga-based oxide and the GaAs substrate [156]. Farrow et al. reported that the linewidths and relative intensities of the 200–cm^{-1} and 258–cm^{-1} peaks were comparable [156]. Further, the symmetries they observed for the 200- and 258-cm^{-1} modes are the same as our results, and are consistent with the known symmetry of the optical phonons of crystalline As. Unfortunately, Farrow et al. do not present any TEM results on their samples.

In principle, by using the $[\sin(kL/2)/(kL/2)]^2$ discussed above and the arsenic phonon dispersion curves of Fig. 5.27(a), we should be able to estimate the size of the microcrystallites of As in as-grown LT GaAs. However, since these peaks are weak, such analysis will require more careful measurements.

The measurements of LT GaAs annealed at 600°C (see Fig. 5.24) indicate that these As microcrystallites disperse during the anneal. The disappearance of the As microcrystallites after annealing may be consistent with the results of x-ray diffraction, if we assume that the As microprecipitates contribute to the dilation of the as-grown LT GaAs lattice. More work needs to be done to reconcile this evidence for As microprecipitates with the TEM results of Sec. 5.3.1.

The 223-cm^{-1} mode in unannealed LT GaAs is observed using only the IR dye laser and exhibits Γ_1 symmetry [see Figs. 5.23(a) and (b) and Fig. 5.24]. The peak is fairly narrow (FWHM of 11 cm^{-1}) for a localized mode, indicating that it is associated with a specific point defect [134],[149]. Scattering from localized modes of point defects is known to be characterized by a narrow line shape and resonant enhancement [134]. We tentatively identify this mode as due to As_i based upon its similarity to a mode observed in electron-irradiated GaAs [134],[152]-[155], as is discussed below. That this mode is still observed in annealed LT GaAs, albeit with a reduced intensity relative to the LO line, indicates that As_i is present in the LT GaAs

buffer layer.

In electron-irradiated GaAs, a mode that exhibits Γ_1 symmetry and produces a narrow (FWHM of 7 cm^{-1}) peak at 227 cm^{-1} showing strong resonant enhancement has been extensively investigated by Berg et al. [134],[152]-[155]. They showed that the 227–cm^{-1} mode arises from an intrinsic point defect associated with the displacement of an atom on the As sublattice [155]. This is consistent with the generally accepted theory that the primary defects in electron-irradiated GaAs are dissociated As_i–V_{As} pairs [92]. The gallium interstitial (Ga_i) and V_{Ga} defects are thought to recombine in electron-irradiated GaAs at temperatures less than 300 K and, hence, would not be observed in room-temperature RS measurements [92]. Also, the theoretical calculation of Scheffler and Scherz indicate that the frequency of the Γ_1 breathing mode of V_{As} is considerably lower (<100 cm^{-1}) than 227 cm^{-1} [171]. Thus, based on the absence of the Ga-related defects in electron-irradiated GaAs, and the low expected frequency for V_{As}, Berg et al. concluded that their 227-cm^{-1} mode was due to As_i.

We believe that the Γ_1 mode at 223 cm^{-1} in as-grown LT GaAs is the same as the Γ_1 mode at 227 cm^{-1} in electron-irradiated GaAs. The observed symmetry and resonance enhancement of the two peaks is the same. Furthermore, the 4-cm^{-1} difference in peak position and the 4-cm^{-1} difference in FWHM of the peaks can be accounted for by the different temperatures used for the two measurements; the LT GaAs and electron-irradiated GaAs RS measurements were made at 300 and 100 K, respectively. Such a frequency shift is typical as the sample is cooled [149], and the broader lineshape at room temperature is consistent with shorter phonon lifetimes at higher temperatures [149].

The only significant difference between the electron-irradiated GaAs mode at 227-cm^{-1} mode and the LT GaAs mode at 223 cm^{-1} is the annealing temperature.

The 227-cm^{-1} mode in the electron-irradiated material anneals at a temperature of ~250°C [134], whereas the 223-cm^{-1} defect is still present in LT GaAs annealed at 600°C. However, since the defects in electron-irradiated GaAs are thought to be dissociated As_i-V_{As} pairs, a low annealing temperature is not unreasonable. In contrast, the point defects present in LT GaAs are As_{Ga} (see Sec. 5.5), As_i, and V_{Ga} (see below), which, unlike an As_i–V_{As} pair, cannot disappear by simple recombination. Hence, a higher annealing temperature is expected for the 223–cm^{-1} mode in LT GaAs.

Further support for the identification of the 223-cm^{-1} defect as As_i is provided by the AES, PIXE, and ion-channeling measurements. Since LT GaAs is arsenic rich (see Sec. 5.2) the As_i defect is more likely to be present in our crystal than V_{As}. As noted in Sec. 5.3.3, ion-channeling measurements indicate the presence of large concentrations of interstitial defects in LT GaAs, and provide evidence for the presence of interstitial defects with tetrahedral symmetry. Lastly, since the 223-cm^{-1} peak is present in the annealed LT GaAs epilayer, and since this material still contains a 1 at.% excess of As, again As_i is a possible defect in this material. For the reasons discussed here we propose that the 223-cm^{-1} mode in LT GaAs is associated with the As_i point defect.

We have also observed a mode at 47 cm^{-1} in unannealed LT GaAs [see Figs. 5.23(a), (c), and (e)]. This mode is observed for all three excitation wavelengths (see Table 5.5) and evidences nearly Γ_{15} symmetry. A 47-cm^{-1} mode was observed for the first time in GaAs only recently [163]. Holtz et al. observed this mode in GaAs that had been implanted with either Be or Si and that was not annealed [163]. As is the case for our 47-cm^{-1} mode, their 47-cm^{-1} mode was pronounced for all wavelengths investigated; however, they determined the symmetry of their mode to be mixed Γ_1 and Γ_{15} [163]. Although the symmetry of our 47-cm^{-1} mode and Holtz

et al.'s 47-cm^{-1} mode is different, this does not necessarily imply that the modes arise from different defects. Since high-dose ion implantations ($> 5\times10^{13}$ cm^{-2}) are known to produce considerable damage to the GaAs lattice [157]-[160], it is possible that this damage leads to a breakdown in the selection rules of the defect, resulting in their observed mixed symmetry. Holtz et al. attribute their 47-cm^{-1} mode to GaAs acoustical vibration modes occurring in the interfacial regions between GaAs microcrystals [163]. However, they present no TEM data to support their assertion of GaAs microcrystals. Since 200°C-grown LT GaAs is known to be crystalline (see Sec 5.3), it is unlikely that Holtz et al.'s explanation is the correct interpretation of our 47-cm^{-1} mode.

Another possible explanation for the 47-cm^{-1} mode is that it is associated with DAFORS from the As microcrystals discussed above. This assignment is not likely for two reasons. First, the crystalline arsenic density of states is small at 47 cm^{-1} [see Fig. 5.27(b)], and, second, DAFORS peaks typically evidence Γ_1 not Γ_{15} symmetry [149],[154]. Thus, the observed Γ_{15} symmetry of our 47-cm^{-1} mode suggests that this mode is due to a point defect rather than a cluster of defects.

Since a 47-cm^{-1} mode was not observed in electron-irradiated GaAs [134],[152]-[155], where the point defects are known to be associated with the As sublattice, we speculate that the defect responsible for this mode is associated with the Ga sublattice. Possible point defects include As_{Ga}, the gallium-antisite defect (Ga_{As}), V_{Ga}, and Ga_i. Theoretical calculations indicate that the vibrational frequencies of the antisite defects are greater than ~200 cm^{-1} [171]. Also, we rule out the Ga_i defect since LT GaAs is arsenic rich, and, hence, extra Ga atoms in the lattice seem unlikely.

Thus, by a process of elimination, we speculate that the 47-cm^{-1} mode in LT GaAs is associated with V_{Ga}. This point defect is consistent both with the

stoichiometry of the crystal and the small "spring constants" required to yield a low vibrational frequency. The presence of V_{Ga} in unannealed LT GaAs epilayers has also been inferred recently from thermally stimulated photo-EPR experiments [17]. Although not providing direct evidence for V_{Ga} in LT GaAs, the PL peak at 1.18 eV in Si-doped GaAs layers on LT GaAs was attributed to V_{Ga}–Si_{Ga} pairs (see Sec. 5.4.1). It is possible that excess arsenic and/or V_{Ga} present in the LT GaAs layer diffuse into the Si-doped GaAs epilayer during growth at 580°C. Further, the creation of V_{Ga} by ion implantation is possible, and thus, our assignment may be consistent with the experimental results of Holtz et al. [163]. Why other researchers who have studied ion-implantation-damaged GaAs have not observed a 47-cm^{-1} mode is not known.

In conclusion, Raman scattering has been shown to provide considerable information on the crystal structure of LT GaAs. Both annealed and unannealed LT GaAs are of high crystal quality, as evidenced by the optical phonon modes. Specific peaks in the RS spectrum of unannealed LT GaAs grown at 200°C have been attributed to scattering from localized vibrational modes associated with clusters of defects (As microcrystals) and point defects (As_i and V_{Ga}) as well as from DAFORS. Although the identification of the localized modes presented here has not been proved, the assignments are consistent with the known experimental data [152]-[169] and existing theoretical calculations [171]. In contast to unannealed LT GaAs, only one localized mode, attributed to As_i, was observed in 200°C-grown LT GaAs that was annealed *in situ* at 600°C for 10 min.

For completeness, several additional points about RS should be noted. First, we cannot rule out the presence of point defects other than those previously identified in LT GaAs. If the frequency of a localized mode from a point defect overlaps with stronger modes (for instance a DAFORS peak), the weak localized mode will be

obscured. Also, if the coupling of incident light to a localized vibration is weak, this mode may not manifest itself in the Raman spectra. Effects such as stray light and allowed two-phonon scattering can also obscure the weak signals associated with localized modes. It is for this reason that we have used three different wavelengths of incident light in our measurements in the hope of achieving resonant-enhancement of weak Raman signals.

A second important point to note is that the frequency of a localized mode can depend on the charge state of the defect [149]. Thus, if the charge state of the defect is different in different samples of GaAs, the mode may appear in the Raman spectrum of one material and not in the Raman spectrum of the other. Thus, although we have observed only the 223-cm^{-1} mode in 600°C-annealed LT GaAs, we cannot rule out the presence of other point defects, such as As_{Ga} or V_{Ga}, in this material. Similarly, although we know that As_{Ga}^{+} is present in unannealed 200°C LT GaAs by EPR measurements (see Sec. 5.5.1), we have not identified any modes in the spectra of Figs. 5.23 or 5.24 as arising from this defect.

Lastly, it should be noted that the penetration depth of the light used in this study restricted our measurements to only the upper ~0.5 μm of the epilayers. If the density of the point defects in LT GaAs varies as a function of film thickness, we would not be able to detect such variations with this set of experiments.

5.5 Electrical

This section summarizes the results of EPR and temperature-dependent Hall-effect measurements of LT GaAs. These experiments provide additional insight into both the microscopic and macroscopic properties of LT GaAs. EPR has been used to identify As_{Ga}^{+} in unannealed LT GaAs epilayers grown at $T_s \leq$ 200°C. From temperature-dependent Hall-effect measurements of LT GaAs, we find that the

conductivity of the as-grown and annealed material is consistent with a hopping mechanism. As LT GaAs is annealed, the film becomes increasingly resistive, until its resistivity exceeds our ability to measure at room temperature.

5.5.1 EPR

EPR has been used to identify the point defect As_{Ga}^{+} in LT GaAs grown at temperatures less than or equal to 200°C and unannealed [16]. However, LT GaAs grown at higher temperatures or annealed at higher temperatures does not exhibit the characteristic As_{Ga}^{+} EPR spectra. The EPR results presented in this section were measured using a commercial X-band EPR spectrometer [16].

In the technique of EPR, defects with unpaired spins can be detected by measuring the microwave absorption of the sample in a magnetic field. In a magnetic field, the degenerate states of the unpaired electrons are split by the well-known Zeeman and hyperfine interaction effects [95],[172]. The number and spacing of the energy levels is governed by a spin Hamiltonian, which in general is a complicated tensor expression [172]. By observing the absorption at a fixed microwave frequency as a function of the magnitude and orientation of the magnetic field, onc can determine the parameters in the spin Hamiltonian and can frequently identify the defect responsible for the EPR spectra [94],[95],[172],[173]. For the As_{Ga}^{+} defect, which has T_d point-group symmetry and one unpaired electron (see below), the spin Hamiltonian is of the form

$$H = g\mu_B \mathbf{H}\cdot\mathbf{S} + A\mathbf{I}\cdot\mathbf{S} \qquad (5.3)$$

where the first term is the Zeeman effect and the second term is the hyperfine interaction, and where g is the Lande g-factor, μ_B is the Bohr magnetron, **H** is the magnetic field, **S** is the electronic spin, **I** is the nuclear spin, and A is the hyperfine

interaction parameter [95].

A simple schematic illustration of the EPR system, the Zeeman effect of a S=1/2 defect, and the measured signal for an S=1/2 defect are shown in Fig. 5.28(a), (b), and (c), respectively [172]. A klystron is used to generate the microwave signal. A microwave frequency of 9.4 GHz is used for all the measurements discussed in this section. An isolater is used to prevent back microwave reflections from the sample into the source. The sample under test is placed in a microwave cavity with a high Q and is cooled to cyrogenic temperatures (~10 K). A frequency of 100 kHz is typically used to modulate the applied H field, thereby making possible the use of lock-in detection schemes to enhance sensitivity. The dewar has optical ports to permit the study of the EPR signal from the defect as a function of illumination (so-called photo-EPR).

In the EPR measurement, the microwave frequency of the klystron is held constant as the magnetic field is increased from 0 to ~15 kG. For most values of magnetic field the detector senses no change in the microwave signal because there is no absorption by the sample. However, when the Zeeman and hyperfine splitting of the degenerate electronic spin energy levels corresponds to the energy of the microwaves, the sample becomes absorbing and the detector senses a decrease in the microwave signal.

An example of the Zeeman splitting for an S=1/2 unpaired electron is shown in Fig 5.28(b), and the corresponding EPR signal is shown in Fig. 5.28(c) [172]. In both figures the abscissa is magnetic field strength. In Fig. 5.28(b), the degenerate S=1/2 energy level is split into two levels by the applied magnetic field. The energy of one level increases as $g\mu_B H/2$, while the energy of the other level decreases as $-g\mu_B H/2$ [174]. At one value of H, the energy difference $g\mu_B H$ between the two levels equals $h\nu$, where ν is the frequency of the microwave signal from the klystron.

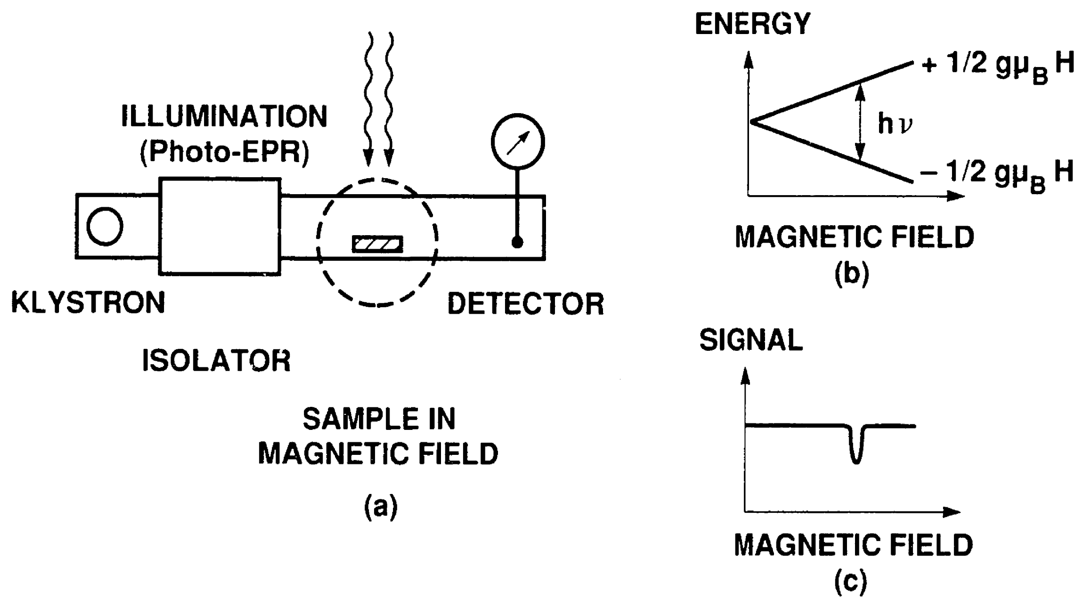

Fig. 5.28 (a) Schematic illustration of EPR experimental configuration, (b) Zeeman effect for S=1/2 defect, and (c) EPR absorption spectrum for S=1/2 defect. After Weber [172].

The microwave signal induces a transition between the lower occupied energy state and the higher unoccupied state. The transition results in an absorption of the microwave signal, and, hence, a plot of detected microwave signal versus applied magnetic field shows a dip, as is seen in Fig. 5.28(c).

The magnitude of the observed microwave absorption depends on both the density of the paramagnetic center in the sample and the spin-lattice relaxation time [172]. The spin-lattice relaxation time governs the rate at which the excited electrons relax back to the ground state. If the spin-lattice relaxation time is long, the population of the Zeeman levels becomes equal at resonance, leading in turn to a saturation of the microwave absorption. The magnitude of the spin-lattice relaxation time can provide information on the crystal quality of the sample, as will be discussed below.

The structures of numerous defects in semiconductors have been identified by their characteristic EPR spectra. Some defects that have been identified include substitutional P in Si, P_{Ga} in GaP, and As_{Ga} in GaAs [172]. As discussed in Sec. 5.1, an As atom on a Ga lattice site has five valence electrons, while only three are needed for covalent bonding. When the two extra electrons reside on As_{Ga}, this defect is not EPR active because the spins are paired. Similarly, when both electrons have been removed from the As_{Ga} site, the defect is again not EPR active. However, if only one electron has been removed, creating As_{Ga}^{+}, the lone spin is unpaired and can be detected by EPR, as discussed qualitatively below.

The idealized EPR spectra observed for the Zeeman splitting for an S=1/2 electron was shown schematically in Fig. 5.28(c). The EPR spectra for the As_{Ga}^{+} defect is more complex, because both Zeeman and hyperfine splitting must be considered. The unpaired electron on As_{Ga}^{+} is in a S=1/2 state and the ^{75}As nucleus has a spin I=3/2 [95],[172]. The hyperfine interaction splits the S=1/2 level into two hyperfine levels characterized by total angular momentum F = 2 and F = 1, where the allowed values

of F are given by I+S and $|I-S|$ (note L=0) [174],[175]. The F = 2 level is 5-fold degenerate (magnetic quantum number m_F = -2, -1, 0, 1, 2) and the F = 1 level is 3-fold degenerate (m_F = -1, 0, 1) in the absence of a magnetic field [175]. When a magnetic field is applied, the degeneracy is lifted by the Zeeman effect and eight distinct energy levels are formed, each of which corresponds to a well-defined value of the quantum number m_F [175].

These eight energy levels can be calculated for As_{Ga}^+ in GaAs from first principles, and the energy of these levels as a function of magnetic field strength is shown in Fig. 5.29 [95]. The calculation of Fig. 5.29 used g = 2.04 and A = 0.89 cm^{-1} [95]. As expected from the previous discussion, for H=0 only two energy levels are shown, corresponding to F=1 and F=2. As H is increased, the degeneracy is lifted and eight energy levels result. The splitting of these levels increases as the magnitude of the H-field is increased. The transitions shown with arrows in the figure are the observed transitions of energy equal to $h\nu$, where in the calculation ν was assumed to be 9.73 GHz [95]. Although a microwave frequency of 9.4 GHz was used the measurements discussed here, the magnetic field strength of the four transitions is only slightly shifted from the values shown in the figure.

As can be seen from Fig. 5.29, the EPR spectrum of As_{Ga}^+ should evidence four absorption peaks at magnetic fields of approximately 1.8, 2.5, 3.3, and 4.8 kG. The four-peaked EPR spectrum of As_{Ga}^+ is also expected to be isotropic (i.e., independent of orientation of the magnetic field) because the environment around the As_{Ga}^+ defect is tetrahedrally symmetric. The four nearest neighbors are As ligands tetrahedrally bonded to the As_{Ga}^+ defect. Although superhyperfine interactions between the unpaired spin and the nearest-neighbor nuclei are observed for some defects (e.g., P_{Ga} in GaP [172]), no superhyperfine structure is observed for As_{Ga}^+ because the interaction is too weak [94],[95],[172],[173]. An example of an As_{Ga}^+ EPR spectrum

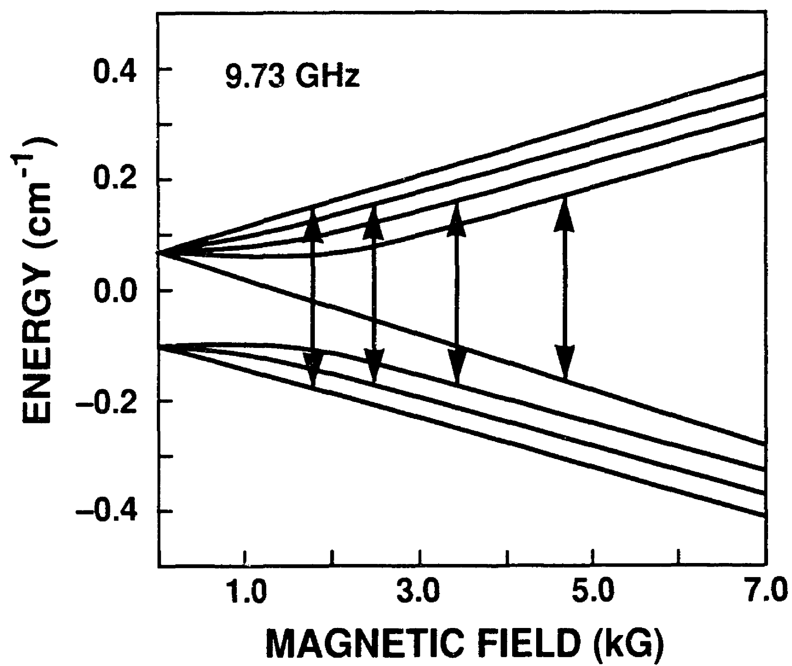

Fig. 5.29 Analytical calculation of the energy level splitting of the As_{Ga}^{+} defect in GaAs as a function of magnetic field strength. The vertical arrows represent observed transitions of energy equal to hν, where ν = 9.73 GHz. After Worner et al. [95].

is shown in Fig. 5.30. In this figure the derivative of the EPR absorption spectrum in arbitrary units is plotted versus the applied magnetic field. The derivative is plotted because the absorption peaks are weak, and, hence, are not easily distinguished.

EPR studies have been performed on numerous LT GaAs samples, including those listed in Table 5.2. For this discussion of LT GaAs, we address the samples of Table 5.2 together with a reference sample of LEC SI GaAs substrate. The reference sample showed the well-known EPR quadruplet signal that has been attributed to As_{Ga}^{+} [94],[173]. The characteristic feature of these defects in as-grown LEC SI GaAs, namely, metastability under illumination and consequent quenching of the EPR signal [98], was also observed (see Sec. 5.1). The same EPR signal, exhibiting illumination quenching, was seen in all samples except 3-1593. Since the intensity of this metastable signal scaled with the amount of bulk LEC GaAs substrate, it can be attributed to the substrate.

Sample 3-1593 also showed an EPR quadruplet signal, but with different properties. Its spectrum was precisely the same as that of the As_{Ga}^{+} defect in the substrate, i.e., four lines characterized by $g = 2.04$ and $A = 0.09$ cm^{-1}. This result is shown in Fig. 5.31. However, the initial intensity of the signal was much higher than that estimated from the substrate thickness. Moreover, the signal was not quenched by illumination, but instead increased in intensity after illumination with white light, as will be discussed below (see Fig. 5.33). This behavior leads to the conclusion that the EPR signal observed for sample 3-1593 is due primarily to the GaAs epilayer. Based on the identical g-factor and A parameter, we believe that the observed defect in the 200°C unannealed LT GaAs layer is an As_{Ga}^{+}–related defect. However, since the As_{Ga}^{+} signal in LT GaAs is not metastable, it is clear that these defects in LT GaAs behave differently than those in LEC SI GaAs.

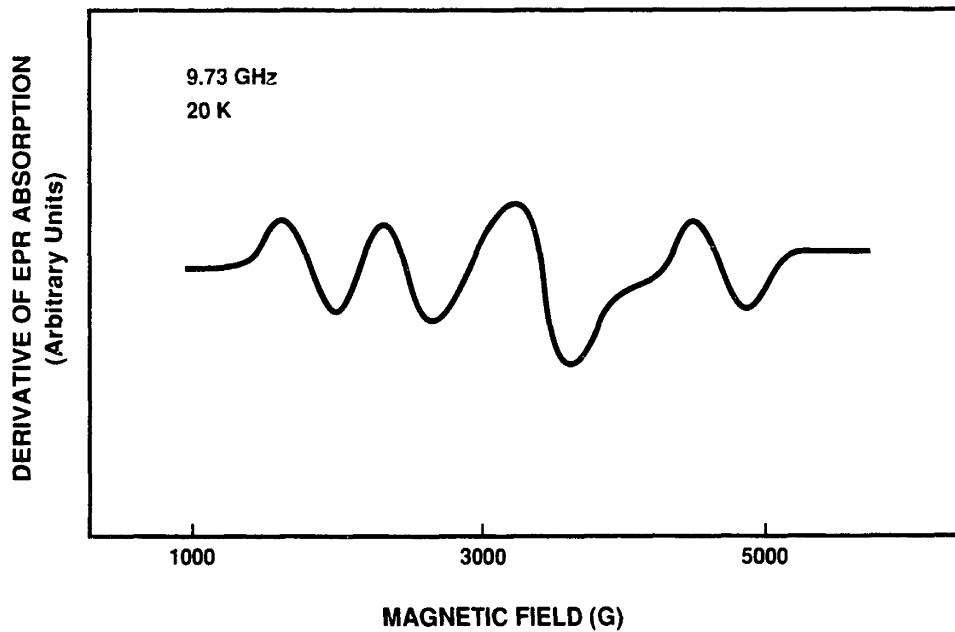

Fig. 5.30 Derivative of the EPR absorption spectrum of the As_{Ga}^{+} defect in neutron-irradiated GaAs at 20 K. After Worner et al. [95].

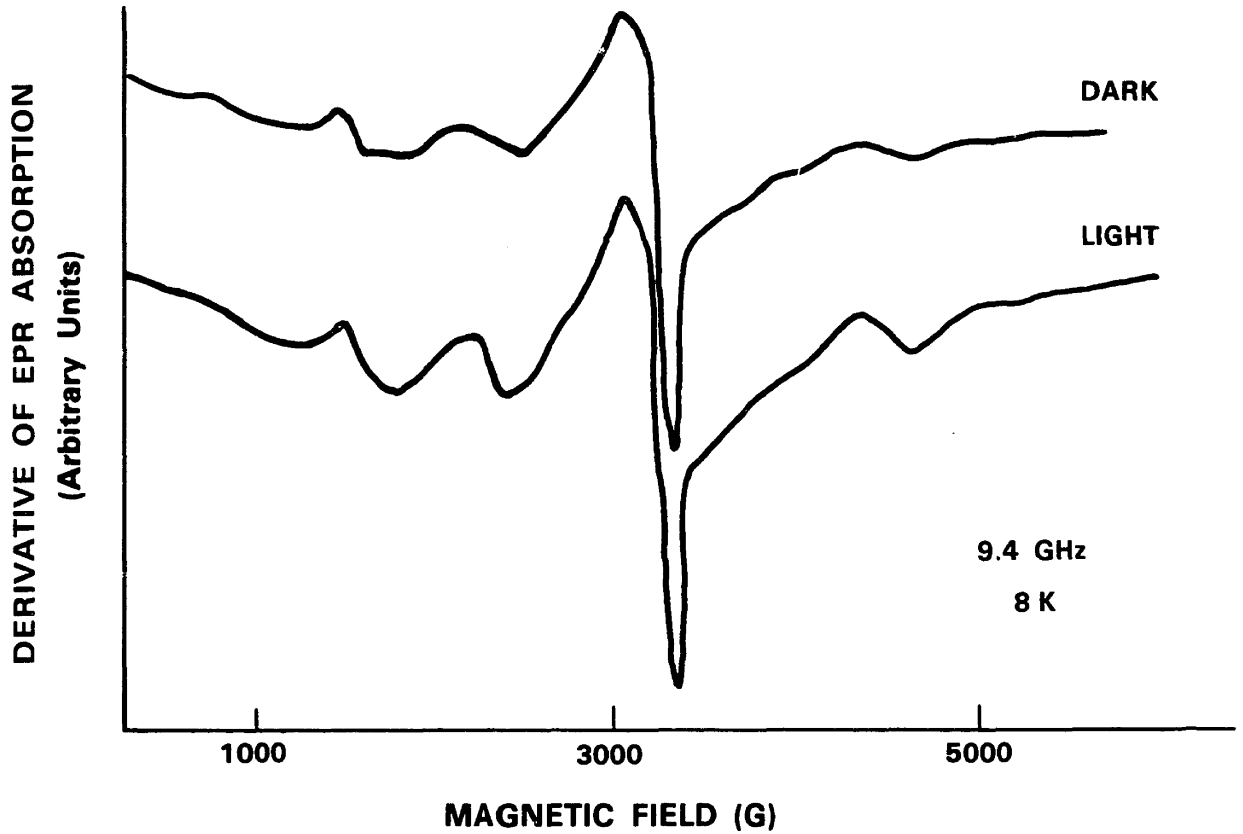

Fig. 5.31 Derivative of the EPR absorption spectrum of LT GaAs sample 3-1593 at 8 K (a) after cooling down in the dark, and (b) after subsequent illumination with white light. The third EPR antisite line is obscured by a quartz background line.

By comparing the intensity of the four EPR lines (integrated intensity of the absorption spectra) of the LT GaAs sample with the SI GaAs substrate, and knowing the As_{Ga}^{+} concentration in the SI GaAs substrate, we calculate the concentration of the As_{Ga}^{+}–related defect in the unannealed 200°C LT GaAs epilayer to be ~5×10^{18} cm^{-3}.

The EPR signal due to the As_{Ga}^{+}–related defects observed for the other samples of Table 5.2 could be entirely attributed to the substrate. Apparently the concentration of As_{Ga}^{+}–related defects in the layers annealed at 600°C or grown at 270°C is below the EPR detection limit of ~10^{18} cm^{-3} for epilayers of thickness between 2 and 4 µm.

As noted in Sec. 5.1, the EPR quadruplet signal has been observed before for as-grown bulk GaAs [173], and for bulk GaAs after plastic deformation [86] or electron [94] or neutron [95] irradiation. Our observation of the EPR quadruplet signal in LT GaAs was the first reported for an MBE-grown epilayer [16]. Furthermore, the concentration of $5\text{x}10^{18}$ cm^{-3} of As_{Ga}^{+}–related defects in LT GaAs is the highest concentration of such defects ever observed. In as-grown bulk GaAs, the typical concentration of these defects is 0.8 - 2 x 10^{16} cm^{-3} [173]; in plastically deformed GaAs it reaches 10^{17} cm^{-3} [86]; in electron-irradiated GaAs it reaches $8\text{x}10^{17}$ cm^{-3} [94]; and in neutron-irradiated GaAs it can reach $2\text{x}10^{18}$ cm^{-3} [95]. Such a high concentration of As_{Ga}^{+}–related defects in the unannealed LT GaAs layer is consistent with a strongly arsenic-rich deviation from stoichiometry.

A comparison of the EPR quadruplet parameters, the behavior of the signal under illumination, and the annealing temperature for removing the As_{Ga}^{+}–related defect are presented in Table 5.6 for different GaAs samples [86],[94]-[97],[173],[176],[178]-[183]. The saturation of the EPR signal with increasing microwave power for 200°C unannealed LT GaAs is similar to that of as-grown bulk

GaAs CRYSTAL	g-FACTOR	A (cm^{-1})	SPIN-LATTICE RELAXATION TIME (s)	BEHAVIOR UNDER ILLUMINATION	ANNEALING TEMPERATURE (°C)
AS-GROWN	2.04±0.01[a]	0.090±0.001[a]	SEVERAL[b]	QUENCHING[c]	850[d]
PLASTIC DEFORMATION	2.04±0.01[e]	0.090±0.001[e]	LOWER THAN FOR BULK[f]	NO QUENCHING[g]	450[d]
ELECTRON IRRADIATION	2.037±0.003[h]	0.0867±0.012[h]	$<5\times10^{-4}$; NO SATURATION[i]	NO QUENCHING[j]	
NEUTRON IRRADIATION	2.04[k]	0.09[k]	$<4\times10^{-6}$; NO SATURATION[i]	NO QUENCHING[l]	600[m]
LT GaAs (3-1593)	2.04	0.09	SATURATION	NO QUENCHING	<600

[a]Ref. 173; [b]Ref. 178: [c]Ref. 176; [d]Ref. 96; [e]Ref. 86; [f]Ref. 179; [g]Ref. 97; [h]Ref. 94; [i]Ref. 180; [j]Ref. 181; [k]Ref. 95; [l]Ref. 182; [m]Ref. 183

Table 5.6 Comparison of EPR parameters of As_{Ga}-related defects in different GaAs samples: g-factor, hyperfine interaction constant A, spin-lattice relaxation time τ, behavior under illumination, and approximate annealling temperature of the As_{Ga}^{+}–spectrum.

GaAs. Since the EPR signal does not saturate for irradiated GaAs, it appears that damage-induced defects shorten the spin-lattice relaxation time. Thus, the observed saturation demonstrates the high crystal quality of the LT GaAs layer, consistent with the small number of dislocations observed by TEM.

The absence of EPR signals in LT GaAs epilayers grown at higher temperatures or annealed shows that most of the As_{Ga}^{+}–related defects in LT GaAs are less thermally stable than similar defects in as-grown bulk GaAs. To determine the annealing temperature at which the As_{Ga}^{+} signal falls below detectable levels, we investigated the samples of the furnace-annealing and the MBE-annealing experiments. The results of the furnace-annealing experiment are shown in Fig. 5.32. For both sets of samples, the measured concentration of As_{Ga}^{+}–related defects drops below detectable levels for an annealing temperature of ~350°C. This temperature is roughly comparable to that observed in Sec. 5.3 for the relaxation of the LT GaAs lattice parameter to that of GaAs. Clearly the changes taking place in the LT GaAs lattice are responsible for the disappearance of the EPR signal of As_{Ga}^{+}–related defects.

This annealing temperature of ~350°C is similar to the temperatures reported for annealing some of the defects created by plastic deformation and neutron irradiation [96]. However, the annealing of As_{Ga}^{+}–related defects in plastically deformed GaAs showed a large fraction of these defects to be present after annealing up to 625°C [96]. Since the detection limit of EPR for As_{Ga}^{+}–related defects in thin epitaxial layers is near 10^{18} cm^{-3}, any antisite defects below this concentration level remain undetected. Thus, the absence of an EPR signal from the annealed LT GaAs epilayer does not necessarily imply that all of the As_{Ga}^{+}–related defects have been removed in the annealing procedure (see Sec. 5.6).

We have also investigated the EPR response of a number of films of LT GaAs grown at a variety of temperatures between 190 and 400°C. We do not observe the

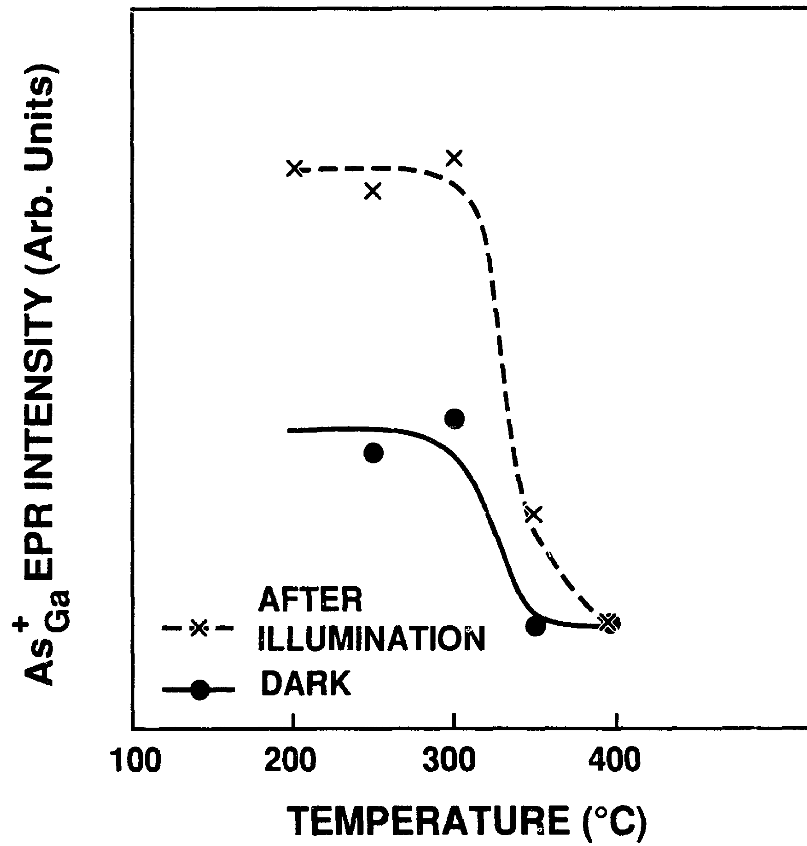

Fig. 5.32 Intensity of the EPR As^{+}_{Ga} signal in 200°C LT GaAs at 8 K before and after white light illumination, as a function of furnance annealing temperature.

As_{Ga}^{+}–related defect spectrum for LT GaAs samples grown at temperatures above 200°C. However, for LT GaAs samples grown at temperatures less than ~195°C, we always observe the As_{Ga}^{+}–related defect signal at an intensity corresponding to ~$5x10^{18}$ cm^{-3}. The observation of the As_{Ga}^{+} EPR signal is a sensitive function of T_s near 200°C. Reproducibility of MBE-grown GaAs epilayers is discussed in Sec. 5.7.

Figure 5.33 shows the EPR signal measured for an as-grown sample of 200°C LT GaAs as a function of the photon energy of the light incident on the sample. A lamp and monochrometer were used to apply the different wavelenghts of light on the LT GaAs sample. The wavelengths were sequentially scanned from low energy to high energy. The sample was illuminated for 30 min at each wavelength. This time was long enough such that the change in EPR intensity had stopped before the light was turned off. All EPR measurements were made at 8 K in the dark (after the monochromatic light was turned off). The EPR intensity is seen to increase as the photon energy increased from 0.5 to ~1.3 eV. However, for energies greater than ~1.3 eV the EPR intensity is observed to decrease slightly. The change in EPR intensity shown in Fig. 5.33 corresponds to approximately a doubling in the As_{Ga}^{+}–related defect concentration. Our calculations indicate that in the dark the As_{Ga}^{+}–related defect concentration is ~2.5×10^{18} cm^{-3}, whereas after illumination at ~1.3 eV it is ~5×10^{18} cm^{-3}, the value reported above.

The behavior shown in Fig. 5.33 is markedly different from that of Fig. 5.1 for plastically deformed material. Unlike the sharp steps in EPR intensity shown in Fig. 5.1, we observed only a slow change in the As_{Ga}^{+}–related defect concentration in as-grown LT GaAs as a function of the energy of illumination. Further, Fig. 5.33 shows a general increase of signal with photon energy, whereas Fig. 5.1 shows a general decrease. At the present time, we can not fully explain the results of Fig. 5.33; however, some speculations about this behavior will be made in Sec. 5.6, after

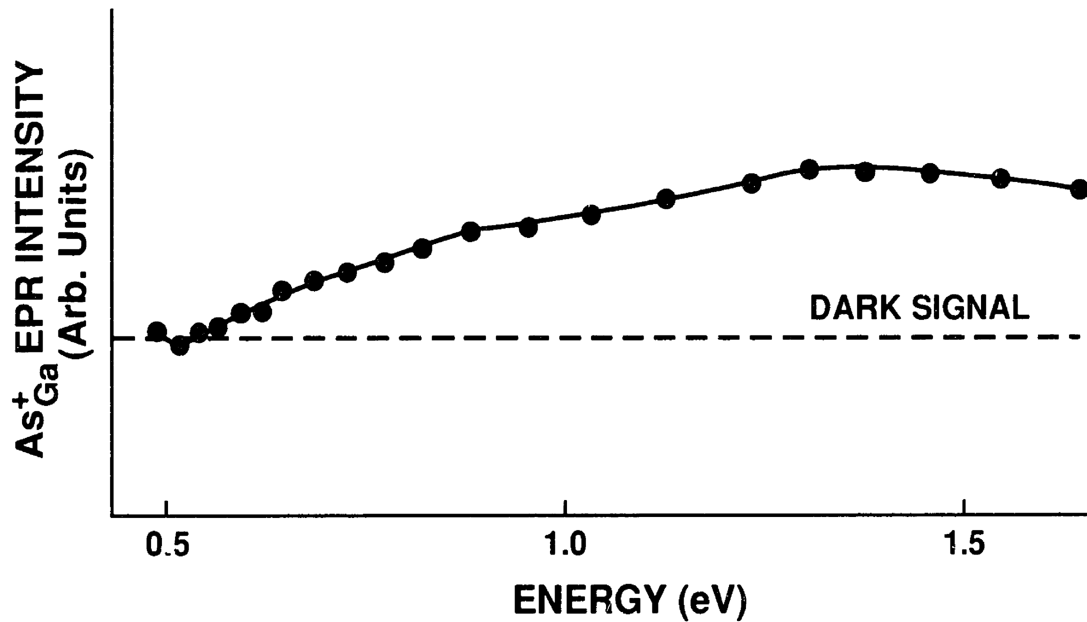

Fig. 5.33 Intensity of the EPR As^{+}_{Ga} signal in unannealed 200°C LT GaAs at 8 K as a function of the photon energy of the monochromatic illumination. The EPR signal level in the dark before illumination is shown by the dashed line.

all of the experimental results from the different characterization techniques have been summarized.

5.5.2 Electrical Conductivity

Temperature-dependent Hall-effect measurements of as-grown and annealed LT GaAs epilayers were made using a low-current setup [116]. The conductivity of these layers as a function of temperature are discussed first. After this, measurements of the sidegate current I_{sg} flowing from the isolated sidegate electrode to the source electrode of the MESFET discussed in Chapter 3 for a device with the LT GaAs buffer are presented. The sidegate current was measured as a function of V_{sg} and temperature using a picoammeter and shielded test configuration [184]. The results of both measurement techniques indicate that the conductivity of LT GaAs, as grown and annealed, follows a hopping mechanism for temperatures less than ~40°C.

5.5.2.1 Hall Effect

Hall-effect measurements were made on LT GaAs samples from the growth-temperature, MBE-annealing, and furnace-annealing experiments [116]. Since the results of the furnance-annealing and MBE-annealing experiments are similar, only the results of the MBE-annealing samples will be presented here. The measurements to be discussed were all made on large-area square samples (~0.5 by 0.5 cm) using the van der Pauw test configuration [185],[186]. Small, circular, metal contacts were evaporated onto the corners of the sample using a shadow-mask technique. The diameter of the dots was small (~0.1 mm) by comparison with the area of the sample. This test configuration satisfies the assumptions inherent in the van der Pauw analysis [185],[186], namely, that the contacts be widely separated and symmetrically distributed.

The contacts to the epilayers were unalloyed since we did not want to subject the LT GaAs epilayers to the high-temperature anneal required in the standard alloying procedure ($T_{alloy} \approx 400°C$). To investigate the influence of contact metallurgy on the results, we used three types of contacts, In, Ge/Au, and In/Au, on a number of as-grown and annealed LT GaAs epilayers. We found that the conductivity measured for these samples was independent of the contact metallurgy over the temperature range investigated. Further, for each of the contacts on the various samples, we measured the current between the contacts as a function of the applied voltage. In all cases, and over the temperature range of interest, we found that the currents were ohmic. This result confirms the findings of Sec. 4.5 and indicates that ohmic contacts are formed to LT GaAs for all the metallurgies that we investigated. Researchers at the Avionics Laboratory of the Wright-Patterson Air Force Base have also observed this same result [187]. Thus, the conductivity data presented in this section arise from the LT GaAs and are not influenced by the contacts.

All the data reported here were obtained by sensing the voltage in two of the contacts located diagonally opposite to each other, in response to a current of ~100 nA forced between the other two contacts. The conductivity results to be reported were found to be essentially insensitive to the current bias for currents between 1 and 1000 nA.

Figure 5.34 shows the conductivity σ as a function of reciprocal temperature for the samples of the growth-temperature experiment. We present data only for conductivity greater than 10^{-6} $(\Omega\text{-cm})^{-1}$ because this value is the limit of our measurement system. As can be seen, samples grown at temperatures less than ~300°C exhibit distinctly different behavior from samples grown at 300°C or above.

Samples grown at temperatures greater than or equal to 300°C show an activated conductivity with an activation energy E_A of ~0.75 eV. Simple single-

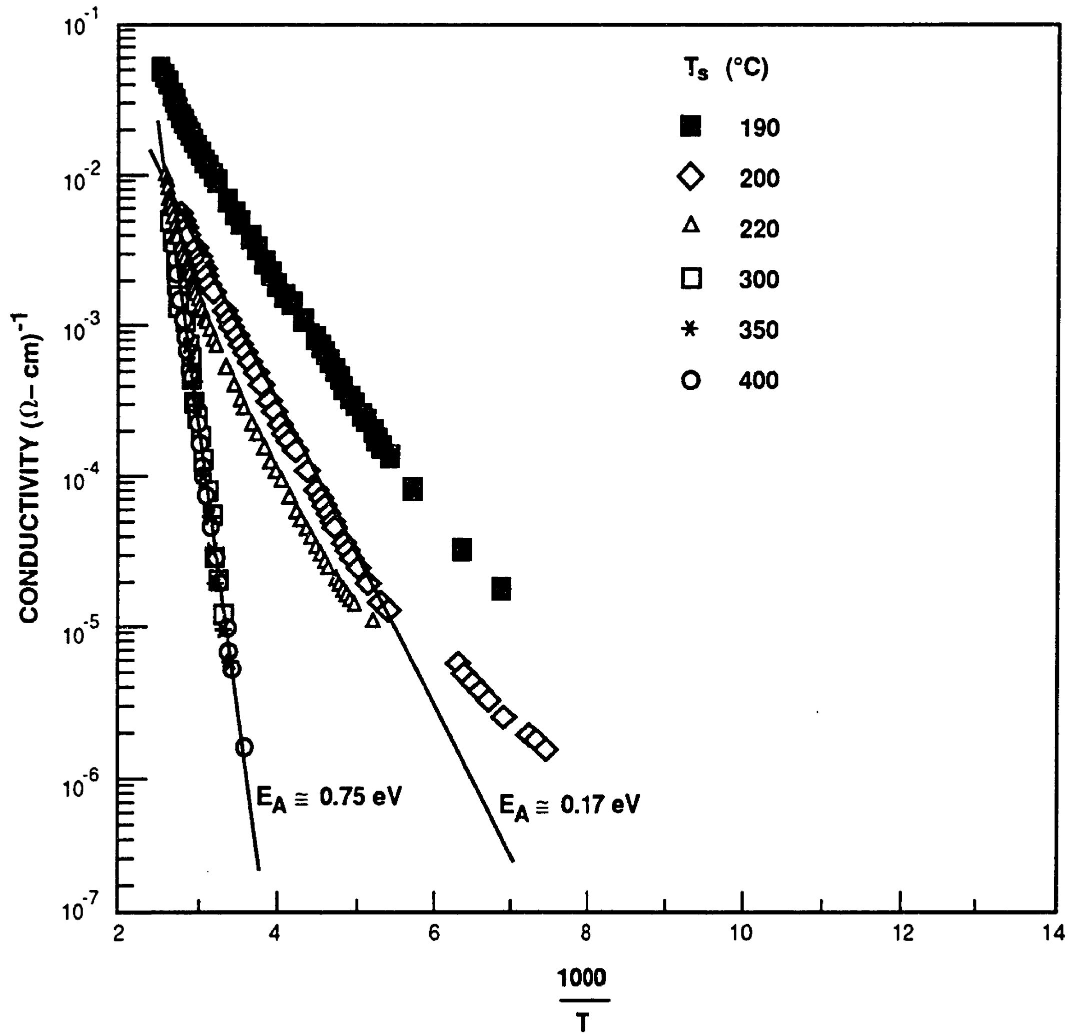

Fig. 5.34 Arrhenius plot of the conductivity of the LT GaAs growth-temperature-experiment samples. The lines are included only as a convenience in visualizing the data.

carrier analysis [186] of the Hall-effect data implies that the carriers are electrons with a mobility of ~1000 $cm^2/V \cdot s$ at room temperature. These results are indicative of a conduction mechanism arising from free electrons in the conduction band. As was discussed in Sec. 5.1, EL2 introduces a deep level at ~0.75 eV below the conduction band that is responsible for the semi-insulating property of SI GaAs. Thus, based upon the activation energy, mobility of carriers, similarity to SI GaAs, and the IR absorption evidence for EL2-like defects in LT GaAs, we hypothesize that the conductivity mechanism for LT GaAs grown at $T_s \geq 300°C$ can be described by electrons in the conduction band excited from EL2-like deep levels. Mathematically, this conductivity mechanism can be described by

$$\sigma = \sigma_0 \, e^{-\frac{E_c - E_f}{k_B T}} \tag{5.4}$$

where σ_0 is a prefactor and E_f is the Fermi energy [188],[189], which is pinned at the EL2-like defect near the middle of the energy gap.

We have also measured the conductivity of the SI GaAs substrates on which these layers were grown and find that the behavior of the conductivity of the substrate with temperature is identical to that observed in Fig. 5.34 for the LT GaAs samples grown at T_s greater than or equal to 300°C. Thus, it is possible that the conductivity measured above room temperature may comprise conduction in both the LT GaAs epilayer and the substrate. However, from the IR results of Sec. 5.4.2 and the EPR results of the previous section, we believe that Eq. (5.4) describes the LT GaAs conductivity in the region above room temperature. More work is needed to prove this assertion and to measure the LT GaAs conductivity independent of the substrate conduction.

As can be seen from Fig. 5.34, the three LT GaAs samples grown at

$T_s < 300°C$ show a distinctly different behavior from the simple activated conductivity discussed above. A number of observations can be noted. The lower the growth temperature, the larger is the conductivity. At temperatures greater than ~40°C, the data appear to approach that of the samples grown at $T_s \geq 300°C$. In other words, for elevated temperatures, the samples grown at $T_s < 300°C$ appear to evidence the conduction mechanism of Eq. (5.4). The Hall mobility calculated from the simple analysis [186] of this data supports this assertion since the carrier mobility is ~1000 $cm^2/V{\cdot}s$ for the three LT GaAs samples grown at $T_s < 300°C$.

However, for temperatures less than ~0°C and greater than approximately -90°C, the conductivity of these three LT GaAs samples can be fit by a temperature-activated conduction mechanism with $E_A \approx 0.17$ eV (see discussion below). Further, simple calculations of the Hall mobility in this temperature region indicate that the mobility rapidly decreases with temperature for temperatures less than ~0°C and is of the order of 1 $cm^2/V{\cdot}s$ for most of this temperature range. Also, the sign of the Hall coefficient in this temperature range indicates that the charge carriers are holes. Simple calculations of the Hall mobility and carrier concentration are not valid for materials with such low mobility and a more rigorous analysis is required [186],[188]. As will be discussed below, analysis of the Hall-effect data from low-mobility materials is often difficult and simple models are of questionable utility [188]. For this reason, I will not attempt such an analysis here; however, the low mobility calculated from the simple analysis is significant in that it is consistent with the hopping conductivity mechanisms [188],[189] to be discussed below.

Another important feature of the data shown in Fig. 5.34 for the LT GaAs epilayers grown at $T_s < 300°C$ is that for temperatures less than approximately -90°C the measured σ vs 1000/T data begin to deviate from an activated conductivity behavior. In other words, the data in this region lie above the straight line of E_A =

0.17 eV. The results for the 190°C LT GaAs epilayer are replotted in Fig. 5.35(a) to illustrate this point more clearly. In this figure log σ is again plotted vs 1000/T. The deviation from linearity is clearly evident at the lowest temperatures. This same data are also replotted in Fig. 5.35(b), except that in this figure the conductivity is plotted vs $T^{-0.25}$. Using these axes, we see that the data points at temperatures less than ~0°C follow a linear dependence of log σ on $T^{-0.25}$.

The data in Fig. 5.35 show that log σ of as-grown LT GaAs for measurement temperatures between ~0 and -90°C largely follow a linear dependence when plotted versus either T^{-1} or $T^{-0.25}$. The ability to fit the conductivity data of disordered materials, over a limited temperature range, with a linear dependence on either T^{-1} or $T^{-0.25}$ is not unique to as-grown LT GaAs. Plots of log σ vs T^{-1} and $T^{-0.25}$ for amorphous Ge thin films both result in a straight line for temperatures between approximately 0 and -90°C [188]. Differentiating between these two types of temperature-activated conductivity behavior is therefore difficult.

It is important to recognize that the three conduction mechanisms implied by the data of Figs. 5.34 and 5.35, and to be discussed below, do not begin and end at specific temperatures. At any given temperature, conduction by all three mechanisms is possible.

The conductivity vs temperature behavior of LT GaAs epilayers grown at $T_s <$ 300°C can be summarized as follows: (1) the lower the temperature of growth, the larger σ; (2) at temperatures greater than ~40°C, σ is temperature activated with $E_A \approx 0.75$ eV and the carrier mobility is ~1000 $cm^2/V{\cdot}s$; (3) at temperatures between ~0 and -90°C, the carrier mobility is of the order of 1 $cm^2/V{\cdot}s$ and log σ can be fitted either by a temperature-activated behavior with $E_A \approx 0.17$ eV or by a $T^{-0.25}$ behavior; and (4) at temperatures less than -90°C, the carrier mobility is again of the order of 1 $cm^2/V{\cdot}s$ and log σ is proportional to $T^{-0.25}$.

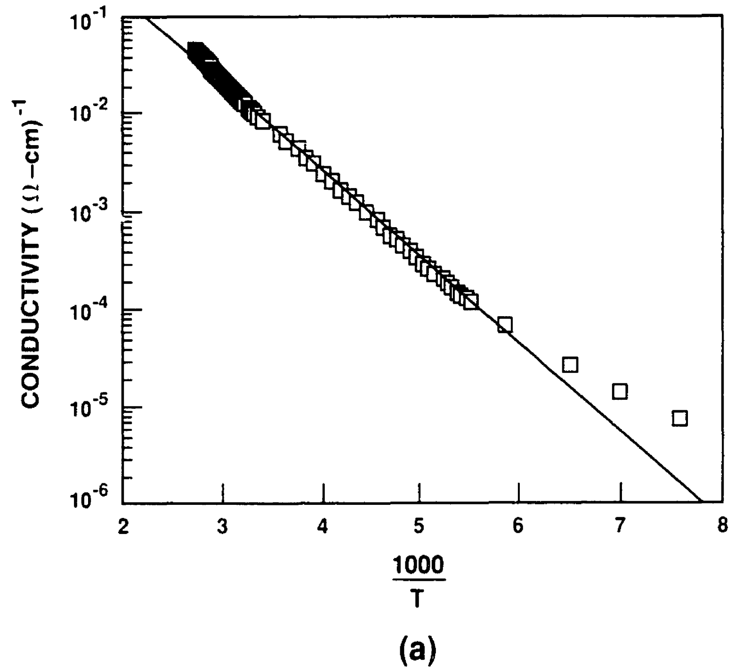

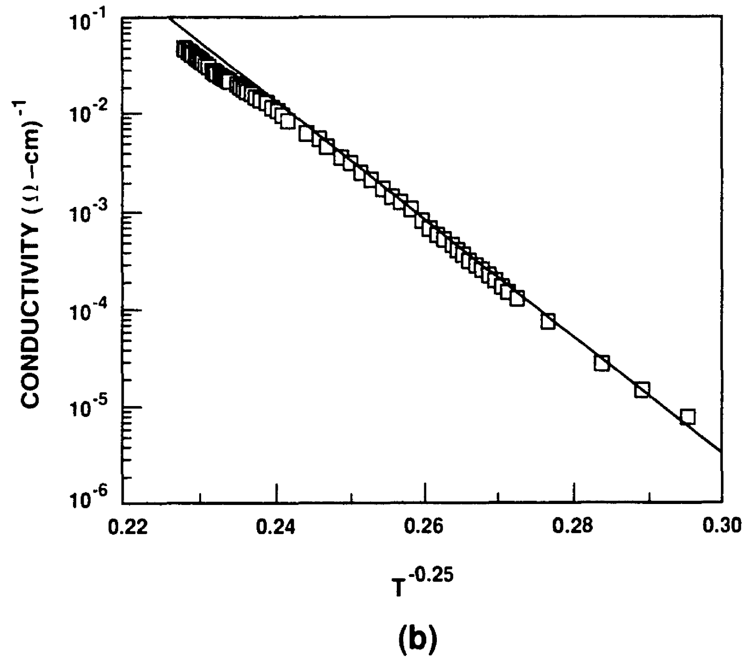

Fig. 5.35 The conductivity of the 190°C LT GaAs epilayer of Fig. 5.34 plotted vs (a) 1000/T and (b) $T^{-0.25}$. The lines are included only as a convenience in visualizing the data.

These observations are consistent with Mott's theory of electronic conduction in disordered semiconductors [188]. Since Mott's theory has been summarized in his monograph [188] and in Ref. [189], this discussion will be brief. Mott's theory of electronic conduction in disordered solids can apply both to conduction in band-tail states induced by disorder and in impurity or defect bands located within the energy gap. Since we believe, for reasons to be explained, that the conduction in LT GaAs is occurring in a defect band, the following discussion will address this case.

As defects are introduced into the crystal, deep levels are formed. If the density of these deep levels is high enough, a defect band can form [188],[189]. The formation of a defect band can be explained by two different physical mechanisms [189]. The first is often called disorder broadening [189]. In this mechanism, the energy of the deep levels associated with the defects are perturbed by a change in their local environment, as, for instance, by some other nearby charged defect or crystal imperfection. The disordered distribution of these other defects (especially charged defects) represents a fluctuating potential, which shifts the energy of the deep levels under consideration. This effect leads to an energy spread in the deep levels and contributes to the formation of the deep-level band.

Another possible explanation for the formation of a defect band is the wave funtion overlap of the defect states. The greater the density of the defects, the greater is the wave function overlap, and, hence, the greater is the broadening of the deep level energy band. This effect is analogous to the tight-binding approximation used to describe the formation of energy bands in crystals [189].

Below we will see evidence for the formation of an As_{Ga}–related defect band in LT GaAs. The As_{Ga}–related defect band presumably forms as a result of the large density of defects such as As_i, As microclusters, and especially the charged V_{Ga} compensating acceptors (see below). The contribution of the tight-binding-like effect

discussed above to the formation of the As_{Ga}–related defect band is expected to be small for LT GaAs since the As_{Ga}–related defects are spaced, on average, a distance ≥ 20 Å apart in the as-grown and annealed material.

Trapped carriers can hop from one defect state to another within a defect band [188],[189]. Two types of hopping mechanisms are possible. At higher temperatures the trapped carriers can escape from the localized potential well of the deep levels with the assistance of a phonon. If the density of deep levels is not too large, so that there is not significant overlap between the wave functions of the deep levels [188],[189], carriers hop between nearest-neighbor deep levels. This type of hopping mechanism is called nearest-neighbor hopping and can be described mathematically by the following temperature-activated conductivity formula:

$$\sigma = \sigma_2 \, e^{-\frac{W}{k_B T}} \tag{5.5}$$

where σ_2 is a prefactor and W is the mean energy difference between nearest-neighbor defect states, which is of the order of the FWHM of the energy distribution of the defect band [188],[189].

At low temperatures, fewer phonons of the energy needed in the nearest-neighbor hopping process are available [188],[189]. Thus, at low temperatures, Mott [188] predicts that the conductivity given by Eq. (5.5) becomes dominated by a phenomenon known variable-range hopping. The term variable-range derives from the fact that in this model trapped carriers hop to another deep level of about the same energy rather than to a nearest-neighbor deep level [188]. Mott has shown that this conductivity mechanism is of the form

$$\sigma = \sigma_3 \, e^{-\left[\frac{T_o}{T}\right]^{\frac{1}{4}}} \tag{5.6}$$

where σ_3 is a prefactor and T_o is a constant that is dependent on the spatial extent of the localized wave functions and the density of states in the defect band [188],[189].

Just as Mott's theory predicts that nearest-neighbor hopping is dominated by variable-range hopping at low temperatures, so too does his theory predict that at high temperatures nearest-neighbor hopping is dominated by carrier excitation from the defect band to the conduction or valence band. This mechanism is described by Eq. (5.4). Which of the three conduction mechanisms described by Eqs. (5.4)-(5.6) is operative in a given material depends upon a number of factors including the density and energy distribution of the deep levels, the position of E_f, and the temperature.

We can describe the conduction in LT GaAs grown at T_s < 300°C by Mott's model. At low temperatures (T < -90°C), log σ is approximately proportional to $T^{-0.25}$ in agreement with Eq. (5.6). For -90°C < T < 0°C, as we have previously discussed, the conductivity data can be fitted by either Eq. (5.5) or Eq. (5.6). If the nearest-neighbor hopping process described by Eq. (5.5) is the physically operative mechanism in this temperature range, then the fit to the data yields a value of 0.17 eV for the width of the defect band. Finally, above room temperature, the conductivity is dominated by free carriers that have been excited from the defect band into the conduction or valence band. The activation energy of this conduction process, 0.75 eV, implies that the defect band is situated in energy near the middle of the band gap. The sign of the Hall coefficient tells us that the carriers are electrons in the conduction band. This result also is consistent with our speculation that the defect band arises from the As_{Ga}^o-related defects located in the middle of the band gap (see below), because, as was noted in Sec. 5.1, EL2 is known to be a deep donor in GaAs.

Since we know from the IR absorption measurements (see Sec. 5.4.2) that the density of As_{Ga}^o-related defects is of the order of 10^{20} cm^{-3}, and further since we

know from the EPR measurements that only a fraction of these deep levels are unoccupied, we speculate that the hopping conductivity observed in LT GaAs is dominated by hole conduction in this As_{Ga}^{o}–related defect band. A mobility of the order of 1 $cm^2/V{\cdot}s$ is consistent with this hopping mechanism [188]. Mott has stated that Hall-effect measurements of disordered materials are difficult to interpret [188]. Other scientists have attempted such analyses (see citations in Ref. [188]), but their models will not be discussed here. More work is needed to accurately calculate the carrier mobility and density of LT GaAs in the hopping conduction regimes. It is possible that such calculations can provide quantitative information on the density of states in the defect band, the detailed position of E_f, and the extent of overlap of the localized wave fuctions of the deep levels.

The increased conductivity for the samples grown at lower T_s is also consistent with Mott's model. From Mott's theory, the greater the density of states in the defect band, the greater is the hopping probability, and, hence, the greater is the conductivity [188]. As was noted in Sec. 5.4.2, the IR absorption is larger the lower the growth temperature. Thus, the lower T_s, the larger is the concentration of As_{Ga}^{o}–related defects, as inferred from the Martin formula [88]. Increased hopping conductivity with increased defect density has also been observed for neutron-irradiated GaAs [100]. For large doses, the conductivity of neutron-irradiated GaAs follows Eq. (5.6), and the higher the dose, the larger is the measured conductivity, again in agreement with Mott's predictions [188]. As discussed in Sec. 5.5.1, neutron-irradiated GaAs also contains large concentrations of As_{Ga}^{+}. Coates and Mitchell find that at high temperatures the conductivity of their material follows Eq. (5.4) with $E_A \approx 0.75$ eV. Although they do not make such a speculation, it is possible that the conductivity mechanism in their neutron-irradiated material is associated with an As_{Ga}^{o}–related defect band. Using Eq. (5.6) with their data, they calcu-

late that $T_o^{0.25} \approx 100\ K^{0.25}$. From the data of Fig. 5.35(b) we calculate that $T_o^{0.25}$ in our material is ~140 $K^{0.25}$, in rough agreement with the neutron-irradiated GaAs results.

Figure 5.36 shows the results of σ vs 1000/T for the samples of the MBE annealing experiment. The two as-grown samples are seen to be quantitatively reproducible and follow the same behavior as shown in Fig. 5.35. However, the annealed samples show different behavior from the as-grown material. As was the case for the data of Fig. 5.34, the low temperature ($T \leq 30°C$) conductivity data can be fitted equally well by either Eq. (5.5) or Eq. (5.6). Fitting the data shown in Fig. 5.36 for the annealed material by an activated conductivity of the form of Eq. (5.5), we calculate that the low-temperature activation energy for the annealed samples is ~0.04 eV, as compared with 0.17 eV for the as-grown material at intermediate temperatures. Alternatively, fitting the same data using the $T^{-0.25}$ behavior described by Eq. (5.6), we calculate that $T_o^{0.25} \approx 50\ K^{0.25}$. As the annealing temperature is increased, the conductivity is seen to decrease. However, for measurement temperatures in excess of ~50°C, the 0.75-eV activated conduction dominates.

These results are consistent with the qualitative model discussed above and with the IR results of Sec. 5.4.2. As the LT GaAs epilayers are annealed, the As_{Ga}^{o}–related deep levels anneal, leading to a decrease in the temperature sensitivity of the conductivity. Using Eq. (5.5) to calculate the activation energy, we find that the activation energy of the conductivity decreases from ~0.17 eV for as-grown material to ~0.04 eV for annealed LT GaAs. This calculation, of course, assumes that the conduction is physically described by Eq. (5.5). In the Mott theory, a reduction in the activation energy of the hopping conductivity described by Eq. (5.5) implies an approximately equal narrowing of the width of the defect band. The annealing temperature for this change in the conductivity of LT GaAs is in the vicin-

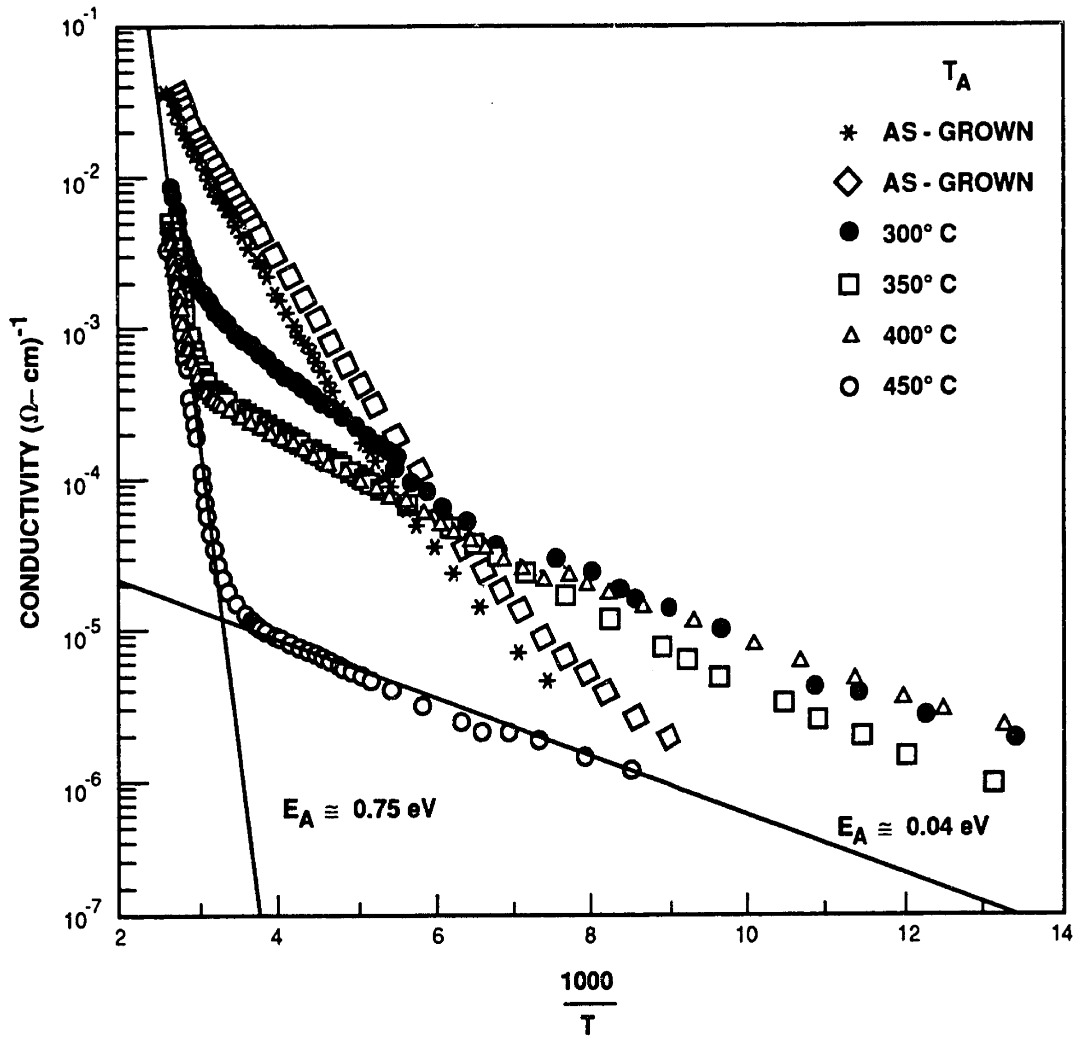

Fig. 5.36 Arrhenius plot of the conductivity of the LT GaAs MBE-annealing-experiment samples. The lines are included only as a convenience in visualizing the data.

ity of ~300°C. More work is needed to investigate the behavior of the LT GaAs conductivity for annealing temperatures near 300°C.

Although we have tried to measure the conductivity as a function of temperature for 200°C LT GaAs annealed *in situ* at 600°C, we have been unable to do so for temperatures less than ~30°C because the conductivity is less than 10^{-6} $(\Omega\text{-cm})^{-1}$. For temperatures greater than ~30°C, the conductivity of 200°C LT GaAs annealed at 600°C follows the activated conductivity mechanism of Eq. (5.4) with $E_A \approx 0.75$ eV. The behavior of the conduction current of annealed LT GaAs is discussed in more detail below.

5.5.2.2 I-V-T

Figure 5.37 shows the measured I_{sg} as a function of reciprocal temperature for the MESFET shown in Figs. 3.2 and 3.5 with an LT GaAs buffer [184]. As noted in Chapter 3, the LT GaAs epilayer was annealed *in situ* for 10 min under an As overpressure at 600°C prior to the deposition of the n-GaAs active layer. Further, the LT GaAs epilayer was effectvely annealed for an additional 20 min at 600°C during the growth of the active layer. The sidegate was spaced 15 µm from the source and drain electrodes for this measurement. I_{sg} was measured from the sidegate electrode to the source electrode. The drain and Schottky gate of the device were left floating.

These data again follow Mott's conductivity model. As was the case for the results presented previously, the MESFET conductivity data for measurement temperatures less than ~0°C can be fitted almost equally well by Eq. (5.5) or Eq. (5.6). Using Eq. (5.5) to fit the low temperature data, we calculate $E_A \approx 0.03$ eV. This E_A is comparable with the value of 0.04 eV found for the 450°C-annealed LT GaAs sample of Fig. 5.36. Alternatively, using Eq. (5.6) to fit the data, we calculate $T_o^{0.25} \approx 40\ K^{0.25}$, in rough agreement with the results of the previous section.

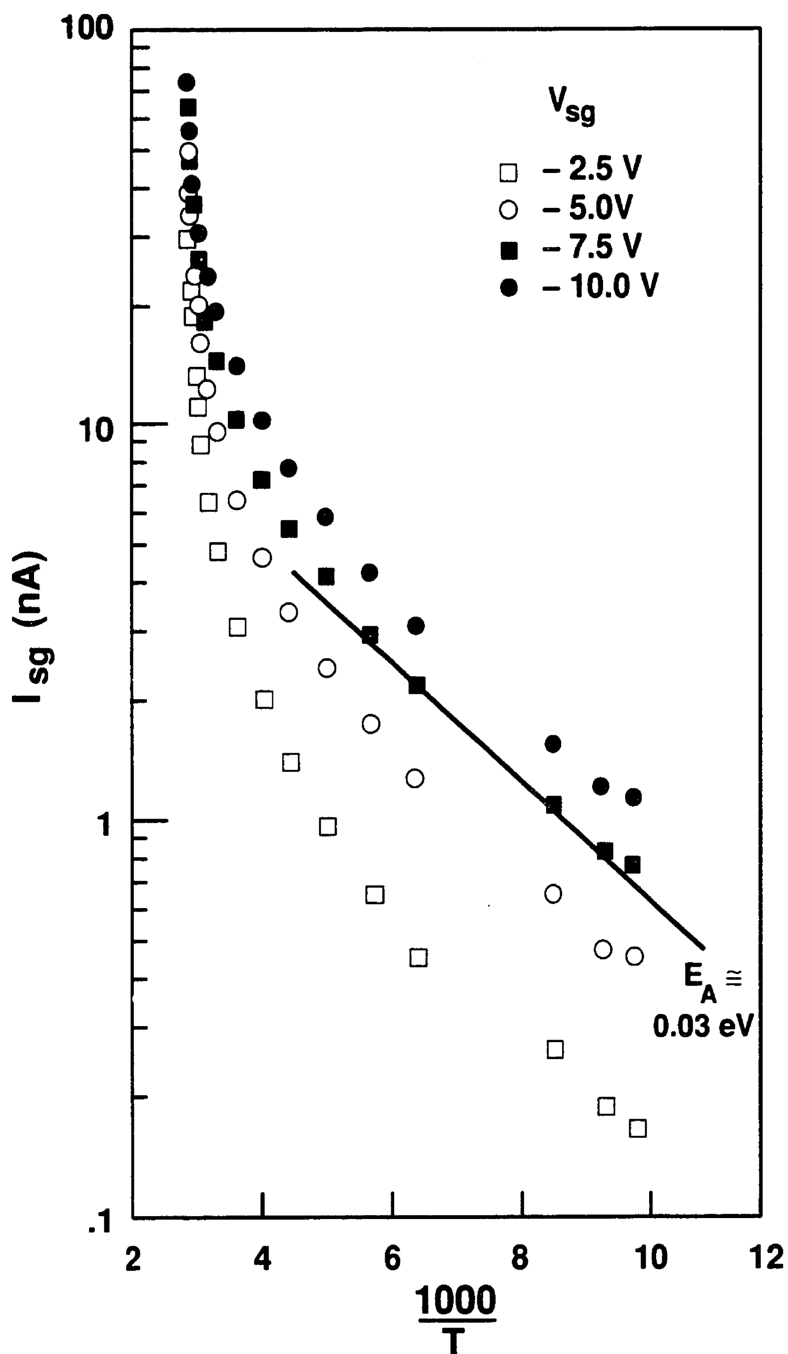

Fig. 5.37 Arrhenius plot of I_{sg} for the MESFET of Figs. 3.2 and 3.5 for various sidegate voltages. The sidegate was spaced 15 μm from the MESFET. The lines are included only as convenience in visualizing the data.

Further, I_{sg} was observed to be ohmic in this low temperature region, again in agreement with Mott's theory of nearest-neighbor hopping [188]. At high temperatures, the data of Fig. 5.37 follow Eq. (5.4) with $E_A \approx 0.75$ eV.

If we assume that all of I_{sg} flows through the 2-μm-thick LT GaAs buffer layer, simple calculations indicate that the conductivity of that layer is less than 10^{-7} $(\Omega\text{-cm})^{-1}$ at room temperature. This result overestimates the conductivity of annealed LT GaAs because substrate conduction also contributes to the measured current. More work is needed in order to differentiate between the current carried in the LT GaAs buffer layer and the current carried in the substrate. Nonetheless, our finding that the resistivity of LT GaAs at room temperature is in excess of 10^7 Ω-cm is consistent with the value of 2.2 x 10^8 Ω-cm found by researchers at the University of Texas for the resistivity of their LT GaAs samples [190]. Their LT GaAs epilayers were grown at nominally 250°C (see Sec. 5.7.1) and were annealed *in situ* at 600°C for 10 min [190]. They measured the resistivity of their LT GaAs samples using a metal-insulator-semiconductor (MIS) structure; however, they did not report the temperature dependence of the LT GaAs resistivity.

5.6 Discussion

As a result of the numerous characterization results presented in the preceding sections, it is possible to advance semi-quantitative models of both as-grown and annealed LT GaAs. This work was done in collaboration with Dr. Maria A. Kaminska of the University of California, Berkeley. In Figs. 5.38 and 5.39, pictures of the density of states and band diagrams characterizing these models are shown for as-grown and annealed LT GaAs, respectively. Since more quantitative information is known for as-grown LT GaAs, this material is discussed first. Using the model of as-grown LT GaAs as a basis, we then describe the model proposed for the annealed

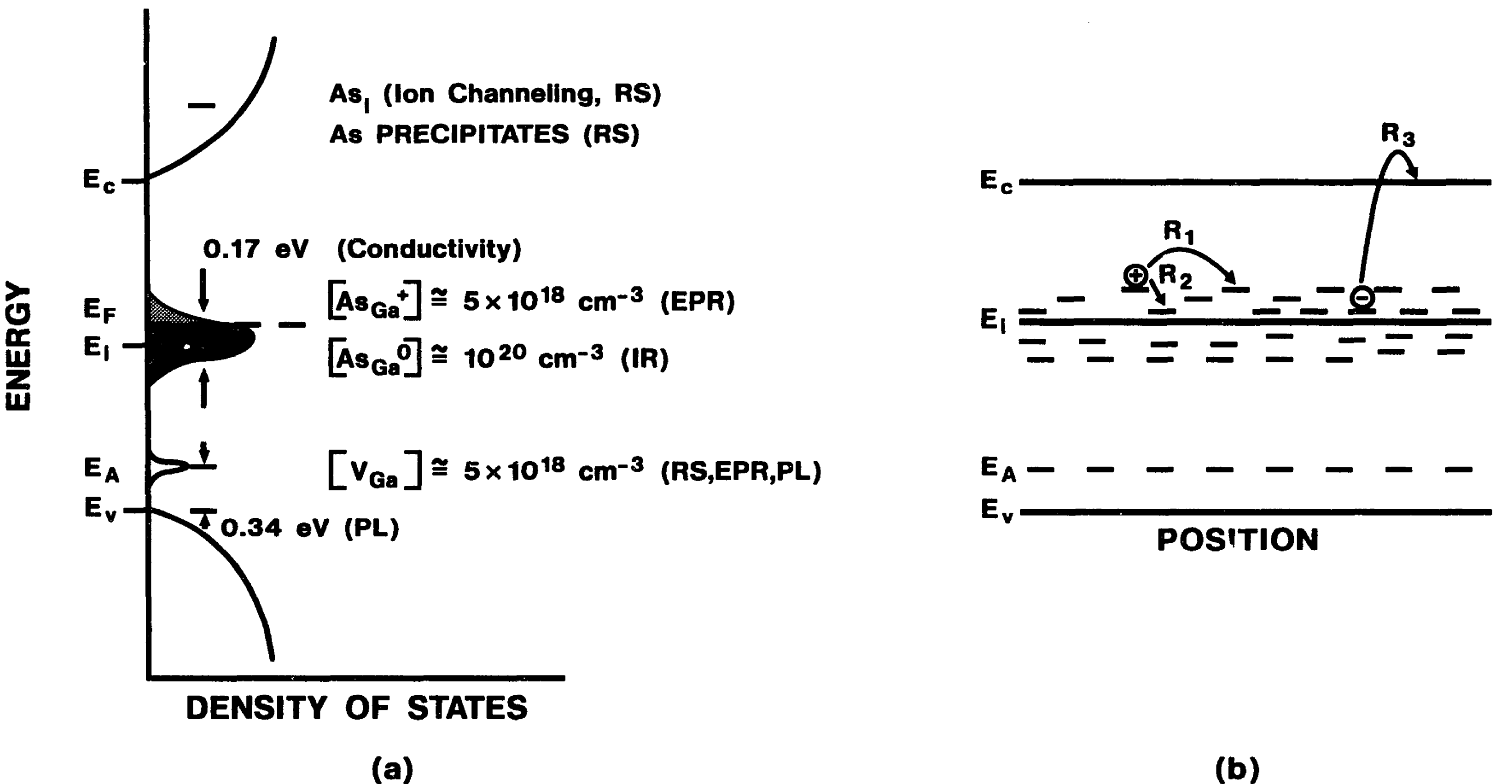

Fig. 5.38 Preliminary model for as-grown LT GaAs. (a) Density of states and (b) band diagram. The techniques used to identify the defects in (a) are shown in parentheses. R1, R2, and R3 in (b) refer to the three conduction mechanisms discussed in Sec. 5.5.2.1.

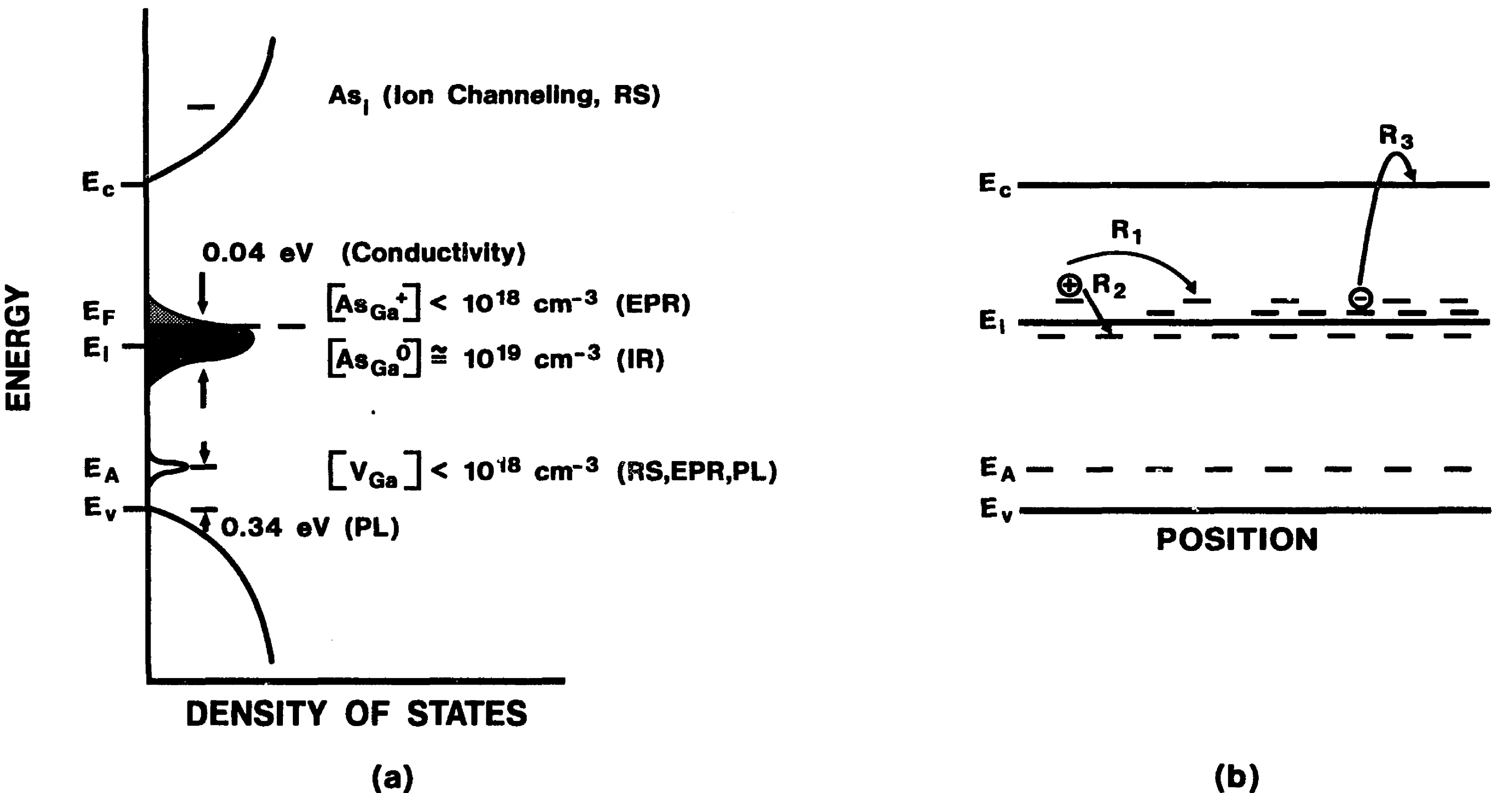

Fig. 5.39 Preliminary model for 200°C LT GaAs annealed at 600°C for 10 min. (a) Density of states and (b) band diagram. The techniques used to identify the defects in (a) are shown in parentheses. R1, R2 and R3 in (b) refer to the three conduction mechanisms discussed in Sec. 5.5.2.1.

material. Although the models discussed in this section can explain most of the experimental observations noted in this chapter, the explanation of some phenomena remain unclear. These issues are addressed last.

Figure 5.38 summarizes most of the experimental observations and inferences noted in this chapter for as-grown LT GaAs. Although we have not shown definitively that the as-grown material has distinct band edges, the IR absorption and conductivity measurements are consistent with a band description. While it is possible that some band tailing [188] of the conduction and valence bands may result from the disorder in the crystal, such effects are not shown in Fig. 5.38(a) since we have no experimental evidence for this. Hence, the density of states in the conduction and valence bands are shown as having the well-known square-root dependence on energy. As usual, E_i is the intrinsic energy level, located approximately at the center of the band gap.

In the center of the band gap (~0.75 eV below the conduction band) a large deep-level density is depicted as a defect band. From the IR absorption measurements of Sec. 5.4.2 we inferred that ~10^{20} cm^{-3} As_{Ga}^{o}–related defects are present in as-grown LT GaAs. Of these, we have identified 10% as EL2 from the observed metastability. Similarly from the EPR measurements of Sec. 5.5.1 we know that ~5×10^{18} cm^{-3} As_{Ga}^{+}–related defects are present in the material. Since only a fraction (~5%) of the As_{Ga}–related defects are ionized, E_f must be positioned above the middle of the As_{Ga}–related defect band. To first order, those As_{Ga}–related defects above E_f are ionized and those below are neutral. In Fig. 5.38(a) the As_{Ga}^{+}–related defects are shown as a lighter shade of gray than the As_{Ga}^{o}–related defects, and E_f is depicted as the dividing line between the two shades of gray.

Since we have no direct evidence for As_{Ga}^{2+}–related defects, the concentration for this defect is not estimated. The concentration of As_{Ga}^{2+}–related defects in as-grown

LT GaAs is presumably negligible since the second ionization energy of As_{Ga} at E_v + 0.52 eV lies below E_f.

The width of the As_{Ga}–related defect band is estimated from the Mott theory of phonon-assisted hopping, as was discussed in Sec. 5.5.2.1. In that section, we showed that for -90°C < T < 0°C the observed low-temperature conductivity data could be fit equally well by either Eq. (5.5) or Eq. (5.6). As a result it is not clear which hopping mechanism, nearest-neighbor or variable-range, is dominant in that temperature range. However, if nearest-neighbor hopping is responsible for the observed conductivity behavior, then the activation energy of 0.17 eV can be identified as the width of the defect band. More experiments, such as measuring the ac conductivity, and more detailed theoretical calculations, such as calculating the carrier concentration and mobility from the Hall-effect data, need to be done to determine the width of the As_{Ga}–related defect band more precisely.

For two reasons we hypothesize that an acceptor concentration of $\sim 5 \times 10^{18}$ cm^{-3} must be present in the material. First, the conductivity results of Sec. 5.5.2 indicate that for temperatures less than ~40°C the conduction mechanism involves hopping, not free carriers in the conduction or valence bands. Second, if the ionized electrons from the As_{Ga}^{+}–related defects are not located in the conduction band, then they must be bound to compensating acceptors. Since the background acceptor concentration in MBE-grown LT GaAs is of the order of only 10^{14} cm^{-3}, impurities alone cannot account for the number of As_{Ga}^{+}–related centers. From the RS data of Sec. 5.4.3 we have evidence for a strong peak at 47 cm^{-1}, which we tentatively identified as V_{Ga}. It is known that V_{Ga} or V_{Ga} complexes can introduce acceptor levels in GaAs [137]. An example of such a complex is the V_{Ga}–Si_{Ga} defect that forms an acceptor level in n-GaAs [137], as was discussed in Sec. 5.4.1. It is possible that V_{Ga} or a V_{Ga} complex introduces an acceptor level into LT GaAs.

For these reasons we hypothesize a V_{Ga}–related acceptor concentration of ~5×10^{18} cm^{-3} in as-grown LT GaAs, as shown in Fig. 5.38(a), where the energy level is labeled E_A. This energy level is shown at E_v + 0.34 eV based upon the PL results of Sec. 5.4.1 that identified a deep-level PL peak at 1.16 eV as arising from a transition between the conduction band and a V_{Ga}–related acceptor. Clearly this identification is only tentative at this time and more work is needed to prove the hypothesis.

From the ion-channeling and RS results of Secs. 5.3.3 and 5.4.3 we know that As microclusters and As_i are also present in as-grown LT GaAs. Theoretical calculations indicate that As_i should be a donor with an energy level degenerate with the conduction band [191]. For this reason the energy level of As_i is shown in Fig. 5.38(a) in the conduction band. More work is needed to experimentally determine, if possible, the energy levels of As_i and the As microclusters. If As_i is a donor degenerate with the conduction band, then it would be ionized since E_f is near the middle of the energy gap. This fact implies either that the acceptor density is sufficient to compensate the As_i donors or that the As_i defects are complexed with some other lattice defect to form a neutral pair.

Although this model is only preliminary, it does summarize most of the experimental findings of this chapter for as-grown LT GaAs. The electrical conductivity results of Sec. 5.5.2 can be explained using the band diagram shown in Fig. 5.38(b). The As_{Ga}–related defect band is depicted qualitatively as a series of closely spaced discrete energy levels. At low temperatures the conduction mechanism is hole hopping as depicted by paths R_1 and R_2. Path R_1 symbolizes Mott's variable-range hopping model [188] and path R_2 represents Mott's nearest-neighbor hopping model [188]. The hopping is identified with holes from the sign of the Hall coefficient. Further, hole conduction is consistent with most of the As_{Ga}–related defects being

neutral [see Fig. 5.38(a)].

At elevated temperatures free electrons and holes are formed in the conduction and valence bands, respectively. Even though these free carriers are of very low density, they have sufficiently high mobility that they dominate the observed conductivity. If we assume that the conduction and valence bands of LT GaAs are not significantly perturbed from those of high purity GaAs, then the effective density of states in the valence band N_v is a factor of ~15 greater than the effective density of states in the conduction band N_c [147]. Hence, E_i is about 1.4kT above the middle of the band gap. However, E_f will remain pinned slightly above E_i by the large As_{Ga}–related defect density, as shown in Fig. 5.38, so that the free electron concentration should be larger than the free hole concentration. Since the mobility of the electrons should not be smaller than that of the holes, we therefore expect the electron conduction to dominate. This conclusion is in agreement with the Hall measurements at elevated temperatures. The free-electron conduction process is depicted by path R_3 in Fig. 5.38(b).

The photo-EPR results of Fig. 5.33 can also be qualitatively explained using Fig. 5.38 and the inset of Fig. 5.1. As the photon energy of illumination is increased, the density of As_{Ga}^{+}–related centers increases. For energies of illumination greater than ~0.75 eV, the increase in the concentration of As_{Ga}^{+}–related centers results from ionization of the As_{Ga}^{0}–related defect. As can be seen from the inset to Fig. 5.1, for illumination at photon energies ≥ 0.75 eV, the As_{Ga}^{+} EPR signal can either be enhanced or reduced depending upon whether an electron in an As_{Ga}^{0}–related state is ionized into the conduction band or an electron is ionized from the valence band into an As_{Ga}^{+}–related state. These two processes are competitive and which one dominates depends upon the relative transition probabilities. These probabilities in turn depend upon the matrix elements for the transitions, the equilibrium concentrations of

the As_{Ga}^{o}–related and As_{Ga}^{+}–related defects, and N_c and N_v in the material. In Fig. 5.1 the As_{Ga}^{+} EPR signal in plastically deformed GaAs is observed to decrease for photon energies ≥ 0.75 eV. In contrast, the LT GaAs data of Fig. 5.33 show an enhancement of the As_{Ga}^{+} EPR signal for photon energies ≥ 0.75 eV. The difference in the photo-EPR behavior of LT GaAs and plastically deformed GaAs is not unreasonable since the aforementioned parameters may be different in the two materials. Although such an analysis will not be attempted here, it may be possible to quantitatively model the data of Fig. 5.33 if the transition probabilities for the two processes depicted in the inset to Fig. 5.1 are calculated for LT GaAs.

In Fig. 5.33, the onset of the increase in the As_{Ga}^{+} EPR signal at ~0.5 eV may arise from stray light of higher energy that is passed through the spectrometer. This could have occurred because the low-energy spectral limit of the grating used in our spectrometer is approximately 0.5 eV. Since the As_{Ga}^{2+}–related defect concentration is negligibly small, excitation of electrons from the valence band to the As_{Ga}^{2+}–related level to form As_{Ga}^{+}–related centers cannot explain the increase in the EPR signal observed at ~0.5 eV.

The slight decrease in the EPR signal at photon energies greater than ~1.4 eV may be due to either of two mechanisms. First, the decrease may occur because of quenching of the metastable EL2 defects. Since only 10% of the total As_{Ga}^{o}–related defects are EL2, this effect is expected to be small. A second possible explanation arises because the penetration depth of light in LT GaAs decreases as the photon energy increases. This occurs because the absorption coefficient of LT GaAs is greater for higher photon energies (see Sec. 5.4.2). For the measurement of Fig. 5.33, the LT GaAs sample was heated to above ~130°C and then was cooled to 8 K before each data point was recorded. By this means, the EPR As_{Ga}^{+}–related signal in the dark was restored before illumination at each energy. Thus, for illumination with

photons of larger energies, only a smaller volume of the LT GaAs epilayer was probed, and, hence, the change in the measured As_{Ga}^{+}–related signal was less.

As noted repeatedly throughout this chapter, the large defect density in as-grown LT GaAs, especially As_i and the As microclusters, may be responsible for the structural disorder observed by ion channeling (see Sec. 5.3.3) and the dilation of the lattice constant observed by x-ray diffraction (see Sec. 5.3.2). The large defect density quenches the near-band-gap and deep-level PL, as is also the case for damaged and irradiated material (see Sec. 5.1).

As LT GaAs is annealed, the disorder in the crystal is monotonically reduced. The lattice constant relaxes back to that of GaAs and the backscattered yield measured by ion channeling decreases. The reduction in disorder is also reflected in the deep-level density in the crystal as measured by RS, IR, and conductivity measurements. Figure 5.39 depicts a tentative density of states and band diagram for 200°C LT GaAs that has been annealed *in situ* at 600°C for 10 min. The model is similar to that shown in Fig. 5.38 for as-grown material, but the defect concentrations are lower.

From IR absorption measurements, the As_{Ga}^{o}–related defect density was calculated to be of the order of $\sim 10^{19}$ cm^{-3}, where approximately 10% of the defects are EL2 (see Sec. 5.4.2). If the low-temperature conductivity is physically described by Eq. (5.5), then, as we showed in Sec. 5.5.2.2, the width of the defect band has narrowed to ~0.04 eV. Unlike the case of as-grown LT GaAs, EPR measurements of annealed material did not detect the As_{Ga}^{+}–related defect. Since the minimum concentration of As_{Ga}^{+}–related defects that can be detected in a 3-μm-thick epilayer is $\sim 10^{18}$ cm^{-3}, the concentration of these defects in annealed LT GaAs must be less than this amount. Although we have been unable to measure the concentration of the As_{Ga}^{+}–related defect in annealed LT GaAs, we know that such defects must be

present since holes are necessary for the hopping conductivity mechanism in the As_{Ga}–related defect band. Because the sign of the Hall coefficient indicates that holes are responsible for the measured conductivity, E_f is positioned above the middle of the As_{Ga}–related defect band, as in Fig. 5.38.

Again by analogy to the as-grown material, the ionized As_{Ga}–related defects require compensating acceptor defects. The acceptor defect density must also be less than 10^{18} cm^{-3}. Although the 47-cm^{-3} peak was not detected in annealed LT GaAs, it is possible that some smaller concentration of V_{Ga}–related acceptors remains. As was done in Fig. 5.38(a), E_A is shown at E_v + 0.34 eV. Alternatively, the compensating acceptors may arise from a residual MBE impurity such as carbon. More experiments and analysis are needed to determine precisely the concentration of the As_{Ga}^{+}–related defects and the identity of the compensating acceptors in annealed LT GaAs.

Despite the fact that the As microprecipitates are removed during the annealing process, As_i defects remain, as was shown by the RS measurements of Sec. 5.4.3. Again the As_i energy level is shown degenerate with the conduction band. As discussed above, the As_i defects are either complexed to form a neutral defect or they require a commensurate number of compensating acceptor levels.

The energy band diagram reflects the narrower As_{Ga}–related defect band that is inferred from using Eq. (5.5) to fit the low-temperature conductivity behavior. The variable-range and nearest-neighbor hopping mechanisms are illustrated by paths R_1 and R_2, respectively, and path R_3 depicts conduction by free electrons in the conduction band, as in Fig. 5.38.

The high resistivity and large deep-level density of the annealed material can largely explain the device results of Chapters 3 and 4. The sidegating and short-channel effects are discussed first. The switch results are then briefly analyzed.

Although LT GaAs grown at 200°C and annealed *in situ* is of high resistivity, its conductivity measured as discussed in Sec. 5.5.2 and shown in Figs. 5.34 to 5.37 is actually greater than or equal to that of SI GaAs. This follows from the fact that at high temperatures (≥ 40°C) the annealed LT GaAs conductivity is comparable to that of SI GaAs. However, as the temperature is reduced, the SI GaAs conductivity continues to decrease expontentially [see Eq. (5.4)] with $E_A \approx 0.75$ eV, but the annealed LT GaAs conductivity decreases much more slowly, as shown in Fig. 5.36. As a result, LT GaAs is more conductive than SI GaAs for the measurement conditions used in Sec. 5.5.2 at temperatures below ~30°C.

In Sec. 3.2.1 it was noted that a high resistivity buffer layer was needed to eliminate sidegating. Since LT GaAs is in fact less resistive than SI GaAs for the measurement conditions used in Sec. 5.5.2, clearly some additional explanation for the elimination of sidegating by the LT GaAs buffer must be considered. In the following discussion one possible additional explanation for the elimination of sidegating is advanced that is consistent with the properties of LT GaAs and the known behavior of sidegating in MESFET's fabricated on SI GaAs substrates.

Lee et al. showed that sidegating in MESFET's fabricated by direct ion implantation into a SI GaAs substrate was small (less than a 1% reduction in I_{dss}) until a threshold sidegating voltage was exceeded [6]. They showed that the threshold voltage for the start of pronounced sidegating was the same as for the onset of space-charge-limited conduction from the nominally isolated sidegate to the MESFET [6]. To explain their results, Lee et al. invoked a model proposed by Lampert and Mark [192].

According to the work of Lampert and Mark [192], space-charge-limited conduction can be observed in a semiconductor or insulator with traps. For the case of deep traps, Lampert and Mark show that the current-voltage characteristics of the

semiconductor or insulator follow a complex behavior as the voltage is increased. At low voltages an ohmic behavior is observed. As the voltage is increased, the ohmic conductivity is replaced by a square-law regime where the current is proportional to the square of the voltage. At a still larger voltage, called the trap-filled-limited voltage V_{TFL}, space-charge-limited conduction becomes dominant and the current rapidly increases with voltage. This behavior is depicted in Fig. 1.4 of Ref. [192].

The I_{sg} vs V_{sg} data of Lee et al. for their ion-implanted MESFET's follow the predictions of the Lampert and Mark theory [192]. Lee et al. found that $V_{TFL} = 3$ V for a sidegate spaced 26 μm from the MESFET. Pronounced sidegating occurred in their devices for $V_{sg} > V_{TFL}$ [6]. The small sidegating currents that flow in the low-voltage ohmic and square-law regimes were insufficient to induce sidegating.

By analogy to the results of Lee et al., the LT GaAs buffer may eliminate sidegating because V_{TFL}, if it exists, is substantially larger than the voltages used in the sidegating experiments discussed in Sec. 3.2.1 or in Refs. [18] or [193]. The slightly higher conductivity of LT GaAs as compared with SI GaAs at low voltages may well be irrelevant for sidegating.

Researchers at Hewlett-Packard have measured the sidegating effect for $V_{sg} \leq 70$ V across a 3 μm spacing between a sidegate and MESFET fabricated on the LT GaAs buffer [18],[193]. Despite the large electric field (~2×10^5 V/cm) across the LT GaAs buffer, they observed less than a 1% decrease in I_{dss} [18],[193], indicating that sidegating is eliminated even for this large applied field. From their result, we can infer that V_{TFL} in LT GaAs, if it exists, is greater than 70 V across a 3 μm spacing. We now show that such a lage value of V_{TFL} is consistent with the results of Lee et al. and the theory of Lampert and Mark.

Lee et al. found that the critical voltage for sidegating in their devices was 3 V across 26 μm. In the theory of Lampert and Mark it is the electrical field that is the

determining factor in the onset of space-charge-limited conduction [192]. Given this, we can estimate that for a spacing of 3 μm, V_{TFL} would occur at a bias of ~0.35 V in the devices of Lee et al. Lampert and Mark also predict that the onset of space-charge limited conduction should increase linearly with the density of deep traps. While the density of EL2 in SI GaAs is ~10^{16} cm^{-3}, in annealed LT GaAs the density of As_{Ga}–related deep levels is ~10^{19} cm^{-3}. Extrapolating the results of Lee et al. to LT GaAs, we calculate that V_{TFL} would be ~350 V for a 3 μm spacing between the sidegate and the MESFET, consistent with the Hewlett Packard results.

In Sec. 3.2.1 it was shown that the breakdown voltage of LT GaAs was ~400 V across a 15 μm spacing. Scaling this result, we find that breakdown should occur at ~80 V for a 3 μm spacing. It is possible, therefore, that dielectric breakdown may occur in LT GaAs before V_{TFL} is reached. If this is the case, then V_{TFL} for LT GaAs would not be exceeded for any allowed operating voltage, which explains why the LT GaAs buffer eliminates sidegating.

One other aspect of sidegating should also be briefly mentioned. As discussed in Sec. 3.2.1 the interface between the buffer layer or substrate and the n-GaAs active layer is an important element in sidegating. It is only because the space-charge layer at the interface can be modulated that sidegating occurs. Although some form of space-charge layer presumably exists at the interface between the LT GaAs buffer and the n-GaAs active layer as a result of the difference between E_f in the two materials, the details of this interface are not known. More experiments are needed to characterize this interface. Such a study, coupled with a more complete description of the behavior of the high-field conductivity of the LT GaAs buffer, might result in a quantitative model to explain the sidegating results of Chapter 3.

The reduction in short-channel effects observed in submicrometer-gate-length MESFET's incorporating the LT GaAs buffer (see Sec. 3.3) can also be qualitatively

explained using the model presented in this section. Short-channel effects have often been attributed to conduction through the substrate when the device is nominally pinched off [46]. This parasitic conduction becomes more pronounced and, hence, the short-channel effects become more severe as the gate length is reduced, since the electric field associated with the Schottky-barrier gate becomes larger for shorter gate lengths [46]. It has been shown that if a heterostructure barrier or pn junction is included underneath the active layer, short-channel effects are reduced [45],[194]. As discussed above, the large deep-level density in LT GaAs may lead to considerably lower currents at high electric fields as compared with the SI GaAs substrate or conventional buffer layers. More work is needed to characterize in detail the short-channel effects in both the conventional and the LT GaAs buffered devices of Sec. 3.3.

The extremely fast switching speeds observed for the LT GaAs photoconductive switch may also be attributable to the large deep-level density near the middle of the band gap. Although the recombination mechanism operative in the electron-hole plasma in the LT GaAs epilayer following excitation by a high-intensity femtosecond laser pulse is presumably more complex than that described by the Shockley-Read-Hall (SRH) formalism [195], nevertheless the SRH model predicts that the photoexcited carrier lifetime should decrease as the deep-level density increases. Further, the SRH model predicts that deep levels near the center of the band gap are the most efficient recombination centers. Thus, the large deep-level density in LT GaAs that is centered at the middle of the band gap is qualitatively consistent with an extremely short photoexcited carrier lifetime. The relatively large mobility of the photoexcited carriers is also consistent with the conductivity results of Sec. 5.5.2.

Although the models summarized in Figs. 5.38 and 5.39 and discussed above account qualitatively for most of the results presented in this thesis, one question

remains unanswered. While all the characterization measurements indicate that the disorder and deep-level density in the LT GaAs epilayer are reduced in the annealing process, the deviation from stoichiometry as measured by AES and PIXE remains largely unchanged. As a result of the anneal, the As^{o}_{Ga}–related defect density is reduced by an order of magnitude, as inferred from the IR absorption measurements; the As microclusters and V_{Ga} RS peaks disappear; and the As_i concentration decreases, as inferred from the ion-channealing measurements. Where the excess arsenic goes during the anneal, and how it is incorporated in the annealed LT GaAs lattice, are unanswered questions. It is possible that clusters of As-excess-related defects form that are undetected by the numerous characterization techniques employed during this thesis. Why such clusters would not be observed by lattice-imaging TEM or detected by RS are not known. More work is needed to answer this question and the other questions posed in this section.

5.7 Reproducibity of MBE-Grown Epilayers

Although the properties of annealed 200°C LT GaAs layers are relatively insensitive to the growth conditions, slight differences between properties of different unannealed LT GaAs layers grown under nominally identical conditions are observed. As was seen in Section 5.5.1, the EPR signal of as-grown 200°C LT GaAs epilayers was shown to depend critically on the growth parameters. Slight variations in, for instance, the growth temperature can alter the properties of the material. Although MBE is an excellent research tool, the uniformity and reproducibility of epilayers grown by most MBE systems are insufficient for GaAs IC manufacturing. Making MBE more reproducible is a goal of the system vendors, and MBE machines for manufacturing are becoming available, as is discussed in Sec. 5.7.3. Several sources of nonuniformity in MBE-grown epilayers, and possible solutions, are discussed

below.

5.7.1 Substrate Temperature Variation

Measuring temperature in a vacuum is difficult. In our MBE system the GaAs sample is mounted on a molybdenum block using In solder. The molybdenum block is then mounted on a sample holder in the growth chamber (see Fig. 2.1). A thermocouple is placed in close proximity behind the molybdenum block and measures the temperature of the block by blackbody radiation. Variations in the reflectivity of the backside of different blocks can lead to different temperatures measured by the thermocouple for the same power setting. In the growths discussed in this thesis, the thermocouple temperature was calibrated using an optical pyrometer and the congruent sublimination point of GaAs (defined as 640°C as measured by the optical pyrometer). Temperatures were then referenced to T_{cs}. However, since the observed T_{cs} can change as a function of As background pressure in the growth chamber and as a function of the reflectivity of the In- and GaAs-coated front surface of the block, the actual temperature and the measured temperature may differ by as much as 5 to 10°C [196]. Further, since the optical pyrometer can only measure temperatures greater than ~400°C, at the low temperatures used to grow LT GaAs only the thermocouple was used to measure temperature.

Another source of temperature variation in the Lincoln Laboratory MBE system is the use of In bonding. Mounting GaAs samples using In bonding is difficult and invariably the In wetting of the backside of the sample is nonuniform. This nonuniform bonding can lead to temperature gradients across the wafer surface of as much as 5 to 10°C. Thus, even if the same block is used for two different growths, the temperature of the sample may be different due to the nonuniformity of the In bonding.

The position of the thermocouple relative to the molybdenum block can also alter the measured temperature. Virtually every time the sample holder in the MBE system was repaired or modified, the controller setting at which T_{cs} is found for a given block changed, as did the controller setting that corresponded to 200°C. Hence, during the time period over which this thesis was performed (~3 years), what the thermocouple read as 200°C may have changed by as much as 10°C.

5.7.2 Nonuniform Flux Distribution

Another factor affecting the reproduciblity of MBE-grown epilayers is the flux distribution emanating from the effusion cells. A number of sources for nonuniform flux distributions exist. Since the eight effusion cells are located equidistant from the substrate holder, but at different directions and angles of inclination to the substrate, even if the sources generate a uniform flux at the end of the cell, the distribution over the surface of the substrate can be nonuniform. This nonuniformity can occur in both the radial and axial (r and ϕ in cylindrical coordinates) directions. The axial inhomogenities can be minimized by rotating the substrate, but the radial variations remain. Researchers at Honeywell have found that the threshold voltage V_T of their InGaAs/InAlAs HEMT's can change by as much as 10% from the center to the edge of a 3-in. wafer [21].

The position of the sample holder relative to the substrate can also affect the flux distribution incident on the sample. The sample (z-axis) should be perpendicular to the plane of the sources. However, since the sample holder is rotated by 180° to insert and remove the sample from the growth chamber, it is difficult to always position the sample in the same location. Further, the position of the ion guage when the BEP of the sources is measured should be in the same position as the sample during growth. This guarantees that the fluxes measured by the ion guage are identical to

the fluxes incident on the sample. Again this is often difficult to achieve during routine growths. Also the flux distribution incident on the sample can change if the position of the crucible containing the elemental source material is changed. Since the crucibles are removed and reinserted approximately every 3 to 4 months to refill the sources, the position of the mouth of the crucibles relative to the sample also changes with the same frequency.

The ion gauge used to measure the BEP of the sources can also introduce irreproducibility. We have found that for the same Ga effusion cell, the measured Ga BEP required for a GaAs growth rate of 1 μm/h can change by as much as 10% when one ion gauge is substituted for another. Clearly, growth rates must be calibrated for each ion gauge, and after any maintenance to the ion-gauge/sample-holder assembly.

In addition to the above geometrical and mechanical sources of irreproducibility, two additional problems can be identified. First, the measured BEP changes as the background pressure in the growth chamber changes. The BEP measured with a low background pressure in the system is different from that measured when a high background pressure exists in the system, even though the actual flux rate is unchanged. We have also observed slow drifts in the BEP from a given effusion cell as a result of oscillations in the temperature of the cell. Such drifts in BEP are generally small, however, being of the order of <5%. Lastly, the BEP measured immediately after the shutter covering a group III effusion cell is opened is always larger than that observed after the cell has been open for ~4 min. Changes of ~15% in BEP are typical [196]. We attribute the enhanced BEP when the shutter is first opened to built-up pressure in the effusion cell wtih the shutter closed. This variation is less significant in long runs such as for the relatively thick films of LT GaAs reported in this thesis, but can be significant in the growth of quantum-well structures.

5.7.3 Improved MBE Reproducibility

A number of improvements to MBE systems have been, or can be, made to improve the reproducibility of epilayer growths. To improve the reproducibility of temperature measurements, holders wihout In can be used [124]. These holders eliminate the use of In bonding and molybdenum blocks, which can dramatically reduce the problems discussed in Sec 5.7.1. Larger volume and area sources can be used to minimize the flux nonuniformities discussed in the previous section [124]. The larger volume increases the thermal mass, and, hence, reduces slow temperature drifts, and the larger area can improve the radial uniformity. Gas sources can also improve the uniformity of the flux distribution.

RHEED oscillations can be used to quantitatively measure the flux incident on the sample, thereby eliminating the problems associated with positioning the sample and measuring BEP's with the ion guage. A computer-controlled video camera and digital signal processing can be used to precisely control growth rates and layer thickness as well as to provide information on growth kinetics [197].

With holders that do not use In and growth rate calibration by RHEED oscillations, it should be possible to obtain reproducibly the same thermocouple temperature for the same setting on the controller. For LT GaAs growth, the 200°C growth temperature measured by the thermocouple on our MBE system can be scaled to any other system by measuring the time it takes for the LT GaAs layer to become polycrystalline, as observed by RHEED (see Fig. 2.5). In fact, users of MBE systems with sample holders that do not use In have found that a therocouple reading of ~300°C on their systems is roughly equivalent to our 200°C, as verified by the thickness at which the LT GaAs layer becomes polycrystalline (see Sec. 2.3) [198],[199].

A number of Japanese vendors have not only incorporated these changes in

MBE systems designed for manufacturing, but have also added multiple wafer growth capability. The ability to grow up to seven 2-in. or three 3-in. wafers simultaneously should markedly improve the wafer-to-wafer uniformity of MBE epilayer growth. Japanese researchers have obtained standard deviations in HEMT V_T across the active area of a 3-in. wafer of less than 15 mV [200]. This uniformity is superior to that currently achieved by commercial GaAs MESFET digital IC manufacturers using a fully ion-implanted process [201].

CHAPTER 6. CONCLUSIONS

The use of LT GaAs in GaAs electronic and optoelectronic devices and circuits has led to profound performance improvements. By using LT GaAs as a buffer layer in GaAs MESFET's, we have demonstrated that dc and time-dependent sidegating effects can be eliminated. The resistive component of RF coupling and the duty cycle effect which are significant problems for analog and digital circuits, respectively, are eliminated by using the LT GaAs buffer. Microwave devices fabricated with the LT GaAs buffer show no variation of input impedence with sidegate bias, in contrast to dievices fabricated with other buffer layers or by other means. The coupling between monolithically integrated digital and microwave circuits as well as short-channel effects are markedly reduced by using the LT GaAs buffer. The larger breakdown strength of LT GaAs as compared with SI GaAs and the ability to eliminate sidegating will permit higher voltage and denser GaAs circuits to be fabricated than was heretofore possible. State-of-the-art frequency divider circuits fabricated by Hughes [19] and high-performance analog circuits fabricated by Hewlett-Packard [50],[193],[198] corroborate this assertion.

Photoconductive switches fabricated with LT GaAs have demonstrated record performance for speed, sensitivity, and peak voltage. Instrument-limited switching speeds of 450 fs have been measured for photoconductive-gap switches fabricated on coplanar striplines. Time-resolved photoreflectance measurements [202] of LT GaAs demonstrate that the lifetime of the photoexcited carriers in LT GaAs is ~150 fs [72], again a record. The short photoexcited carrier lifetime coupled with the large dielectric breakdown strength have made possible the generation of pulses with a peak voltage in excess of 16 V and a duration of ~1 ps. Such large voltage picosecond pulses may be useful in a number of applications, as will be briefly discussed later in this chapter.

As a result of numerous characterization experiments, a qualitative model of LT GaAs has been formulated. LT GaAs grown at ~200°C and unannealed contains a large number of point defects including $\sim 10^{20}$ cm^{-3} As_{Ga}^{o}–related defects, $\sim 5\times 10^{18}$ cm^{-3} As_{Ga}^{+}–related defects, V_{Ga}–related defects, As_i, and As microprecipitates. These defects arise from approximately a 1 at.% arsenic excess in the crystal. We hypothesize that the excess arsenic is incorporated into the film because, at the low temperatures used for growth, the excess arsenic flux incident on the sample surface does not desorb during growth of the film. The arsenic excess and arsenic-related deep levels in the film lead to a dilated lattice constant (~0.1%) and constricted channels. The large As_{Ga}–related defect concentration results in a strong deep-level IR absorption, a hopping conductivity at low temperatures (< 40°C), and quenches both near-band-gap and deep-level PL.

The higher the temperature used for growth or the higher the post-growth annealing temperature, the smaller is the disorder and the deep-level density in the crystal. The technologically important material for electronic and optoelectronic device and circuit applications is LT GaAs grown at 200°C and subsequently annealed *in situ* at 600°C for ~10 min. The 200°C growth temperature was chosen because this was the lowest temperature at which relatively thick (~3 μm) epilayers could be deposited and still maintain the film single crystal. The *in situ* anneal under an arsenic overpressure maintains the ~1 at.% arsenic excess in the crystal and leads to the high resistivity and large trap density that results in the elimination of sidegating in electronic devices and a low dark current and short photoexcited carrier lifetime in photoconductive switches.

Annealed LT GaAs also contains a large deep-level density including $\sim 10^{19}$ cm^{-3} As_{Ga}^{o}–related defects and As_i. However, the As_{Ga}^{+}–related defect, V_{Ga}, and As microprecipitate densities are reduced below detectable levels. The large

As_{Ga}–related defect density results in a large deep-level IR absorption, a low-temperature (< ~0°C) hopping conductivity, and quenched PL. More work is needed to quantitatively determine the identity and density of the compensating acceptors in both as-grown and annealed LT GaAs. Further, although the defect density in LT GaAs is reduced during the *in situ* annealing process, the excess arsenic concentration does not change. This paradox is the most important unresolved question about LT GaAs.

As a result of our publications and the dramatic improvements possible in electronic and optoelectronic devices and circuits with LT GaAs, numerous industrial, governmental, and academic institutions throughout the world are now actively investigating LT GaAs and other LT-grown materials. Table 6.1 lists a number of U.S. corporations that are now pursuing LT GaAs technology. Those organizations listed with asterisks are incorporating LT GaAs into products either for sale to customers or for internal use. In addition to LT GaAs, other LT-grown III-V semiconducting materials such as LT InAlAs and InGaAs are attracting considerable attention.

Although this thesis demonstrates a number of device applications of LT GaAs and a model of LT GaAs has been proposed, numerous opportunities for future investigations of LT GaAs remain. Some of these material, device, and circuit experiments are briefly discussed in the following few paragraphs. Other possible experiments were also mentioned throughout Chapters 3, 4, and 5.

The LT growth of other III-V semiconductors and a more quantitative model of LT GaAs are two important areas for future research. The LT growth of InAlAs, InGaAs, AlGaAs, and InP, among others, holds significant promise for electronic and optoelectronic device and circuit applications, and their growth and characterization may provide additional insight into the physics of LT GaAs. Investigation of the physics of LT GaAs using TEM, RS, ion channeling, IR absorption, and conductivity

ELECTRONIC DEVICES AND CIRCUITS	PHOTOCONDUCTIVE SWITCH	WAFER VENDORS
HEWLETT-PACKARD*	IBM	NESI*
HUGHES*	AT&T	KOPIN
HONEYWELL*	EG&G	
AT&T	TEKTRONIX	
MOTOROLA		
IBM		
TRW		
RAYTHEON		
ALPHA		
CELERITEK		

Table 6.1 Summary of the transfer of LT GaAs technology to domestic industry. The organizations listed with an asterisk are incorporating LT GaAs into their production processes.

measurements of the same epilayers should be continued. By this means the information provided by each technique can be correlated. The use of LT GaAs membranes (see Sec. 5.4.2) may be particularly useful for the conductivity studies. Also using As, As_2, as well as the standard As_4 sources would allow the role that the As species has on the defect formation and stoichiometry of LT GaAs to be studied. Different growth conditions such as growth rate, As to Ga flux, and annealing time and temperature should also be investigated.

Capacitance-voltage measurements of MIS structures may provide additional information on the deep levels in LT GaAs. LT GaAs may also hold promise for surface passivation in GaAs IC's. The quality of the active layer deposited on top of the LT GaAs layer can be characterized using DLTS [203]. Also the ability of the LT GaAs buffer layer to withstand ion-implantation annealing temperatures (~800°C) should be investigated.

A number of future experiments involving the LT GaAs photoconductive switch can be envisioned. Thin alternating layers of GaAs and LT GaAs may allow the sensitivity of the switch to be improved without sacrificing speed [14]. The LT GaAs switch might be integrated with GaAs devices and circuits for ultrahigh-speed testing applications [14]. The generation of high-voltage (>100 V) picosecond electrical pulses with LT GaAs could be attempted. By launching these pulses into free space [204], one may be able to use these high voltage pulses for applications in communication or radar systems.

Lastly, the growth of LT GaAs by other epitaxial techniques such as organometallic chemical vapor deposition (OMCVD) is an important area of future research. Growth of LT GaAs by OMCVD will create new opportunities for the commercialization of this technology.

The growth, characterization, and applications of LT GaAs and other LT-grown semiconductors should continue to be fertile areas of research and product development in the future.

REFERENCS

[1] J. Barrera, in *Proc. IEEE/Cornell Conf. on High Speed Semiconductor Devices and Circuits, 1975* (IEEE, New York, 1975), p. 135.

[2] W. J. Schaff, L. F. Eastman, B. Van Rees, and B. Liles, J. Vac. Sci. Technol. B **2,** 265 (1984).

[3] H. Goronkin, M. S. Birrittella, W. C. Seelbach, and R. L. Vaitkus, IEEE Trans. Electron Devices **ED-29,** 845 (1982).

[4] T. H. Miers, W. M. Paulson, and M. S. Birrittella, Inst. Phys. Conf. Ser. No. **65,** 339 (1982).

[5] C. Kocot and C. A. Stolte, IEEE Trans. Electron Devices **ED-29,** 1059 (1982).

[6] C. P. Lee, S. J. Lee, and B. M. Welch, IEEE Electron Device Lett. **EDL-3,** 97 (1982).

[7] M. S. Birrittella, W. C. Seelbach, and H. Goronkin, IEEE Trans. Electron Devices **ED-29,** 1135 (1982).

[8] F. W. Smith, A. R. Calawa, C. L. Chen, M. J. Manfra, and L. J. Mahoney, IEEE Electron Device Lett. **9,** 77 (1988).

[9] F. W. Smith, A. R. Calawa, C. L. Chen, L. J. Mahoney, M. J. Manfra, and J. C. Huang, in *Proc. IEEE/Cornell Conf. on High Speed Semiconductor Devices and Circuits* (IEEE, New York, 1987), p. 229.

[10] F. W. Smith, C. L. Chen, G. W. Turner, M. C. Finn, L. J. Mahoney, M. J. Manfra, and A. R. Calawa, in *Technical Digest IEEE International Electron Devices Meeting* (IEEE, New York, 1988), p. 838.

[11] C. L. Chen, F. W. Smith, A. R. Calawa, L. J. Mahoney, and M. J. Manfra, IEEE Trans. Electron Devices **36,** 1546 (1989).

[12] A. N. Birbas, B. Brunn, A. D. van Rheenen, A. Gopinath, C. L. Chen, F. W. Smith, and A. R. Calawa (unpublished).

[13] F. W. Smith, H. Q. Le, V. Diadiuk, M. A. Hollis, A. R. Calawa, S. Gupta, M. Frankel, D. R. Dykaar, G. A. Mourou, and T. Y. Hsiang, Appl. Phys. Lett. **54,** 890 (1989).

[14] F. W. Smith, S. Gupta, H. Q. Le, M. Frankel, V. Diadiuk, M. A. Hollis, D. R. Dykaar, G. A. Mourou, and A. R. Calawa, to be published in *Picosecond Electronics and Optoelectronics III,* edited by D. M. Bloom and T. C. L. G. Sollner (OSA, Washington, 1989).

[15] S. Gupta, J. A. Valdmanis, G. A. Mourou, F. W. Smith, and A. R. Calawa, in *Conference on Lasers and Electro-Optics Technical Digest* (OSA, Washington, 1989), p. 346.

[16] M. Kaminska, Z. Liliental-Weber, E. R. Weber, T. George, J. B. Kortright, F. W. Smith, B-Y. Tsaur, and A. R. Calawa, Appl. Phys. Lett. **54,** 1881 (1989).

[17] M. Kaminska, E. R. Weber, Z. Liliental-Weber, R. Leon, and Z. Rek, J. Vac. Sci. Technol. B **7,** 710 (1989).

[18] B. J. Lin, D. E. Mars, and T. S. Low, presented at the IEEE 46th Annual Device Research Conf., Boulder, CO, June, 1988.

[19] M. J. Delaney, S. S. Chou, L. E. Larson, J. F. Jensen, D. S. Deakin, A. S. Brown, W. W. Hooper, M. A. Thompson, L. G. McCray, and S. E. Rosenbaum, IEEE Electron Device Lett. **10,** 355 (1989).

[20] F. W. Smith, G. W. Turner, Z. Liliental-Weber, and A. R. Calawa (unpublished).

[21] D. E. Grider, S. E. Swirhum, D. H. Narum, and V. Sokolov, presented at the Electronic Materials Conf., Cambridge, MA, June, 1989.

[22] A. S. Brown, U. K. Mishra, C. S. Chou, C. E. Hooper, M. A. Melendes, M. Thompson, L. E. Larson, S. E. Rosenbaum, and M. J. Delaney, IEEE Electron Device Lett. **10,** 565 (1989).

[23] A. Y. Cho and J. R. Arthur, in *Progress in Solid-State Chemistry,* edited by G. Somorjai and J. McCaldin (Pergammon, NY, 1975), vol. 10, p. 276.

[24] E. H. C. Parker, ed., *The Technology and Physics of Molecular Beam Epitaxy* (Plenum Press, NY, 1985).

[25] L. L. Chang and K. Ploog, eds., *Molecular Beam Epitaxy and Heterostructures* (Martinus Nijhoff, Dordrect, 1985).

[26] M. B. Panish, J. Electrochem. Soc. **127,** 2729 (1980).

[27] A. R. Calawa, Appl. Phys. Lett. **38,** 701 (1981).

[28] B. A. Joyce, in *Molecular Beam Epitaxy and Heterostructures,* edited by L. L. Chang and K. Ploog (Martinus Nijhoff, Dordrect, 1985), p. 37; also C. T. Foxon and B. A. Joyce, Surf. Sci. **50,** 434 (1975), and C. T. Foxon and B. A. Joyce, Surf. Sci. **64,** 293 (1977).

[29] A. Y. Cho, in *The Technology and Physics of Molecular Beam Epitaxy,* edited by E. H. C. Parker (Plenum Press, NY, 1985), p. 191; also A. Y. Cho, J. Vac. Sci. Technol. **8,** S31 (1971).

[30] J. H. Neave and B. A. Joyce, J. Cryst. Growth, **43,** 204 (1978).

[31] T. Murotani, T. Shimanoe, and S. Mitsui, J. Cryst. Growth **45,** 302 (1978).

[32] C. E. C. Wood, J. Woodcock, and J. J. Harris, Inst Phys. Conf. Ser. No. **45,** 28 (1979).

[33] J. H. Neave, P. Blood, and B. A. Joyce, Appl. Phys. Lett. **36,** 311 (1980).

[34] R. A. Stall, C. E. C. Wood, P. D. Kirchner, and L. F. Eastman, Electron. Lett. **16,** 171 (1980).

[35] G. M. Metze and A. R. Calawa, Appl. Phys. Lett. **42,** 818 (1983).

[36] M. Missous and K. E. Singer, Appl. Phys. Lett. **50,** 694 (1987).

[37] Y. Horikoshi, M. Kawashima, and H. Yamaguchi, Jpn. J. Appl. Phys. **27,** 169 (1988).

[38] E. A. Wood, J. Appl. Phys. **35,** 1306 (1964).

[39] D. J. Chadi, J. Vac. Sci. Technol. A **5,** 834 (1987).

[40] A. Mitonneau, G. M. Martin, and A. Mircea, Inst. Phys. Conf. Ser. No. **33a,** 73 (1977).

[41] M. Naganuma and K. Takahashi, Phys. Status Solidi A **31,** 187 (1975).

[42] R. Ludeke, R. M. King, and E. H. C. Parker, in *The Technology and Physics of Molecular Beam Epitaxy,* edited by E. H. C. Parker (Plenum Press, NY, 1985), p. 555.

[43] L. F. Eastman and M. S. Shur, IEEE Trans. Electron Devices **ED-26,** 1359 (1979).

[44] T. Nozaki, M. Ogawa, H. Terao, and H. Wantanabe, Inst. Phys. Conf. Ser. No. **24,** 46 (1975).

[45] K. Yamasaki, N. Kato, and M. Hirayama, IEEE Trans. Electron Devices **ED-32,** 2420 (1985).

[46] W. Patrick, W. S. Mackie, S. P. Beaumont, C. D. W. Wilkinson, and C. H. Oxley, IEEE Electron Device Lett. **EDL-6,** 471 (1985).

[47] K. Yokoyama, M. Tomizawa, and A. Yoshii, IEEE Electron Device Lett. **EDL-6,** 536 (1985).

[48] T. C. Edwards, *Foundations for Microstrip Circuit Design* (Wiley, NY, 1981), Chapters 6 and 7.

[49] B. Hughes, N. G. Fernandez, and J. M. Gladstone, IEEE Trans. Electron Devices **ED-34,** 733 (1987).

[50] B. J. F. Lin, C. P. Kocot, D. E. Mars, and R. P. Jaeger, IEEE Trans. Electron Devices **37,** 46 (1990).

[51] A. Ezis and D. W. Langer, IEEE Electron Device Lett. **EDL-6,** 494 (1985).

[51] M. R. Melloch, D. C. Miller, and B. Das, Appl. Phys. Lett. **54,** 943 (1989).

[53] R. Zuleeg, in *VLSI Electronics: Microstructure Science,* edited by N. G. Einspruch and W. R. Wisseman (Academic Press, NY, 1985), vol. 11, p. 391.

[54] A. S. Brown and U. K. Mishra (unpublished).

[55] G. Turner, H. K. Choi, J. P. Mattia, S. J. Eglash, C. L. Chen, and B-Y. Tsaur, paper presented at the MRS Spring Meeting, Reno, NV, April, 1988.

[56] U. K. Mishra, J. F. Jensen, A. S. Brown, M. A. Thompson, L. M. Jelloian, and R. S. Beaubien, IEEE Electron Device Lett. **9,** 482 (1988).

[57] D. H. Auston, J. Quantum Electron. **QE-19,** 639 (1983).

[58] D. H. Auston, in *Ultrashort Laser Pulses and Applications,* edited by W. Kaiser, Topics Appl. Phys. Vol. 60 (Springer-Verlag, Berlin, 1988), p. 183.

[59] G. T. Turner, G. M. Metze, V. Diadiuk, B-Y. Tsaur, and H. Q. Le, in *Technical Digest IEEE International Electron Devices Meeting* (IEEE, New York, 1985), p. 468.

[60] A. G. Foyt and F. J. Leonberger, in *Picosecond Optoelectronic Devices,* edited by C. H. Lee (Academic, Orlando, 1984), p. 271.

[61] D. H. Auston, K. P. Cheung, and P. R. Smith, Appl. Phys. Lett. **45,** 284 (1984).

[62] D. H. Auston, in *Picosecond Optoelectronic Devices,* edited by C. H. Lee (Academic, Orlando, 1984), p. 73.

[63] J. A. Valdmanis and G. Mourou, IEEE J. Quantum Electron. **QE-22,** 69 (1986).

[64] J. A. Valdmanis, Electron. Lett. **23,** 1308 (1988).

[65] M. B. Ketchen, D. Grischkowsky, T. C. Chen, C-C. Chi, I. N. Duling, III, N. J. Halas, J-M. Halbout, J. A. Kash, and G. P. Li, Appl. Phys. Lett. **48,** 754 (1986).

[66] M. C. Nuss, Appl. Phys. Lett. **54,** 57 (1989).

[67] D. Grischkowsky, C.-C. Chi, I. N. Duling, III, W. J. Gallagher, N. H. Halas, J.-M. Halbout, and M. B. Ketchen, in *Picosecond Electronics and Optoelectronics II,* edited by F. J. Leonberger, C. H. Lee, F. Capasso, and H. Morkoc, eds. (Springer-Verlag, Berlin, 1987), p. 11.

[68] P. M Downey and B. Schwartz, Appl. Phys. Lett. **44,** 207 (1984).

[69] W. D. Goodhue, G. D. Johnson, and T. H. Windhorn, Inst. Phys. Conf. Ser. **83,** 349 (1987).

[70] T. F. Carruthers and J. F. Weller, in *Technical Digest IEEE International Electron Devices Meeting* (IEEE, New York, 1985), p. 483; T. F. Carruthers and J. F. Weller, Appl. Phys. Lett. **48,** 460 (1986).

[71] B. H. Kolner and D. M. Bloom, IEEE J. Quantum Electron. **QE-22,** 79 (1986).

[72] S. Gupta, J. A. Valdmanis, G. A. Mourou, F. W. Smith, and A. R. Calawa (unpublished).

[73] E. A. Chauchard, C. H. Lee, V. Diadiuk, and G. W. Turner, in *Picosecond Electronics and Optoelectronics II,* edited by F. J. Leonberger, C. H. Lee, F. Capasso, and H. Morkoc (Springer-Verlag, Berlin, 1987), p. 237.

[74] J. Schneider, in *Semi-Insulating III-V Materials,* edited by S. Makram-Ebeid and B. Tuck (Shiva Publishing, Nantwich, UK, 1982), p. 144.

[75] S. Makram-Ebeid, P. Langlade, and G. M. Martin, in *Semi-Insulating III-V Materials,* edited by D. C. Look and J. S. Blakemore (Shiva Publishing, Nantwich, UK, 1984), p. 184.

[76] G. M. Martin and S. Makram-Ebeid, in *Deep Centers in Semiconductors,* edited by S. T. Pantelides (Gordon and Breach, New York, 1986), p. 399.

[77] M. Kaminska, Physica Scripta **T19,** 551 (1987).

[78] E. R. Weber and M. Kaminska, in *Semi-Insulating III-V Materials,* edited by G. Grossman and L. Ledebo (Adam Hilger, Bristol, UK, 1988), p.111.

[79] H. J. von Bardeleben and D. Stievenard, in *Defects in Electronic Materials,* edited by M. Stavola, S. J. Pearton, and G. Davies, MRS Symposium Proc. Vol. 104 (MRS, Pittsburgh, 1988), p. 351.

[80] E. R. Weber, K. Khachaturyan, M. Hoinkis, and M. Kaminska, in *Point and Extended Defects in Semiconductors,* edited by G. Benedek, A. Cavallini, and W. Schroter (Plenum Press, New York, 1989), p. 39.

[81] K. R. Elliott, R. T. Chen, S. G. Greenbaum, and R. J. Wagner, in *Semi-Insulating III-V Materials,* edited by D. C. Look and J. S. Blakemore (Shiva Publishing, Nantwich, UK, 1984), p. 239.

[82] J. Lagowski, J. M. Parsey, M. Kaminska, K. Wada, and H. C. Gatos, in *Semi-Insulating III-V Materials,* edited by S. Makram-Ebeid and B. Tuck (Shiva Publishing, Nantwich, UK, 1982), p. 154.

[83] W. Guangyu and Z. Yuanxi, in *Semi-Insulating III-V Materials,* edited by G. Grossman and L. Ledebo (Adam Hilger, Bristol, UK, 1988), p. 387.

[84] H. J. von Bardeleben, D. Stievenard, J. C. Bourgoin, and A. Huber, in *Semi-Insulating III-V Materials,* edited by H. Kukimoto and S. Miyazawa (Ohmsha, Tokyo, Japan, 1986), p. 355.

[85] J. Lagowski, M. Matsui, M. Bugajski, C. H. Kang, M. Skowronski, H. C. Gatos, M. Hoinkis, E. R. Weber, and W. Walukiewicz, Inst. Phys. Conf. Ser. No. **91,** 395 (1987).

[86] E. R. Weber, H. Ennen, U. Kaufman, J. E. Windscheif, J. Schneider, and T. Wosinski, J. Appl. Phys. **53,** 6140 (1982).

[87] M. Tajima, in *Semi-Insulating III-V Materials,* edited by G. Grossman and L. Ledebo (Adam Hilger, Bristol, UK, 1988), p. 119.

[88] G. M. Martin, Appl. Phys. Lett. **39,** 747 (1981).

[89] J. Dabrowski and M. Scheffler, in *Semi-Insulating III-V Materials,* edited by G. Grossman and L. Ledebo (Adam Hilger, Bristol, UK, 1988), p. 37.

[90] J. Dabrowski and M. Scheffler, Phys. Rev. Lett. **60,** 2183 (1988).

[91] R. Coates and E. W. J. Mitchell, Adv. Phys. **24,** 593 (1975).

[92] D. Pons and J. C. Bourgoin, J. Phys. C **18,** 3839 (1985).

[93] D. V. Lang, Inst. Phys. Conf. Ser. No. **31,** 70 (1977).

[94] N. K. Goswami, R. C. Newman, and J. E. Whitehouse, Solid State Commun. **40,** 473 (1981).

[95] R. Worner, U. Kaufmann, and J. Schneider, Appl. Phys. Lett. **40,** 141 (1982).

[96] E. Weber, in *Semi-Insulating III-V Materials,* edited by D. C. Look and J. S. Blakemore (Shiva Publishing, Nantwich, UK, 1984), p. 296.

[97] P. Omling, E. R. Weber, and L. Samuelson, Phys. Rev. **B33,** 5880 (1986).

[98] E. R. Weber and P. Omling, in *Festkorperprobleme/Advances in Solid State Physics XXV,* edited by R. Grosse (Vieweg, Braunschweig, 1985), p. 623.

[99] M. Hoinkis and E. R. Weber, submitted to Phys. Rev. B.

[100] R. Coates and E. W. J. Mitchell, J. Phys. C **5**, L113 (1975).

[101] R. E. Williams, *Gallium Arsenide Processing Techniques* (Artech House, Dedham, MA, 1984).

[102] L. C. Feldman and J. W. Mayer, *Fundamentals of Surface and Thin Film Analysis* (Elsevier, NY, 1986).

[103] *Handbook on Auger Electron Spectroscopy* (Perkin-Elmer Corp., Eden Prairie, MN, 1978).

[104] *Handbook of X-Ray Photoelectronic Spectroscopy* (Perkin-Elmer Corp., Eden Prairie, MN, 1979).

[105] G. R. Larrabee, in *VLSI Electronics: Microstructure Science,* vol. 2, edited by N. G. Einspruch (Academic, NY, 1981), p. 37.

[106] J. C. Bravman, in *Proc. Soc. Photo-Opt. Instrum. Eng. 439* (SPIE, Bellingham, WA, 1986), p. 18.

[107] D. B. Williams, *Practical Analytical Electron Microscopy in Materials Science* (Philips Electronic Instruments, Inc., Mahwah, NJ, 1984).

[108] R. G. Musket and W. Bauer, Appl. Phys. Lett. **20,** 411 (1972).

[109] P. P. Pronko and R. S. Bhattacharya, in *Proc. Soc. Photo-Opt. Instrum. Eng. 524* (SPIE, Bellingham, WA, 1985), p. 25.

[110] F. Folkman, in *Material Characterization Using Ion Beams,* edited by J. P. Thomas and A. Cachard (Plenum Press, London, 1978), p. 239.

[111] D. K. Bakale, R. Linder, and C. E. Bryson, III, in *Proc. Soc. Photo-Opt. Instrum. Eng. 524* (SPIE, Bellingham, WA, 1985), p. 2.

[112] G. Peterson, H. Krasinski, W. J. Tanski, F. W. Smith, and A. R. Calawa (unpublished).

[113] M. C. Finn, M.I.T. Lincoln Laboratory (private communication).

[114] Z. Liliental-Weber, Lawrence Berkeley Laboratory (private communication).

[115] M. A. Kaminska and K-M. Yu, Lawrence Berkeley Laboratory (private communication).

[116] M. Kaminska, Z. Liliental-Weber, K-M. Yu, E. R. Weber, F. W. Smith, and A. R. Calawa (unpublished).

[117] Z. Liliental-Weber, in *Proc. Soc. Photo-Opt. Instrum. Eng. 623* (SPIE, Bellingham, WA, 1986), p. 237.

[118] P. B. Hirsch, A. Howie, R. B. Nicholson, D. W. Pashley, and M. J. Whelan, *Electron Microscopy of Thin Crystals* (Butterworths, London, 1971).

[119] B. D. Cullity, *Elements of X-Ray Diffraction* (Addison-Wesley, Reading, MA, 1978).

[120] W-K. Chu, J. W. Mayer, and M-A. Nicolet, *Backscattering Spectrometry* (Academic, NY, 1978).

[121] L. C. Feldman, J. W. Mayer, and S. T. Picraux, *Materials Analysis by Ion Channeling* (Academic, NY, 1982).

[122] C. M. H. Driscoll, A. F. W. Willoughby, J. B. Mullin, and B. W. Straughan, Inst. Phys. Conf. Ser. **24,** 275 (1975).

[123] K. Tershima, O. Ohmori, A. Okada, M. Wantanabe, and T. Nakanisi, in *Semi-Insulating III-V Materials,* edited by H. Kukimoto and S. Miyazawa (Ohmsha, Tokyo, Japan, 1986), p. 187.

[124] M. A. Herman and H. Sitter, *Molecular Beam Epitaxy: Fundamentals and Current Status* (Springer-Verlag, Berlin, 1989).

[125] W. J. Bartels, J. Vac. Sci. Technol. B **1,** 338 (1983).

[126] J. W. Matthews and A. E. Blakeslee, J. Crystal Growth **27,** 118 (1974).

[127] B. W. Dodson and J. Y. Tsao, Appl. Phys. Lett. **51,** 1325 (1987).

[128] F. W. Smith, M. J. Manfra, and A. R. Calawa (unpublished).

[129] M. Ilegems, in *The Technology and Physics of Molecular Beam Epitaxy,* edited by E. H. C. Parker (Plenum Press, NY, 1985), p. 83.

[130] W. Hayes and R. Loudon, *Scattering of Light by Crystals* (Wiley, New York, 1978).

[131] J. I. Pankove, *Optical Processes in Semiconductors* (Dover, NY, 1971).

[132] A. S. Barker and A. J. Sievers, Rev. Mod. Phys. **47,** suppl. 2 (1975).

[133] R. C. Newman, *Infra-red Studies of Crystal Defects* (Taylor and Francis, London, 1973).

[134] R. S. Berg, Ph.D. thesis, University of California, Berkeley, 1985 (unpublished).

[135] G. W. Turner, F. W. Smith, and A. R. Calawa (unpublished).

[136] J. E. Fouquet, R. R. Saxena, and G. A. Patterson, IEEE J. Quantum Electron. **25,** 1025 (1989).

[137] E. W. Williams, Phys. Rev. **168,** 922 (1968).

[138] S. Y. Chiang and G. L. Pearson, J. Luminescence **10,** 313 (1975).

[139] W. J. Turner, G. D. Petit, and N. G. Ainslie, J. Appl. Phys. **34,** 3274 (1963).

[140] V. V. Batavin and G. V. Popov, Sov. Phys. Semicond. **7,** 1194 (1974).

[141] M. Tajima, in *Defects and Properties of Semiconductors: Defect Engineering,* edited by K. Sumino and K. Wada (KTK Scientific Publishers, Tokyo, 1987), p. 37.

[142] P. W. Yu, in *Semi-Insulating III-V Materials,* edited by D. C. Look and J. S. Blakemore (Shiva Publishing, Nantwich, UK, 1984), p. 278.

[143] A. Mircea-Roussel and S. Makram-Ebeid, Appl. Phys. Lett. **38,** 1007 (1981).

[144] P. W. Yu and D. C. Look, Avionics Laboratory, Wright-Patterson Air Force Base (private communication).

[145] E. Yablonovitch, T. Gmitter, J. P. Harbison, and R. Bhat, Appl. Phys. Lett. **51,** 2222 (1987).

[146] B. F. Aull, M.I.T. Lincoln Laboratory (private communication).

[147] M. Shur, *GaAs Devices and Circuits* (Plenum Press, New York, 1987).

[148] M. Kaminska, M. Skowronski, J. Lagowski, J. M. Parsey, and H. C. Gatos, Appl. Phys. Lett. **43,** 302 (1983).

[149] R. S. Berg, N. Mavalvala, F. W. Smith, and A. R. Calawa, submitted to Phys. Rev. B.

[150] D. E. Aspnes and A. A. Studna, Phys. Rev. B **27,** 985 (1983).

[151] M. Cardona, in *Light Scattering in Solids II,* edited by M. Cardona and G. Guntherodt (Springer-Verlag, Berlin, 1982), p. 19.

[152] R. S. Berg, P. Y. Yu, and E. R. Weber, Appl. Phys. Lett. **47,** 515 (1985).

[153] R. S. Berg and P. Y. Yu, Phys. Rev. B **33,** 7349 (1986).

[154] R. S. Berg and P. Y. Yu, Phys. Rev. B **35,** 2205 (1987).

[155] R. S. Berg, N. Mavalvala, H. Warriner, and B. Zhang, Phys. Rev. B **39,** 620 (1989).

[156] R. L. Farrow, R. K. Chang, S. Mroczkowski, and F. H. Pollak, Appl. Phys. Lett. **31,** 768 (1977).

[157] T. Nakamura and T. Katoda, J. Appl. Phys. **53,** 5870 (1982).

[158] C. S. Ramo Rao and S. Sundaram, J. Appl. Phys. **54,** 1808 (1983).

[159] M. Holtz, R. Zallen, O. Brafman, and S. Matteson, Phys. Rev. B **37,** 4609 (1988).

[160] K. K. Tiong, P. M. Amirtharaj, F. H. Pollak, and D. E. Aspnes, Appl. Phys. Lett. **44,** 122 (1984).

[161] S. Ushioda, Solid State Commun. **15,** 149 (1974).

[162] J. E. Smith, Jr., M. H. Brodsky, B. L. Crowder, and M. I. Nathan, in *Light Scattering in Solids,* edited by M. Balkanski (Flammarion, Paris, 1971), p. 330.

[163] M. Holtz, R. Zallen, and O. Brafman, Phys. Rev. B **38,** 6097 (1988).

[164] H. Richter, Z. P. Wang, and L. Ley, Solid State Commun. **39,** 625 (1981).

[165] R. Shuker and R. W. Gammon, Phys. Rev. Lett. **25,** 222 (1970).

[166] J. L. T. Waugh and G. Dolling, Phys. Rev. **132,** 2410 (1963).

[167] G. Dolling and R. A. Crowley, Proc. Phys. Soc. **88,** 463 (1966).

[168] H. Bilz and W. Kress, *Phonon Dispersion Relations in Insulators* (Springer-Verlag, Berlin, 1979).

[169] W. Reichardt and K. H. Rieder, *Proc. of the Conf. on Neutron Scattering* (Gatlinburg, TN, 1976), p. 181.

[170] R. S. Berg (private communication).

[171] M. Scheffler and U. Scherz, in *Defects in Semiconductors,* edited by H. J. von Bardeleben (Trans Tech Publications, Aedermannsdorf, 1986), p. 353.

[172] E. R. Weber, in *Proc. Soc. Photo-Opt. Instrum. Eng. 524* (SPIE, Bellingham, WA, 1985), p. 160.

[173] R. J. Wagner, J. J. Krebs, G. H. Strauss, and A. M. White, Solid State Commun. **36,** 15 (1980).

[174] R. M. Eisberg, *Fundamentals of Modern Physics* (Wiley, New York, 1961).

[175] C. Cohen-Tannoudji, B. Diu, and F. Laloe, *Quantum Mechanics* (Wiley, New York, 1977).

[176] M. Baeumler, U. Kaufmann, and J. Windscheif, Appl. Phys. Lett. **46,** 781 (1985).

[177] M. Baj and P. Dreszer, in *Proc. 15th International Conference of Defects in Semiconductors,* edited by G. Ferenczi, Materials Science Forum, Vol. 38-41 (Trans Tech Publications, Aedermannsdorf, 1989), p. 101.

[178] D. M. Hoffman, B. K. Meyer, F. Lohse, and J. M. Spaeth, Phys. Rev. Lett. **53,** 1187 (1984).

[179] D. M. Hoffman, J. M. Spaeth, and B. K. Meyer, in *Defects in Semiconductors,* edited by H. J. von Bardeleben (Trans Tech Publications, Aendermannsdorf, 1986), p. 311.

[180] A. Goltzene, B. Meyer, and C. Schwab, J. Appl. Phys. **57,** 5196 (1985).

[181] H. J. von Bardeleben, D. Stievenard, and J. C. Bourgoin, Appl. Phys. Lett. **47,** 970 (1985).

[182] J. Wosik, M. Palczewska, and M. Kaminska, Acta Phys. Pol. **A69,** 431 (1986).

[183] A. Goltzene, B. Meyer, and C. Schwab, J. Appl. Phys. **57,** 1332 (1985).

[184] G. A. Maracas, K. Wadhera, D. A. Johnson, F. W. Smith, and A. R. Calawa (unpublished).

[185] L. J. van der Pauw, Philips Res. Repts. **13,** 1 (1958).

[186] D. C. Look, *Electrical Characterization of GaAs Materials and Devices* (Wiley, New York, 1989).

[187] D. C. Look, D. C. Walters, M. O. Manasreh, J. R. Sizelove, C. E. Stutz, and K. R. Evans, submitted to Phys. Rev. B.

[188] N. F. Mott and E. A. Davis, *Electronic Processes in Non-crystalline Materials* (Clarendon Press, Oxford, 1979).

[189] O. Madelung, *Introduction to Solid-State Theory* (Springer-Verlag, Berlin, 1978), Chapter 10.

[190] A. C. Campbell, G. E. Crook, T. J. Rogers, and B. G. Streetman, presented at the 10th Molecular Beam Epitaxy Workshop, Raleigh, NC, September, 1989.

[191] G. A. Baraff and M. Schluter, Phys. Rev. Lett. **55,** 1327 (1985).

[192] M. A. Lampert and P. Mark, *Current Injection in Solids* (Academic, New York, 1970).

[193] D. C. D'Avanzo, Hewlett Packard (private communication).

[194] W. I. Wang, S. Judaprawira, C. E. C. Wood, and L. F. Eastman, Appl. Phys. Lett. **38,** 708 (1981).

[195] J. P. McKelvey, *Solid State and Semiconductor Physics* (Krieger, Malabar, FL, 1984), Chapter 10.

[196] M. J. Manfra and A. R. Calawa (unpublished).

[197] G. W. Turner, B. A. Nechay, and S. J. Eglash, presented at the 10th Annual MBE Workshop, Raleigh, NC, Sept., 1989.

[198] G. A. Patterson, Hewlett-Packard (private communication).

[199] R. Mariella, Lawrence Livermore (private communication).

[200] S. Notomi, Y. Awano, M. Kosugi, T. Nagata, K. Kosemura, M. Ono, N. Kobayashi, H. Ishiwari, K. Odani, T. Mimura, and M. Abe, in *Technical Digest IEEE GaAs IC Symposium* (IEEE, New York, 1987), p. 177.

[201] Y. D. Shen, M. R. Wilson, M. McGuire, D. A. Nelson, and B. M. Welch, in *Technical Digest IEEE GaAs IC Symposium* (IEEE, New York, 1987), p. 125.

[202] M. C. Nuss and D. H. Auston, in *Picosecond Electronics and Optoelectronics II,* edited by F. J. Leonberger, C. H. Lee, F. Capasso, and H. Morkoc (Springer-Verlag, Berlin, 1987), p. 72.

[203] D. V. Lang, J. Appl. Phys. **45,** 3023 (1974).

[204] A. P. DeFonzo, C. R. Lutz, and M. Jarwala, in *Picosecond Electronics and Optoelectronics II,* edited by F. J. Leonberger, C. H. Lee, F. Capasso, and H. Morkoc (Springer-Verlag, Berlin, 1987), p. 280.

BIOGRAPHICAL SKETCH

Frank W. Smith is a summa cum laude graduate of Yale University with a B.S. degree in engineering and applied science. He received the S.M. degree in electrical engineering from the Massachusetts Institute of Technology in 1985.

Between his undergraduate and graduate programs he was employed by IBM in the manufacturing and development of silicon bipolar integrated circuits. As a research assistant in the Microsystems Technology Laboratory at MIT, his work involved the study of the electrical and mechanical properties of VLSI materials and integrated microsensor technology. Since 1986, as a research assistant at the MIT Lincoln Laboratory, he has been investigating the device applications and characterization of nonstoichiometric GaAs grown by molecular beam epitaxy for his Ph.D. degree at MIT. Following the completion of this thesis, he will become a Member of the Technical Staff, in the Solid State Division, of the M.I.T. Lincoln Laboratory.

Mr. Smith is a member of Phi Beta Kappa, Tau Beta Pi, and Sigma Xi. He received the best student presentation award of the 1985 Electronic Materials Conference.